University of Tasmania

Doctoral Thesis

# The evolution of anticyclonic eddies of the Tasman Sea: vertical velocity and other properties


*Author:*
Gabriela Semolini Pilo
BSc., MSc.

*Supervisors:*
Dr. Peter Oke
Prof. Richard Coleman
Dr. Tatiana Rykova
Mr. Ken Ridgway


A thesis submitted in fulfilment of the requirements for the degree of

*Doctor of Philosophy in Quantitative Marine Science*

a joint programme between the

Institute for Marine and Antarctic Studies and CSIRO Oceans & Atmosphere

April 2018

# *Abstract*

Eddies play a critical role in the distribution of heat and other properties in the oceans. They are most intense in regions of western boundary currents, where the kinetic energy associated with eddies is one order of magnitude greater than the kinetic energy associated with the mean flow. The East Australian Current (EAC) is the western boundary current of the South Pacific Ocean. Its flow and related mesoscale variability extend through the Tasman Sea - a region characterised by high variability associated with a complex field of eddies.

Here, the path of long-lived anticyclonic eddies originating in the EAC is explored. In addition, the evolution of their properties and dynamics over time is also investigated, with a focus on their vertical velocity. These eddies are studied in fields from a free-running ocean model, from a data-assimilating ocean model, and from gridded satellite altimetry. In this thesis, I choose to examine case studies of eddies. This approach contrasts to most recent studies of eddies that tend to undertake statistical analyses of a large number of eddies. Moreover, the eddies are manually tracked - again, in contrast to a large portion of the community who have embraced datasets generated by automatic eddy-tracking algorithms. The improved accuracy and reliability of a manual approach warrants the additional time and effort to carefully track each eddy.

Analysis of anticyclonic eddies that form from the EAC indicates that such eddies can "live" for over 5 years. I find that some of these eddies leave the Tasman Sea, propagate around Tasmania, and move towards the Indian Ocean. As they propagate, their amplitude is often impacted by interactions with other eddies and with the continental slope. Additionally, the speed at which eddies propagate varies considerably - with some eddies stalling in the same latitude for up to six months. As eddies propagate out of the Tasman Sea, their circulation becomes systematically more barotropic - with deeper penetrating velocities.

One of the most interesting findings of this thesis is that the vertical velocity in eddies often shows alternating upward and downward cells. Such cells have been previously reported - but were not fully explained, in terms of their dynamics. Here, a dynamical explanation for these cells is provided. Specifically, the alternating cells are shown to relate to a process referred to in this thesis as "eddy distortion". Eddy distortion refers to the change of shape of an eddy - that is, when an eddy becomes more, or less, isotropic. This distortion can be quantified by the change of sea level anomaly (SLA) associated with the eddy in time - also seen as alternating positive and negative cells. This quantity can be linked to the eddy interior dynamics and, ultimately, vertical velocity. In a region of inward distortion of an anticyclonic eddy, the SLA decreases and the water

column below the permanent pycnocline vertically stretches, generating cyclonic relative vorticity and inducing upward motion. Conversely, in a region of outward distortion, the SLA increases and the water column below the permanent pycnocline vertically squeezes, generating anticyclonic relative vorticity and inducing downward motion. I find that the alternating cells are remarkably long-lived and spatially coherent. These cells typically extend from 2000 m depth to the base of the thermocline and their magnitude are often 20-50 m/d. The alternating upward and downward cells explain 30-60% of the variance of the vertical velocity within each eddy. The vertical circulation within eddies, described here, is expected to significantly impact the distribution of ocean properties, including heat, freshwater, and marine biota.

Recognition of the link between eddy distortion - quantified by the temporal change of SLA - and the vertical circulation within eddies opens the door for the development of algorithms that link sea level to ocean productivity, and other oceanographic metrics. This has not been explored here - but is an exciting topic for future work.

# Declaration of Authorship

This thesis contains no material which has been accepted for a degree or diploma by the University or any other institution, except by way of background information and duly acknowledged in the thesis, and to the best of my knowledge and belief no material previously published or written by another person except where due acknowledgement is made in the text of the thesis, nor does the thesis contain any material that infringes copyright.

Signed: _____

Date: 09/05/2018

# Authority of Access

This thesis may be made available for loan and limited copying and communication in accordance with the *Copyright Act 1968*.

Signed: _____

Date: 09/05/2018

## Published work contained in the thesis

A number of scientific articles have been or are in the process of being published as a result of this work.

While the following articles have co-authors, the analysis, figures, and text included in this thesis have been produced by myself. I note that I did not run or fully assessed the global, eddy-resolving ocean model used throughout this thesis.

The methods described in **Chapter 2** and most of the results from **Chapters 3** have been published in: Pilo, G. S., Oke, P. R., Rykova, T., Coleman, R., and Ridgway, K., 2015, **Do East Australian Current anticyclonic eddies leave the Tasman Sea?**, Journal of Geophysical Research: Oceans, 120, 8099-8114, doi:10.1002/2015JC011026. In this paper, I contributed with the analysis, figures, and text. This paper is fully reproduced in Appendix A.

**Chapter 4** has been published as: Pilo, G. S., Oke, P. R., Coleman, R., Rykova, T., and Ridgway, K., **Patterns of eddy vertical velocity induced by eddy distortion in an ocean model**, Journal of Geophysical Research: Oceans, 123, doi:10.1002/2017JC013298. In this paper, I contributed with the analysis, figures, and text.

**Chapter 5** will be published as: Pilo, G. S., Oke, P. R., Coleman, R., Rykova, T., and Ridgway, K., **Impact of data assimilation on vertical velocities in an eddy resolving ocean model**, submitted to Ocean Modelling. In this paper, I contributed with the analysis, figures, and text.

Some of the results from **Chapters 3 and 4** will be published in the following review paper: Oke, P. R., Roughan, M., Cetina-Heredia, P., Pilo, G. S., Ridgway, K., Rykova, T., Archer, M. R., Coleman, R., Kerry, C. G., Rocha, C., Sloyan, B. M., Vitarelli, E., **Revisiting the circulation of the East Australian Current: its path, separation and eddy field**, to be submitted to Progress in Oceanography. In this paper, I contributed with figures, text, and editing. Therefore, this paper includes my contribution, but it is not claimed as an original work by me.

# Statement of Co-authorship

The following people and institutions contributed to the publication of work undertaken as part of this thesis:

**Candidate:** Gabriela Semolini Pilo, IMAS and CSIRO Oceans and Atmosphere
**Author 1:** Peter Oke, CSIRO Oceans and Atmosphere
**Author 2:** Richard Coleman, IMAS and Antarctic Climate and Ecosystems CRC
**Author 3:** Tatiana Rykova, CSIRO Oceans and Atmosphere
**Author 4:** Ken Ridgway, CSIRO Oceans and Atmosphere.

In the paper entitled "Do East Australian Current anticyclonic eddies leave the Tasman Sea?" the candidate was the primary author, and all authors contributed to the research, its formalisation and development. Author 1 contributed with writing.

In the paper entitled "Patterns of eddy vertical velocity induced by eddy distortion in an ocean model", the candidate was the primary author, and all authors contributed to the research, its formalisation and development.

In the paper entitled "Impact of data assimilation on vertical velocities in an eddy resolving ocean model", the candidate was the primary author, and performed the analysis. Author 1 contributed with most research ideas and development. Authors 2, 3, and 4 contributed with formalisation of the manuscript.

I, the undersigned, agree with the above stated co-authorship for each of the above published and submitted peer-reviewed manuscripts contributing to this thesis:

---

**Prof. Richard Coleman**
*Supervisor and Executive Director*
Institute for Marine and Antarctic Studies,
University of Tasmania
Date: 09/05/2018

# *Acknowledgements*

I could have not asked for a better team of supervisors. Each one of them contributed in different, but fundamental, ways to my growth as a researcher. I would like to thank Peter, Richard, Tatiana, and Ken, for their supervision and, most important, for their friendship - the outcome of my PhD would have been completely different without it.

I thank the team of researchers at CSIRO, at IMAS, and at the physical oceanography department at UNSW, for exciting discussions and continuous revisions of my work. The joint programme between IMAS and CSIRO gave me the opportunity to interact with researchers from both organisations. I feel fortunate to be part of this community. I also thank the reviewers of this thesis, who made a valuable contribution to this work.

I would also like to thank my parents, for always providing me with a safe harbour, for continually supporting me on my decisions, and for being so close while being so far. My thanks also go to my grandparents - who dealt with the long distance between Brazil and Australia over the years - and to my partner Leandro - who supported me during the final stages of this work.

I am grateful to all the friends who came and went during the PhD years. Each one of you contributed in your own way to keep me motivated and to have a balanced life. Thank you.

Finally, I thank the Brazilian Government and the QMS programme for financial support, the Bluelink team for the development and maintenance of the ocean models used here, and the OceanCurrent team for preparation and distribution of the altimetry data.

**Gabriela Semolini Pilo**

December, 2017

# Contents

***"I felt that nauseating vertigo that arises from long-continued whirling."***

when the *Nautillus* meets the maelstrom
in Twenty Thousand Leagues Under the Sea, by Jules Verne.

# Chapter 1

# Introduction

The highest kinetic energy of mesoscale variability in the ocean occurs in regions of western boundary currents (WBCs; Figure 1.1). In these regions, the eddy kinetic energy (i.e., the energy associated with the mesoscale) is between one and two orders of magnitude higher than the mean kinetic energy (i.e., the energy associated with the mean flow; e.g., Wyrtki et al., 1976, Qiu et al., 1991, Boebel et al., 2003, Oliveira et al., 2009, Oke et al., 2010). Roughly 90% of the Eddy Kinetic Energy (EKE) in WBC regions is attributed to the geostrophic eddy field (Wunsch and Stammer, 1998, Ferrari and Wunsch, 2009). Eddies in WBC regions are the most energetic in the ocean (Wyrtki et al., 1976, Olson, 1991, Fu et al., 2010), and they play a critical role in the conversion of energy (e.g., Gill et al., 1974, Waterman and Jayne, 2011), and in the transport of heat, salt, and other chemical constituents within and beyond these regions (e.g., Stammer, 1998, Wunsch, 1999, Roemmich and Gilson, 2001, Jayne and Marotzke, 2002, Booth and Kamenkovich, 2008, Dong et al., 2014).

The East Australian Current (EAC; Figure 1.2) is the WBC of the South Pacific subtropical gyre (Boland and Church, 1981, Lindstrom et al., 1987, Tomczak and Godfrey, 2013, Ganachaud et al., 2014). It is characterised by a warm, poleward current that flows - on average - as a jet between $\sim$20-31$^o$S off eastern Australia, before separating from the coast at 28-34$^o$S (Wyrtki, 1960, Godfrey et al., 1980, Boland and Church, 1981, Ridgway and Godfrey, 1997, Cetina-Heredia et al., 2014, Sloyan et al., 2016, Ypma et al., 2016). The EAC separation from the coast has been attributed to the orientation of the coastline (Godfrey et al., 1980), the effect of Rossby waves coming from the east (Nilsson and Cresswell, 1981, Marchesiello and Middleton, 2000, Hill et al., 2010), the effect of the basin-wide wind stress curl (Tilburg et al., 2001), and vorticity dynamics (Kiss, 2002).

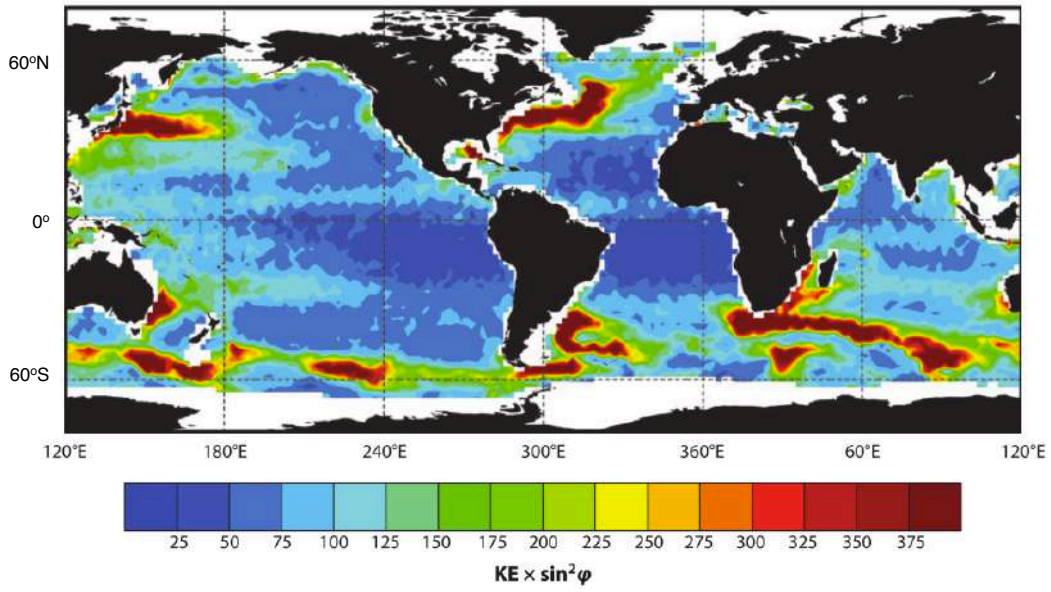


FIGURE 1.1: Weighted eddy kinetic energy (EKE) at the sea surface, in $cm^2/s^2$, estimated from four years of TOPEX/POSEIDON satellite altimetry data. The weighted EKE is the EKE multiplied by $\sin(\varphi)$, where $\varphi$ is the latitude, to avoid the equatorial singularity in noisy data (reproduced from Wunsch and Stammer, 1998).

Unlike the strength of other WBCs, the strength of the EAC varies substantially with time, and often a single continuous current cannot be identified (Godfrey et al., 1980, Ridgway and Godfrey, 1997, Wilkin and Zhang, 2007, Ridgway and Hill, 2009). The EAC poleward transport at $27^oS$ is 22.1±7.5 Sv (Sloyan et al., 2016). This transport is much smaller than transports associated with the Agulhas Current (∼70 Sv; Bryden et al., 2005), the Gulf Stream (31-150 Sv; Hogg, 1992, Beal et al., 2008), and the Kuroshio (∼ 43 Sv; Imawaki et al., 2001, Jayne et al., 2009), but comparable to the Brazil Current transport at this current's separation point (∼22 Sv; Peterson et al., 1991). The maximum poleward transport within eddies of the EAC is ∼6 Sv (Cetina-Heredia et al., 2014) - almost 1/3 of the poleward transport associated with the current itself. Therefore, eddies play an important role in the region's variability and heat advection.

After the EAC separates from the coast, its flow branches into an eastward and a southward component (Figure 1.2). The eastward component of the EAC follows the Tasman Front, flowing across the Tasman Sea and reaching the northern tip of New Zealand (Andrews et al., 1980, Godfrey et al., 1980, Ridgway and Dunn, 2003). The path of this front is defined by the system of ridges between Australia and New Zealand (Ridgway and Dunn, 2003). The southward component of the EAC evolves into a complex field of mesoscale eddies (Nilsson and Cresswell, 1981, Ridgway and Godfrey, 1997, Ridgway

and Dunn, 2003, Mata et al., 2006). This eddy field, averaged over time, forms the poleward flow called the "EAC extension" (Cresswell, 2000, Ridgway and Dunn, 2003).

The eastward transport at the Tasman Front and the poleward transport at the EAC extension are anti-correlated (Hill et al., 2011). That is, there is a "gating" of EAC waters flowing along the Tasman Front and the EAC extension (Hill et al., 2011, Sloyan et al., 2016). The EAC strength, and its role in the "gating" partitioning, changes in interannual and decadal scales (Hill et al., 2011). While the ENSO signal is weak on the interannual scale, it strongly affects the decadal scale (Ridgway, 2007). Changes in the decadal scale respond to the variability of the basin-wide wind stress curl, attributed to variations in the El Nino Southern Oscillation (Sasaki et al., 2008, Hill et al., 2011, Sloyan et al., 2016). As the wind stress curl shifts the subtropical gyre of the South Pacific southwards, more waters are fed into the EAC extension, at the expense of waters fed into the Tasman Front. In climate change projections, the volume transport of the EAC extension is expected to increase, also at the expense of the flow along the Tasman Front (Oliver and Holbrook, 2014).

The EAC extension feeds the Tasman Leakage. This leakage is reported to be an intermediate-depth poleward flow off south-eastern Australia, around the southern tip of Tasmania, and extending towards the Indian Ocean (Speich et al., 2002, van Sebille et al., 2012, Rosell-Fieschi et al., 2013; Figure 1.2). Around half of the Tasman Leakage is carried out within cyclonic and anticyclonic eddies, while the other half is seen as a continuous flow (van Sebille et al., 2012). The Tasman Leakage is a component of the Southern Ocean super-gyre, a circulation that comprises all three sub-tropical basins of the Southern Hemisphere (Speich et al., 2002, Ridgway and Dunn, 2007). As part of the super-gyre, the Tasman Leakage distributes Subantarctic Mode and Antarctic Intermediate Waters between the basins of the South Pacific and the Indian Ocean, before it spreads to the global ocean (Speich et al., 2007, Rosell-Fieschi et al., 2013). Therefore, understanding the Tasman Leakage, and the role of eddies in the water exchange involved in it, is essential in terms of both regional and global circulation.

EAC anticyclonic eddies form in the EAC separation region approximately every 90-120 days (Nilsson and Cresswell, 1981, Marchesiello and Middleton, 2000, Bowen et al., 2005, Mata et al., 2006, Wilkin and Zhang, 2007, Ridgway et al., 2008). These eddies often pinch-off from the EAC meander formed during the EAC separation process (Figure 1.3), and carry source waters originating equatorward of the EAC (Rykova et al., 2017). EAC cyclonic eddies may form from cooler waters found between the continental shelf and the EAC (Marchesiello and Middleton, 2000, Macdonald et al., 2016). EAC eddies are important for the regional circulation, influencing water mass distribution and transformation in the Tasman Sea (Waugh et al., 2006), coastal upwelling (Tranter

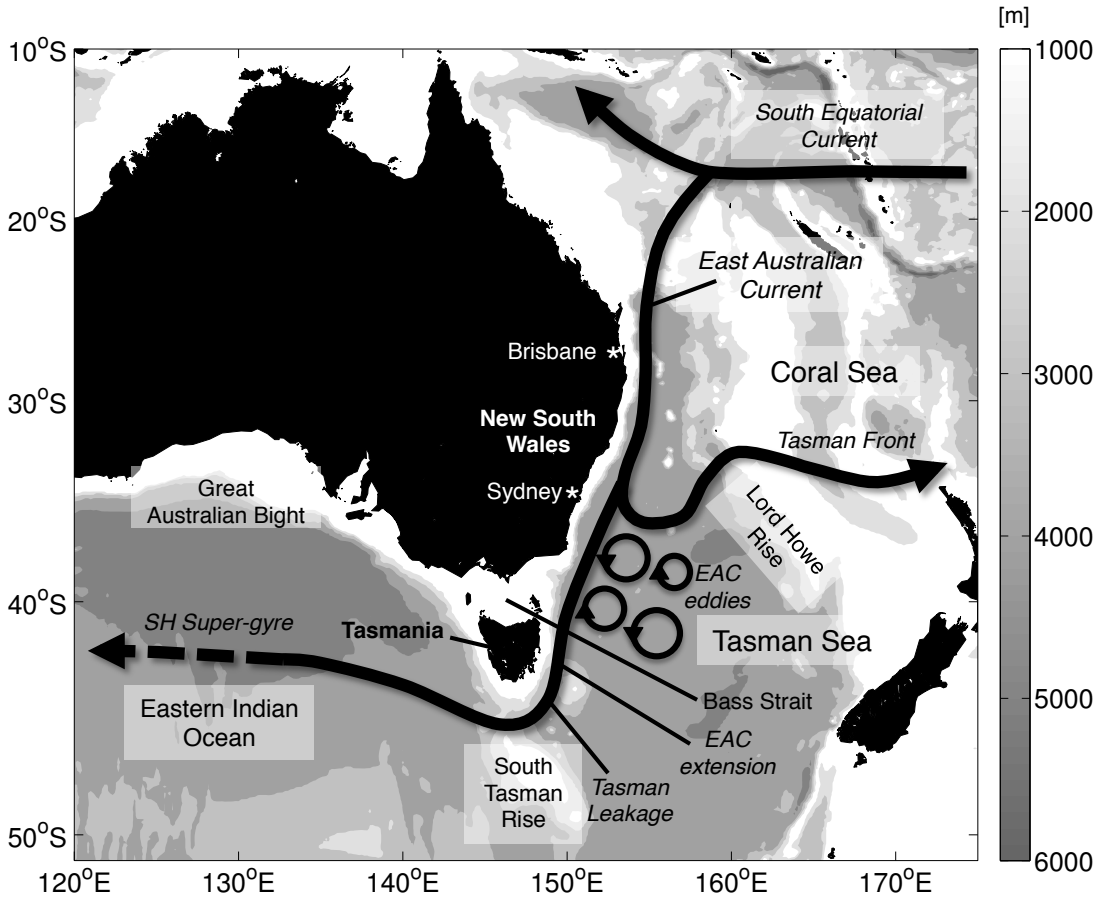


FIGURE 1.2: Map of the oceans off eastern and southern Australia depicting main oceanographic and bathymetric features.

et al., 1982, Marchesiello and Middleton, 2000, Oke and Griffin, 2011), primary productivity (Tranter et al., 1980, Everett et al., 2012), and distribution of marine organisms (Suthers et al., 2011 and references therein; Condie and Condie, 2016). EAC eddies transport heat, salt, and other properties, and interact with the mean flow. Therefore, it is important to understand their dynamics, propagation, and evolution.

Previous analyses of EAC eddies indicate that they often stay close to the continental slope between their formation region and about 40$^o$S (Nilsson and Cresswell, 1981, Cresswell and Legeckis, 1986, Brassington et al., 2011, Everett et al., 2012, Pilo et al., 2015). The clustering of eddies close to the coast is influenced by bathymetry, as the Tasman Sea basin is limited to the west by the Australian continent and to the east by the Lord Howe Rise (Ridgway and Dunn, 2003; Figure 1.2). The high number of eddies within the deep Tasman Sea basin explains an intense variability in the region (Morrow et al., 1992, Qiu and Chen, 2004, Bowen et al., 2005, Mata et al., 2006). Indeed, that region within the Tasman Sea has high EKE (Figure 1.1). However, some large eddies - first identified off south-eastern Tasmania - have been reported propagating south of

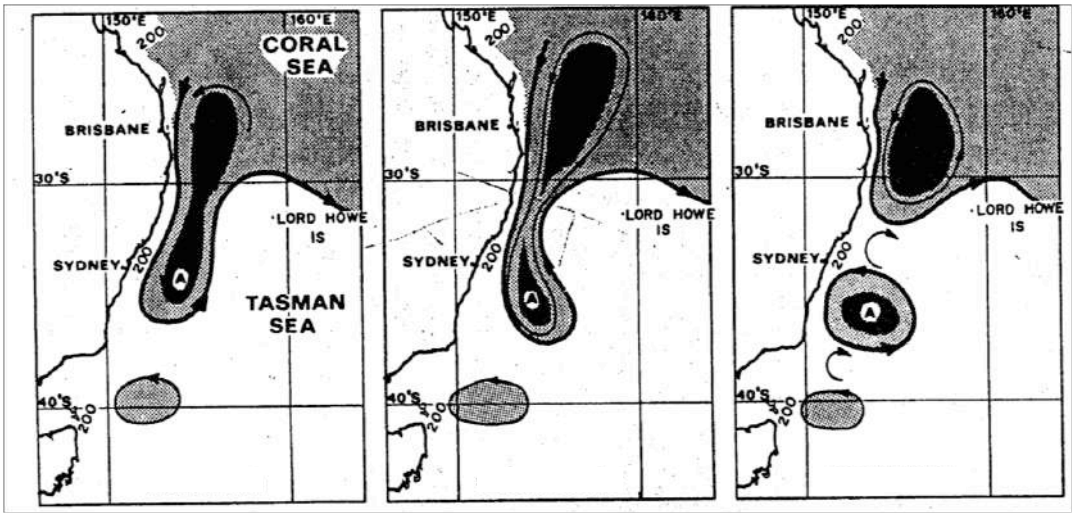


FIGURE 1.3: Drawing depicting the shedding of an anticyclonic eddy by the EAC. The thick black lines separate the Coral Sea warm waters from the Tasman Sea cold waters (adapted from Nilsson and Cresswell, 1981).

Tasmania, and advecting westwards in the Eastern Indian Ocean (Baird and Ridgway, 2012, Pilo et al., 2015, Oliver et al., 2015). While it is agreed that EAC anticyclonic eddies propagate southwards to about 40$^o$S, the link between eddies shed by the EAC and the large eddies first identified off Tasmania that propagate towards the Eastern Indian Ocean is unclear. In addition, whether eddies form within the Tasman Sea, then follow the Tasman Front - in a process similar to eddies in the Agulhas Return Current (e.g., Lutjeharms and Ansorge, 2001, Pilo et al., 2015) - is also unknown.

Various aspects of EAC eddies have been investigated using shipboard observations (Andrews and Scully-Power, 1976, Nilsson and Cresswell, 1981, Cresswell, 1982, Cresswell and Legeckis, 1986, Tranter et al., 1986, Everett et al., 2014, Roughan et al., 2017), autonomous gliders observations (Baird et al., 2011, Baird and Ridgway, 2012), Argo float observations (Rykova and Oke, 2015), remote sensing data (Morrow et al., 1992, 1994, Everett et al., 2012, Pilo et al., 2015), and numerical models (Oke and Griffin, 2011, Rykova et al., 2017). These studies show that typical EAC anticyclonic eddies have 95 km radii, are associated with 24 cm positive sea level anomaly (SLA), and rotate at 50 cm/s (Everett et al., 2012). They exist - on average - for 6 months, but can live up to five years and propagate over long distances, between the EAC separation region and east of Tasmania (Pilo et al., 2015). About 70% of EAC anticyclonic eddies are associated with positive sea surface temperature anomalies (Everett et al., 2012). EAC anticyclonic eddies have a mean volume of $3\times10^{13}$ m$^3$, and mean heat content anomaly of $2\times10^{20}$ J in their interior (Rykova et al., 2017). Conversely, typical EAC cyclonic eddies have 92 km radii, are associated with 23 cm negative SLA, and rotate at 45 cm/s (Everett et al., 2012). They also exist - on average - for 25 weeks, and also propagate within

the Tasman Sea (Pilo et al., 2015). About 70% of EAC cyclonic eddies are associated with negative sea surface temperature anomalies (Everett et al., 2012). EAC cyclonic eddies have a smaller mean volume than anticyclonic eddies ($2\times10^{13}$ $m^3$), but the same - although negative - mean heat content anomaly in their interior ($2\times10^{20}$ J; Rykova et al., 2017). Roughly 65% of EAC cyclonic eddies have a positive surface chlorophyll-a anomaly in their interior; at the same time, only 15% of EAC anticyclonic eddies have positive chlorophyll-a anomalies (Everett et al., 2012).

EAC eddies from the literature have similarities and differences to eddies from other WBCs (e.g, Olson, 1991, Nilsson and Cresswell, 1981, Lentini et al., 2006, Rykova et al., 2017). The radius and rotation speed of large, long-lived EAC eddies reported in early studies are comparable to other large, long-lived WBCs eddies (Olson, 1991) - except for the Agulhas Rings, which have larger radii (e.g., Olson, 1991, Schmid et al., 2003). However, when datasets with a higher spatial resolution are considered - and hence smaller eddies are included in the comparison -, the SLA associated with EAC eddies is smaller than with other WBCs eddies (Rykova et al., 2017). This is also valid for the sea surface temperature anomalies, volume, and heat content anomalies associated with EAC eddies, when compared to other eddies (Rykova et al., 2017). In addition, EAC eddies are less barotropic than eddies from other WBCs (Rykova et al., 2017).

EAC eddies have been reported interacting with the mean flow (Nilsson and Cresswell, 1981, Mata et al., 2006, Baird et al., 2011), with bathymetry (Oke and Griffin, 2011, Roughan et al., 2017), and with other eddies (Cresswell and Legeckis, 1986). These studies show that all these interactions affect the three-dimensional properties and structure of eddies. For this reason, it is expected that long-lived EAC eddies undergo many changes over time.

While there are several studies of the properties of EAC eddies, not many studies focus on the change of these properties over time. In an early study, Nilsson and Cresswell (1981) describe, using hydrographic and satellite data, the evolution of two anticyclonic eddies in the Tasman Sea. Over 11 months, the eddies decay, contract horizontally, and have alternating layers formed by winter convective cooling and by summer mixing (Figure 1.4b). This analysis, however, is limited to the top 500 m of the ocean, and only provides a synoptic view - because it takes from 2 to 5 days to sample each eddy. In a more recent study, Roughan et al. (2017) describe, using hydrographic and satellite data, the formation and evolution of two cyclonic eddies off the eastern coast of Australia. The eddies are ∼1000 m deep, short-lived, highly productive, and vertically tilting towards the continental shelf break. These eddies, however, only represent two case studies. These two examples are some of the few studies reporting the evolution of EAC eddies. Therefore, despite the thorough description of the three-dimensional

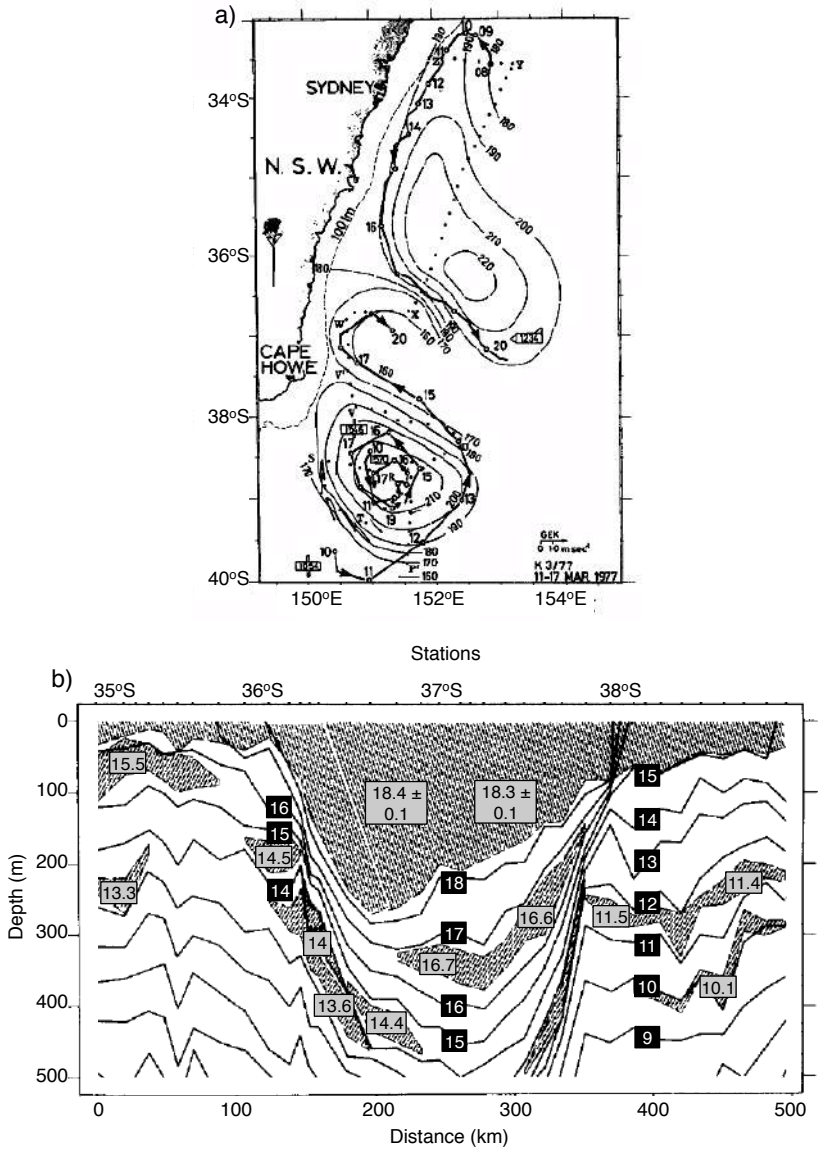


FIGURE 1.4: a) Map of dynamic topography D(0/1300) dyn cm off eastern Australia depicting two anticyclonic eddies sampled in 1976 and 1977; b) Vertical section (0-500 m) of temperature from XBT (expendable bathythermograph) data along the north-south dashed line in the northern eddy from (a) in October 1976. The hatched areas in (b) denote isothermal or nearly isothermal mixed waters, and the boxes denote temperature values (adapted from Nilsson and Cresswell, 1981).

properties of EAC eddies in the literature, the change of these properties over time requires further investigation. More specifically, the evolution of the three-dimensional properties of long-lived EAC eddies remains unknown.

The vertical circulation within eddies has received less attention than other aspects of eddy dynamics. This circulation impacts the transport of properties between the ocean surface and the ocean interior (e.g., Nurser and Zhang, 2000, Roemmich and Gilson, 2001), and ecological and biogeochemical processes (e.g., Falkowski et al., 1991,

McGillicuddy et al., 1998, Sweeney et al., 2003, Siegel et al., 2008, Klein and Lapeyre, 2009, Siegel et al., 2011, Gaube et al., 2013, Waite et al., 2016). Notwithstanding the importance of the vertical circulation within eddies, little is known about the details. The broadly accepted conceptual model of the vertical circulation within eddies includes upward motion in the centre of cyclonic eddies, and downward motion in the centre of anticyclonic eddies, as depicted in the seminal papers by McGillicuddy and Robinson (1997) and McGillicuddy et al. (1998) on eddies and primary production (Figure 1.5). The schematic in Figure 1.5 paints a simplified picture of the vertical circulation within eddies. Despite the insights into the effect of eddies on primary production shown in those studies, they have led to a wide-spread conceptual misunderstanding. Indeed, this simplified schematic has led many researchers - from several fields of marine research - to refer to "upwelling eddies" and to "downwelling eddies" (e.g., Tilburg et al., 2002, Uysal, 2006, Alpine and Hobday, 2007, Paterson et al., 2007, Nemcek et al., 2008, Oliver and Holbrook, 2014). This early schematic was later revisited by Flierl and McGillicuddy (2002) and McGillicuddy (2016), where it is acknowledged that the motion in the centre of eddies is only upwards or downwards during the formation, or intensification, of eddies. Other studies, however, show that the vertical circulation is more complicated than the patterns depicted in these schematics (e.g., Franks et al., 1986, Martin and Richards, 2001, Pallas-Sanz and Viudez, 2007, Hu et al., 2011, Siegel et al., 2011, Nardelli, 2013, Pidcock et al., 2013, Waite et al., 2016). This conceptual misunderstanding, and the different patterns of vertical circulation within eddies, are motivations to better understand the vertical circulation within EAC eddies.

To date, only one study describes the vertical circulation within an EAC eddy in a data-assimilating, eddy-resolving ocean model (Oke and Griffin, 2011). The authors suggest that, as the cyclonic EAC eddy interacts with the continental shelf break, it develops an upward motion close to the coast, and a downward motion away from the coast. It is unknown if the pattern of vertical circulation reported by Oke and Griffin (2011) is common in cyclonic EAC eddies. In addition, the vertical circulation within EAC anticyclonic eddies - as well as the temporal change of this circulation - requires investigation.

## 1.1 Thesis objectives

The focus of this thesis is on the three-dimensional structure of EAC anticyclonic eddies. Here, I focus on EAC anticyclonic eddies because they are large, long-lived, and propagate further than their cyclonic counterparts. The specific goals of this thesis are to better understand:

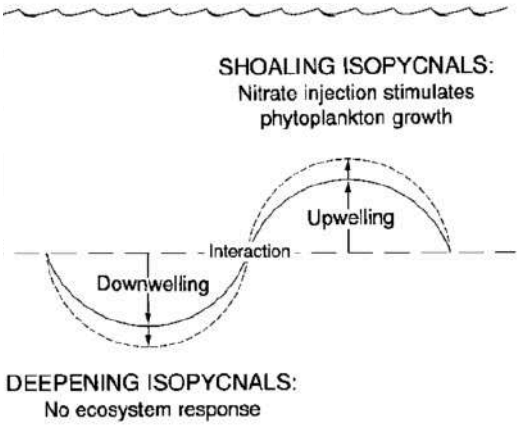


FIGURE 1.5: A schematic representation of upwelling and downwelling associated with an anticyclonic and a cyclonic eddy. The solid line depicts the deepening and shoaling of an individual isopycnal caused by the eddies, and the dashed line depicts a further perturbation of the isopycnal caused by the interaction of the two eddies (adapted from McGillicuddy et al., 1998).

- the pathway of large, long-lived EAC anticyclonic eddies;
- the spatial and temporal changes of the three-dimensional properties of EAC anticyclonic eddies; and
- the vertical circulation within EAC anticyclonic eddies.

## 1.2 Thesis outline

**Chapter 2** contains a description of the datasets used in this thesis and the methods employed. Specifically, it describes the altimetry products and the global, eddy-resolving ocean model used throughout the thesis. Due to the nature of the goals proposed in this thesis, and to reveal details of the evolution of eddies over time, most analyses undertaken here involve a careful examination of case studies. The small number of case studies permits an individual approach to eddy analyses, and a manual approach to eddy-tracking. **Chapter 3** identifies a common pathway of EAC eddies, and describes changes of the three-dimensional properties of these eddies over time. In **Chapter 4**, upward and downward cells within EAC eddies - and their link to changes in eddy shape ("eddy distortion") - are explored. **Chapter 5** is a study focused on the effect of data assimilation on the vertical circulation within EAC eddies in a global, eddy-resolving ocean model. Finally, **Chapter 6** concludes this thesis, stating the main contributions of this work, and suggesting directions for future studies of EAC eddies.

# Chapter 2

# Data and Methods

## 2.1 Introduction

This Chapter contains a description of the global, eddy-resolving ocean model analysed in Chapters 3 and 4, of the altimetry products used in Chapter 3, and of the manual eddy-tracking method applied in Chapters 3, 4, and 5.

Most of the recent studies of ocean eddies include analyses of global datasets (e.g., Chaigneau et al., 2009, Chelton et al., 2011b, Faghmous et al., 2015) and eddy composites (e.g., Dong et al., 2012, Kang and Curchitser, 2013, Pegliasco et al., 2015, Frenger et al., 2015, Amores et al., 2017). The approach used in this thesis, by contrast, is to select a set of representative eddies and to study them in detail. The analysis of case studies permits a meaningful investigation of eddy properties that would, otherwise, be poorly represented in mean fields and composite fields. While this approach may sacrifice some generality and statistical validity, it permits the exploration of more subtle aspects of the eddy dynamics.

## 2.2 Ocean Forecasting Australia Model

### 2.2.1 Description

In this study the output from the last 18 years (1993-2011) of a 36-year run of the Ocean Forecasting Australia Model, version 3, is used (Oke et al., 2013a, OFAM). OFAM is a near-global eddy-resolving configuration of the GFDL Modular Ocean Model, version 4p1 (Griffies et al., 2004). The model has 1/10° horizontal grid spacing between 75°S and 75°N. The vertical grid is $z^\star$ (Griffies, 2009), with 51 vertical levels, with 5 m

spacing near the surface, 10 m spacing at 200 m depth, 120 m spacing at 1000 m depth, and coarser below that. Many model results contained in this thesis are taken from outputs between 500 and 1500 m, where the vertical spacing ranges from 60 to 150 m. The model is run for 36 years, with an 18-year spin-up, and forced with 3-hourly surface heat, freshwater, and momentum fluxes from ERA-interim (Dee and Uppala, 2009), with restoring to monthly sea surface temperature (SST; Reynolds et al., 2007, 10-day restoring time-scale); weak restoring to surface climatological salinity (Ridgway and Dunn, 2003, 180-day restoring); and weak restoring to climatological temperature and salinity below 2000 m depth (restoring time-scale of 365 days). Because of the climatological restoring at depth and coarse vertical resolution, only the top 2000 m of the ocean model fields are considered throughout this study. The output fields of OFAM, analysed throughout this thesis, include daily averages of temperature, salinity, sea level, and the three components of velocity.

### 2.2.2 Limitations

There are limitations associated with OFAM that must be considered in this study. The model grid spacing is $1/10^o$. However, a minimum of 5 grid points are needed to properly "resolve" a mesoscale eddy (Figure 2.1). This means that features with scales smaller than the ones resolved by 5 grid points (i.e., smaller than $\sim$50 km in length) are not represented by the model. These non-resolved features include the smaller spectrum of the mesoscale, and the sub-mesoscale.

Other limitations of the ocean model include errors in topography and accuracy of surface fluxes - in addition to limitations associated with their resolution. The wind forcing, for example, has a $1.5^o$ horizontal resolution. Therefore, features driven by atmospheric forcing with scales smaller than a few hundred kilometres are not represented by the model.

As in other ocean models, the mixing effect of tides, and the background vertical diffusivity and viscosity are parameterised (Table 2.1). These parameterisations may result in imprecise mixing fluxes in some regions of the ocean - for example, regions of large-amplitude tides, such as waters off north-west of Australia.

It is widely understood that global ocean models require a long time to properly "spin up". Climate models, for example, are typically run for tens of thousands of years (e.g., Oke and England, 2004) to properly represent the deep ocean processes (e.g., bottom water formation). However, the computational cost of running OFAM - used here - is too great for running such long runs. Instead, OFAM is run with "deep restoring"

to climatology, where the modelled temperature and salinity fields are nudged to climatology with an e-folding timescale of 365 days, as described in the previous section. This deep restoring may be important for the analyses presented in this thesis. Indeed, this limitation is largely the reason I consider only the top 2000 m of the ocean model throughout this thesis.

### 2.2.3 Assessment

Oke et al. (2013a) provide a comprehensive description and assessment of OFAM. Their assessment includes comparisons between observed and modelled fields of mean sea level (MSL; Figure 2.2a), mixed layer depth (MLD; Figure 2.2b), and volume transports (a subset is shown in Table 2.2). Oke et al. (2013a) also presents an assessment of the modelled sea surface temperature (including the seasonal cycles, seasonal anomalies, and several climate indices), zonally averaged temperatures and salinity (compared to climatology), timeseries from moorings (for the Indonesian region), and analysis of the meridional overturning streamfunction. In addition, EKE fields modelled and derived from observations, and a modelled and an observed EAC eddy, are also compared here (Figures 2.3 and 2.4, respectively). Together, these results indicate that the mean state of the ocean model, and its variability, are realistic.

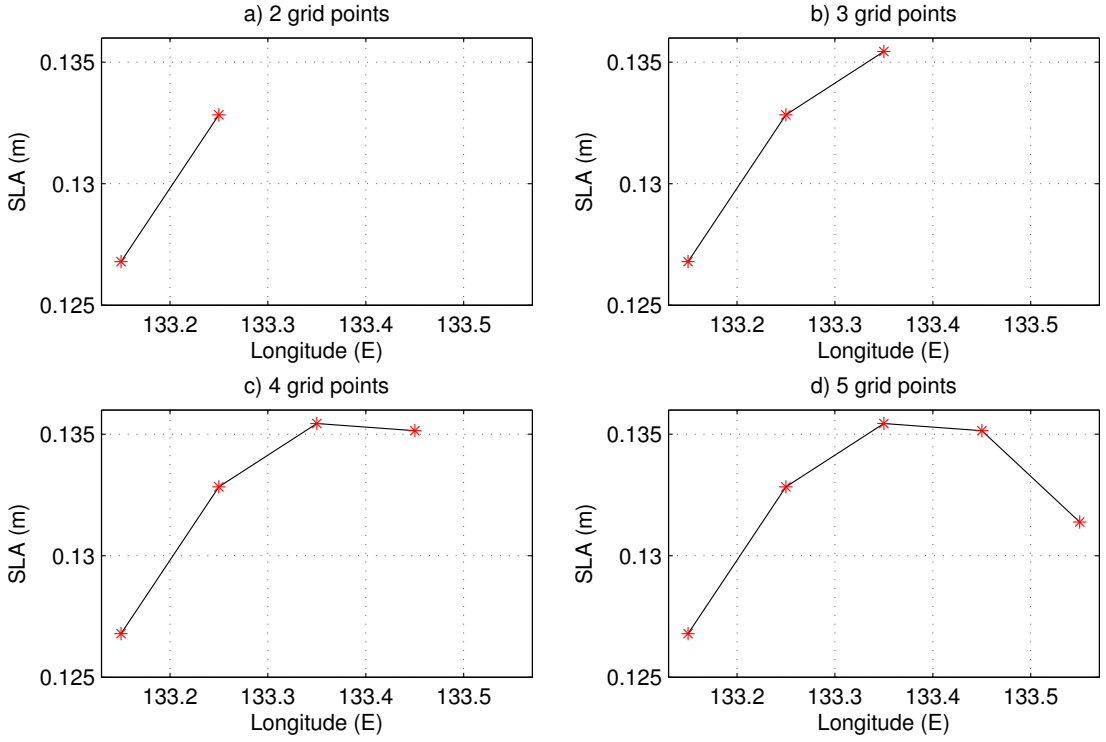


FIGURE 2.1: A series of a) 2, b) 3, c) 4, and d) 5 grid points (red stars) of the model showing the SLA associated with a mesoscale eddy.

Table 2.1: Parameterisations employed in OFAM

| Process | Reference | Description |
|---|---|---|
| Tidal Mixing | Lee et al. (2006) | Implements stronger mixing in regions of large-amplitude tides (using a Munk-Anderson-P and Munk-Anderson-Sigma parameter of 0.25 and 3, respectively). Enhanced mixing is spatially-varying, but time-invariant. |
| Vertical Mixing | Oke et al. (2013a) | Explicit convective adjustment is applied every time-step to eliminate any unstable profiles. |
| Horizontal Mixing | Griffies and Hallberg (2000) | Explicit horizontal diffusion is zero. Horizontal viscosity is resolution and state-dependent using a biharmonic Smagorinsky viscosity scheme with an isotropic parameter of 3 and an anisotropic parameter of 3. |
| Mixed Layer | Chen et al. (1994) | Hybrid bulk and Richardson-number scheme. Background (maximum) diffusivity and viscosity is $1x10^{-5}$, ($5x10^{-3}$) and $1x10^{-4}$ ($2.5x10^{-3}$) $m^2/s$. |

For results contained in this thesis, OFAM's performance in the EAC region and in the Tasman Sea is particularly relevant. In these regions, the patterns of the modelled and observed MSL are in good agreement, indicating that the mean circulation in the ocean model is realistic (Figure 2.2a, left and centre). Here, the MSL from OFAM is built by averaging the model's sea level between 1993 and 2001. The observed MSL, in turn, is based on the mean dynamic topography from CNES V1.1 between 1993 and 1999, relative to a geoid computed from 4.5 years of GRACE data. The difference between the modelled and observed MSL, however, suggests a slight displacement of the Tasman Front - with the EAC separating farther north in the model than in observations (Figure 2.2a, right). High values of the difference between the observed and the modelled MSL ($\sim$0.3 m) are associated with the Antarctic Circumpolar Current - suggesting that the latitude of this current in OFAM is shifted. Comparisons between the transport associated with the EAC in the ocean model and in observations further confirm that the circulation in OFAM is realistic (Table 2.2).

Fields of modelled and observed MLD generally agree, despite a systematically deeper mixed layer in OFAM (Figure 2.2b, left and centre). For this comparison, the averaged MLD is calculated using data from OFAM (1993 - 2011) and from CSIRO Atlas of Regional Seas (1950 - 2009; Ridgway and Dunn (2003)). In both datasets, the MLD is determined as the depth over which the potential density increases by 0.3 $kg/m^3$ and the temperature decreases by $0.2^oC$ from the surface value (de Boyer Montégut, 2004) In the study region, the modelled MLD is typically 30 m deeper than the observed MLD (Figure 2.2b, right). The largest differences in MLD (up to 90 m) are associated

with the Antarctic Circumpolar Current, and south of Tasmania as well. Results in this thesis mostly use fields below the surface mixed layer, and so this systematic error in the modelled MLD is not crucial for the analyses performed here. A more detailed analysis of the MLD in OFAM is found in Schiller and Ridgway (2013).

The magnitude and patterns of the EKE mean field in the ocean model in the Tasman

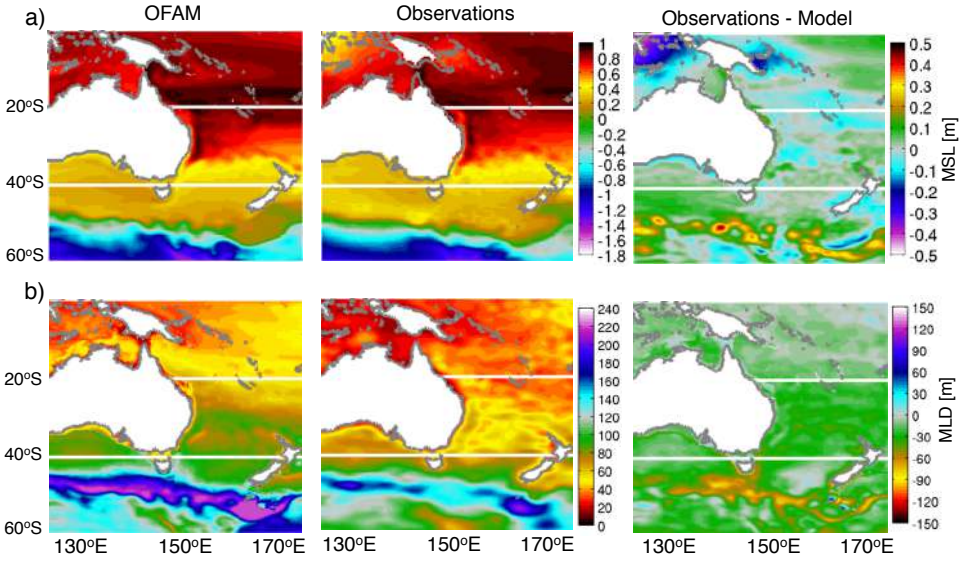


FIGURE 2.2: a) MSL in the ocean model (left), mean dynamic topography from CNES-CLS09 V1.1 (centre; Rio et al., 2009), and the difference between the observations and the modelled MSL field (right); b) as in (a) but for MLD in the ocean model and CARS climatology (Ridgway and Dunn, 2003); the modelled MLD is calculated from daily means using the MLD definition described by de Boyer Montégut (2004) (adapted from Oke et al., 2013a).

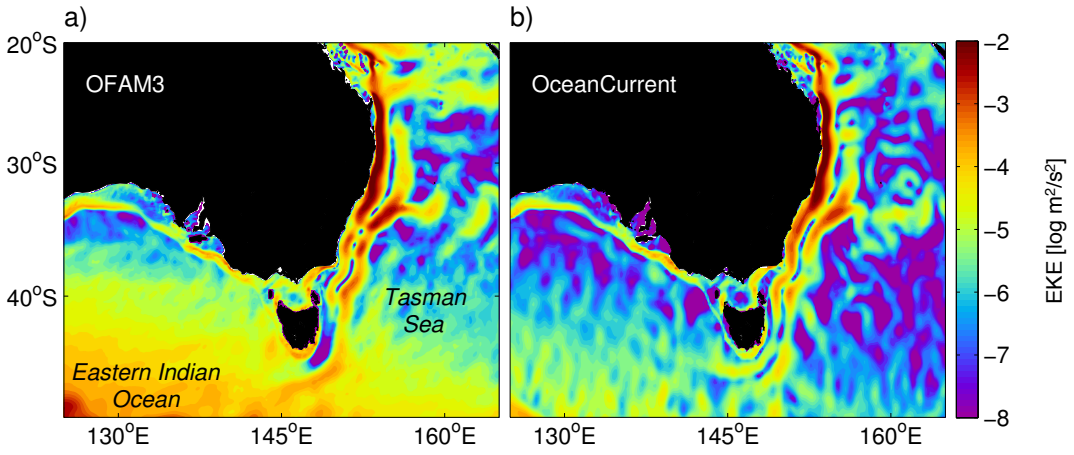


FIGURE 2.3: Maps of the time-averaged (2000-2005) EKE from (a) OFAM and (b) OceanCurrent altimetry products.

TABLE 2.2: Comparison of mean and maximum volume transports associated with the EAC in the ocean model and geostrophic velocities along frequently repeated XBT lines, referenced to 2000 db. The longitude of the maximum transport is also indicated (from Oke et al., 2013a).

| | | Modelled (Sv) | Observed (Sv) |
|---|---|---|---|
| EAC mean | Brisbane - New Caledonia | -8.6 ± 8.6 | -9.6 ± 5.4 |
| | Sydney - Wellington | -6.8 ± 5.6 | -10.7 ± 5.6 |
| EAC maximum | off Brisbane (155.1$^o$E) | -21.6 ± 10.6 | -19.8 ± 9.3 |
| | off Sydney (153.5$^o$E) | -16.2 ± 19.6 | -17.2 ± 17.6 |

Sea are in close agreement with the EKE mean field derived from satellite altimetry (Figure 2.3). Here, both the modelled and the altimetry-derived EKE is calculated using surface geostrophic currents. The agreement between the modelled and the observed EKE indicates that the modelled eddy field is realistic within this region. More specifically, the model reproduces both the location and strength of the high EKE region off the east Australian continental shelf. This high EKE region is associated with the meandering EAC and its train of eddies (Mata et al., 2006, Everett et al., 2012), extending from the EAC separation region ($\sim$32$^o$S) to the east of Tasmania ($\sim$42$^o$S). In fact, the model realistically reproduces a band of minimum of EKE located between two bands of maximum EKE off eastern Australia. In higher latitudes (i.e., south of 45$^o$), however, the ocean model is more energetic. This might be a result of the length scales chosen in OceanCurrent in the SLA mapping process (i.e. less energy between altimeter tracks), or it could be a systematic error in the model. These high latitudes, however, are not the focus of this study.

Comparisons between an EAC eddy from OFAM and an observed EAC eddy are also in general agreement (Figure 2.4). The observed eddy used for comparison was sampled in May 2001 in full depth CTD casts (Ridgway et al., 2008, Figures 2.4d-f). OFAM is a free-running model, intended to realistically represent the mesoscale variability of the ocean, rather than specific mesoscale events that agree spatially and temporally with observations. Consequently, it is not mandatory for the dates of the observed eddy and the modelled eddy to be the same for this qualitative comparison. EAC eddies, however, vary seasonally, being warmer and fresher in summer and colder and saltier in winter (Rykova and Oke, 2015). This seasonality is valid for both cyclonic and anticyclonic eddies. Therefore, it is important to compare eddies from the same season. The modelled eddy in Figures 2.4a-c dates from May 1996. Despite being stronger than the observed eddy used for this comparison (i.e. higher SLA, horizontal velocity and temperature anomaly), the dynamics and three-dimensional structure of the modelled eddy are realistic. In both eddies, the horizontal velocity (Figure 2.4b and

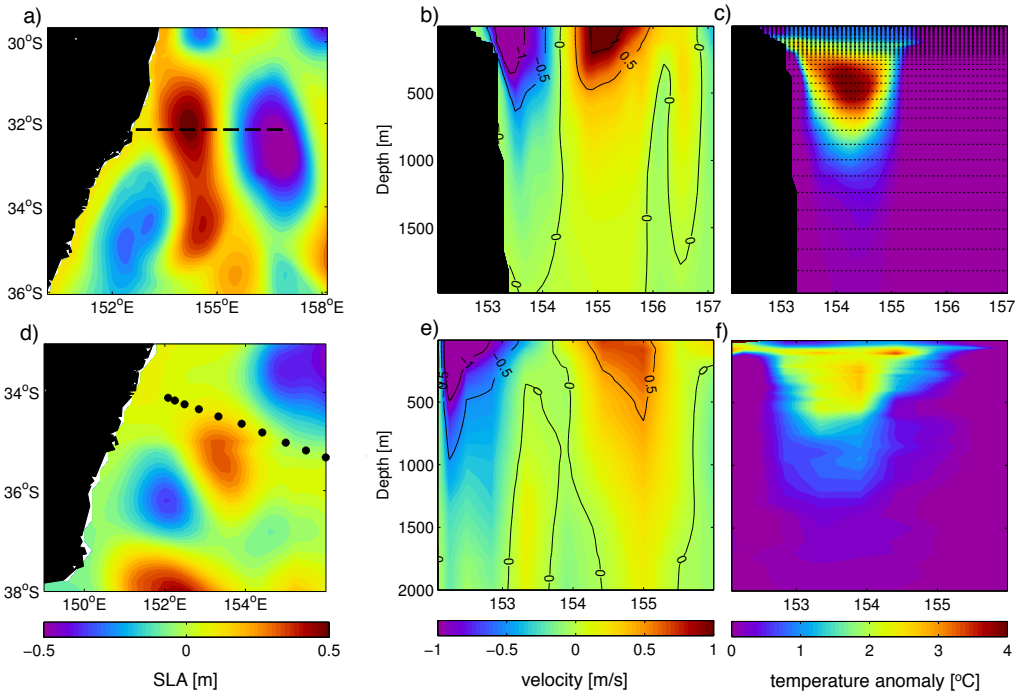


FIGURE 2.4: (a) SLA daily-averaged field associated with an EAC anticyclonic eddy in the ocean model. The SLA field is the model's sea level with the model's MSL (1993-2011) removed; the dashed line indicates the location of the vertical section shown in (b) and (c); (b) modelled meridional velocity (colours and contours, spaced every 0.5 m/s) and (c) modelled temperature anomaly associated with the eddy shown in (a). the dotted vertical lines represent vertical levels of OFAM; (d) SLA from OceanCurrent altimetry products associated with a sampled EAC anticyclonic eddy (adapted from Ridgway et al., 2008); the black dots indicate CTD sampling stations. The SLA product is the gridded sea surface height above mean sea level; (e) geostrophic current relative to 2000 dB computed from temperature and salinity fields (colours and contours, spaced every 0.5 m/s); (f) observed temperature, with CARS climatology (Ridgway and Dunn, 2003) removed.

e) and temperature (Figure 2.4c and f) signals penetrate below 1000 m, with maximum temperature anomaly between ∼200-600 m.

OFAM has been used in a variety of studies that assess different aspects of the modelled circulation. These studies include analyses of eddies (Condie and Condie, 2016, Dufois et al., 2016, Rykova et al., 2017), mixed layer variability (Schiller and Oke, 2015), coastally trapped waves (Woodham et al., 2013), properties (Rykova and Oke, 2015), transport (Langlais et al., 2015), and seasonality (Ridgway and Godfrey, 2015) of wind-driven currents, and climate change projections (Matear et al., 2013, Oliver and Holbrook, 2014, Feng et al., 2016). The broad uptake of this ocean model and the assessment reproduced here, provides me with confidence to analyse OFAM's output to achieve the goals proposed in this thesis.

## 2.3 Satellite altimetry products

### 2.3.1 Description

The analyses of the ocean model fields contained in this thesis are supplemented by two gridded SLA products. These products are the Aviso Reference Series (Ducet et al., 2000, 1/3° grid, 7-day maps), and the OceanCurrent gridded SLA maps (Deng et al., 2011, 1/4° grid, 4-day maps). The Aviso Reference Series is built using data from two altimeters (i.e., Topex/Poseidon, Jason-1 or Jason-2 measurements with ERS-1, ERS-2 or ENVISAT measurements). The OceanCurrent maps are built using data from all available altimeters, and de-tided coastal tide gauges estimates of adjusted SLA mapped onto a grid. OceanCurrent is an Australian dataset produced under the Australian Integrated Marine Observing System (IMOS). These products, besides using a different number of available altimeters, are processed independently. The length scales used for the objective mapping range from 100 km in the zonal and meridional directions at 60°S-60°N, to 250 (350) km in the meridional (zonal) direction at the equator.

### 2.3.2 Limitations

Despite satellite altimetry allowing oceanographers to advance the knowledge of mesoscale dynamics (Morrow and Le Traon, 2012, and references therein), there are some limitations to the satellite altimetry products used here.

The altimeter products depend strongly on the assumed decorrelation length-scales and on the sampling of the altimeter tracks. Two altimeters is the minimum requirement to resolve mesoscale eddies (Ducet et al., 2000, Le Traon and Dibarboure, 2002). The Aviso Reference Series product used here (i.e., two satellites only) resolves features larger than 100 km in wavelength, and the OceanCurrent product (i.e., all available satellites) resolves features larger than 80 km in wavelength. For the Aviso Reference Series, the sea level is mapped with an error of 6-10% of the signal variance (Figure 2.5a), and the surface velocity is mapped with an error of 20-40% of the signal variance (Le Traon and Dibarboure, 2002, 2004). However, the sea level mapping error can reach more than 25% of the signal variance in the Tasman Sea (see the formal mapping error $90^{\text{th}}$ percentile in Figure 2.5b). Note that, here, the Aviso Reference Series is used instead of the Aviso Updated Series (i.e., all available satellites). Despite the Updated series having better sampling, the Reference series is homogeneous in time (Dibarboure et al., 2009). In addition, the two-satellite weekly Aviso product is used here, instead of the all-satellite product, to allow a comparison between manually tracked eddies and eddies from an automated eddy dataset (Chelton et al., 2011b; Section 2.4.2.2).

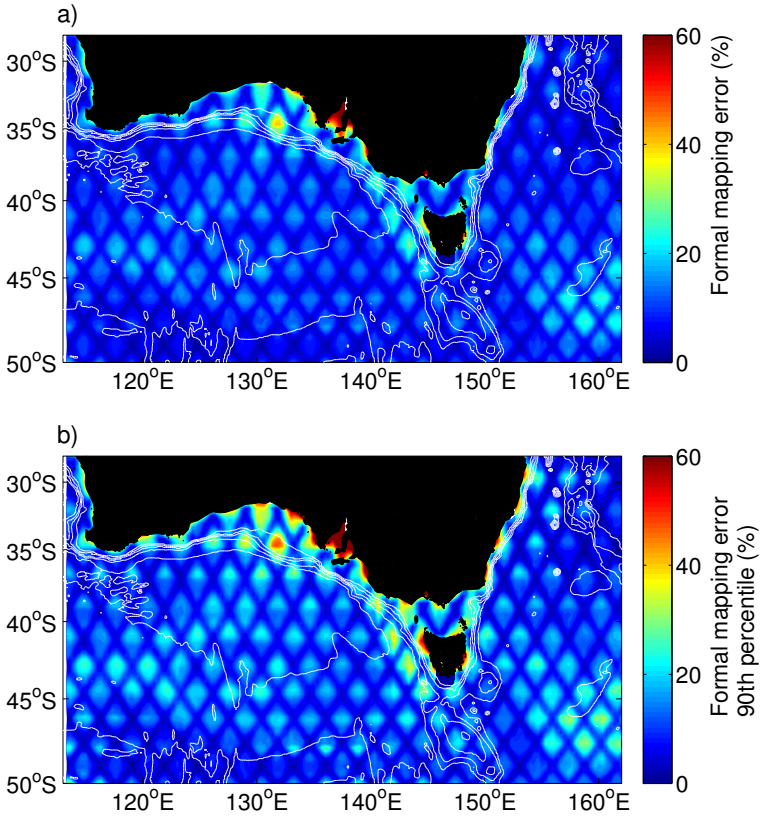


FIGURE 2.5: Maps of (a) the time-averaged (1993-2012) formal mapping error and (b) its 90% percentile, presented as a percentage of the signal variance, for the Aviso Reference Series gridded SLA altimetry. White contours show bathymetry from 1000 m to 6000 m, spaced every 1000 m.

Critical limiting factors for satellite altimetry are the absence of knowledge of a high-resolution marine geoid (Wunsch and Stammer, 1998, Fu and Cazenave, 2000, Mazloff et al., 2014, Bingham et al., 2014, Stammer and Cazenave, 2017), and the presence of land masses (e.g., Bouffard et al., 2008). In addition, other sources of error in altimetry measurements originate from the uncertainties in satellite performance, such as measurement noise, wave height contribution, tidal and orbit errors, and atmospheric interference (Fu and Cazenave, 2000, Stammer and Cazenave, 2017). Corrections aimed to minimise these errors are applied to the gridded SLA products used here (e.g., Le Traon et al., 1998, Ducet et al., 2000, Deng et al., 2011).

Considering the temporal and spatial limitations of the altimetry products, it is reasonable to expect that the altimeter SLA maps do not reproduce all of the true mesoscale variability of the ocean.

## 2.4 Methods

### 2.4.1 Overview

Throughout this thesis, eddies representative of the study region are investigated as case studies. This means that ocean model fields associated with each selected eddy are carefully examined. This approach warrants a detailed description of the propagation and temporal evolution of each eddy.

To date, studies of individual eddies mostly rely on idealised simulations (e.g., Nof, 1983, Flierl and Mied, 1985, Chapman and Nof, 1988, Grimshaw et al., 1994, Simmons and Nof, 2000, Davidson et al., 2006, Early et al., 2011, Sutyrin, 2016), ship-board hydrographic samplings (e.g., Nilsson and Cresswell, 1981, Yasuda et al., 1992, Nencioli et al., 2008, Rossby et al., 2011, Nan et al., 2011, Nakano et al., 2013, Pidcock et al., 2013), or both (Martin and Richards, 2001, Waite et al., 2016). These studies provide insights into the dynamics and evolution of the vertical structure of eddies. However, results from idealised simulations, by their very nature, only provide a simplified picture of real ocean eddies. Hydrographic sampling, in turn, provides realistic information about eddies, but is limited in time and space. Therefore, such observations are not capable of capturing the full suite of properties, and their changes, needed for a dynamical analysis.

To address the issues related to idealised simulations and scarce hydrographic sampling, recent eddy studies use either the output from more realistic eddy-resolving numerical models (Dong et al., 2012, Kang and Curchitser, 2013, Petersen et al., 2013, Nakano et al., 2013, McGillicuddy, 2015, Rykova et al., 2017), or the extensive coverage of Argo float profiles (Chaigneau et al., 2011, Yang et al., 2013, 2015, Holte et al., 2013, Zhang et al., 2013, Rykova and Oke, 2015, Pegliasco et al., 2015, Frenger et al., 2015, Amores et al., 2017). Due to the large amount of data, these studies rely on the advantages and robustness of eddy composites (i.e., averages of eddy properties). These composites provide insights into the main vertical structure of the eddy types within a region. However, by averaging eddy properties a lot of information on eddy dynamics and evolution is lost.

Selecting eddies in an ocean model as case studies - as the approach taken throughout the thesis - minimised the limitations associated with idealised scenarios, limitations of hydrographic sampling, and averaging of a large group of eddies.

### 2.4.2 Manual tracking of eddies

In this thesis, eddies are manually tracked in SLA fields from the datasets described in sections 2.2 and 2.3. The manual approach is chosen because it provides accurate and reliable results, and the small number of eddies selected as case studies allowds me to track each eddy carefully. This careful tracking is crucial during complex events, such as merging, observation gaps, and periods when the eddy becomes anisotropic. This is especially important in the region off the eastern Australian coast, where there is extensive eddy-eddy and eddy-mean flow interaction (Cresswell and Legeckis, 1986, Bowen et al., 2005, Mata et al., 2006).

The most common methods used in eddy-tracking algorithms are based on the Okubo-Weiss parameter (Isern-Fontanet et al., 2003, Morrow, 2004, Chelton et al., 2007, Henson and Thomas, 2008), wavelet analyses (Siegel and Weiss, 1997, Doglioli et al., 2007), and geometry of SLA contours (Sadarjoen and Post, 2000, Chaigneau et al., 2009, Chelton et al., 2011b, Faghmous et al., 2015, Mason et al., 2014). One of the most popular datasets, described by Chelton et al. (2011b), is cited 746 times between 2011 and November 2017. In comparison, a manual tracking of eddies is used only in a small number of studies (e.g., Fang and Morrow, 2003, Andrade and Barton, 2000, Arhan et al., 2011, Hall and Lutjeharms, 2011, Cotroneo et al., 2013, Rousselet et al., 2016). While automatic eddy-tracking algorithms prevail in ocean sciences, the manual tracking of features has a long history in the atmospheric and meteorological sciences, and is considered more accurate than automated methods by that community (e.g., Streten and Troup, 1973, Kep, 1984, Pook et al., 2012, Hope et al., 2014).

Datasets generated by automatic eddy-tracking algorithms are essential for understanding the general propagation and distribution of eddies in large oceanic regions (e.g., Morrow, 2004, Chelton et al., 2011a, Chaigneau et al., 2011, Gaube et al., 2013, Samelson et al., 2014, McGillicuddy, 2016). However, the developers of automatic eddy-tracking algorithms note that the automatic tracking is not perfect (e.g., Chaigneau et al., 2008, Chelton et al., 2011b). Specifically, they note that such algorithms may perform poorly when eddies merge or when the flow field is particularly complex. In those studies, eddies tracked by an algorithm are validated against eddies tracked manually, indicating that a manual tracking is still the less ambiguous tracking method. In these validations, the manual tracking is considered as the "truth" (Isern-Fontanet et al., 2003, Lankhorst, 2006, Henson and Thomas, 2008, Chaigneau et al., 2008, Mason et al., 2014).

The manual eddy-tracking used in this thesis is performed as follows. The first step is a preliminary viewing of animations of SLA fields - from both OFAM and the altimetry products - evolving in time within the study region. This preliminary analysis allows

me to gain an understanding of the regional dynamics and to identify the eddies that are the focus of the study. Here, I select large, long-lived anticyclonic eddies that form in the EAC separation region (∼28-34$^o$S; Godfrey et al., 1980, Ridgway and Godfrey, 1997, Cetina-Heredia et al., 2014). I define an EAC long-lived eddy as an eddy that lives for at least one year - and therefore has enough time to leave its formation region. I start tracking these eddies as soon as they are independent features with closed SLA contours (Figure 2.6b).

The next step is to locate closed positive SLA contours every seven (OFAM and Aviso) or four (OceanCurrent) days and click the pointer on what I visually identify as the maximum SLA within the contour (Figure 2.6b-f). The script then searches for the real maximum SLA within a $1^o$x$1^o$ region around the selected grid cell - as it is, sometimes, difficult to visually determine its location. This search for an objectively chosen maximum SLA minimises errors, guaranteeing that the eddy centre is always the maximum SLA associated with the eddy. The date, latitude, and longitude of the eddy centre is, then, stored in a separate file.

An eddy is considered to be continuous in time if it is evident at consecutive timesteps. However, if an eddy is not clearly seen in consecutive timesteps, I search for it in the following SLA fields. If the eddy is seen again, and if it reappears in the SLA fields in a location consistent with its propagation speed and interaction with the surrounding environment, it is considered to be the same eddy. If the eddy is not seen again, its trajectory is terminated. The manual tracking allows for a case-by-case decision in a possible eddy location after a momentaneous "disappearance". Therefore, a previously defined threshold of missing timesteps was not applied here.

Sometimes, eddies interact or merge with other eddies as they propagate. In this study, I assume that if one eddy merges with another eddy its trajectory continues, as shown in Figure 2.7. This assumption is consistent with the observations described by Cresswell (1982), where two EAC anticyclonic eddies merge and the resulting eddy has the properties of the original eddies - with two layers of different water masses located at different depths.

In general, as eddies propagate they lose energy and SLA decreases in time (Souza et al., 2011, Kurczyn et al., 2013, Rykova and Oke, 2015). I track each eddy until the SLA associated with the closed SLA contour associated with it becomes smaller than 0.05 m in OFAM and 0.1 m in Aviso and OceanCurrent (Figure 2.8). A larger threshold for the observational products is used because they have a smaller signal-to-noise ratio, mainly due to sampling error. By contrast, the ocean model does not include noise due to sampling error.

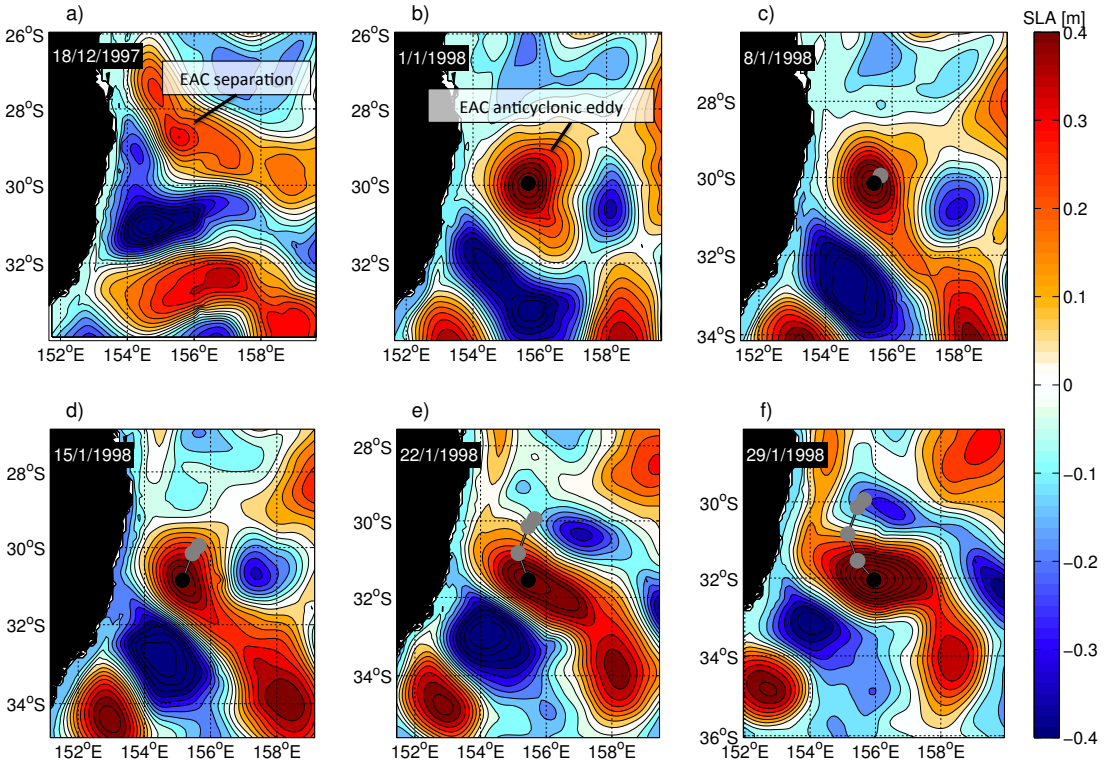


FIGURE 2.6: Daily mean SLA fields from OFAM associated with the (a) EAC separating from the coast, before shedding an anticyclonic eddy to be tracked, (b) an EAC anticyclonic eddy 2 weeks after (a), and (c-f) the same eddy propagating in time. Black dots indicate the location of the SLA maximum within the positive SLA contour in the daily mean. Grey dots indicate previous locations of the black dots. The black line indicates the eddy track.

To demonstrate the eddy tracking process, animations showing the propagation of modelled SLA fields for the study region and the tracked eddies using both modelled and observed fields are available online at http://www.youtube.com/GabrielaPilo.

#### 2.4.2.1 Limitations

Tracking eddies manually is labour intensive and time consuming. Therefore, this method can only be applied when focusing on a small, but representative, number of eddies.

Manual tracking of eddies is somewhat subjective - relying on the oceanographer's judgment to make the correct decisions about continuing or ceasing tracking. However, automated eddy tracking is also subjective, regulated by the rules of the algorithm. An example of the subjectivity of eddy tracking algorithms is that different methods often produce different outcomes, even though they use the same gridded SLA altimetry

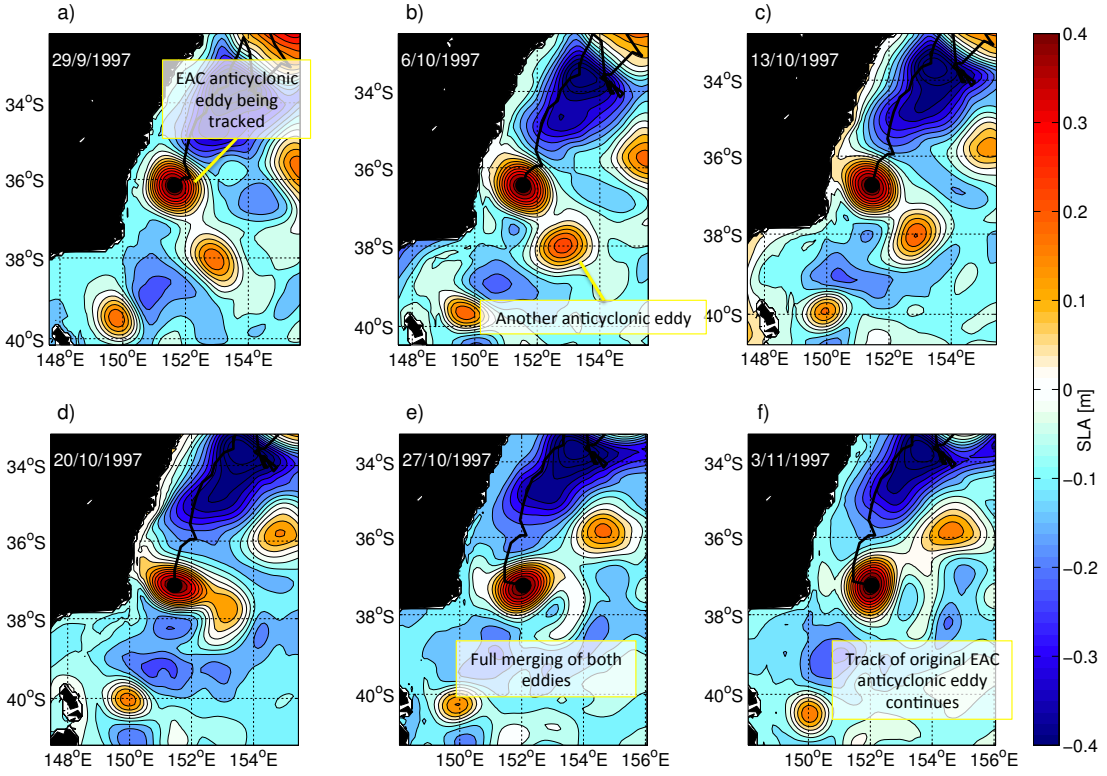


FIGURE 2.7: a-f) Daily mean SLA fields from OFAM associated with an EAC anticyclonic eddy being tracked. In (c-d) the eddy interacts with another anticyclonic eddy, resulting in a full merging. Black dots indicate the location of the maximum SLA within the positive SLA contour on the daily means. The black line indicates the eddy track.

product (e.g., Souza et al., 2011). The decisions "taken" by the algorithm while tracking an eddy are more limited to the decisions taken by an oceanographer. An oceanographer with knowledge of the region and of the dataset limitations is able to make more appropriate decisions than the algorithm, at each timestep.

#### 2.4.2.2 Assessment

To assess the manual eddy tracking method, a comparison of eddy tracks using Chelton et al. (2011b)'s Global Eddy Dataset version 3, and manually tracked eddies is undertaken. For this comparison, the eddies are tracked manually in satellite SLA fields from Aviso Reference Series (described in section 2.3), the same used in version 3 of the eddy database. These comparisons with Chelton's database show cases when tracks from the automated method end due to eddy anisotropy (Figures 2.9a and c), eddy interaction (Figure 2.9b), and temporary eddy weakening (Figure 2.9d).

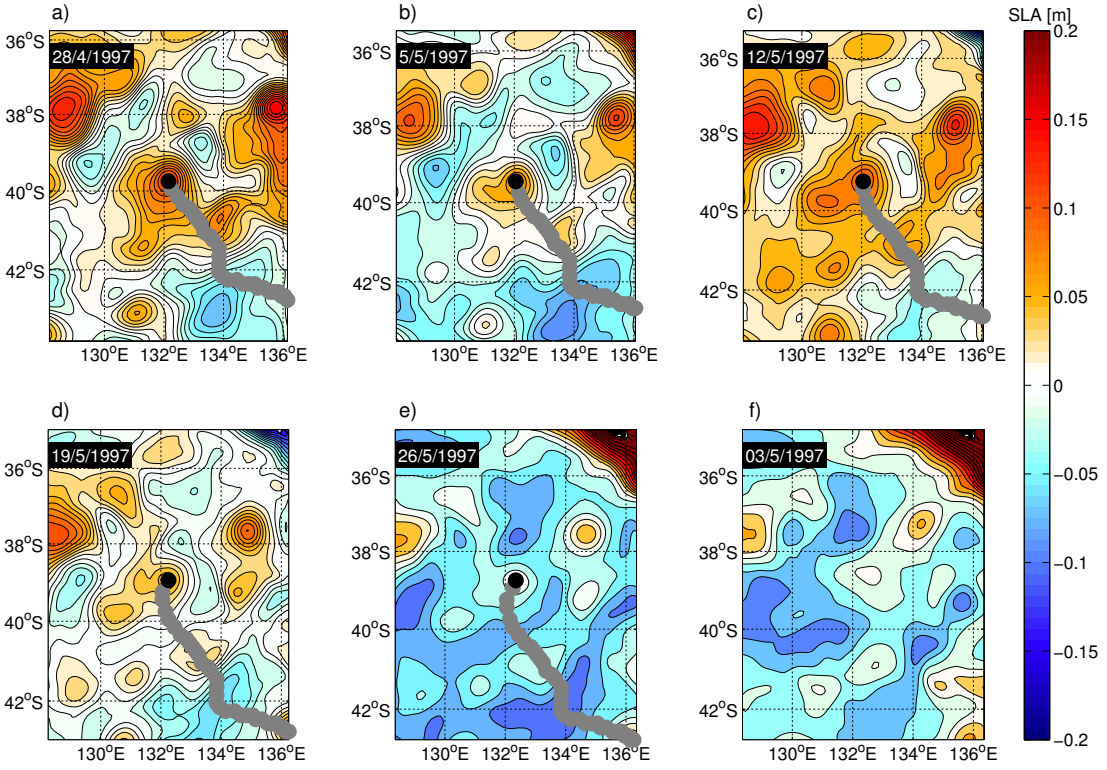


FIGURE 2.8: a-f) Daily mean SLA fields from OFAM associated with an anticyclonic eddy, with its final location shown in (e); Black dots indicate the location of the maximum SLA within the positive SLA contour on the daily mean. Grey dots indicate previous locations of the black dots.

The coloured maps in Figure 2.9 show SLA from Aviso around the time when the different tracking methods yield different results. In Figures 2.9a and c, the eddies change their shape, becoming elongated, and are no longer considered the same eddies by the automated eddy detection algorithm. In Figure 2.9b, the tracked eddy interacts with a different (larger) eddy, but the two eddies do not merge. The automated eddy detection algorithm subsequently tracks the other eddy instead (red circles in SLA maps in Figure 2.9b). The manual approach continues tracking the original eddy as it moves southwards (yellow circles in SLA maps in Figure 2.9b). Finally, in Figure 2.9d, the SLA associated with the tracked eddy is temporarily close to zero. At this moment, the algorithm terminates eddy-tracking. However, the positive SLA contours are still observed, and the SLA associated with the eddy increases in the following days. Therefore, I continue to manually track the eddy.

### 2.4.3 Extraction of ocean model fields associated with eddies

After manually tracking the eddies, all ocean model fields are extracted from OFAM at each timestep (i.e. every seven days), in 4°× 4°× 2000 m "data cubes". These cubes

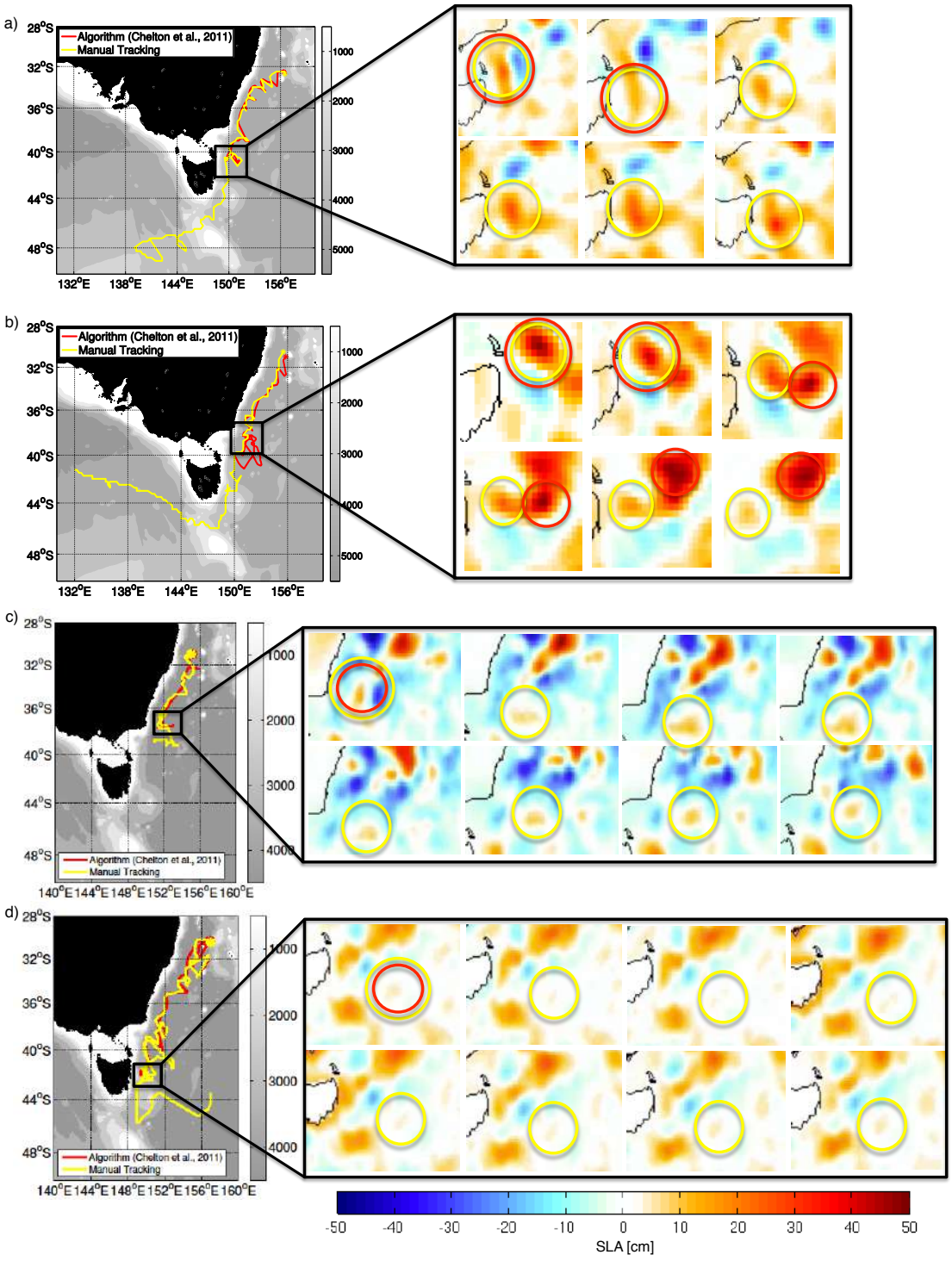


FIGURE 2.9: (a-d) Examples of eddy tracks using automated eddy detection (red; Chelton et al., 2011b) and manual tracking (yellow). Eddies are tracked in Aviso Reference Series SLA gridded datasets. The panels on the right show a sequence of weekly SLA maps spanning the time when the tracks diverge; red (yellow) circles show the eddy perimeters from the automatic (manual) approach.

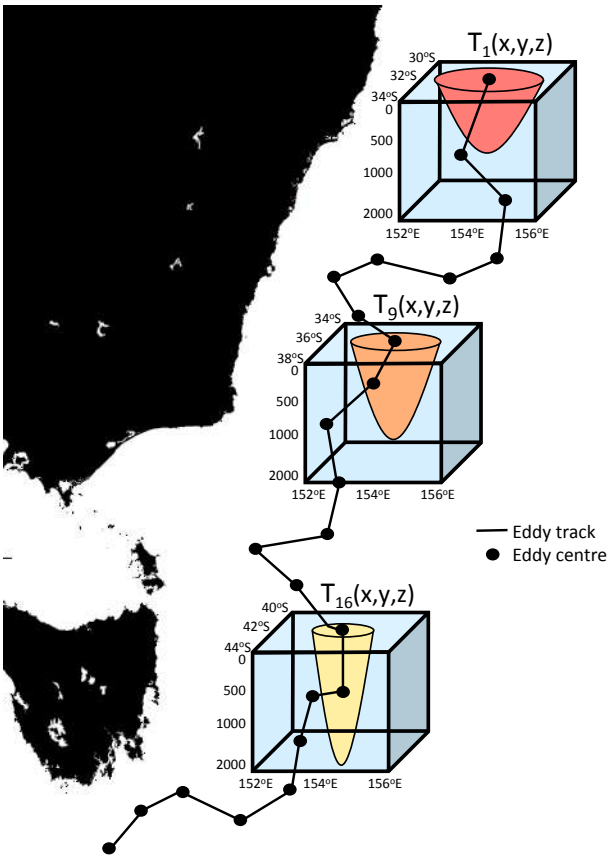


FIGURE 2.10: Schematic of the datasets used in this thesis, with temperature (T) as an example, in times 1, 9, and 16 ($T_1$, $T_9$, and $T_{16}$, respectively). The $4° \times 4° \times$ 2000 m cubes are extracted from OFAM at each timestep of the eddy manual tracking (black line). The centre of the surface level of the cube is the eddy centre (i.e., maximum SLA within the closed positive SLA contour; black dots).

are schematically shown in Figure 2.10, using ocean temperature as an example. For this procedure, the centre of the surface layer of the "data cube" is the centre of the eddy, given by the local SLA maximum within the positive SLA contour. Hence, the extracted cubes "follow" the eddies as they propagate.

The variables extracted from OFAM, at each timestep, are daily-averages of are two-dimensional fields of sea surface height and SLA, and daily-averages of three-dimensional fields of temperature, salinity, and the three components of velocity.

These "data cubes" are used to investigate changes in eddy properties in time in Chapter 3, and the vertical circulation within eddies in Chapters 4 and 5.

In this Chapter, the datasets used and the methods of analysis have been described. In the next Chapters, they will be used to investigate the propagation, spatial and temporal changes of three-dimensional properties of EAC anticyclonic eddies.

# Chapter 3

# Propagation and evolution of long-lived EAC anticyclonic eddies

## 3.1 Introduction

In this Chapter, the pathway and evolution of large, long-lived EAC anticyclonic eddies is investigated. As noted in the introduction to this thesis (Chapter 1), previous analyses of EAC eddies show that such eddies frequently propagate to the southern Tasman Sea, off eastern Tasmania (e.g., Cresswell and Legeckis, 1986, Everett et al., 2012). Moreover, several studies show that eddies first identified south of Tasmania often propagate westwards, towards the Eastern Indian Ocean (e.g., Baird and Ridgway, 2012, Oliver et al., 2015, Pilo et al., 2015). However, to date, the link between these propagation paths has not been made. This Chapter addresses this knowledge gap, and explores why a full understanding of the pathway of EAC eddies has been allusive.

In addition to the pathway itself, this Chapter also contains a description of the properties and evolution of such eddies. Other similar studies, examining eddy properties, have used both observations (e.g., Nilsson and Cresswell, 1981, Rykova and Oke, 2015, Roughan et al., 2017) and model fields (e.g., Oke and Griffin, 2011, Rykova et al., 2017). A more extensive introduction to the topic of this Chapter is presented in Chapter 1.

The study presented here intends to address the first two objectives of this thesis, namely the goal of better understanding the pathway of EAC eddies, and of better understanding their spatial and temporal changes.

Section 3.2 refers to the datasets and methods used in this Chapter. Section 3.3 describes the propagation pathway of EAC eddies, and the spatial and temporal changes of these eddies as they advect along this pathway. The discussion and conclusions related to these findings are summarised in Section 3.4.

This Chapter is based on a paper published as:

Pilo, G. S., P. R. Oke, T. Rykova, R. Coleman, and K. Ridgway (2015), **Do East Australian Current anticyclonic eddies leave the Tasman Sea?**, *Journal of Geophysical Research: Oceans*, 120, 8099-8114, doi:10.1002/2015JC011026.

This paper is reproduced in Appendix A of this thesis, and its Supporting Information is reproduced in Appendix B.

## 3.2 Data and methods

Most of the analysis in this Chapter uses model fields - with "data cubes" that follow the path of the manually tracked eddies. Satellite altimetry products are used to validate eddy tracks in the model. Details of the model, the satellite altimetry products, and the method used here for eddy tracking, are extensively described in Chapter 2.

## 3.3 Results

### 3.3.1 Eddy pathway

The tracks of the EAC anticyclonic eddies identified in the ocean model and in maps of gridded satellite altimetry are shown in Figure 3.1. In total, 16 eddies in the modelled SLA field, 16 eddies in OceanCurrent SLA maps, and 11 eddies in Aviso SLA maps are tracked. Many of the tracked eddies that leave the Tasman Sea follow a consistent pathway. This pathway begins in the EAC separation region, then extends southwards, adjacent to the continental slope of south-eastern Australia, to the southern tip of Tasmania; and then continues towards the Eastern Indian Ocean. All 16 of the eddies tracked in the ocean model roughly follow this pathway. Only 2 out of 16 eddies tracked in OceanCurrent and 3 out of 11 eddies tracked in Aviso "survive" beyond Tasmania (i.e., only a 15–25% survival rate). Note that eddies tracked in OceanCurrent and Aviso products are not always the same. This indicates that there are differences even between the observation-based products (due in part to different processing techniques and the number of altimeters used to build the gridded products), and not only between the

observations and the ocean model. Remember that the focus of this study is on large, long-lived EAC anticyclonic eddies, and that only these features are manually tracked.

To examine the temporal variability along the mean eddy pathway – which is clearest in the ocean model results (Figure 3.1a) – Hovmöller diagrams of SLA from each dataset along an idealised pathway are produced (Figure 3.2). This idealised pathway represents the mean path that large, long-lived EAC eddies take, from the EAC separation to the Eastern Indian Ocean. The idealised pathway (denoted "A–G" in Figure 3.2a) is not perfect, because the eddies do not precisely follow this path (Figure 3.1). Despite this limitation, the evolution of positive SLAs on this idealised pathway is very clear in the ocean model fields (Figure 3.2c), with all anomalies transiting beyond Tasmania, and 11 out of 16 making it to "G". These eddies take up to 5 years to complete their path.

In the model, ∼2 large-amplitude anticyclonic eddies are shed per year at the EAC separation region (positive SLA in "A" in Figure 3.2c). This shedding frequency increases to ∼2.8 eddies per year in the observations (Figure 3.2d-e). Both values fall in the lower spectrum of the 1.7-4 eddies/year shedding frequency found in the literature (e.g., Mata et al., 2006). However, not all these eddies are large-amplitude or leave the region, and many remain there interacting with other eddies (Mata et al., 2006). Considering shedding rates found in the literature, I expect 65-75 eddies to be generated at the EAC separation region over a 19-year period. Here, 11-16 eddies formed in the EAC separation are tracked until their dissipation in the Tasman Sea (Figure 3.1). Therefore, 25-30% of large anticyclonic EAC eddies leave the area and propagate southwards, following the eddy pathway.

High SLA standard deviation values at the EAC separation region are represented in the Hovmöller diagrams (Figure 3.2c; between "A" and "B"). Between these locations there is a mix of cyclonic and anticyclonic eddies (negative and positive anomalies in Figures 3.2c-e), indicating the high mesoscale activity in this area.

The propagation of EAC anticyclonic eddies between "C" and "D" and beyond "E" is less clear in the observations (Figures 3.2d-e). However, I suggest that eddies in the ocean do propagate along these paths - but, as they lose SLA amplitude, their signal in the gridded products becomes less clear. Note that the section between "C" and "D", in Figure 3.2a, spans a region where the mapping error is relatively high (between 20-25% of the signal variance and more than 25% in the $90^{\text{th}}$ percentile; Figure 2.5). Sometimes, the analysis suggests that eddies continue propagating along the idealised pathway - despite a lack of signal in the gridded SLA in the observations. These cases are denoted with black dashed lines in Figures 3.2c-d, and are discussed further below.

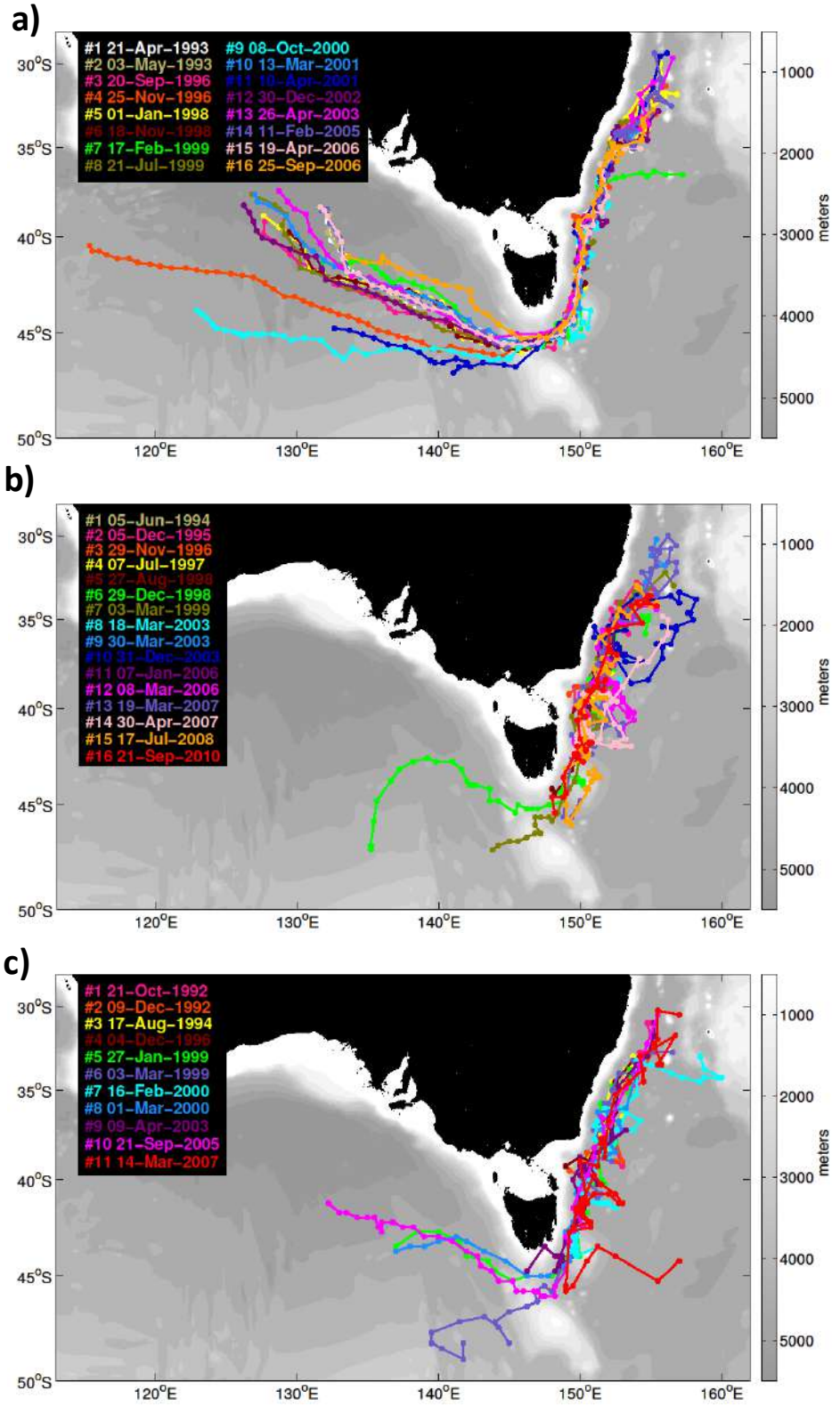


FIGURE 3.1: Tracks of anticyclonic eddies (colours) from (a) the ocean model, (b) OceanCurrent and (c) Aviso. Each eddy is identified in the legend by its start date. Grey shading denotes bathymetry and the dots on the eddy tracks denote monthly time steps.

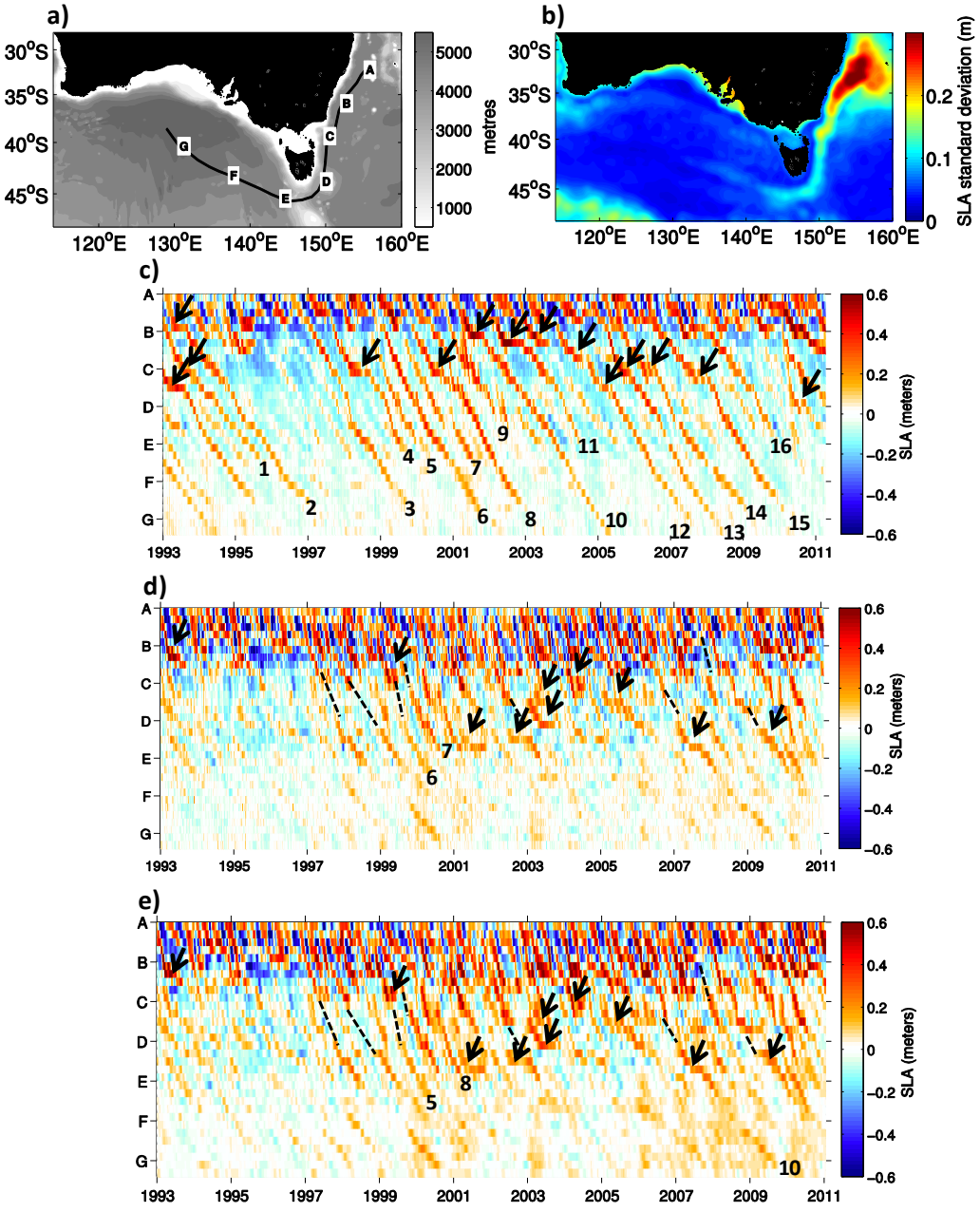


FIGURE 3.2: a) Idealised pathway of anticyclonic eddies shed at the EAC separation region in the ocean model, overlaid on bathymetry; b) SLA standard deviation in the model between 1993 and 2012 (colours). The letters ("A" to "G") indicate key locations of the pathway. Hovmöller diagrams of SLA from (c) the ocean model, (d) OceanCurrent, and (e) Aviso along "A–G" pathway with numbers relating to eddies from Figure 3.1; dashed lines indicate unresolved connections between observed eddies; black arrows denote moments when eddy propagation "stalls" at certain locations of the pathway.

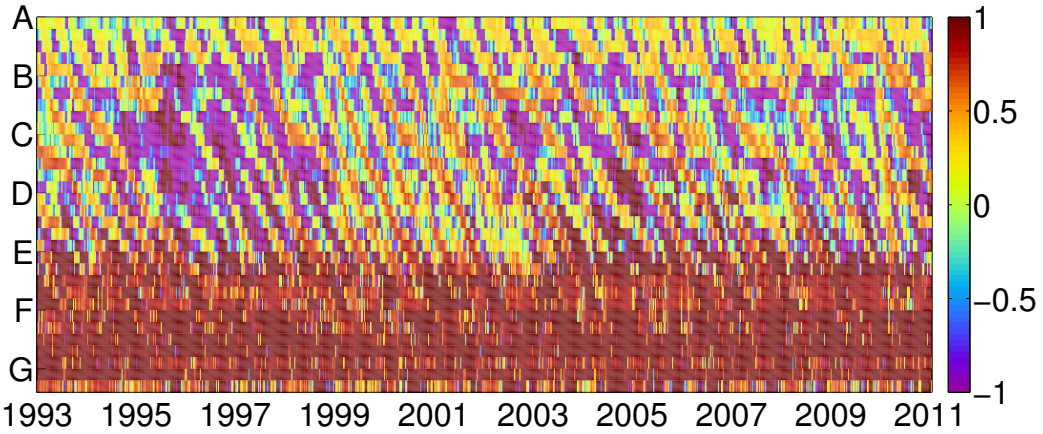


FIGURE 3.3: Hovmöller diagram of the SLA/SSH ratio from the ocean model along the "A-G" pathway.

An eddy from the gridded altimetry products is not expected to be evident in the ocean model at the same time and location. This is because OFAM is a free-running model, with no data assimilation, and because eddy formation is somewhat chaotic. However, the model is expected to generate eddies with realistic characteristics (size, shape, and amplitude), and evolving similarly to observations (with a similar path and time-evolution; Oke et al., 2008, Schiller et al., 2008, Oke et al., 2013a).

Despite eddy merging and eddy decay being the primary causes for changes in eddy amplitude, the effect of the background sea surface height (SSH) must also be considered. The observed changes in the SLA associated with eddies might not necessarily relate to the eddy dynamics, but to changes in the SSH along the eddy pathway. The effect of the background SSH is especially important in this case, because the eddy pathway extends from a region with high mean SSH - the EAC separation - to a region with low mean SSH - the Eastern Indian Ocean. When moving through these different regions, the SLA/SSH ratio within the eddies varies between 0.4 and 0.6 (Figure 3.3). In surrounding waters, this ratio varies between -1 and 1. Therefore, the effect of the changing background SSH is present, however small.

As part of their southward propagation, many of the eddies "stall" at some point. These events are denoted by black arrows in Figures 3.2c-e. In the ocean model fields, the eddies often stall near "B" and "C" locations, off Sydney and off Bass Strait respectively. In the gridded SLA fields, 3–4 eddies stall around Bass Strait, and 4–5 eddies stall off south-eastern Tasmania (with just one eddy stalling near Sydney). These "stalling" events often last for several months when EAC anticyclonic eddies are quasi-stationary.

There are differences between the propagation speeds of eddies in the ocean model and in altimetry, seen in the Hovmöller diagrams (Figure 3.2). These different speeds are

TABLE 3.1: Mean propagation speed of eddies tracked in OFAM and Aviso between the EAC separation region and off Sydney ("A–B"), off Sydney and south of Tasmania ("B–E"), and at the deep basin south of Australia ("E–G"). Aviso's "E–G" section speed was calculated based on four eddies only.

| | **A-B [m/s]** | **B-E [m/s]** | **E-G [m/s]** |
|---|---|---|---|
| **OFAM** | 5.5±1.4 | 2.8±0.4 | 3.2±0.4 |
| **Aviso** | 8.0±1.6 | 6.9±1.4 | 3.6±2.8 |

summarised in Table 3.1, indicating that the propagation speed of the observed and modelled eddies are comparable when they first form and as they propagate towards the Eastern Indian Ocean; but the observed eddies propagate about twice as fast as the modelled eddies as they move southwards towards Tasmania. In part, the discrepancy between "B" and "E" is because the modelled eddies tend to "stall" for longer than the observed eddies. The background circulation might also play an important role in the propagation speed of eddies as they move southwards. Indeed, the mean modelled EAC transport off the Eastern Australian coast is smaller than the transport estimated from observations ((-6.8 ±5.6 and -10.7 ±5.6 respectively, Table 2.2).

It was noted above that several observed eddies following the idealised pathway appear discontinuous (see the dashed lines in Figures 3.2d-e). The location where the eddies "disappear" is often between "C" and "D", off eastern Tasmania (where the mapping error has a local maximum; Figure 2.5). It is noteworthy that the horizontal diffusion of the model may affect the propagation pattern of eddies. This diffusion may facilitate the proximity of the modelled eddies to the coast - in a way that modelled eddies "hug" the bathymetry more closely. This characteristics of the model impacts the stability of the eddies and of their propagation. This discontinuity of eddy tracks in Figures 3.2d-e might also be related to the deviation of eddies from the idealised pathway. Indeed, 3 eddies tracked in OceanCurrent and 2 eddies tracked in Aviso temporarily move off the idealised pathway between "C" and "D" (Figure 3.1b-c). In addition, one eddy tracked in Aviso moves away from the idealised pathway, heading eastwards after reaching south of Tasmania (Figure 3.1c).

Despite these eddies deviating from the path, most of the tracked eddies in the altimetry products remain close to the continental shelf break off the Eastern Tasmania, following the idealised pathway. As noted above, the SLA associated with the eddies when they "disappear" is small (<0.1 m), and hence close to the merged altimetry SLA product resolution. Next, I further explore the relationship between the "disappearance" of eddies and the small SLA associated with them.

To test the altimeter sampling of the region off eastern Tasmania during periods of eddy transiting, four eddies tracked in OceanCurrent gridded SLA maps are chosen (Figure 3.4). Two examples (Figures 3.4a-b), show cases when there is poor altimeter sampling and the eddies "disappear" in the region of relatively high mapping error (Figure 2.5). Two examples (Figures 3.4c-d), show cases when there is good altimeter sampling and the eddy pathway continues beyond Tasmania. Eddies that dissipate (i.e. "disappear") off Bass Strait were under-sampled. Also, due to their reduced SLA (plots in Figure 3.4, showing SLA $\sim$5 cm) the eddies are not well resolved in the SLA gridding process, which has comparable errors ($\sim$5 cm). Therefore, this "disappearance" is partially attributed to relatively high mapping error and poor altimeter sampling of the region off eastern Tasmania during periods of eddy transit (see Figure 2.5 and Figure 3.4).

The fact that the Hovmöller diagrams (Figures 3.2d and 3.2e) show these eddies "re-appearing" at about the right time (assuming approximately steady southward propagation; see dashed lines) suggests that indeed the true eddies do regularly transit following the defined pathway. However, the gridded SLA altimetry fields do a relatively poor job of capturing this variability.

The relatively high mapping error and poor altimeter sampling in key regions of the pathway are not, however, the only causes for the temporary "disappearance" of eddies as they propagate. The decrease in the SLA associated with eddies between the EAC separation ("A") and the Eastern Indian Ocean ("G") in Figures 3.2c-e suggest energy loss - another possible cause for the eddy "disappearance".

To quantify the energy loss of EAC anticyclonic eddies as they propagate along the pathway, the total EKE within each eddy, at each time step, is calculated (Figure 3.5). For this calculation, the eddy perimeter is defined by the 0.1 m SLA contour, projected from 0 to 2000 m, and the EKE ($\frac{u^2+v^2}{2}$) is calculated for each cell within this perimeter and multiplied by the cell volume. Considering all modelled eddies that propagate along the pathway, the total EKE is, on average, $5\times10^{12}$ m$^2$/s$^2$ in the first year of propagation of these eddies, decreasing to less than $2\times10^{12}$ m$^2$/s$^2$ in the final year. Therefore - as expected - eddies are most energetic after formation, losing energy as they propagate along the pathway.

To better understand the EKE decay along the pathway, four eddies in the ocean model are investigated as case studies (Figure 3.6). These eddies are representative of the sample of modelled eddies included in this thesis. For this analysis, the EKE is divided in different depth intervals (different colours in Figure 3.6). In all depth intervals, the EKE fluctuates as eddies propagate, with sudden increases associated with merging events (Figure 3.6a at week 17 and Figure 3.6b at week 75, for example), and a general decrease otherwise. Most of the EKE within the eddies is contained within the 100-550

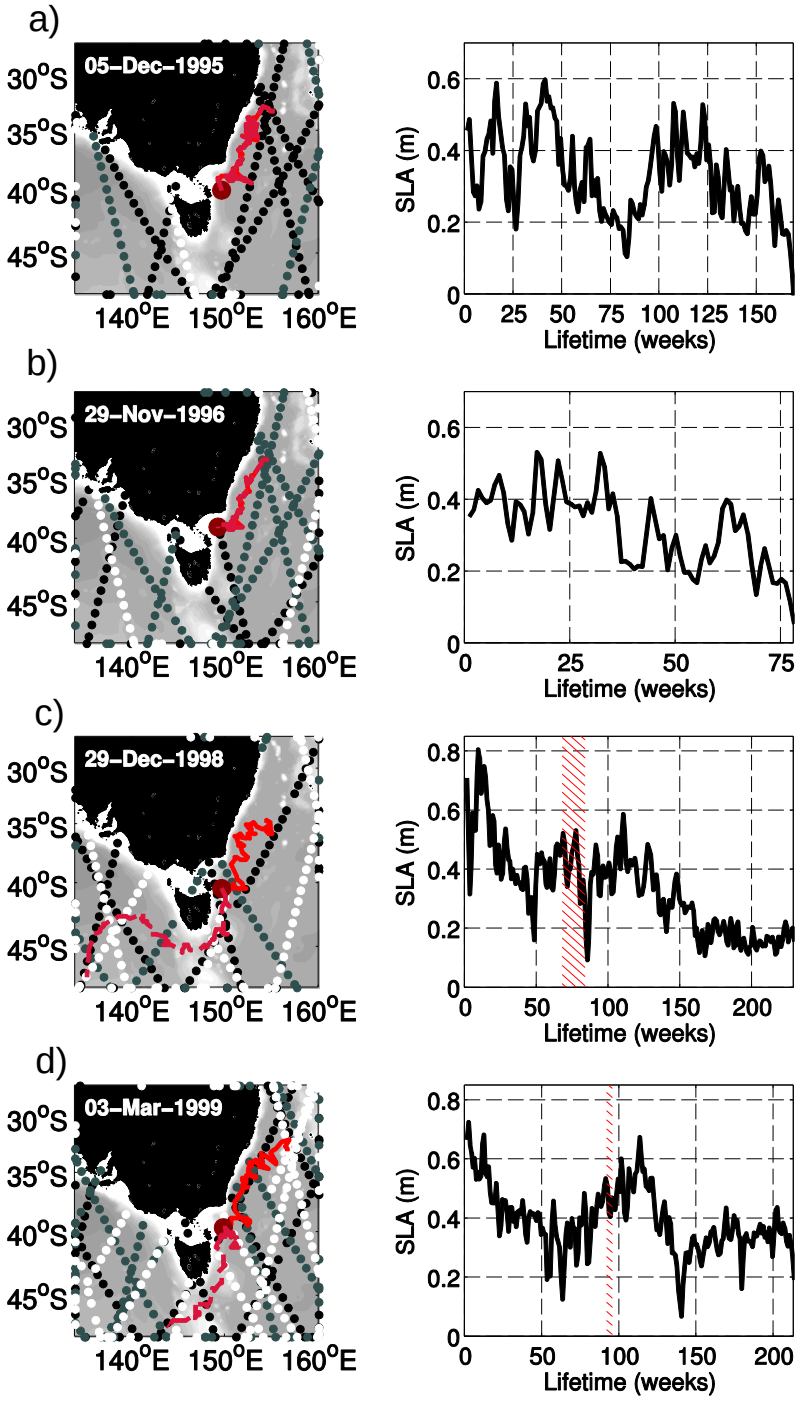


FIGURE 3.4: Maps showing tracked eddies in OceanCurrent (left panels; red lines). The left panels in row (a-b) show tracks that end off Bass Strait; and (c-d) show tracks that extend beyond Tasmania. The dots show data points along altimeter tracks when eddies are off Bass Strait (time $t$). Black, grey and white dots denote times $t$-2, $t$-1 and $t$, respectively. The right panels show times series of SLA for each eddy. The hatched region indicates proximity to Bass Strait slope (~38$^o$S, with 1000–3000 m depths).

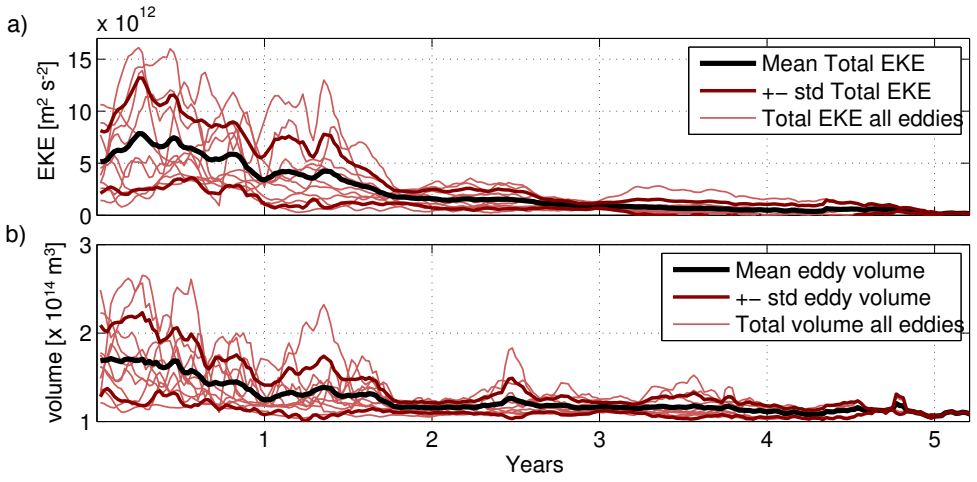


FIGURE 3.5: a) Time series of total EKE within large, long-lived EAC anticyclonic eddies in the ocean model, as they propagate from the Tasman Sea to the Eastern Indian Ocean. The total EKE within each eddy is shown in thin lines. The mean and standard deviation of total EKE considering all eddies is shown in thick black and dark red lines; b) as in (a) but for total eddy volume between 0 and 2000 m. A 4-week running mean filter is used in both time-series. The eddy perimeter used in these calculations is determined by the 0.1 m SLA contour of each eddy, projected from 0 to 2000 m.

m depth interval as they propagate southwards (between "A" and "D"). However, as eddies advect westwards in the Eastern Indian Ocean (between "E" and "G"), the EKE contained in lower levels (600-1000 m depth interval) is as high as in the top levels. In fact, in eddy #3 (Figure 3.6b), the energy contained within the 600-1000 m depth interval is higher than the energy contained in the top 600 m of the eddy. These results show that the part of the eddy with higher velocity becomes deeper as it propagates.

The time series in Figures 3.5 and 3.6 show that the energy within the modelled eddies fluctuates in the Tasman Sea and decays in the Eastern Indian Ocean. The energy within eddies behaves differently due to differences in the oceanographic regime between these two regions. First, there are more eddies, and hence more eddy-eddy interactions, in the Tasman Sea than in the Eastern Indian Ocean. Second, as eddies propagate southwards in the Tasman Sea they interact with its complex bathymetry - and with the continental shelf break (at depths of ∼500–1000 m). This eddy-bathymetry interaction is almost non-existent in the Eastern Indian Ocean, where depths are between 4000 and 6000 m.

### 3.3.2 Eddy non-linearity

The non-linearity of eddies is important because it determines the degree to which fluid is trapped within an eddy. The trapping of fluids is relevant for a range of marine studies,

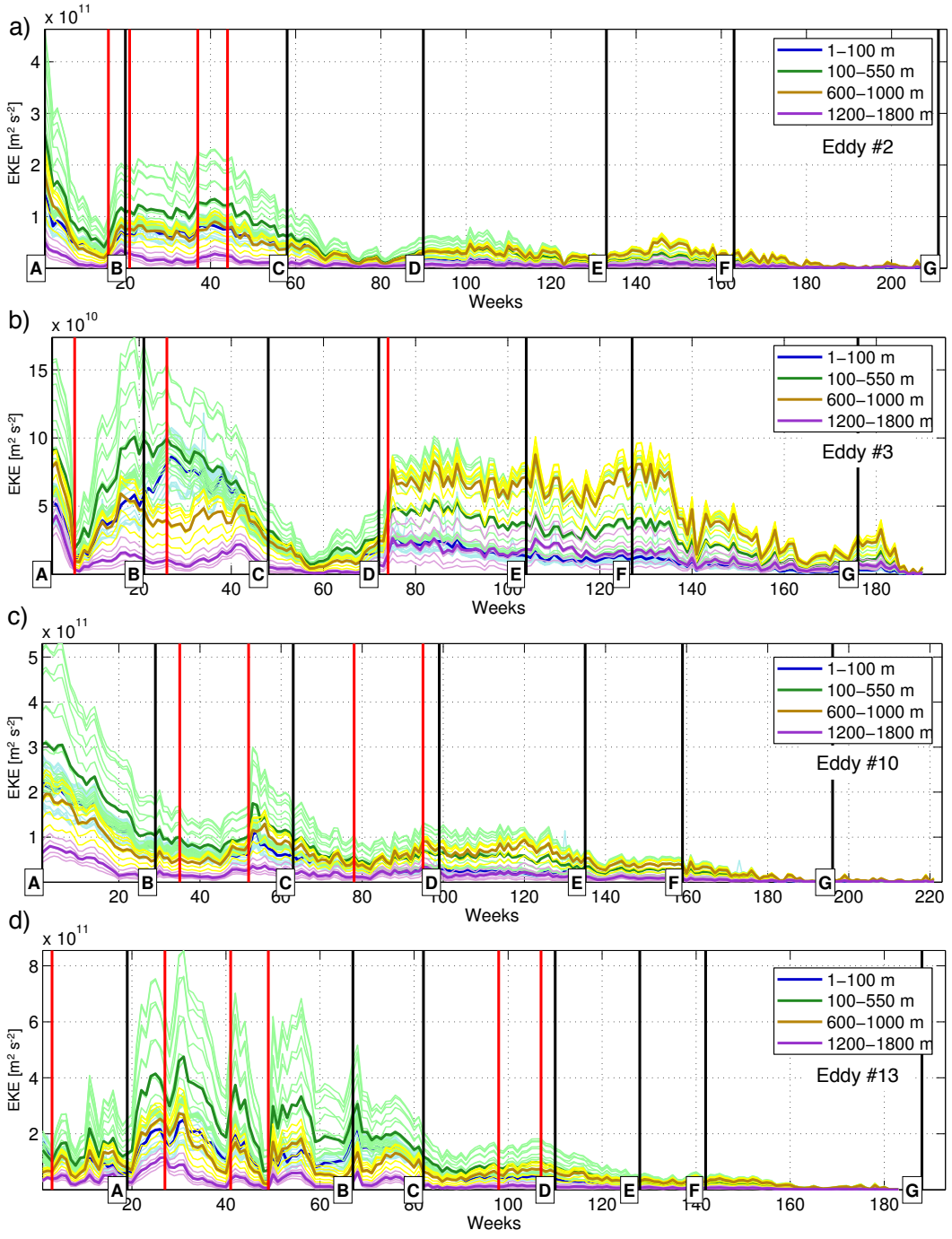


FIGURE 3.6: a) Time series of total EKE for four modelled EAC anticyclonic eddies (a-d) as they propagate from the Tasman Sea to the Eastern Indian Ocean. Eddy numbers refer to eddies tracked in the ocean model in Figure 3.1a. Different colours show total EKE in different depth intervals. Bold coloured lines are the mean total EKE for each depth interval. Black vertical lines indicate "A-G" location along the pathway shown in Figure 3.2a, and red vertical lines indicate merging events. A 4-week running mean filter is used in all time-series. The eddy perimeter used in these calculations is determined by the 0.1 m SLA contour of each eddy, projected from 0 to 2000 m.

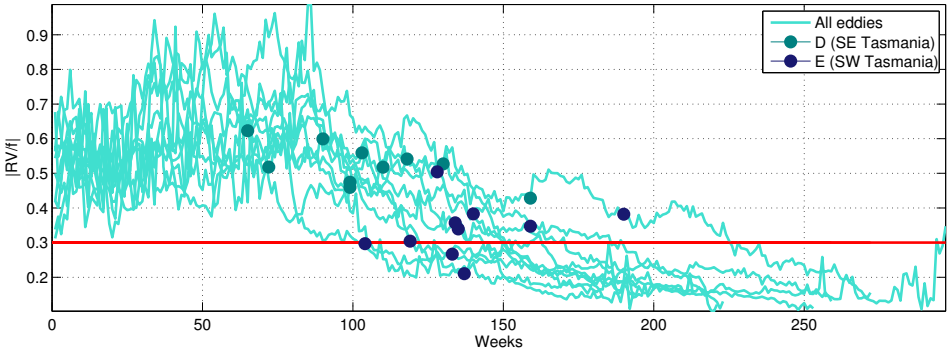


FIGURE 3.7: Rossby number calculated for each EAC anticyclonic eddy propagating from the EAC separation region to the Eastern Indian Ocean in the ocean model. The red line indicates the threshold, where $|\zeta_R/f| > 0.3$ relate to non-linear eddies (as Douglass and Richman, 2015).

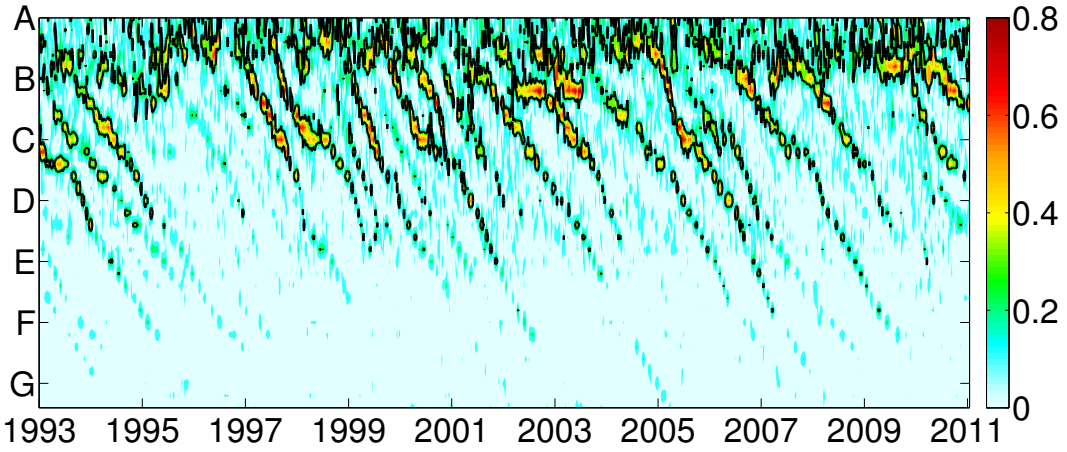


FIGURE 3.8: Hovmoller diagram of $|\zeta_R/f|$ from the ocean model along "A-G" pathway from Figure 3.2a; black contours indicate the 0.3 threshold.

including the ones focused in heat advection, and the dispersal of larvae, and biogeochemical compounds. Here, the non-linearity of the modelled EAC eddies is measured considering the Rossby Number, which is the relationship between the eddy relative vorticity ($\zeta_R$) and the planetary vorticity ($f$; Figure 3.7). To calculate the Rossby number, the $\zeta_R$ used is the maximum anticyclonic $\zeta_R$ at the surface of the eddy (i.e., the first layer of the model, at 5 m). Eddies with $|\zeta_R/f|$ larger than 0.3 are considered to be non-linear (Lee and Brink, 2010, Douglass and Richman, 2015, e.g.,). According to this metric, all eddies are non-linear as they propagate southwards, and then become linear as they move westwards and dissipate. This means that, in their first moments of life, EAC eddies are able to transport waters from their parent current, from a tropical to a temperate region of the ocean. The signature of the non-linear eddies is evident as they propagate along the "A-G" eddy pathway (Figure 3.8), when surrounded by a linear flow.

### 3.3.3 Eddy evolution

#### 3.3.3.1 Temperature and salinity evolution

To examine the temporal variability of sea surface properties within eddies, Hovmöller diagrams of SST (Figure 3.9), Sea Surface Salinity (SSS; Figure 3.10), and their anomalies (SSTA and SSSA) in the ocean model along the idealised pathway are produced.

A SST front between warm tropical waters from the Coral Sea ($> 22^oC$) and cold temperate waters from the Tasman Sea ($< 10^oC$) exists in the region of interest (Figure 3.9a). The mean location of this front is at $\sim 40^oS$, extending further south off the eastern Australia coast, due to advection of warmer waters by the EAC and its eddies. Therefore, eddies propagating along the pathway form in warmer regions and propagate towards colder regions. The SSTA standard deviation is higher close to the EAC separation region and southeast of Tasmania (Figure 3.9b). Here, the seasonal signal is removed, therefore this variability is mainly attributed to local mesoscale variability.

The evolution of SST along the pathway has a strong seasonal signal (Figure 3.9c). This signal hinders the observation of eddy propagation in the SST Hovmöller diagram. Despite this, it is possible to see the SST signature of the eddies previously seen in the ocean model SLA Hovmöller diagram (Figure 3.2b) propagating following the pathway. With the seasonal signal removed, the SSTA associated with the eddies is clearer (Figure 3.9d). Due to their warm-core nature, EAC anticyclonic eddies are seen as a positive SSTA. Although less persistent than the positive SLA associated with eddies (Figure 3.2c), the positive SSTA can be tracked as far as "F", off western Tasmania, in most cases (e.g. eddies 2, 3, 6, 8, 10, 12, 13).

A SSS front between saltier tropical waters from the Coral Sea ($> 35.6$ psu) and fresh temperate waters from the Tasman Sea ($< 35$ psu) is found in this region (Figure 3.10a). The mean location of this SSS front is also at $\sim 40^oS$, extending further south off eastern Australia coast towards Tasmania. The eddy pathway transits through different SSS values, encountering saltier waters of the EAC and fresher waters south of Australia. The standard deviation of SSSA is higher close to the EAC separation region, south of Tasmania and south of Western Australia (Figure 3.10b). This variability is not attributed to a seasonal signal. At the EAC separation region, this variability can be explained by the changes in the location of this current. South of Tasmania, this variability can be explained by movements of the subtropical convergence (Wyrtki, 1960, Ridgway and Dunn, 2003).

The evolution of SSS along the pathway has no strong seasonal signal (Figure 3.10c). In this case, the salinity differences between the Coral and the Tasman Seas (between "C"

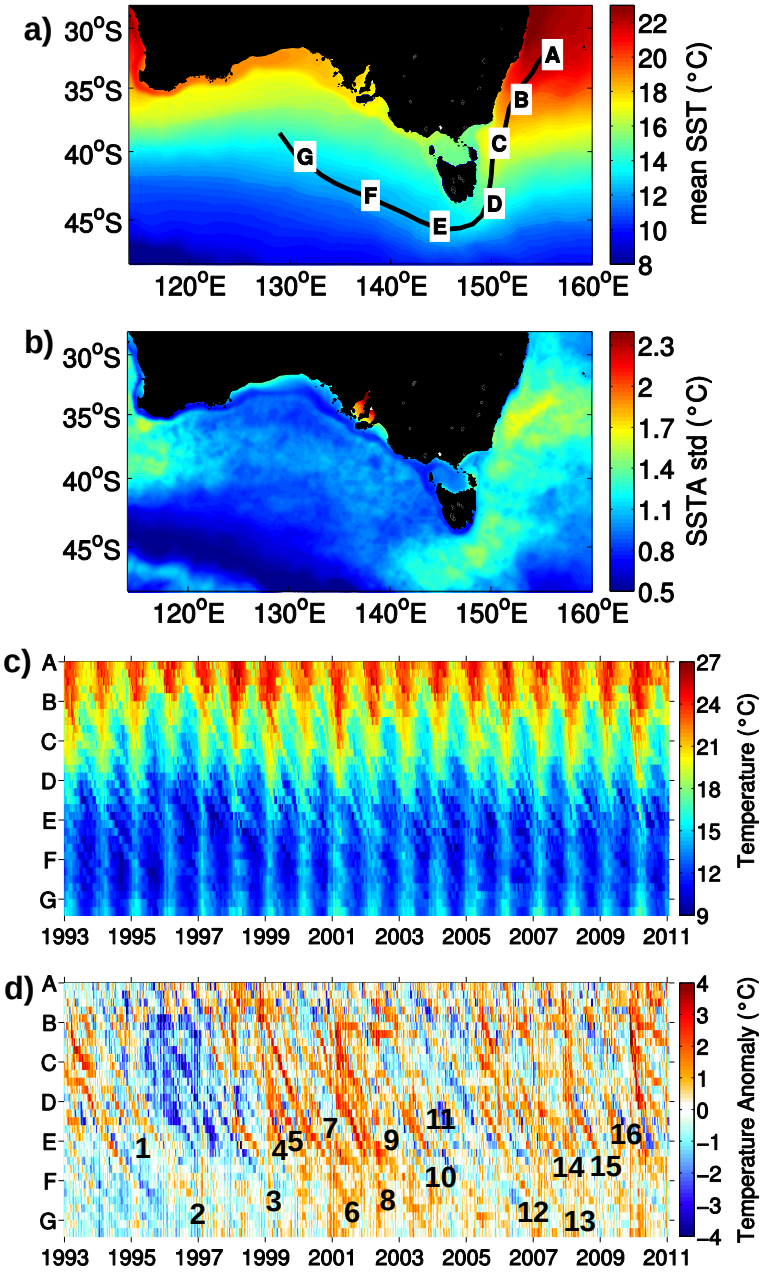


FIGURE 3.9: a) Idealised pathway of anticyclonic eddies shed at the EAC separation region in the ocean model, overlaid on mean SST in the model between 1993 and 2012. The letters ("A" to "G") indicate key locations along the pathway; b) map of SST Anomaly (SSTA) standard deviation in the model between 1993 and 2012; c) Hovmöller diagram of SST in the model on the "A–G" pathway; d) as for (c), but for SSTA, with numbers relating to eddies from Figure 3.1a.

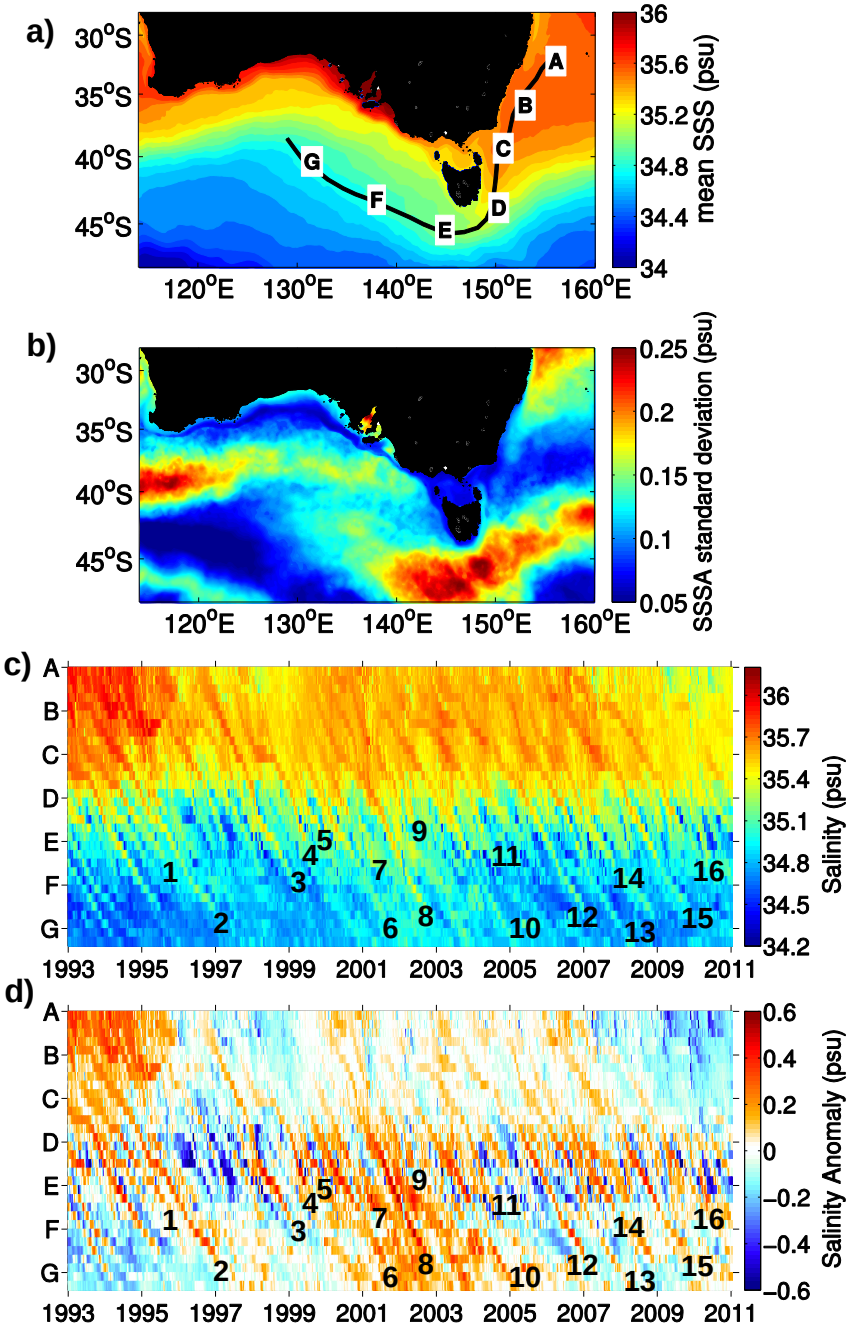


FIGURE 3.10: a) as for Figure 3.9a, but for Sea Surface Salinity (SSS); b) as for Figure 3.9b, but for SSS Anomaly (SSSA); c) as for Figure 3.9c, but for SSS; d) as for Figure 3.9d, but for SSSA.

and "D" in the SSS Hovmöller diagram) are very clear. Even with this strong signal, the signature of the eddy propagation along the pathway is evident. Consideration of seasonal anomalies of SSS yields a clearer picture of the eddy propagation following the pathway (Figure 3.10d). However, after the "D" location, there is a misleading increase in SSSA. This increase does not represent an increase in the SSS associated with the eddies, but a higher SSSA due to the eddy propagating along a highly variable region (Figure 3.10b).

To explore the evolution of the potential temperature ($\theta$) and salinity (S) at depth, $\theta$S diagrams are produced (Figure 3.11). The spread of these properties within all eddies following the pathway ranges from 0 to 25$^o$C and from 34.4 to 35.9 psu, and includes several water masses (Figure 3.11b).

Two regimes are evident when considering $\theta$S within eddies at "A-G" locations along the pathway (Figure 3.11c). These regimes are seen in the scattered data at the surface and sub-surface of eddies located between "A" and "D" (circle 1 in Figure 3.11c), and at the scattered data at the surface and sub-surface of eddies located between "E" and "G" (circle 2 in Figure 3.11c). This scattered data represents the effect of seasonal variability at the surface of the eddy.

The evolution of $\theta$S properties shown in Figure 3.11c is consistent with cooling and freshening of the surface waters of the eddies (Figures 3.9 and 3.10). At the EAC separation (i.e., "A"), eddies are warm and salty, retaining characteristics of their formation region. These characteristics are maintained until the eddies reach Tasmania (i.e., between "C" and "D"). South of Tasmania (i.e., "D"), the surface and sub-surface properties of eddies are cooler and fresher. As eddies advect westwards in the Eastern Indian Ocean (i.e., "E–G"), they no longer carry waters from their formation region at the surface. This is expected, considering that by the time the eddies reach south of Tasmania they are no longer non-linear, and have lost the capacity of trapping fluid. The denser waters within the eddies also change - becoming saltier as eddies propagate (see salinity minimum in the $\theta$S curves).

#### 3.3.3.2 Case studies

The Hovmöller diagrams (Figure 3.2c-e) show that the surface expression of the propagating eddies fluctuates with time. The SLA associated with the eddies often slowly decreases as they propagate, and sometimes increases over just a few weeks, both in the ocean model and the observations. To better understand this, two detailed descriptions of modelled eddies, hereafter Eddy #3 (Figure 3.12) and Eddy #9 (Figure 3.14), are presented. These eddies are representative of the sample of modelled eddies included in

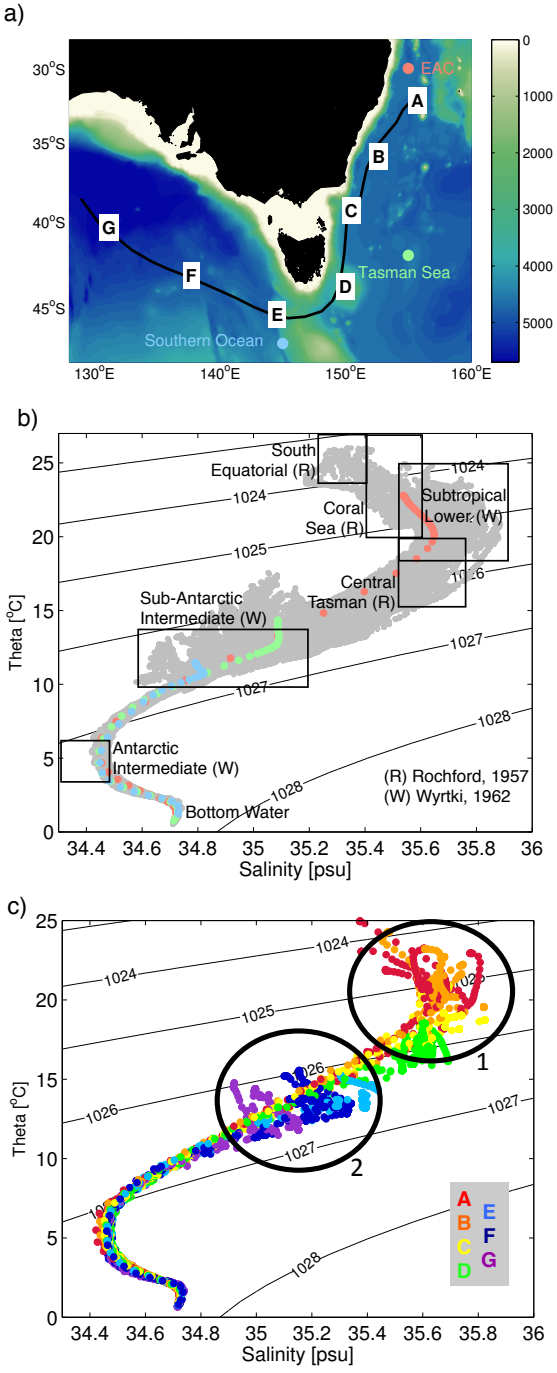


FIGURE 3.11: a) Map indicating the location of the climatology properties in the EAC separation region (pink), the Tasman Sea (green), and the Southern Ocean (blue), and the "A–G" eddy pathway described in Section 3.3.1. The climatology data is the mean $\theta$ and S considering all daily averages from OFAM, between 1993 and 2012, and are shown in (b). Colours indicate bathymetry; b) $\theta$S diagram of properties at the centre of all EAC anticyclonic eddies at each timestep as they propagate from the Tasman Sea to the Eastern Indian Ocean. Water masses are named based on Rochford (1957) and Wyrtki (1962); c) $\theta$S diagram of properties at the centre of all EAC anticyclonic eddies at "A–G" locations (colours) shown in (a). In (b) and (c) background lines indicate potential density (kg/m$^3$). The black circles (1 and 2) indicate two regions of scattered data, discussed in the text.

this study (the same details for all modelled eddies are included in Figures S1–S14 in Appendix B).

Here, various eddy characteristics, as the eddies follow the pathway, are shown. These characteristics include the SLA associated with these eddies, their velocity profile with depth, and their barotropic-baroclinic partitioning. To quantify the barotropic-baroclinic partitioning of the eddies, the normal vertical modes along their path are computed (Figures 3.12c and 3.14c). This is achieved by solving the Sturm-Liouville eigenvalue problem (e.g., Wunsch, 1997, Venaille et al., 2011), using the Coriolis parameter and profiles of velocity and the buoyancy frequency. At each time step, I use profiles that are midway between the eddy centre and the edge of the eddy to the east - usually about 100 km east of the eddy centre. The ratio of the first and second eigenvalue to the sum of all eigenvalues is then computed, quantifying the percentage of the velocity profile that projects onto the zeroth mode (the barotropic mode) and the first baroclinic mode. Sensitivity tests indicate no significant difference to the choice of the eastern/western side of the eddy.

**1$^{st}$ case study: Eddy #3**

The SLA associated with Eddy #3 changes as the eddy propagates (Figure 3.12a). Between the EAC separation region ("A") and southeast of Tasmania ("D"), the SLA associated with the eddy varies between 0.17 and 0.45 m. The SLA increases sharply after eddy merging events (red lines between "A" and "D"), but slowly decreases otherwise. After the eddy propagates beyond Tasmania, the SLA decays, reaching ∼0.1 m before the eddy dissipates completely.

To demonstrate the interactions between Eddy #3 and other anticyclonic eddies, the merging events occurring in "A" and in "D" in Figure 3.12a are shown in Figures 3.13a and 3.13b, respectively. In the event in "A", Eddy #3 and another anticyclonic eddy of the Tasman Sea interact, but do not fully merge (Figure 3.13a). In one month, this interaction doubles the SLA associated with this case study. In the event in "D", Eddy #3 fully merges with another anticyclonic eddy off southeast Tasmania (Figure 3.13b). Because of this full merging, the SLA associated with this case study increases from 0.25 m to 0.35 m in two months.

The velocity profile changes as Eddy #3 propagates along the pathway. To demonstrate that, daily averages of this eddy immediately after it forms (Figure 3.12b, left), when it is located off Bass Strait (Figure 3.12b, centre), and when it propagates towards the Eastern Indian Ocean (Figure 3.12b, right) are shown. Remember that the output of the ocean model used here is comprised of daily averages. Immediately after formation, the

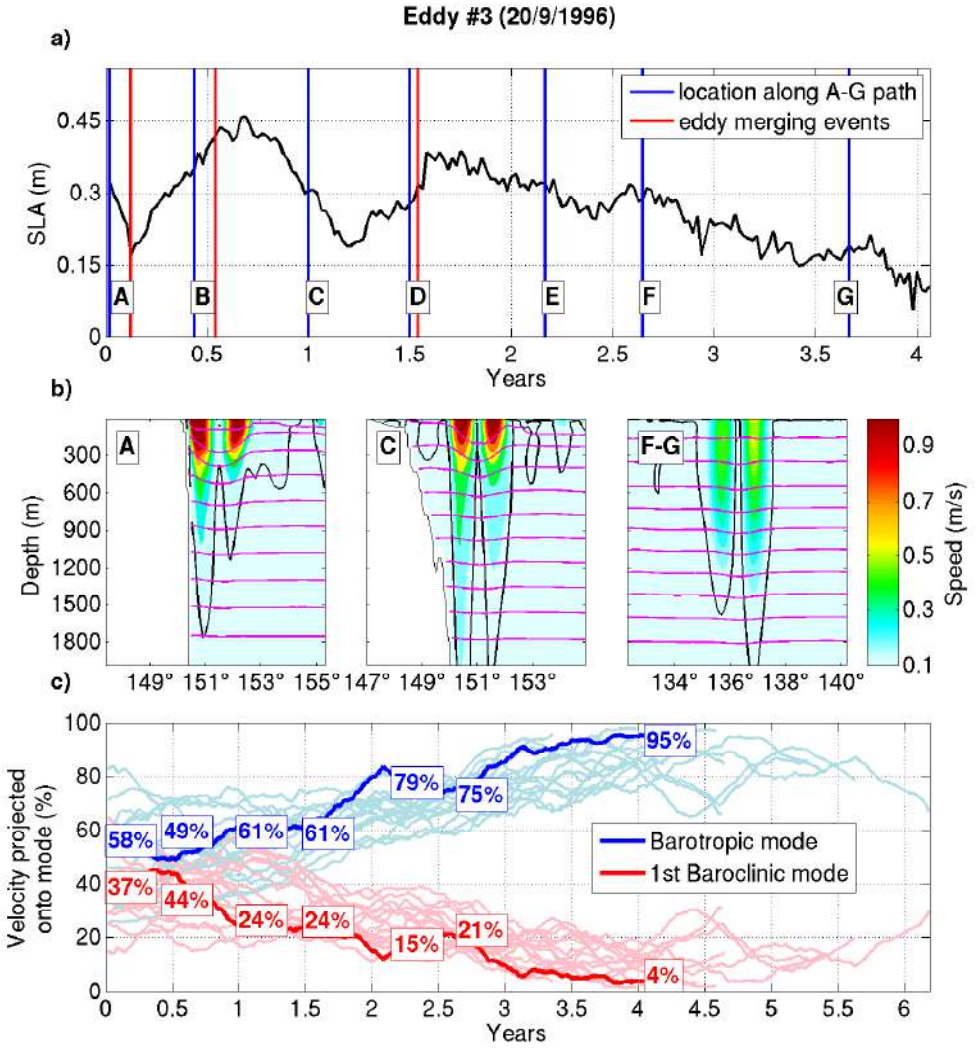


FIGURE 3.12: a) Times series of maximum SLA associated with Eddy #3; b) daily averages of modelled velocity (colour; black contour denoting 0.1 cm/s) and potential density (magenta contours; contour intervals are 0.1 kg/m$^3$) near "A", "C" and "F–G" locations; and c) time-series of the percentage of velocity that projects onto the barotropic (blue) and 1$^{st}$ baroclinic (red) modes for Eddy #3 (bold lines) and for all other modelled eddies (thin lines). The percentages at each point, "A–G", are denoted in boxes. Note that the x-axes in (a) and (c) are different.

velocity field is surface-intensified with values of over 1 m/s, with moderate velocities penetrating to depths of about 1800 m, and with strong vertical shear - characteristic of a strongly baroclinic flow. By the time Eddy #3 propagates to Bass Strait, it has weaker velocity at the surface, compared to its formation period. The eddy still shows deep penetration of the velocities (over 2000 m), and weakening vertical shear. The eddy velocity is much weaker by the time it reaches the Eastern Indian Ocean, and is characterised by a velocity field that shows weak vertical shear - characteristic of a quasi-barotropic flow. Note that the maximum velocities are at sub-surface at "F–G" - centred around 200 m depth. Also note that the velocity in the eastern and western

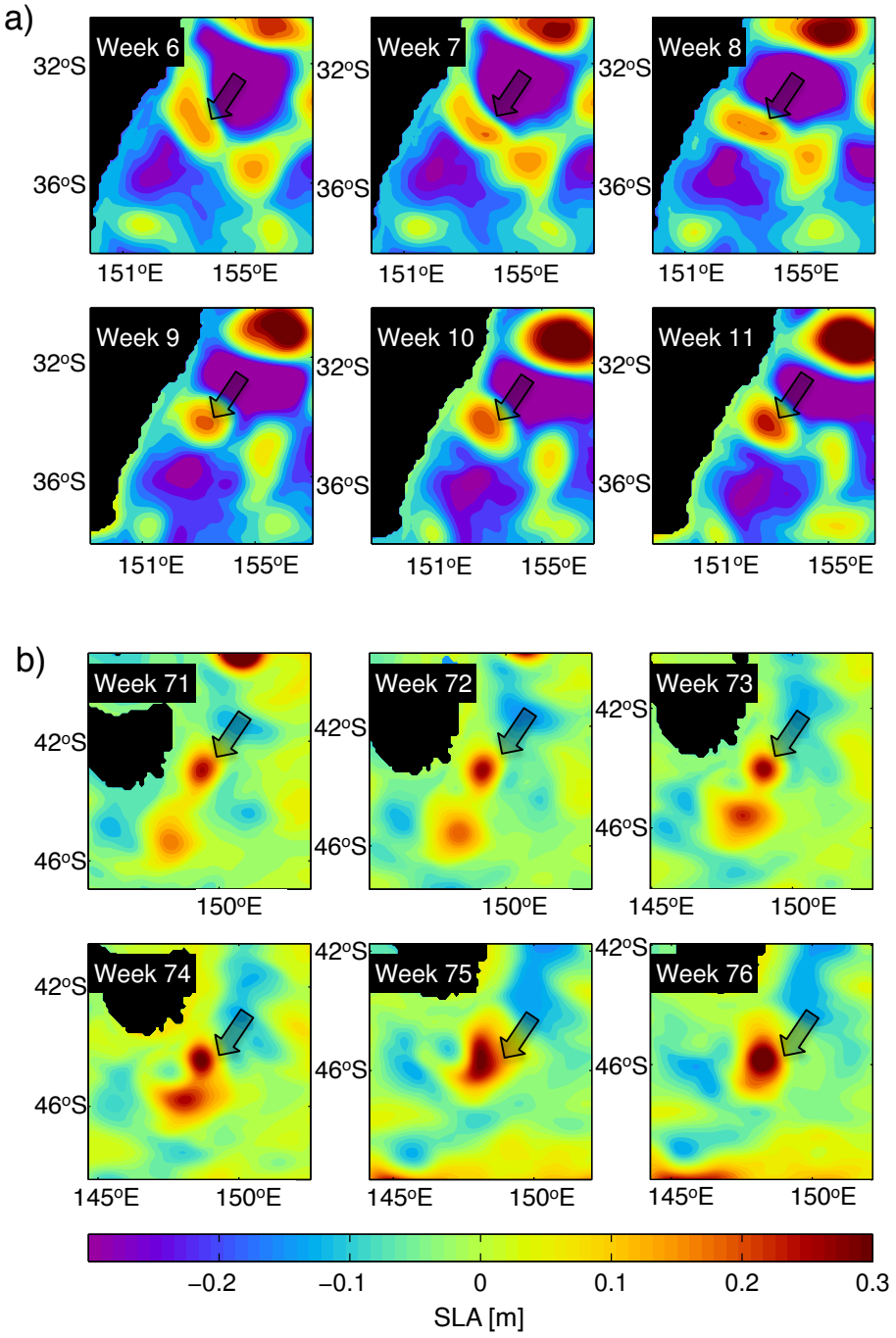


FIGURE 3.13: Daily averages of modelled SLA (colours) showing a merging event close to "A" (a) and close to "D" (b) between Eddy #3 and other anticyclonic eddies. "A" and "D" refer to locations on the eddy pathway shown in Figure 3.2a. The moment of these merging events are indicated by the vertical lines to the left and to the right in Figure 3.12a. The arrows indicate Eddy #3.

flanks of the eddy in "A" and in "F–G" is asymmetric.

The velocity profiles with depth suggest that the eddy is more baroclinic when it first forms, and becomes more barotropic as it propagates following the pathway. Low-pass filtered time-series of the ratio of eigenvalues, quantifying the barotropic-baroclinic partitioning, are shown in Figure 3.12c, with results for Eddy #3 (bold lines) and for all other eddies (thin lines). The results in Figure 3.12c quantify what is evident in Figure 3.12b - namely that Eddy #3 becomes more barotropic as it propagates, with 58% of the velocity explained by the barotropic mode when the eddy forms, increasing to 95% as it reaches the Eastern Indian Ocean. Conversely, the percentage of the velocity field projecting onto the first baroclinic mode decreases from 37%, when Eddy #3 first forms, to 4% as it reaches the Eastern Indian Ocean.

**2$^{nd}$ case study: Eddy #9**

The SLA associated with Eddy #9 changes as the eddy propagates (Figure 3.14a). Here, in one merging event, there is no increase in eddy SLA. Similar to Eddy #3, the SLA varies between the EAC separation ("A") and southeast of Tasmania ("D"), decreasing almost monotonically when the eddy is propagating in the Eastern Indian Ocean (i.e. after "E").

This velocity profile with depth of this eddy - as for Eddy #3 - also changes as it propagates along the pathway. Immediately after formation (Figure 3.14b, left) the velocity field is surface-intensified with values of ∼0.8 m/s, with weaker velocities penetrating deeper than 1800 m. The velocity profile for Eddy #9 is more asymmetric than for Eddy #3, with stronger velocities penetrating deeper on its western flank. I believe this asymmetry to be caused by the eddy interaction with the continental slope. Moreover, this asymmetry suggests a vertical tilt of the main axis of the eddy. By the time Eddy #9 reaches Bass Strait, it has weaker velocity at surface and weaker vertical shear, compared to its formation period. The eddy still shows deep penetration of the velocity (over 2000 m). The eddy velocity, as its vertical shear, is much weaker by the time it reaches the Eastern Indian Ocean. Here, the maximum velocities are also at sub-surface - centred around 300 m depth.

Eddy #9 becomes more barotropic as it propagates, with 54% of its velocity explained by the barotropic mode when the eddy forms, increasing to ∼80% before the eddy dissipates. Conversely, the percentage of the velocity field projecting onto the first baroclinic mode decreases from 41%, when Eddy #9 first forms, to ∼15% before the eddy dissipates.

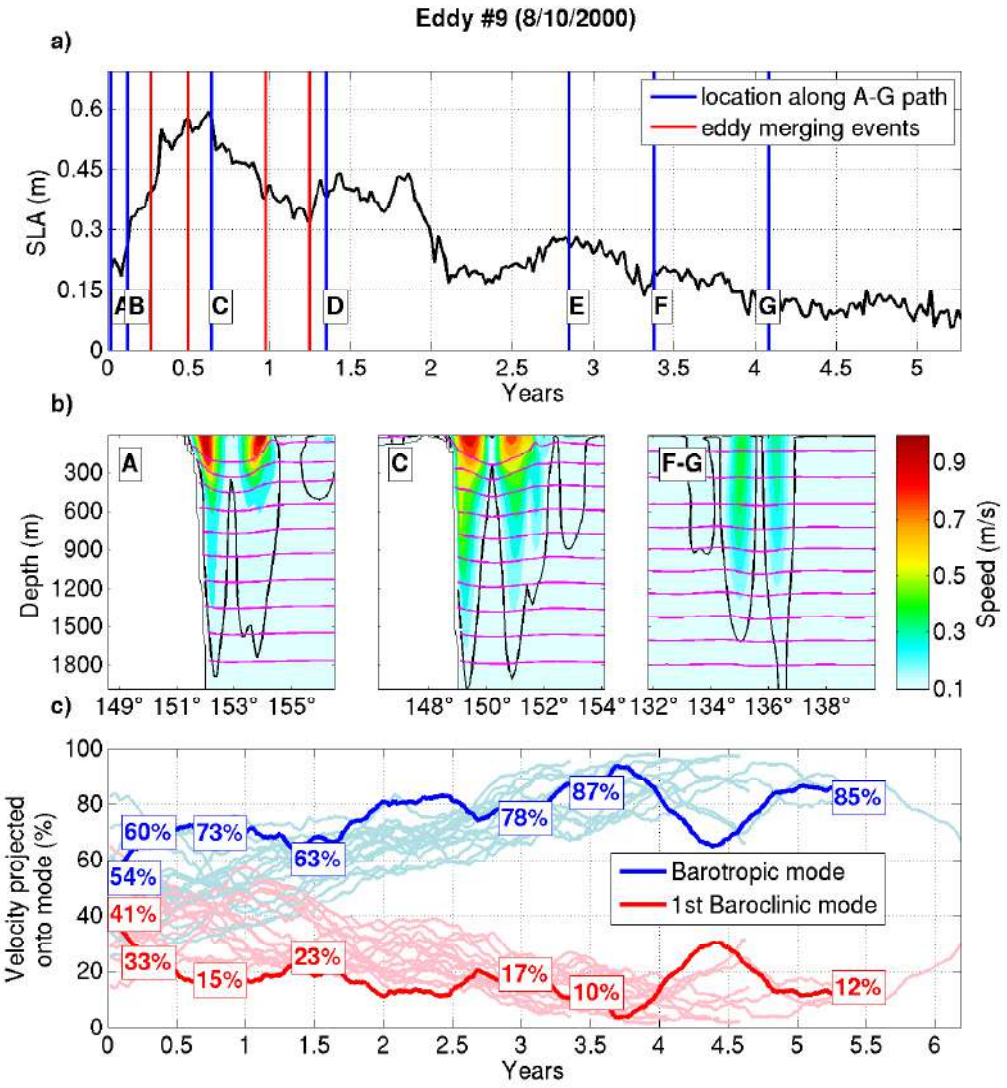


FIGURE 3.14: As in Figure 3.12, but for Eddy #9

#### 3.3.3.3 The subsurface signal of EAC anticyclonic eddies

The velocity maximum within both case studies shown here (and all eddies shown in Appendix B) deepens from the surface to the sub-surface as the eddies propagate following the pathway (Figures 3.12b and 3.14b). This deepening of the velocity maximum suggests that the surface layers of the eddies change in time. To illustrate these changes, daily averages of vertical sections of potential density associated with four eddies are shown (see Figure 3.15). While eddies are still in the Tasman Sea, all isopycnals are depressed (A to E in Figure 3.15). As eddies propagate, the density of their inner waters increases. Therefore, when the eddies reach the Eastern Indian Ocean, they are capped by lighter waters (F to G in Figure 3.15). In these final stages of life, the permanent pycnocline is depressed within the eddy, and the seasonal pycnocline is shoaled (e.g., waters lighter than 1025.8 kg/m$^3$ versus waters denser than 1026.4 kg/m$^3$ in Figure 3.15 G, first

row). Therefore, the structure of EAC eddies that reach the Eastern Indian Ocean resembles the lense-type structure of mode water eddies (Flierl, 1979, McGillicuddy et al., 2007, McGillicuddy, 2015).

## 3.4 Discussion and conclusions

The results show that large, long-lived EAC anticyclonic eddies mostly follow a consistent pathway and leave the Tasman Sea. Specifically, ∼25-30% of anticyclonic eddies that form in the EAC separation region propagate southwards, adjacent to the continental slope, and transit south of Tasmania. Besides advection by the EAC extension, Shi and Nof (1994) suggest that the "image effect" can be the driver for the southward propagation of EAC anticyclonic eddies. This effect explains the advection of an eddy along a free-slip wall due to its image, pushing - in the Southern Hemisphere - an anticyclonic eddy polewards, and a cyclonic eddy equatorwards (Figure 3.16). The increase of the barotropic component of EAC eddies as they propagate may also be responsible for their strong bathymetric steering. This is especially true when eddies move around Tasmania, where 53-71% of their velocity is projected into the barotropic mode (Figures 3.12c and 3.14c, and Appendix B). The restriction imposed to the flow by Tasmania, the Tasman Plateau to the east, and the South Tasman Rise to the south steers these highly barotropic eddies in the coherent pathway described here. After crossing south of Tasmania, the eddies propagate west-north-westwards, towards the Eastern Indian Ocean. This part of the pathway is consistent with the existing literature (Ridgway and Dunn, 2007, Baird et al., 2011). The west-north-westward propagation is also consistent with previous reports of anticyclonic eddy paths in other regions (e.g., Morrow, 2004, Chelton et al., 2011b). Based on the analyses performed here, it is suggested that most EAC anticyclonic eddies that follow the identified pathway finally decay in the deep basin of the Eastern Indian Ocean. However, Cresswell and Peterson (1993) sampled an anticyclonic eddy off the southern tip of Western Australia (∼177 $^{o}$E) carrying Bass Strait waters. Their observations imply that some eddies have propagated further northwest, well beyond the pathway identified in this study.

The interaction between eddies and the mean flow has been extensively studied in WBC of the Northern Hemisphere (e.g., Waterman and Jayne, 2011, and references therein), and in the Agulhas Current (e.g., Biastoch and Krauss, 1999, De Ruijter et al., 1999), and to a smaller extent in the Brazil Current (Oliveira et al., 2009, Rocha et al., 2014) and in the EAC (Bowen et al., 2005, Mata et al., 2006). Within the EAC region, eddies might regulate the local recirculation where the current separates from the coast (Mata et al., 2006).

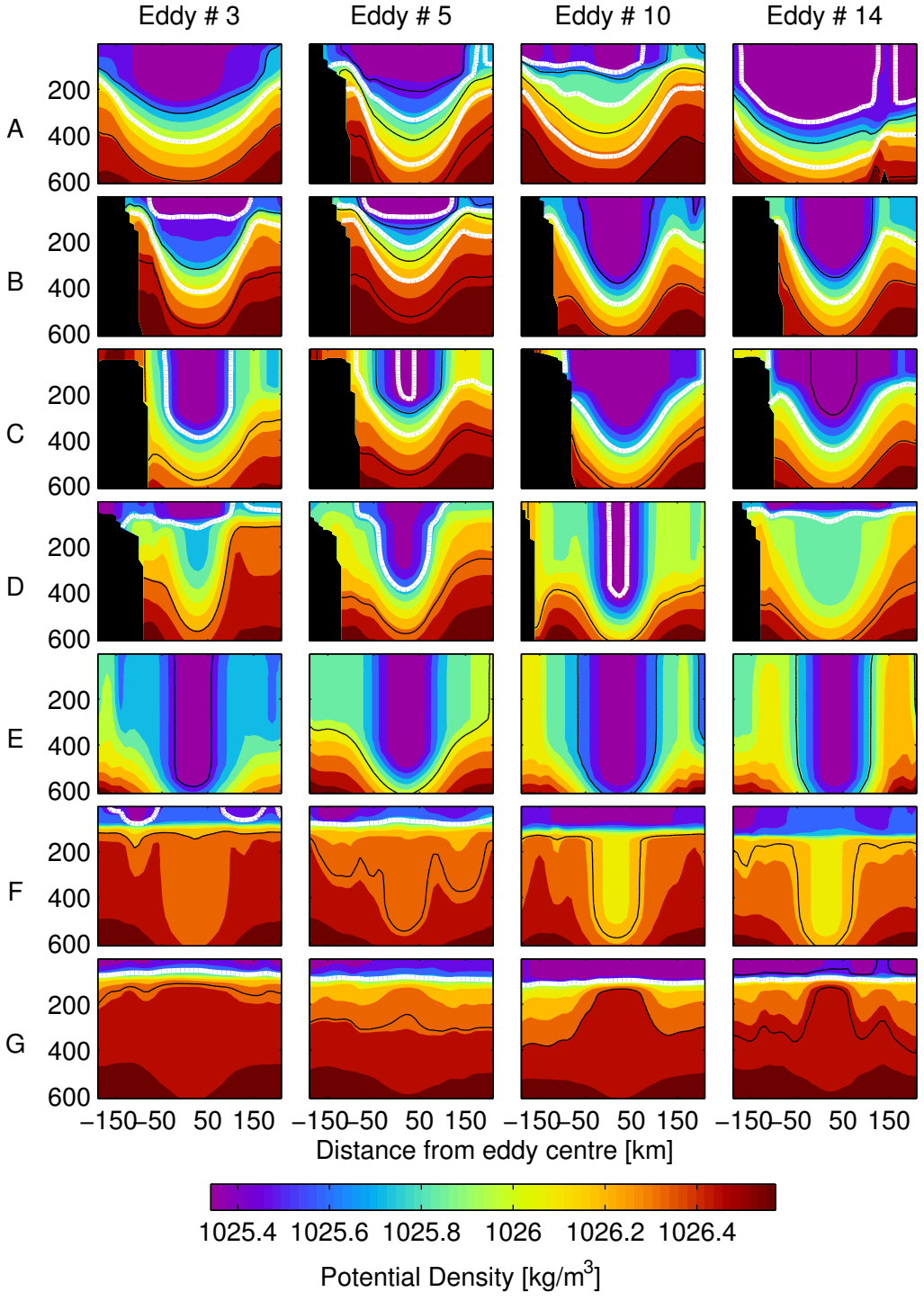


FIGURE 3.15: Daily averages of modelled potential density fields (colours) in the top 600 m of the ocean associated with four EAC anticyclonic eddies that propagate from the EAC separation region (A) to the Eastern Indian Ocean (G). The black lines are isopycnals spaced every 0.1 kg/m$^3$, and the white lines are the 1024, 1025, and 1026 kg/m$^3$ isopycnals. The number of the eddies relates to numbers in Figure 3.1a.

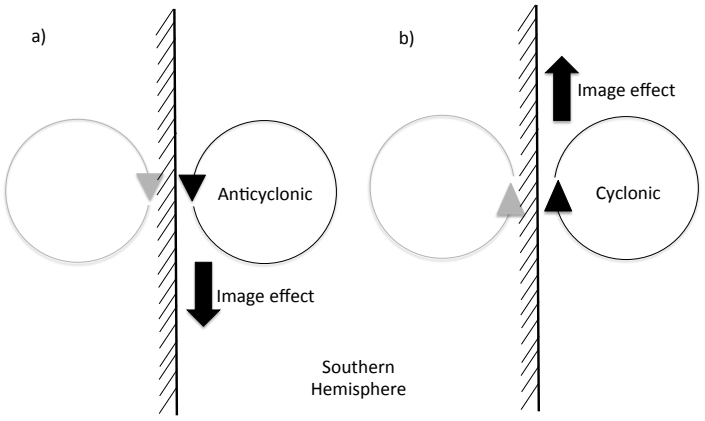


FIGURE 3.16: Image effect in (a) an anticyclonic and (b) a cyclonic eddy in the Southern Hemisphere (adapted from Shi and Nof (1994)).

In the EAC separation, newly formed eddies can either coalesce with the EAC (Nilsson and Cresswell, 1981) or grow and leave the region (Mata et al., 2006, Everett et al., 2012, Pilo et al., 2015). EAC anticyclonic eddies that coalesce with the EAC lose barotropic energy to the mean flow (Mata et al., 2006). EAC anticyclonic eddies that grow and leave the region receive both baroclinic and barotropic energy from the mean flow (Bowen et al., 2005, Mata et al., 2006). As the eddies move southwards, their baroclinic energy is lost back to the mean flow (Mata et al., 2006). The results shown here are consistent with this energy loss (Figures 3.5, 3.6, 3.12a and 3.14a). Exceptions to this slow eddy decay are caused by eddy merging events, as shown here, and by eddy interactions with other local instabilities (Mata et al., 2006). The interaction between eddies and the mean flow clearly impacts the SLA and energy associated with each eddy.

The large, long-lived EAC anticyclonic eddies studied here change from highly baroclinic structures in the Tasman Sea, to highly barotropic structures in the Eastern Indian Ocean (Figures 3.12 3.14). The highly barotropic structure of EAC eddies is clearly seen in the deep, low-stratified vertical section of potential vorticity off Southeastern Tasmania ("E" in Figure 3.15). While EAC eddies lose their baroclinic structure and keep their barotropicity, the opposite is valid for Agulhas Rings (Matano and Beier, 2003). Those rings become more baroclinic as they interact with the bottom topography of that region. More studies are required to determine the causes for this disparity between EAC and Agulhas Current eddies.

The results show that, in the absence of eddy-eddy interactions, the total EKE within eddies - and the SLA associated with them - gradually decreases (Figures 3.5 and 3.6).

Some of the eddies decay faster if they "stall" off certain locations off Australia. During those "stalling" periods, the eddies often "push up" against the continental slope - remaining at a near-constant latitude for several months - and rubbing against the continental slope, possibly explaining a faster decrease in SLA. This "stalling" behaviour has been previously reported by Nilsson et al. (1977). The authors sampled one anticyclonic eddy off New South Wales ($\sim 35^o$S) that remains in the same region for 7 weeks. The volume of that eddy decreases by 10-30% during the stalling period. The reason for the eddies "stalling" near Sydney and Bass Strait is not completely clear. Perhaps eddies stall near Sydney because their southward propagation is interrupted by the presence of other eddies; and perhaps the stalling near Bass Strait may be related to the orientation of the coast (noting the change in the coastline alignment to the north-east of Bass Strait - near point "C" in Figure 3.2a) and the tendency for eddies to propagate westwards (e.g., Cushman-Roisin et al., 1990, van Leeuwen, 2007, Morrow, 2004).

Eddies in the model and in observations stall at different locations. Eddy stalling seems to relate to bathymetric steering and eddy-eddy interactions. While the bathymetric steering of eddies is expected to act similarly in both datasets, the eddy-eddy interactions differs. Remember that OFAM is a free-running model, and the location and intensity of each eddy is not expected to be the same in OFAM and in observations. In addition, in observations, eddy merging is more recurrent than in the model, especially off Eastern Tasmania. This frequent merging off Eastern Tasmania is possibly the reason for a higher number of eddies stalling in that region in observations when compared to the model.

Several other mechanisms may be responsible for eddy decay. These mechanisms include the loss of balance in the upper ocean (sub-mesoscale instabilities; e.g. Drijfhout et al., 2003), lateral entrainment (e.g. Cheney and Richardson, 1976), interaction with internal waves (Polzin, 2010), damping by air-sea fluxes (e.g. Villas Bôas et al., 2015, Xu et al., 2016), the generation of Rossby waves (Flierl, 1984, McDonald, 1998, van Sebille et al., 2010), and interaction with bathymetry (Shapiro et al., 1995, Kamenkovich et al., 1996, Schouten et al., 2000, de Steur and van Leeuwen, 2009).

The SLA amplitude associated with EAC anticyclonic eddies fluctuates along the pathway. The primary cause of these fluctuations is merging with other eddies. Typically, a merging event results in an increase in the maximum SLA by 0.05-0.25 m (an approximate increase of 24% of the SLA associated with the eddy). From the two case studies shown here (and also the eddies shown in Appendix B) I conclude that it is common for an eddy to merge at least three times as it propagates, with most merging events occurring in the Tasman Sea (before "D" in Figure 3.2). The recurrent eddy merging in the Tasman Sea is mostly due to the high number of eddies existing within that

region. However, Valcke and Verron (1997) show that the more baroclinic eddies are, the more likely they are to merge. Therefore, the fact that eddies are more baroclinic when propagating in the Tasman Sea - compared to when propagating in the Eastern Indian Ocean - may also contribute to the recurrent eddy merging in the former location. In a thoroughly investigated merging event between two anticyclonic eddies in the Tasman Sea, Cresswell (1982) describes two stacked cores in the resulting eddy. Stacked cores were not identified after the merging events associated with the eddies studied here. Investigations to determine if the absence of stacked cores in the model is because the model cannot resolve them, or because they are rare in the Tasman Sea, are still required.

It is shown in this Chapter that the maximum velocity of EAC anticyclonic eddies deepens in time, suggesting changes in the structure of these eddies, especially at surface. Changes in the eddy structure may relate to the sinking of eddies as they propagate, and to the erosion of the upper layers of the eddy. The sinking of anticyclonic eddies has been associated with intense cooling of the eddy core, warming of the surrounding fluid, and eddy-wind interactions (Chapman and Nof, 1988, McGillicuddy, 2015). In the northern Tasman Sea, the warmer EAC has been reported overwashing eddies during summer months (Tranter et al., 1982, Baird et al., 2011, Macdonald et al., 2013). As eddies propagate further south, they lose heat - as seen in the SSTA evolution in Figure 3.9d and in the $\theta$S evolution in Figure 3.11c. I speculate that this cooling process reinforces the sinking of the core of these eddies and, therefore, both the cooling of the core and the warming of surrounding waters are important for the sinking of EAC eddies. The effect of wind in the sinking of EAC anticyclonic eddies, however, still requires investigation. The erosion of the surface layers of the eddy, given by horizontal mixing, may also play a role in modifying the structure of these eddies. With a reduced surface velocity, the maximum rotation signal would be found at depths, as observed in Figures 3.15. The effect of one or both of these processes may result in the sub-surface core of the eddies shown here. Anticyclonic eddies with a sub-surface core have been previously observed in the Tasman Sea entrapping coastal waters (Baird and Ridgway, 2012) and shelf-water organisms (Tranter et al., 1982, Baird et al., 2011). Therefore, the sinking and surface erosion of anticyclonic eddies impacts the exchange of waters between coastal and oceanic regions.

The long-lived EAC eddies studied here have a mean $|\zeta_R/f|$ of 0.5 as they propagate southwards (from A to D in the eddy pathway), and 0.2 as they propagate westwards (from E to G; Figure 3.7). The values related to EAC eddies after formation compare to mean $|\zeta_R/f|$ values for Agulhas Rings (0.5, Douglass and Richman, 2015) and eddies from the Gulf Stream (0.4, Douglass and Richman, 2015), known to be highly non-linear. Conversely, the values related to EAC eddies before dissipation compare to mean $|\zeta_R/f|$

values for Brazil Current eddies (0.2, Douglass and Richman, 2015). Another way to determine an eddy's non-linearity is to compare its rotation speed to its propagation speed (U/c, as in Chelton et al., 2011b). Eddies with U/c larger than 1 are considered to be non-linear. According to this metrics, all EAC eddies studied here are highly non-linear, from formation to dissipation, with U/c values ranging between 5 and 60. This results corroborates with the findings from Chelton et al. (2011b), who state that "essentially all of the observed mesoscale features outside of the tropical band $20^o$S-$20^o$N are nonlinear by the metric U/c" and that "approximately 90% of the observed mesoscale features are nonlinear by this measure". However, the propagation speed of eddies in the model is smaller than the propagation speed of eddies in the altimetry datasets. Therefore, the U/c metrics might be unrealistic, and caution must be taken when interpreting these results. Because of these unrealistic eddy propagation speeds in the model, the Rossby Number is used here, as a more reliable metrics.

Despite the non-linearity of eddies in their first stages of life, potential temperature and salinity properties at the surface and interior of the eddies change along the pathway. The signal of $\theta$S properties decreases in the later stages of life of the eddies, with waters within the eddies becoming cooler and fresher in time. This relates to the gain in linearity of these eddies after they cross south of Tasmania. In addition, as eddies propagate southward, they mix with Tasman Sea waters and lose heat at surface layers. By the time eddies reach the Eastern Indian Ocean, their SSTA signature is almost absent compared to their SLA signature. This relates to their decrease in Rossby Number during these final stages (Figure 3.15). An interesting feature of the evolution of temperature and salinity properties within EAC anticyclonic eddies is the shift of dense, bottom waters towards higher salinity values as eddies reach their final stages of life. I believe this shift to also be related to the sinking of eddies in time, but further assessment is still required. In addition to changes in salinity along the pathway, the SSSA Hovmöller diagram also shows changes in time. There is an evident freshening of eddies close to the EAC separation region, between 2005 and 2011, consistent with results based on Argo float data (Rykova and Oke, 2015).

In both the model and observations, there is an interannual variability in the shedding rate of long-lived EAC anticyclonic. Between 1992 and 2011 there are periods of higher eddy-shedding frequency (i.e., 1999-2003) and lower eddy-shedding frequency (i.e., 1995-1999). In all three datasets these periods coincide, suggesting that model forcings, such as the wind, may be involved in the processes that govern eddy shedding. Consideration of Hovmöller diagrams of different variables (Figures 3.2c, 3.9d and 3.10d) reveals a different pattern between 1995 and 1997. During this period no eddies propagate following the pathway. Also, there are smaller values of SLA, SSTA and SSSA compared to post-1997 years. Because of the "gating" described in Chapter 1, the 1995–1997 period

is associated with a reduced southward EAC transport and increased eastward Tasman Front transport (Ridgway et al., 2008, Hill et al., 2011). It is expected that a weaker EAC transport may lead to fewer eddies being shed and a smaller magnitude of SSTA and SSSA in that region.

The asymmetry between the velocity in the eastern and western flanks of the case studies (Figures 3.12b and 3.14b), and in some eddies from Appendix B, suggests a vertical tilt in the main axis of these eddies. A careful investigation of this tilt - conducted at each time step of an eddy chosen as case study - reveals that the misalignment between the eddy centre at the surface and at 2000 m (defined by the minimum velocity within the eddy perimeter) is either absent or a distance of only one horizontal grid cell in the model (i.e. $\sim$110 km). Therefore, despite some evidences of eddy tilting in the results shown here, this tilting is not fully resolved by the model. Nevertheless, this is the first study that reports the vertical tilt in EAC anticyclonic eddies. The literature reports EAC cyclonic eddies tilting towards the coast (Oke and Griffin, 2011, Roughan et al., 2017), and anticyclonic eddies tilting in other oceanic regions (Roemmich and Gilson, 2001, Kurczyn et al., 2013, Zhang et al., 2016). These studies show that the vertical tilt impacts local productivity (Oke and Griffin, 2011, Roughan et al., 2017), and heat distribution (Roemmich and Gilson, 2001, Kurczyn et al., 2013). The vertical tilt of EAC anticyclonic eddies - and its impact on the local and regional oceanography - requires further investigation.

This study shows that altimetry sampling is problematic off eastern Tasmania. There are relatively long periods when no altimeter tracks cross the described eddy pathway, resulting in a local maximum in the mapping error of the gridded SLA (see Figure 2.5). As a result, this identified eddy pathway has not been previously documented. This study, instead, made use of an eddy-resolving ocean model output (which is imperfect, but has sufficient spatio-temporal coverage for studies of mesoscale variability) to complement the analysis of observation-based gridded SLA fields. This allowed me to see the eddy pathway clearly.

The EAC anticyclonic eddy pathway shown here provides a direct connection, albeit over several years, between the EAC separation region and the Eastern Indian Ocean. Thus, it allows for advection of EAC waters well beyond the Tasman Sea. As the eddies propagate southwards, they interact with different regions of the Australian continental shelf break. This interaction can lead to local changes in ocean temperature and biogeochemistry, that ultimately affects habitat conditions for the marine biota.

# Chapter 4

# Patterns of vertical velocity induced by eddy distortion in an ocean model

## 4.1 Introduction

Vertical velocities within ocean eddies play an important role in the exchange of properties between the ocean surface and the ocean interior (e.g., Nurser and Zhang, 2000, Roemmich and Gilson, 2001), and in ecological and biogeochemical processes (e.g., McGillicuddy et al., 1998, Klein and Lapeyre, 2009, Siegel et al., 2011, Gaube et al., 2013). The upward motion within eddies promotes primary productivity, by uplifting high-nutrient waters from the ocean interior to the euphotic zone (e.g., McGillicuddy et al., 1998, Chelton, 2013). The downward motion within eddies exports tracers out of the euphotic zone and into the deep ocean (e.g., McGillicuddy et al., 2003, Klein and Lapeyre, 2009).

Despite its importance, the vertical circulation within eddies has received less attention than other aspects of eddy dynamics. This is mostly because the vertical velocity in the ocean cannot easily be directly measured. Therefore, studies on vertical velocity within eddies rely on indirect diagnostics through the Omega equation (e.g., Tintoré et al., 1991, Pollard and Regier, 1992, Martin and Richards, 2001, Nardelli, 2013) and other methods (Strass, 1994). These indirect diagnostics, however, require observations with high spatial and temporal resolution. Both requirements are hard to achieve when observing mesoscale eddies (Allen et al., 2001, Martin and Richards, 2001). Another way to study the vertical circulation in the ocean is by analysing the output of numerical models (e.g., Flierl and Mied, 1985, Viudez and Dritschel, 2003, Pallas-Sanz and

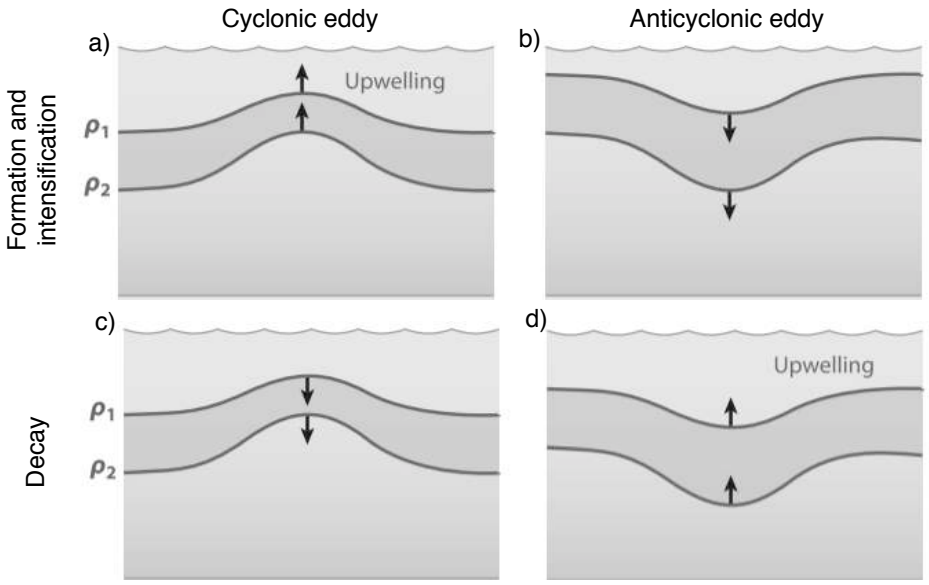


FIGURE 4.1: Schematic of the displacement of the seasonal pycnocline $\rho_1$ and the permanent pycnocline $\rho_2$ associated with eddy pumping during formation and intensification of (a) a cyclonic and (b) an anticyclonic eddy, and during decay of (c) a cyclonic and (d) an anticyclonic eddy (adapted from McGillicuddy, 2016).

Viudez, 2007, Koszalka et al., 2009). Modelled vertical velocity, however, cannot be easily validated against observations, and results from idealised simulations are not always applicable to real ocean eddies.

Due to the difficulties in studying vertical circulation in the ocean, McGillicuddy and Robinson (1997) and McGillicuddy et al. (1998) propose an indirect method to estimate vertical advection by mesoscale eddies - the eddy pumping mechanism. This mechanism relates the vertical movement of isopycnals to the vertical velocity in the eddy centre (Figures 4.1a-b). For example, when a cyclonic eddy forms or intensifies, a negative SLA associated with the eddy is observed.. This decrease in SLA means that there is less pressure acting on the isopycnals below the eddy centre, and that the core of the cyclonic eddy now has a negative density anomaly. As a result, the isopycnals are displaced upwards, and a positive vertical velocity is expected in the eddy core (Figure 4.1a). The opposite response is expected when an anticyclonic eddy forms or intensifies (Figure 4.1b). In this case, the eddy is associated with a positive SLA and a downward displacement of isopycnals below.

The vertical velocity within decaying eddies is the opposite of the vertical velocity induced by the eddy-pumping mechanism in forming and intensifying eddies (Franks et al., 1986, Nelson et al., 1989; Figures 4.1c and d). In this case, the decay of an anticyclonic

TABLE 4.1: Mechanisms that induce vertical velocity within eddies described in the literature, and the order of magnitude of the vertical velocities induced (last column).

| Mechanism | Reference | Vertical velocity [cm/d] |
|---|---|---|
| Wind and SST interaction | Gaube et al. (2015) | o(1-10) |
| Eddy propagation | McGillicuddy et al. (1995) | o(10) |
| Eddy-Ekman pumping | Martin and Richards (2001); Gaube et al. (2015) | o(10) |
| Wind and eddy vorticity interaction | Gaube et al. (2015) | o(10) |
| Eddy-eddy interaction | Pidcock et al. (2013) | o(100) |
| Submesoscale processes | Lévy et al. (2001); Brannigan (2016) | o(100) |
| Eddy-bathymetry interaction | Oke and Griffin (2011) | o(1000) |
| Perturbation of the geostrophic flow | Martin and Richards (2001); Nardelli (2013) | o(1000) |

eddy, for example, means that the isopycnals that deepened during its formation relax back to their steady state (Figure 4.1d). As the isopycnals move upwards, deep, nutrient-rich waters are brought to the euphotic zone - similarly to the eddy pumping in intensifying cyclonic eddies. Due to the eddy decay and relaxation of the isopycnals, anticyclonic eddies have been observed to be as productive as cyclonic eddies (e.g., Everett et al., 2012, Dufois et al., 2014). The opposite is valid for a decaying cyclonic eddy (Figure 4.1c).

As mentioned in Chapter 1, the eddy pumping mechanism has advanced our knowledge on the role of mesoscale eddies in the balance of the nutrient budget in the ocean (e.g., McGillicuddy et al., 1998, Siegel et al., 1999). However, it has also led part of the scientific community to a misunderstanding that cyclonic eddies are always associated with upward motion and anticyclonic eddies are always associated with downward motion. In fact, the terms "upwelling eddy" and "downwelling eddy" have been widely cited in the specialised literature (e.g., Tilburg et al., 2002, Uysal, 2006, Alpine and Hobday, 2007, Paterson et al., 2007, Nemcek et al., 2008, Oliver and Holbrook, 2014). The dominant upward or downward motion in the centre of eddies promoted by eddy pumping is a simplified view, and patterns of vertical velocity within eddies are more complicated.

Besides the eddy pumping mechanism, the vertical circulation within eddies is also affected by eddy propagation, by eddy interactions with the surrounding environment, and by the perturbation of the eddy geostrophic balance. Some of these mechanisms result in higher vertical velocities within the eddies than others (Table 4.1). The highest reported vertical velocities relate to eddy-bathymetry interactions and perturbation of the eddy geostrophic flow.

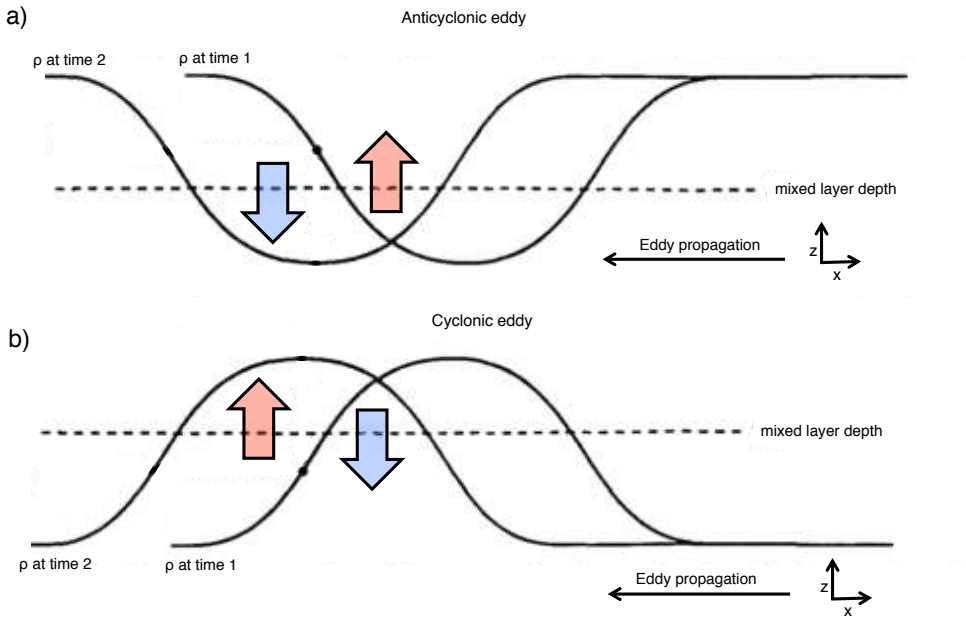


FIGURE 4.2: Schematic of isopycnal displacement associated with (a) an anticyclonic and (b) a cyclonic eddy propagating westwards. Blue arrows indicate downward motion, and red arrows indicate upward motion (adapted from McGillicuddy et al., 1995).

The propagation of an eddy results in opposing upward and downward cells at its leading and trailing parts, depending on the eddy rotation (McGillicuddy et al., 1995; Figure 4.2). For example, an anticyclonic eddy propagating westwards in the ocean moves isopycnals in its leading part (i.e., its western flank) downwards (Figure 4.2a). The leading part of the anticyclonic eddy is, therefore, associated with negative vertical velocity. As this eddy moves, the previously deepened isopycnals relax back to their original state. The trailing part of the anticyclonic eddy (i.e., its eastern flank), is therefore, associated with positive vertical velocity. The opposite is expected for a propagating cyclonic eddy (Figure 4.2b). This pattern of vertical velocity associated with eddy propagation is the same in both the Southern and the Northern Hemispheres.

The interaction with the surface wind field can affect the vertical circulation within an eddy through several mechanisms (Stern, 1965, Dewar and Flierl, 1987, Martin and Richards, 2001, Siegel et al., 2008, 2011, Gaube et al., 2015). One of these wind-related mechanisms is the Eddy-Ekman pumping (Dewar and Flierl, 1987, Martin and Richards, 2001). This mechanism induces upward (downward) motion in the centre of anticyclonic (cyclonic) eddies (Figure 4.3). Consider northerly winds blowing on the surface of an anticyclonic eddy in the Southern Hemisphere (Figure 4.3a). On the western flank of this eddy, the flow is in the same direction as the wind acting on the surface. Here, the stress between the current and the wind is low, as is the eastward Ekman transport. On the eastern flank of this eddy, however, the flow is in the opposite direction of the

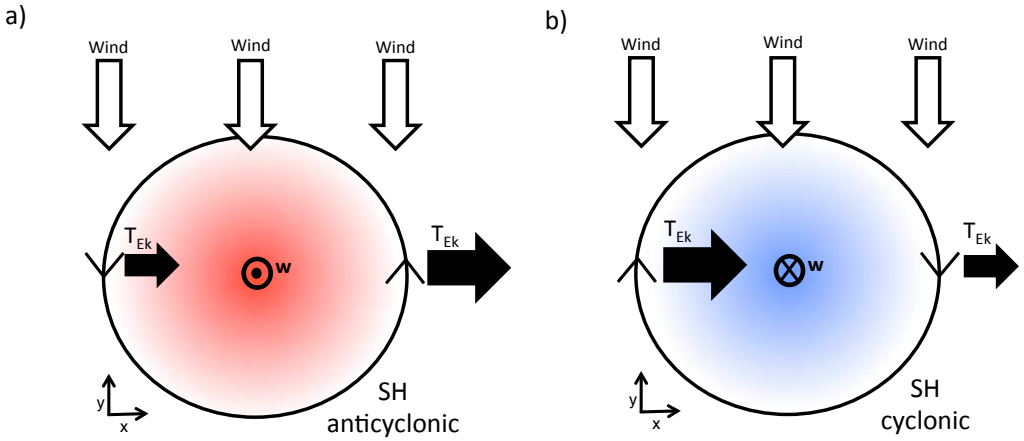


FIGURE 4.3: Schematic of the eddy-Ekman pumping mechanism acting on (a) an anticyclonic and (b) a cyclonic eddy in the Southern Hemisphere (SH). Note that the Ekman transport ($T_{Ek}$) is higher in regions of higher stress between the eddy rotation speed and the wind. The shading indicates the vertical velocity in the eddy interior, induced by this mechanism. Red indicates upward motion, and blue indicates downward motion (adapted from Siegel et al., 2011).

wind acting on the surface. Here, the stress between the current and the wind is high, as is the eastward Ekman transport. As a result, the Ekman transport away from the eddy interior is higher than the Ekman transport towards the eddy interior, resulting in divergence of the flow - and hence upwelling - in the eddy centre. This is valid for anticyclonic eddies in both hemispheres and with winds in any direction. Conversely, the effect of the wind in a cyclonic eddy results in convergence of the flow - and hence downwelling - in the eddy centre (Figure 4.3b).

A second wind-related mechanism that induces vertical velocity within eddies is the interaction of the wind with the surface vorticity of the eddy (Stern, 1965, Gaube et al., 2015). A uniform wind stress acting on an eddy tends to tilt the main axis of this eddy away from the vertical position - similar to a "surface drag". To balance the advective tendency associated with the wind action, the eddy then develops two cells of opposing vertical velocity in its interior. Therefore, the vertical circulation induced by this mechanism is a response of the eddy to maintain its main axis vertically aligned.

A third, and less intense, wind-related mechanism is the interaction of the wind with the SST gradient associated with an eddy (e.g., Gaube et al., 2015). Surface wind speeds are higher over warm waters and lower over cool waters (Chelton et al., 2004, Chelton and Xie, 2010). Therefore, the wind speed changes as the wind blows over eddy cores that are warmer or cooler than the surrounding ocean. As a result, patterns of wind stress curl and divergence are generated at different parts of the eddy. Wind stress curl (divergence) is generated in parts of the eddy where the wind blows parallel to (across)

the SST gradients. This mechanism also induces a bipolar pattern of vertical velocity within the eddy, but with smaller magnitude than the other mechanisms (Table 4.1). However, because of the vertical advection of SST gradients by the eddy rotation speed, these patterns are not as straight-forward as predicted by the theory (Siegel et al., 2008, 2011, Gaube et al., 2015).

The interaction of an eddy with bathymetry and with other eddies can also impact its vertical circulation. Eddies interacting with the coast have been reported to induce coastal upwelling (e.g., Calado et al., 2010, Oke and Griffin, 2011, Roberts et al., 2014). Eddies interacting with eddies of opposing polarity (i.e., dipoles) have also been associated with high vertical velocity (Legal et al., 2007, Pallas-Sanz and Viudez, 2007, Pidcock et al., 2013). In these cases the high vertical velocities are mainly found in the central jet within the eddies of the dipole.

Finally, the perturbation of the geostrophic balance of eddies induces alternating upward and downward cells in the eddy interior (Figure 4.4). This mechanism has been previously described in idealised numerical models (Martin and Richards, 2001, Viudez and Dritschel, 2003), and in fields derived from observed (Martin and Richards, 2001) and synthetic temperature and salinity (Nardelli, 2013). The perturbation of eddies, together with eddy-bathymetry interaction, induces the highest vertical velocities within eddies (Table 4.1).

The alternating upward and downward cells within an oceanic eddy are first described in Martin and Richards (2001). The authors show that the vertical velocity within an anticyclonic eddy in the Northeast Atlantic, derived from observations, is dominated by alternating cells with a north-south orientation (Figure 4.4a). A numerical simulation then shows that this orientation is artificially imposed by the observational sampling grid. The modelled vertical circulation pattern - without gridding problems - is dominated by alternating upward and downward cells that radially extend from the eddy centre to the eddy periphery (Figure 4.4b). These cells result from perturbations to the eddy geostrophic balance, simulated by "lobes" imposed to the eddy circular flow (L1-L4 in Figure 4.4b). The nature, duration, and intensity of the perturbation dictates the number and strength of the vertical velocity cells. Despite describing the cells and linking them to the perturbation of the eddy geostrophic balance, Martin and Richards (2001) do not fully describe the dynamical changes in the eddy interior that lead to the observed patterns.

The upward and downward cells induced by the perturbation of the geostrophic balance of an eddy are further described by Nardelli (2013). He shows that the alternating upward and downward cells are dominant in eddies of the Agulhas Return Current, and that these cells extend to 900 m (Figure 4.4c-d). The author, then, provides indications

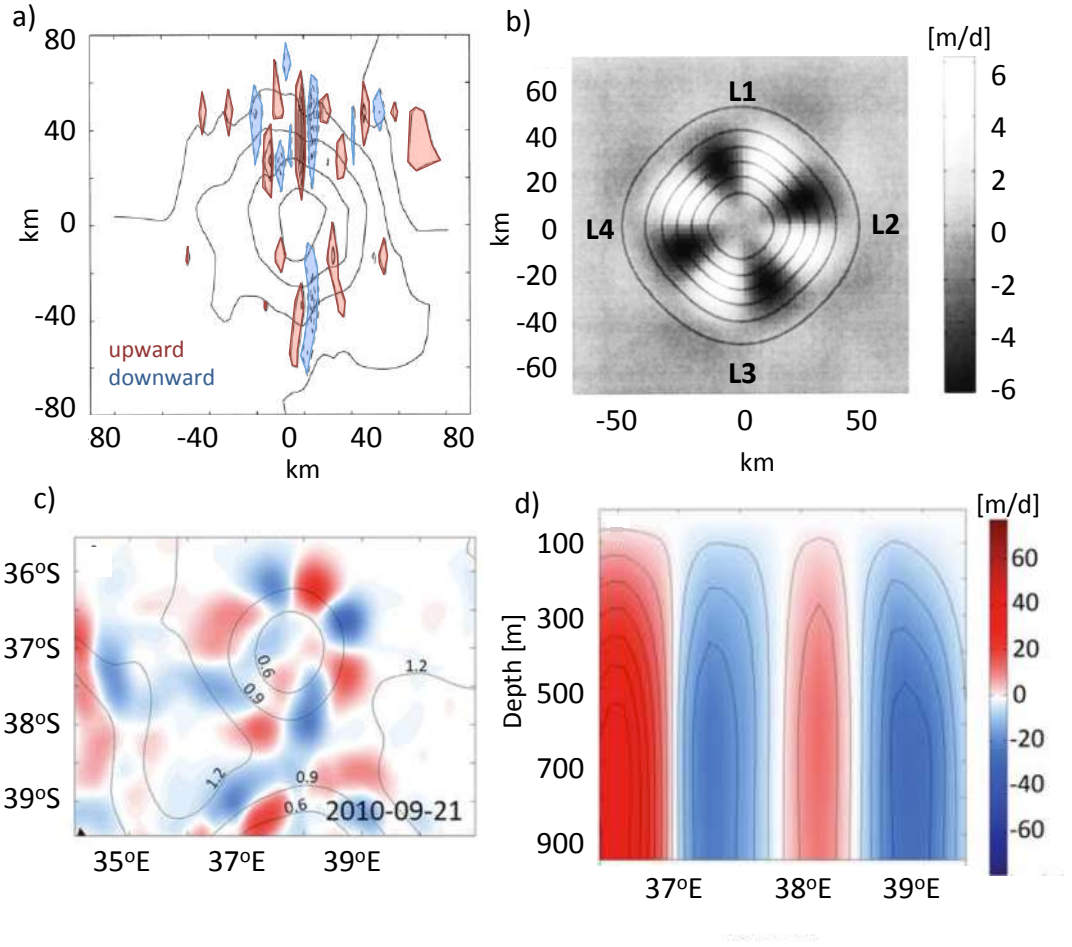


FIGURE 4.4: a) Geopotential (black lines) and vertical velocity (colours) at 72 m depth in an anticyclonic eddy observed in the northeast Atlantic. Blue indicates downward motion, red indicates upward motion, and velocity contour intervals are 5 m/d; b) streamfunction (lines) and vertical velocity (grey) at 72 m depth associated with a modelled anticyclonic eddy with perturbed geostrophic balance. The perturbation is seen in the 4 lobes L1-L4; c) vertical velocity (colours) at 100 m depth within a cyclonic eddy in the Agulhas Return Current. Black lines indicate SLA contours, in metres; d) vertical section of vertical velocity within a cyclonic eddy in the Agulhas Return Current. Colorbar refers to (c) and (d; adapted from Martin and Richards, 2001 and Nardelli, 2013).

that the basic dynamics of the alternating upward and downward cells relate to the propagation of vortex Rossby waves around the eddy (McWilliams et al., 2003). Nardelli (2013) notes, however, that a complete characterisation of the eddy dynamics is complex. Therefore, the changes in the eddy dynamics that link the perturbation of the eddy geostrophic balance to the alternating upward and downward cells still require further investigation.

The focus of this thesis is on mesoscale dynamics. Nevertheless, it is worth noting that recent studies have shown that sub-mesoscale processes are also responsible for

vertical motions within mesoscale eddies (Lévy et al., 2001; Klein and Lapeyre, 2009, and references therein; Mahadevan et al., 2008; Brannigan, 2016).

Eddies are most intense and abundant close to WBCs (Wyrtki et al., 1976, Olson, 1991, Fu et al., 2010). There, eddies often interact with other eddies and with the mean flow (Waterman and Jayne, 2011, Biastoch and Krauss, 1999, Bowen et al., 2005, Mata et al., 2006, Rocha et al., 2014). Due to these interactions, the geostrophic balance of these eddies is perturbed. Hence, the ageostrophic vertical circulation is expected to be stronger within eddies close to WBCs than within eddies in other oceanic regions.

As mentioned in Chapter 1, only one study describes the vertical circulation within an eddy in the EAC region. Oke and Griffin (2011) investigate the properties of a cyclonic eddy interacting with the eastern Australian continental shelf break. They document upwelling where the eddy seems to interact with the shelf break, downwelling in the opposite side of the eddy, and a nutrient enrichment in the euphotic zone in the vicinity of the eddy. It is still unknown if this vertical velocity pattern is common for EAC cyclonic eddies. Moreover, the vertical circulation within EAC anticyclonic eddies has never been described.

Understanding the vertical circulation within long-lived, EAC anticyclonic eddies is particularly important. In Chapter 3, EAC anticyclonic eddies are shown to impact several oceanic regions as they propagate southwards, leave the Tasman Sea, and reach the Eastern Indian Ocean. In other studies, these eddies have been shown to entrap coastal water organisms (Tranter et al., 1982, Baird et al., 2011), and affect the distribution of marine species (Ling et al., 2009). In addition, the number and strength of EAC anticyclonic eddies is predicted to increase in future climate scenarios (Oliver et al., 2015). Therefore, their contribution to water mass transport and mixing in this region of the ocean is also predicted to increase.

The purpose of this Chapter is to investigate patterns in the vertical circulation within EAC anticyclonic eddies. Specifically, this Chapter focusses on the cells of upward and downward motion caused by the perturbation of the geostrophic flow of these eddies. This perturbation is referred to here as "eddy distortion" - the change of eddy shape in time. Here, I aim to further understand the mechanisms that link vertical velocity to eddy distortion, and to increase knowledge of this complex eddy dynamics in the output of a global, eddy-resolving ocean model.

The next section provides a description of the analysis methods employed here. In Section 4.3, patterns of vertical velocity and eddy distortion in EAC anticyclonic eddies

are shown. In Section 4.4, mechanisms that link the change in eddy shape and vertical velocity are discussed, and two case studies are shown. A general discussion and conclusions are presented in Section 5.5.

This Chapter is based on a paper published as:

Pilo, G. S., P. R. Oke, R. Coleman, T. Rykova, and K. Ridgway (2017), **Patterns of vertical velocity induced by eddy distortion in an ocean model**, *Journal of Geophysical Research: Oceans*, 123, doi:10.1002/ 2017JC013298.

This paper is reproduced in Appendix C of this thesis.

## 4.2 Data and Methods

The eddies investigated in this Chapter are from the eddy-resolving, global ocean model described in Chapter 2, section 2.2 (i.e., OFAM). These eddies are manually tracked in daily averaged SLA fields in the model, following the method also described in Chapter 2, section 2.4.2.

Here, the vertical velocity in ten anticyclonic eddies that originate at the EAC separation region ($\sim 31^o$S) is analysed. These ten eddies follow the eddy pathway described in Chapter 3 (Figure 3.2a). After formation at the EAC separation region, they propagate southwards adjacent to the shelf break, cross south of Tasmania, and then advect westwards towards the Eastern Indian Ocean. For some of the analyses in this paper, the eddy pathway is separated according to the main direction of eddy propagation: southwards and westwards. As eddies propagate southwards (i.e., between the EAC separation and off east Tasmania, between "A" and "D" in Figure 3.2a), they interact with bathymetry, with other eddies, and with a strong mean flow. In this part of the pathway, the vertical velocity can be induced by several mechanisms (e.g., the mechanisms related to eddy-eddy and eddy-bathymetry interactions, and to the perturbation of the geostrophic flow). As eddies propagate westwards (i.e., off west Tasmania and the Eastern Indian Ocean, between "E" in Figure 3.2a and their dissipation), they are isolated, and the surrounding flow is quasi-quiescent. In this part of the pathway, eddies are more likely to behave as isolated case studies, and the vertical velocity induced by eddy distortion and eddy propagation to have clearer signals. In addition, as eddies propagate in the region south of Tasmania (i.e., between $146^o$E and $150^o$E) they become highly incoherent, shed a lot of filaments, and interact with seamounts and oceanic rises. Hence, the region south of Tasmania is not included in the analyses performed here.

The vertical velocity is the least reliable variable in any ocean model, including the model used in this study. To eliminate the noise in the modelled vertical velocities, and to isolate the coherent components of the vertical velocity fields, an Empirical Orthogonal Function (EOF) analysis is performed. The patterns of vertical velocity shown here are coherent. For the EOF analysis, $4^o \times 4^o$ maps of depth-averaged vertical velocity ($\tilde{w}$) for each time step of the eddy lifetime are used. First, the variable is de-trended in time. Then, a singular value decomposition of the anomaly field is computed. The depths considered for the EOF analysis range from 0 to 600 m when eddies propagate southwards and from 0 to 2000 m when eddies propagate westwards. This difference is because the southward propagating eddies move through shallower regions and extend to shallower depths than the westward propagating eddies, as described in Chapter 3. The depth-averaging was only performed after a careful analysis of the raw data, and that I was confident that no relevant gradient in the vertical structure of w would have been lost.

A multivariate EOF analysis is performed, combining $\tilde{w}$ and changes in SLA ($\Delta SLA$). $\Delta SLA$ is calculated by subtracting the SLA field in the first timestep from the SLA field in the second timestep, using weekly timesteps. These fields are aligned relative to the eddy centre (maximum SLA). This weekly $\Delta SLA$ is then compared with the $\tilde{w}$ field in the second timestep. For the multivariate EOFs, the variables $\Delta SLA$ and $\tilde{w}$ are normalised (i.e., each variable is divided by their standard deviation), and a combined matrix is built. The combined matrix is then de-trended in time and an EOF analysis of the anomaly field is performed. The variance of individual variables for each mode is calculated by dividing the EOF mode variance of a single variable by the variance of this variable's original signal.

Besides the 7-day interval used in the EOF analyses described above, a shorter (e.g., 3 days) and a longer (e.g., 30 days) time interval were tested. For the shorter time interval, the $\tilde{w}$ cells are absent, and for the longer time interval, the $\tilde{w}$ cells are present - but are less clear than at the 7-day interval. The results from this sensitivity test suggest that the eddy distorts - and hence impacts $\tilde{w}$ - on a time interval between 3 and 30 days, and close to a time interval of 7 days. These results are supported by the findings of Brassington (2010), who shows the ratio between the minor and the major axes of ellipses fitted to the trajectory of two surface drifters trapped in an anticyclonic eddy in the Tasman Sea (Figure 4.5). This ratio - another proxy for eddy distortion - changes every ∼5-10 days, to a large extent (i.e., between the red points in Figure 4.5b). This means that, on time intervals shorter than ∼5-10 days, the eddy does not distort, and in time intervals longer than ∼5-10 days the eddy distorts more than once. For example, between P2 and P7 in Figure 4.5b (30 days apart), the ratio between the minor and the major axes of the ellipses is reduced by 14% (i.e., the eddy becomes more isotropic).

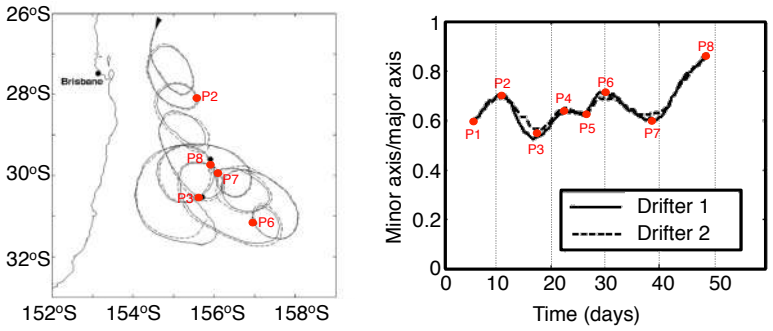


FIGURE 4.5: a) Position of two surface drifters trapped in an anticyclonic eddy in the Tasman Sea between 21 February and 22 April 2007. Red points indicate the averaged location of the drifters 10, 20, 30, 40, and 50 days after their launch; b) Time series of the ratio between the minor and the major axes of ellipses fitted to the trajectories shown in (a). Inflections on ratio curves are indicated by red points (P1-P8; adapted from Brassington, 2010).

However, the ratio changes five times over these 30 days, and the eddy becomes more or less isotropic each time. The change between P2 and P7, therefore, is an unrealistic assessment of eddy distortion. In the same way, an EOF analysis considering $\Delta SLA$ with a 30-day interval would also be unrealistic. Considering the results from the sensitivity tests and the findings by Brassington (2010), the weekly time interval is appropriate for the analyses performed here. This time interval seems to correspond to the time scale on which EAC eddies typically distort, or change shape. However, this time scale might be dependent on the interactions of the eddy with the mean flow, the wind, the bathymetry, and with other eddies.

## 4.3 Results

### 4.3.1 Eddy vertical velocity

The $\tilde{w}$ (surface to 2000 m) in anticyclonic eddies formed in the EAC separation region has alternating upward and downward cells (Figure 4.6, first column). These cells are stronger at depth (500-1500 m), in most cases do not reach the surface, and are, sometimes, asymmetric (Figure 4.6; second and third columns). As eddies propagate, $\tilde{w}$ cells rotate in the same direction as the eddy rotation (i.e., anti-clockwise). The existence of these $\tilde{w}$ cells indicates that the eddies are not in geostrophic balance and are, therefore, ageostrophic.

This pattern of alternating cells is seen along the whole eddy pathway (black line in Figure 3.2a). As eddies propagate southwards, they are relatively strong (maximum SLA $>$ 0.5 cm) and have strong vertical velocity (up to 50 m/d in magnitude; Figure

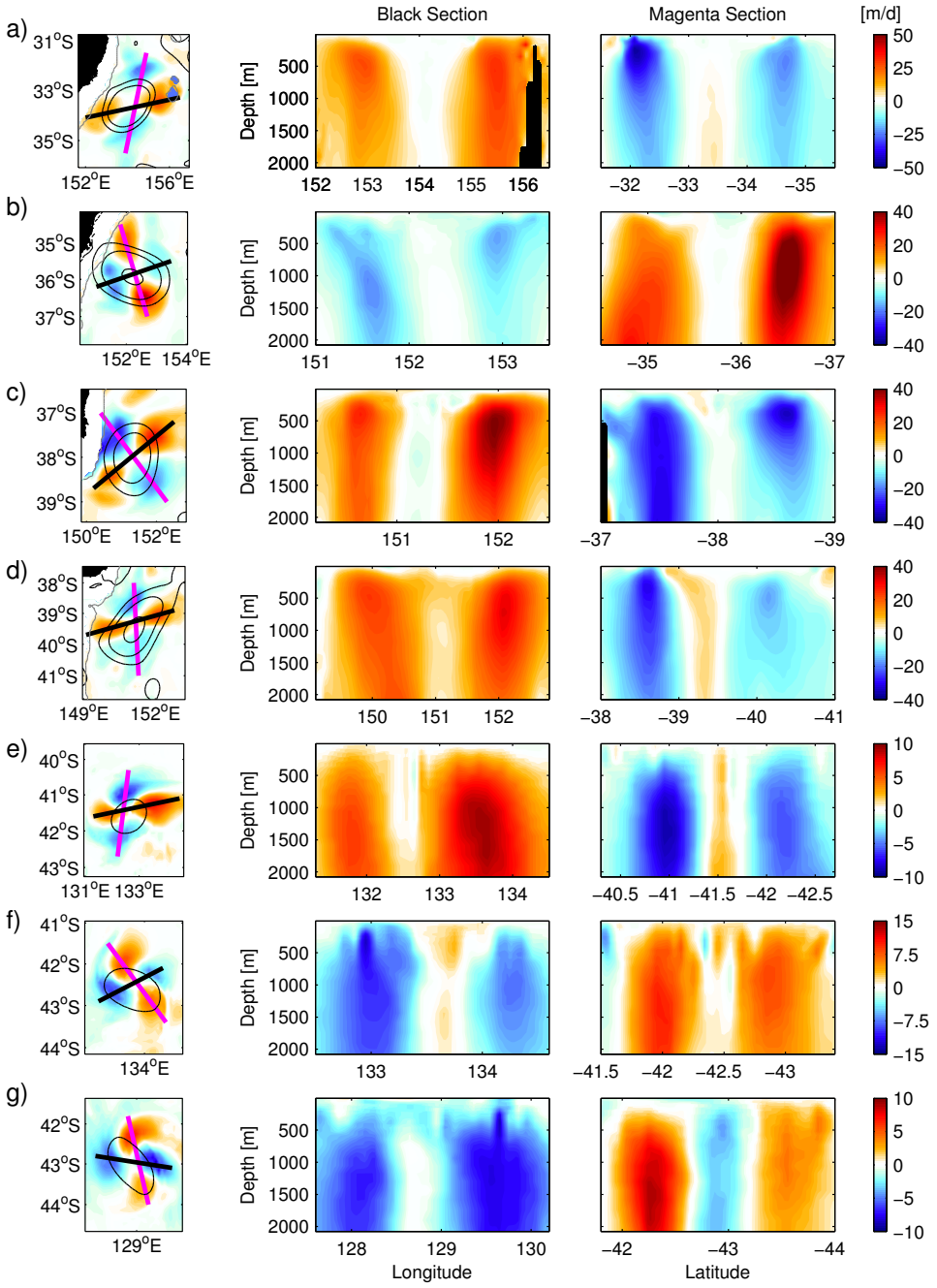


FIGURE 4.6: Depth-averaged (0-2000 m) vertical velocity (left; colours) in seven EAC anticyclonic eddies (a-g) in the ocean model. Black lines indicate 0.1, 0.25 and 0.5 m SLA contours. Grey lines indicate the 3000 m isobath. The bold black (magenta) line indicates the location of the vertical section shown in the centre (right). Note the different scales of vertical velocity for each eddy.

TABLE 4.2: Results from a single-variable EOF analysis of depth-averaged vertical velocity ($\tilde{w}$) for 10 EAC anticyclonic eddies in the ocean model. The modes and the combined variances shown relate to the alternating cells of positive and negative values seen in Figure 4.7. The propagation of the 10 eddies is divided into two sections: southwards, between the EAC separation region and east of Tasmania, and westwards, in the Eastern Indian Ocean. Absent values in the southwards section are due to the presence of shallow regions along the eddy path, that hinder the results of the EOF analysis.

| | Southwards $\tilde{w}$ | | Westwards $\tilde{w}$ | |
|---|---|---|---|---|
| Eddy | EOF modes | Combined variance | EOF modes | Combined variance |
| #1 | 1,2,5 | 45% | 1,2,3 | 49% |
| #2 | 1,2,4,6,7 | 52% | 1,2,3,4,6 | 56% |
| #3 | – | – | 1,2,6 | 31% |
| #4 | – | – | 1,2,3,4,5,6 | 50% |
| #5 | 1,2,6,7 | 47% | 1,2 | 25% |
| #6 | 1,2 | 38% | 1,2,4 | 46% |
| #7 | 1,9 | 22% | 1,2,3 | 38% |
| #8 | 1,2 | 37% | 1,2,4 | 48% |
| #9 | – | – | 1,2 | 45% |
| #10 | – | – | 1,2,3 | 54% |

4.6a-d). Conversely, as eddies propagate westwards, they are relatively weak (maximum SLA $< 0.2$ cm) and have weaker vertical velocity (up to 15 m/d in magnitude; Figure 4.6e-g).

The pattern of alternating cells is expected to be clearer and easier to observe in westward propagating eddies than in southward propagating eddies, owing to the quiescent aspect of the Eastern Indian Ocean. However, in both sections of the pathway, the pattern is clear and explains 22-56% of the combined variance of $\tilde{w}$ (Figure 4.7 and Table 4.2). This high variance is present regardless of the interactions between the eddy, the mean flow, the bathymetry, and other eddies. Here, the combined variance of different EOF modes is considered, because the pattern of alternating cells rotates in time, appearing in up to 6 modes in the simple EOF analysis. In eddy #10, for example, the alternating $\tilde{w}$ cells are seen in modes 1, 2 and 3 (Figure 4.7, third column). Despite this pattern distribution in different EOF modes, the results show that the alternating upward and downward cells are coherent in eddies that are either isolated or interacting with the surrounding environment.

### 4.3.2 Eddy distortion

The isotropy of an eddy changes as it propagates in the ocean (e.g., Cushman-Roisin et al., 1985, Brassington, 2010). Throughout this thesis, these changes in eddy isotropy

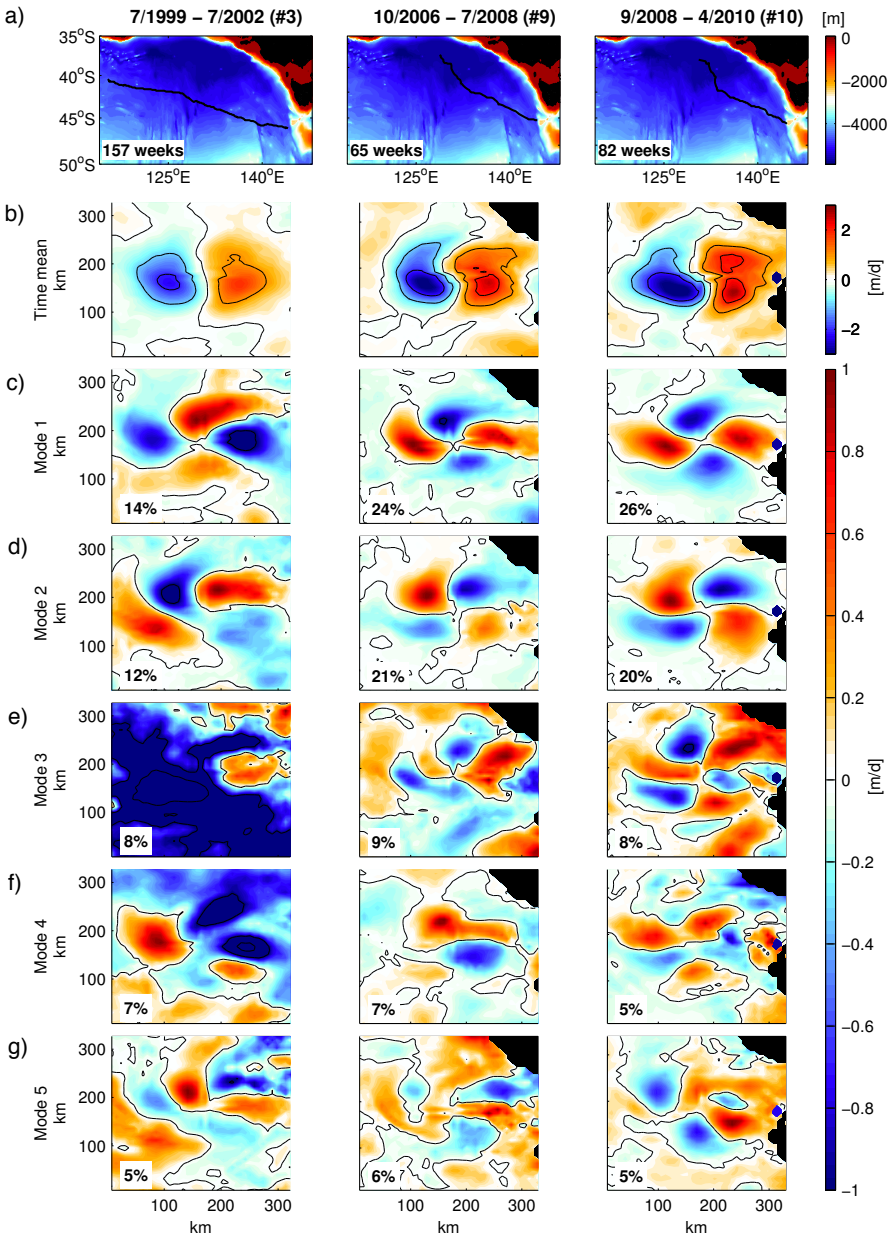


FIGURE 4.7: a) Maps indicating the tracks (black lines) of three anticyclonic eddies propagating in the Eastern Indian Ocean. Colours denote bathymetry, and the numbers in the bottom left corners indicate the number of weeks taken for each eddy to propagate along the tracks. The numbers of the eddies (i.e., #3, #9, and #10) relate to Table 4.2; b) time mean depth-averaged (0-2000 m) vertical velocity ($\tilde{w}$) for each eddy as they propagate along the tracks shown in (a); c-g) EOF modes 1-5 of an EOF analysis of $\tilde{w}$, normalised by the maximum value of each mode, for each eddy. Black lines denote null $\tilde{w}$. The percentages in the bottom left corner are the amount of variance contained in each mode, for each eddy.

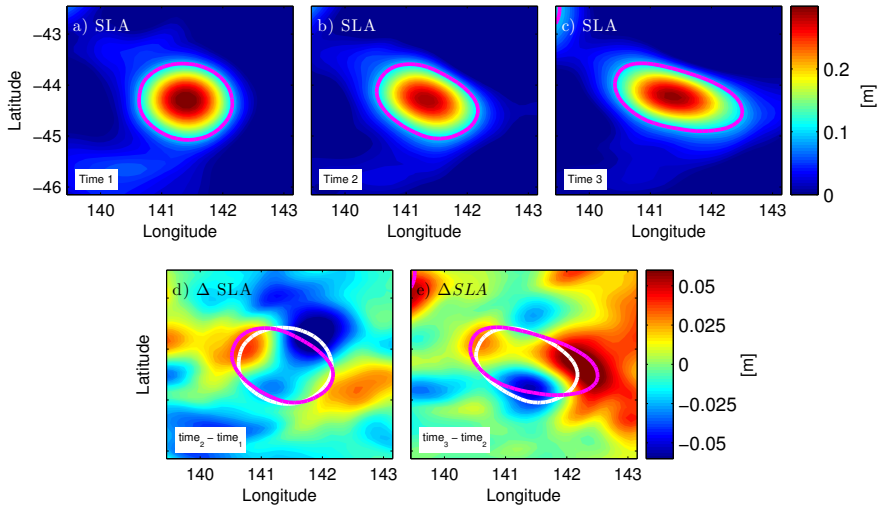


FIGURE 4.8: SLA associated with one anticyclonic eddy at three subsequent weeks (times 1 to 3; a, b, and c). The magenta line denotes the 0.1 m SLA contour; d) change in SLA ($\Delta SLA$) between times 2 and 1. The magenta line denotes the 0.1 m SLA contour in time 2, and the white line denotes the 0.1 m SLA contour in time 1; e) as in (d), but for times 3 and 2.

are referred to as eddy distortion. Several factors are likely to contribute to eddy distortion, including interactions with bathymetry, with the mean flow, and with other mesoscale features. An example of eddy distortion is shown in Figure 4.8, with a semi-isotropic eddy (Figure 4.8a) distorting in the northwest-southeast direction (Figures 4.8b-c) for two weeks. The $\Delta SLA$ field, obtained by subtracting SLA fields between subsequent weeks, shows alternating cells of positive and negative $\Delta SLA$ (Figures 4.8d-e). A positive cell indicates that the eddy distorted **towards** this area, and a negative cell indicates that the eddy distorted **away** from this area, relative to the previous week.

Rotating the SLA field in the first time interval ($SLA_{time1}$) before calculating $\Delta SLA$ is considered (Figure 4.9). This approach would isolate changes associated with eddy distortion from changes associated with eddy rotation. An assumption is made, however, that eddies rotate as a solid body - which is not true. Because there is no rotation value for the eddy as a solid body, different values are considered to quantify the rotation effect, and its omission. This is accomplished as follows. First, $SLA$ fields and $\tilde{w}$ fields are transferred onto a radial grid. Remember that $\tilde{w}$ is the depth-averaged vertical velocity of an eddy, at a given timestep. This grid is built within a ∼160 km radius centred in the maximum SLA associated with the eddy, and has radial resolution of ∼8.3 km × $4.5^o$ (80 radial lines with 20 grid points per line). Then, the $SLA_{time1}$ field is rotated anti-clockwise at different angles before calculating $\Delta SLA$ (Figure 4.9c-k). Remember that $\Delta SLA$ is $SLA_{time2} - SLA_{time1}$. The alternating cells of $\Delta SLA$ are always present when an eddy distorts, and have similar magnitude, regardless of the rotation value of the $SLA_{time1}$ field. However, the location of the alternating cells of $\Delta SLA$ differ

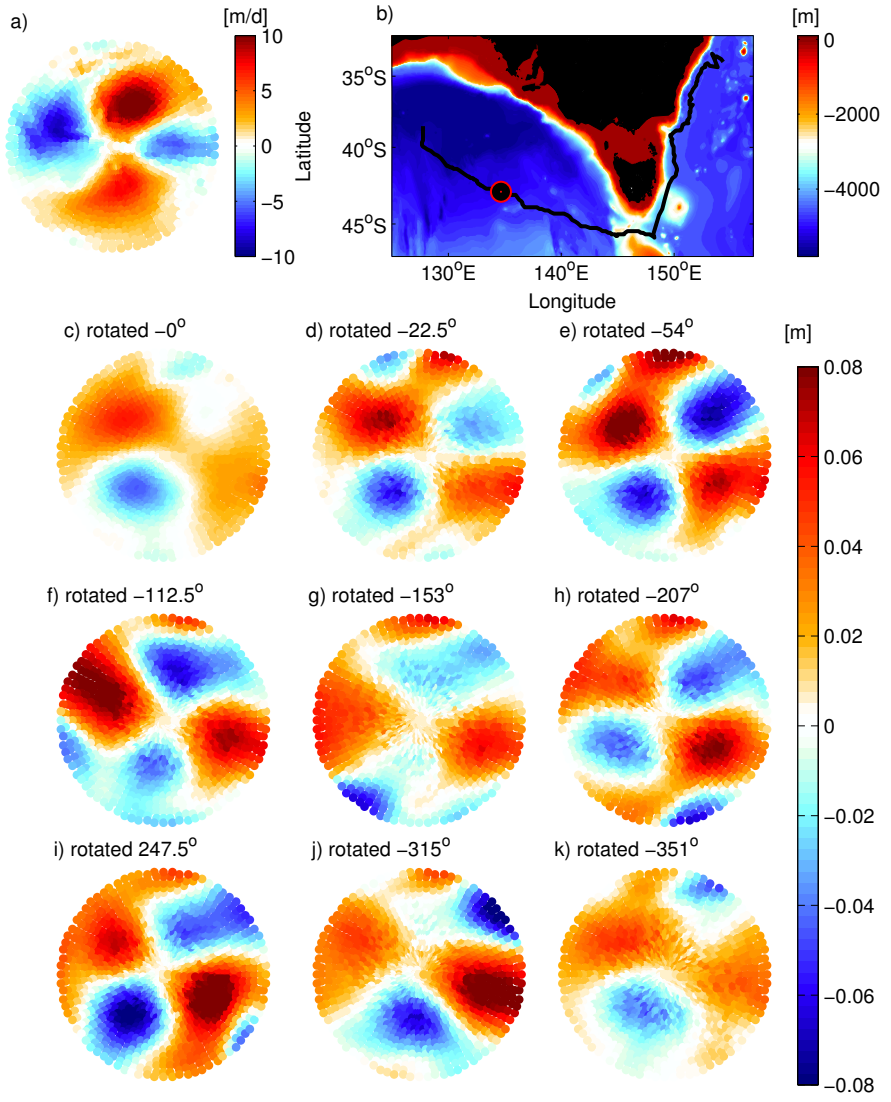


FIGURE 4.9: a) Depth-averaged (0-2000 m) vertical velocity ($\tilde{w}$) of an anticyclonic eddy at *time 2* shown in (b); b) eddy track (black line) over regional bathymetry (colours); the red circle indicates eddy location at *time 2*; c-k) $\Delta SLA$ ($SLA_{time2} - SLA_{time1}$) considering different rotation values for $SLA_{time1}$.

according to the rotation value tested. Depending on how much the $SLA_{time1}$ field is rotated, the $\Delta SLA$ are more or less aligned with the $\tilde{w}$ cells in *time 2* (Figure 4.9a) For example, the $\Delta SLA$ pattern in Figure 4.9f is more aligned with the $\tilde{w}$ pattern in Figure 4.9a than the $\Delta SLA$ pattern in Figure 4.9j. The link between $\Delta SLA$ and $\tilde{w}$ is described in the next section. This indicates that a shift between the $\Delta SLA$ and the $\tilde{w}$ in *time 2* is a consequence of not-rotating the $SLA_{time1}$ fields when calculating $\Delta SLA$. Based on these results, I choose not to rotate the eddy in the first time interval, knowing that the associated error is qualitative, and not quantitative.

TABLE 4.3: As in Table 4.2, but for a multivariate EOF analysis of $\tilde{w}$ and change in SLA ($\Delta SLA$). The modes and the combined variances shown relate to the alternating cells of positive and negative values seen in Figure 4.10.

| | Southwards combined $\tilde{w}$ and $\Delta SLA$ | | Westwards combined $\tilde{w}$ and $\Delta SLA$ | |
|---|---|---|---|---|
| Eddy | EOF modes | Combined variance | EOF modes | Combined variance |
| #1 | 1,2,3,4 | 51% | 1,2,3 | 37% |
| #2 | 1,3,6 | 32% | 2,3,6,7 | 19% |
| #3 | – | – | 2,3 | 10% |
| #4 | – | – | 1,2,3,4,5 | 57% |
| #5 | 1,2 | 38% | 2,3,4 | 15% |
| #6 | 1,2 | 33% | 2,3 | 19% |
| #7 | 1 | 19% | 2,3,4 | 26% |
| #8 | 1,2,6 | 34% | 2,3 | 18% |
| #9 | – | – | 1,2,3 | 53% |
| #10 | – | – | 1,2,3,5 | 58% |

### 4.3.3 Eddy vertical velocity and distortion

Patterns of both $\tilde{w}$ and $\Delta SLA$ have alternating cells of positive and negative values. A multivariate EOF analysis, combining these variables, shows that $\tilde{w}$ and $\Delta SLA$ vary together (Figure 4.10), and explain 18-51% of the combined variance (Table 4.3). Again, the combined variance of different EOF modes is considered here because the patterns of both variables rotate in time, appearing in several EOF modes (Figure 4.10).

Figure 4.10 shows three case studies of eddies propagating westwards in the Eastern Indian Ocean. In these eddies, the pattern of alternating cells for both $\tilde{w}$ and $\Delta SLA$ is seen in the first three modes of variance (Figures 4.10c-e). The $\tilde{w}$ cells are shifted anti-clockwise in relation to the $\Delta SLA$ cells (e.g. Figures 4.10d, first and second panels). This shift is due to the non-rotation of the SLA field in the first time interval (Figure 4.9), as discussed in the previous section. If these were cyclonic eddies in the Southern Hemisphere, the $\tilde{w}$ cells would be shifted clockwise in relation to the $\Delta SLA$ cells. Despite the anti-clockwise shift, all $\Delta SLA$ and $\tilde{w}$ pairs agree, and are inversely related (i.e. the cells of one variable are positive at the same time the cells of the other variable are negative). This means that an outward distortion (positive $\Delta SLA$) is associated with downward motion (negative $\tilde{w}$), and an inward distortion (negative $\Delta SLA$) is associated with upward motion (positive $\tilde{w}$).

To further show the relationship between $\Delta SLA$ and $\tilde{w}$ within eddies, the correlation between these variables is calculated. First, I isolate values of absolute $\Delta SLA$ and absolute $\tilde{w}$ contained within a 140-km radius circle centred in the maximum SLA associated with the eddy. Second, I calculate the spatial mean of these values. This process is

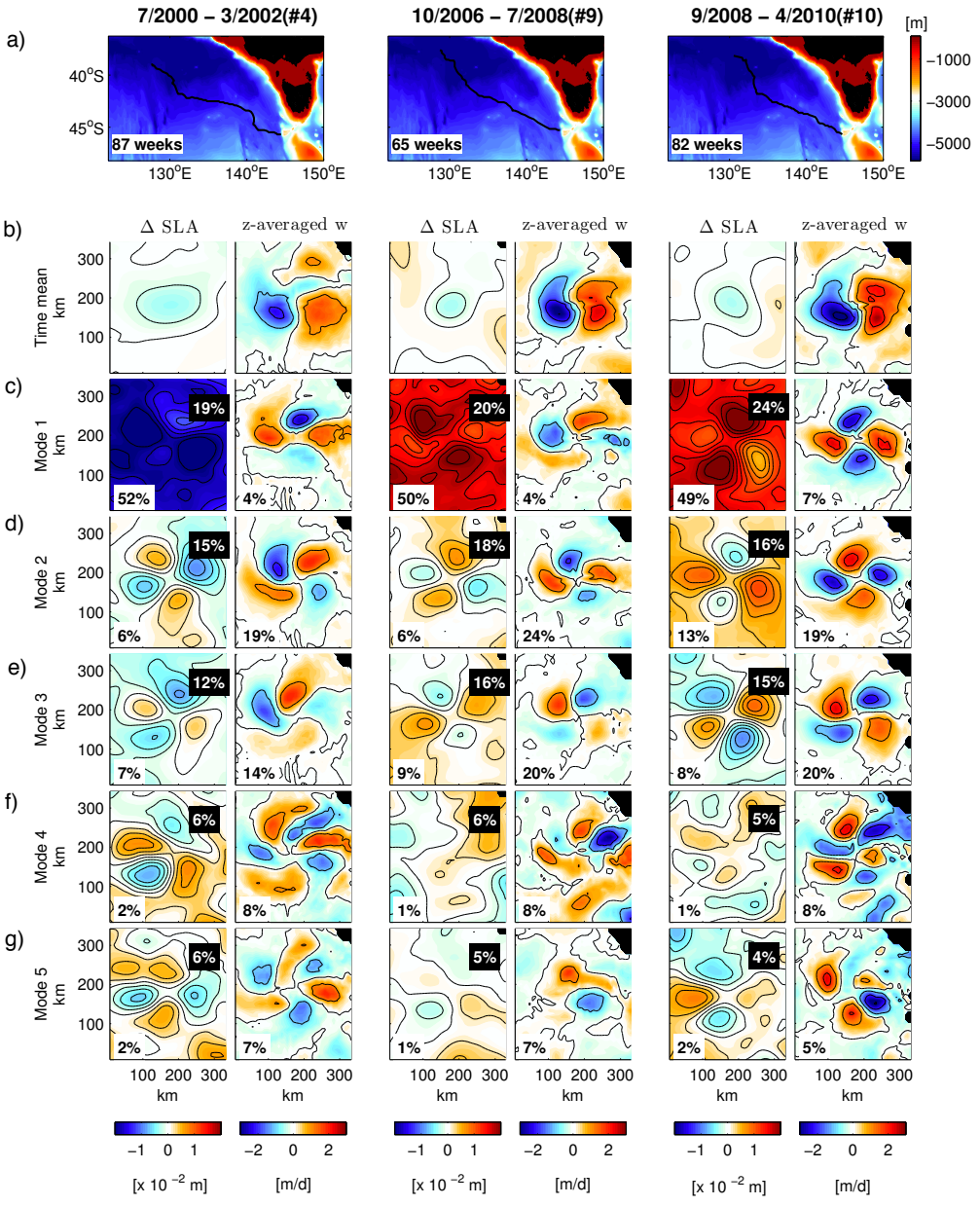


FIGURE 4.10: a) Maps indicating the tracks of three anticyclonic eddies propagating in the Eastern Indian Ocean (black lines). Colours denote bathymetry, and the numbers in the bottom left corners indicate the number of weeks taken for each eddy to propagate along the tracks. The numbers of the eddies (i.e., #4, #9, and #10) relate to Table 4.3; b) time mean change in SLA ($\Delta SLA$) and time mean depth-averaged (0-2000 m) vertical velocity ($\tilde{w}$) for each eddy as they propagate along the tracks shown in (a); c-g) EOF modes 1-5 of the multi-variate EOF analysis of $\Delta SLA$ and $\tilde{w}$, normalised by the maximum value of each mode and then multiplied by each variable's standard deviation, for each eddy (see Section 4.3.3). Black lines denote null values. Percentages in white (black) boxes are the amount of variance contained in each mode for each variable (combined variable).

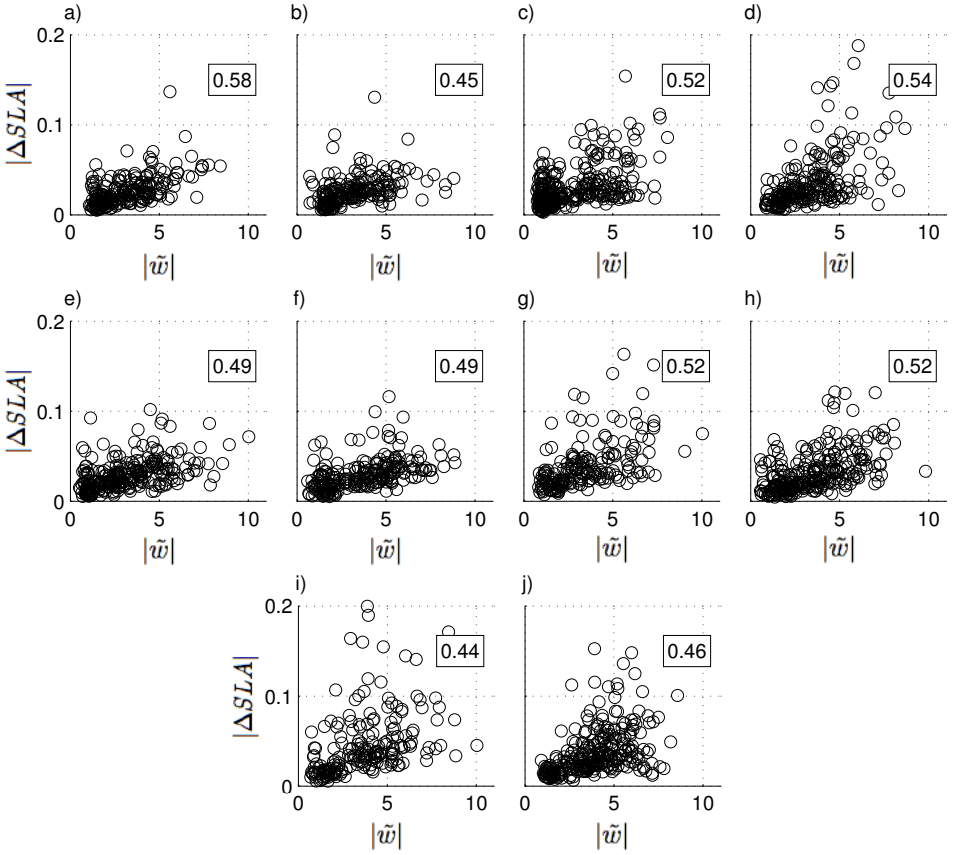


FIGURE 4.11: Values of absolute depth-averaged vertical velocity ($|\tilde{w}|$) and absolute change in SLA ($|\Delta SLA|$) for 10 anticyclonic eddies (a-j) for all timesteps of their propagation between the EAC separation region to the Eastern Indian Ocean. The numbers in the boxes denote the correlation coefficient between these values.

repeated at each time interval as the eddy propagates. Therefore, the variables that are correlated at each time interval are the mean $|\Delta SLA|$ and the mean $|\tilde{w}|$ within the eddy. The rationale for relating these variables is that the stronger the eddy distortion (i.e., the higher the values of $|\Delta SLA|$), the stronger the vertical circulation within the eddy.

For the ten anticyclonic eddies analysed in this Chapter, the correlation between $|\Delta SLA|$ and $|\tilde{w}|$ ranges from 0.44 to 0.58 (Figure 4.11). Note that this correlation is always positive because absolute values of $\Delta SLA$ and $\tilde{w}$ are being compared. Also note that the values within the 140-km radius circle established here mostly include waters from the eddy interior, but there is some contribution from the surrounding ocean. Despite the relatively low correlation values in Figure 4.11, the results indicate that there is some correlation between $|\Delta SLA|$ and $|\tilde{w}|$.

Another way to correlate the $\Delta SLA$ and the $\tilde{w}$ cells is by performing a two-dimensional correlation analysis. In this analysis, the $\Delta SLA$ at each point within the eddy is compared to the $\tilde{w}$ considering the vertical velocity of all depth layers below these points

(again, remember that $\tilde{w}$ is the depth-averaged vertical velocity). However, because of the anti-clockwise shift of $\tilde{w}$ cells in relation to the $\Delta SLA$ cells described above, the correlation coefficient resulting from this two-dimensional analysis is low. To eliminate this shift between the patterns, the $\Delta SLA$ field is rotated anti-clockwise, until it matches the non-rotated $\tilde{w}$ field.

Figure 4.12 shows an example of a two-dimensional correlation analysis for a particularly clear example. For this analysis, $\Delta SLA$ and the $\tilde{w}$ fields are again re-gridded onto a radial grid of ∼8.3 km × $4.5^o$ resolution, and ∼160 km radius (80 radial lines with 20 grid points per line; Figure 4.12a). The re-gridded $\Delta SLA$ values are then rotated one radial line (i.e., $4.5^o$) at a time, from zero to $360^o$. For each rotation, the two-dimensional correlation coefficient is calculated (Figure 4.12d). As the $\Delta SLA$ rotates, the correlation coefficient oscillates between positive and negative values. The first minimum correlation coefficient is searched for (red star in Figure 4.12d), considering that $\Delta SLA$ and $\tilde{w}$ have an inverse relationship (Figure 4.10). For the example shown in Figure 4.12, the correlation coefficient between the non-rotated $\Delta SLA$ pattern and the $\tilde{w}$ pattern is -0.33. After the $\Delta SLA$ pattern is rotated, this value increases to -0.82.

## 4.4 Linking eddy distortion to vertical velocity

Two mechanisms that link eddy distortion to vertical velocity are discussed. One mechanism is based on the conservation of potential vorticity ($Q$) and the other mechanism, on the conservation of volume - relating to the convergence and divergence of the horizontal flow as the eddy distorts.

The first mechanism, based on conservation of potential vorticity ($Q$), focuses on the relationship between stratification and relative vorticity within the eddy. The isopycnic Ertel's potential vorticity $Q$ (Ertel, 1940, Gill, 1982), considering the horizontal velocity components to be depth-independent, is

$$Q = (f + \zeta_R)\frac{N^2}{g}, \tag{4.1}$$

where $f$ is the Coriolis parameter, $\zeta_R$ is the vertical component of the relative vorticity $(\partial v/\partial x - \partial u/\partial y)$, $g$ is the acceleration of gravity, and $N^2$ is the Brunt-Väisälä frequency:

$$N^2 = \frac{g}{\rho_\theta}\frac{\partial \rho}{\partial z}. \tag{4.2}$$

where $\rho_\theta$ is the potential density and $z$ are the depth levels.

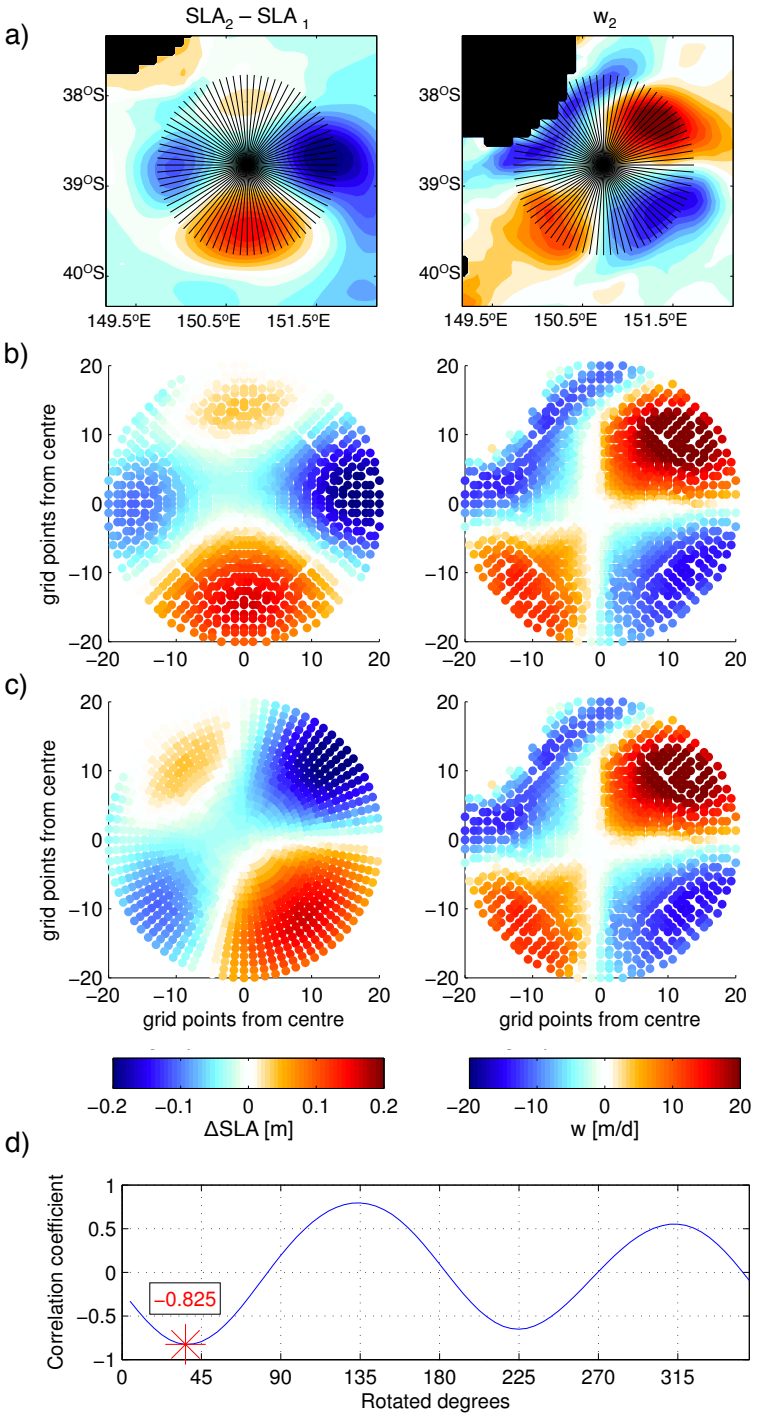


FIGURE 4.12: a) $\Delta SLA$ (left) and $\tilde{w}$ (right; colours) fields associated with an anticyclonic eddy located off Bass Strait. The black lines indicate the grid onto which these fields will be re-gridded; b) as in (a), but with values in a radial grid; c) as in (b), but with $\Delta SLA$ (left) rotated 31.5$^o$ anti-clockwise, to match $\tilde{w}$ (right); d) two-dimensional correlation coefficient between $\Delta SLA$ and $\tilde{w}$ from (b), considering different rotation angles for $\Delta SLA$ (b, left). The star indicates the correlation coefficient between the rotated $\Delta SLA$ and the non-rotated $\tilde{w}$ shown in (c).

$Q$ relates stratification and $\zeta_R$ of a rotating fluid and is conserved in an adiabatic, frictionless motion. Here, $Q$ is assumed to be conservative and $f$ to be constant between time intervals (i.e., the change in $f$ as the eddy propagates in only one week is very small). To conserve $Q$, a change in $N^2$ has a compensating change in $\zeta_R$. Therefore, the conservation of $Q$ connects the eddy distortion to the alternating cells of vertical velocity, and the concept is explained schematically in Figure 4.13. As an eddy distorts, it changes the SLA and the underlying stratification ($N^2$), as isopycnals move vertically (Figure 4.13a-d). The change in SLA impacts the $N^2$ because, to a large extent, the sea surface height represents the integral properties of the water column below (when adiabatic changes in the SLA are disregarded). As $Q$ is conservative, when stratification changes, $\zeta_R$ also changes. A decrease in $N^2$ is compensated by a gain in positive $\zeta_R$, which has anticyclonic torque in the Southern Hemisphere. Conversely, an increase in $N^2$ is compensated by a gain in negative $\zeta_R$, which has cyclonic torque in the Southern Hemisphere. The changes in the sea level and in the eddy interior are seen as alternating cells of $\Delta SLA$, $\Delta N^2$ and $\Delta\zeta_R$ (Figure 4.13e-g). Due to conservation of momentum and the torque associated with the $\Delta\zeta_R$, upward and downward cells develop (Figure 4.13h). These interior changes in the eddy may explain the pattern of alternating cells seen in $\tilde{w}$.

The second mechanism, based on the conservation of volume, relies on the continuity within the eddy as it distorts. The eddies studied here have an ageostrophic component, therefore, the divergence of their horizontal flow is non-zero. An inward distortion relates to divergence of the flow, inducing upward motion (Figure 4.13c). Conversely, an outward distortion relates to convergence of the flow, inducing downward motion (Figure 4.13d). This mechanism results in the same vertical velocity pattern as the mechanism proposed before.

### 4.4.1 Case studies

These mechanisms are tested considering two case studies of anticyclonic eddies, both originating in the EAC separation region. Ocean model fields at two locations along the trajectory of these eddies are analysed. For eddy #1, its structure is investigated when it is located in the Eastern Indian Ocean (Figure 4.14a, red dot). For eddy #2, its structure is investigated when it is located off Bass Strait (Figure 4.14a, purple dot). The structure of these eddies, at these locations, differs in several ways. In the Eastern Indian Ocean, eddy #1 has a sub-surface core, is relatively weak (0.3 m SLA and 0.4 m/s rotation speed), and is isolated from bathymetric features and from strong mean flow interactions. Off Bass Strait, eddy #2 is surface-intensified, relatively strong (0.5 m SLA and 1.2 m/s rotation speed), and interacts with the continental shelf break.

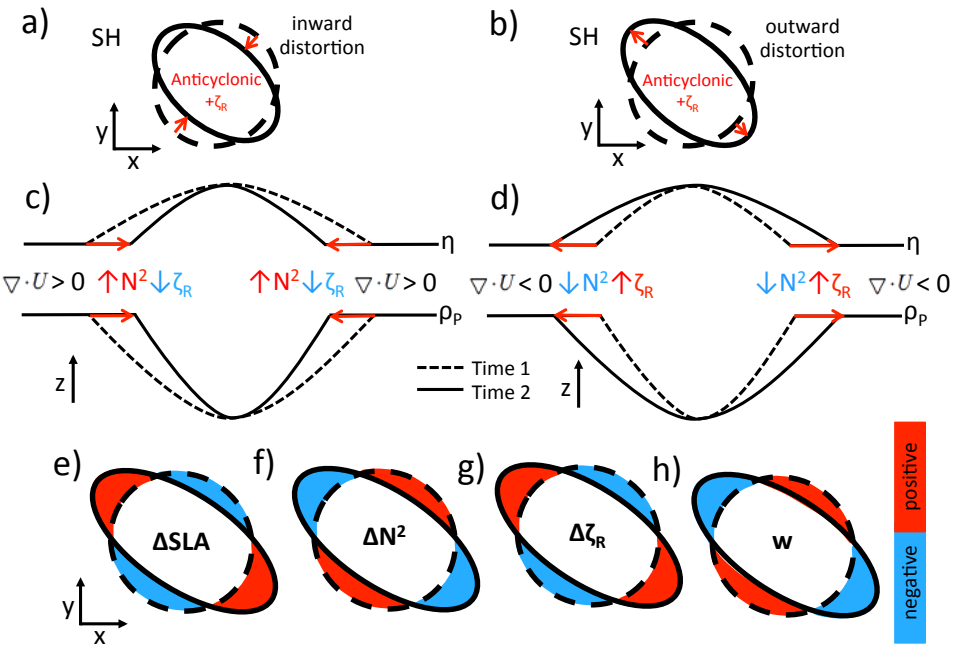


FIGURE 4.13: Schematics of a Southern Hemisphere (SH) anticyclonic eddy distorting inwards (a) and outwards (b); changes in stratification ($N^2$) and in relative vorticity ($\zeta_R$) in the eddy interior associated with an inward (c) and outward (d) distortion shown in (a) and (b); $\eta$ is the ocean's free surface and $\rho_P$ is the isopycnal at the bottom of the permanent pycnocline; changes in SLA ($\Delta SLA$; e), stratification ($\Delta N^2$; f), and relative vorticity ($\Delta\zeta_R$; g) between subsequent timesteps associated with eddy distortion. The vertical velocity pattern in the final timestep associated with these distortions is shown in (h). The dashed black lines indicate the eddy shape before distortion, and the solid black line indicates the eddy shape after distortion.

Surface intensified eddies depress both the seasonal and the permanent pycnoclines. Eddies with a sub-surface core have a thick layer of water that deepens the permanent pycnocline but shoals the seasonal pycnocline, as the eddies in the Eastern Indian Ocean shown in Figure 3.15, right (e.g., mode water eddies; e.g., McGillicuddy, 2015). The permanent pycnocline is defined here as the maximum vertical density gradient that is not associated with the surface mixed layer. This pycnocline can be relatively shallow in surface intensified eddies (Figure 4.14b-c; purple lines) and relatively deep in eddies with a sub-surface core (Figure 4.14b-c; red lines).

#### 4.4.1.1 Eddy #1 in the Eastern Indian Ocean

In the Eastern Indian Ocean, eddy #1 has a mixed layer extending down to 500 m and a permanent pycnocline located at ∼1300 m (Figures 4.14b-c). The thick mixed layer

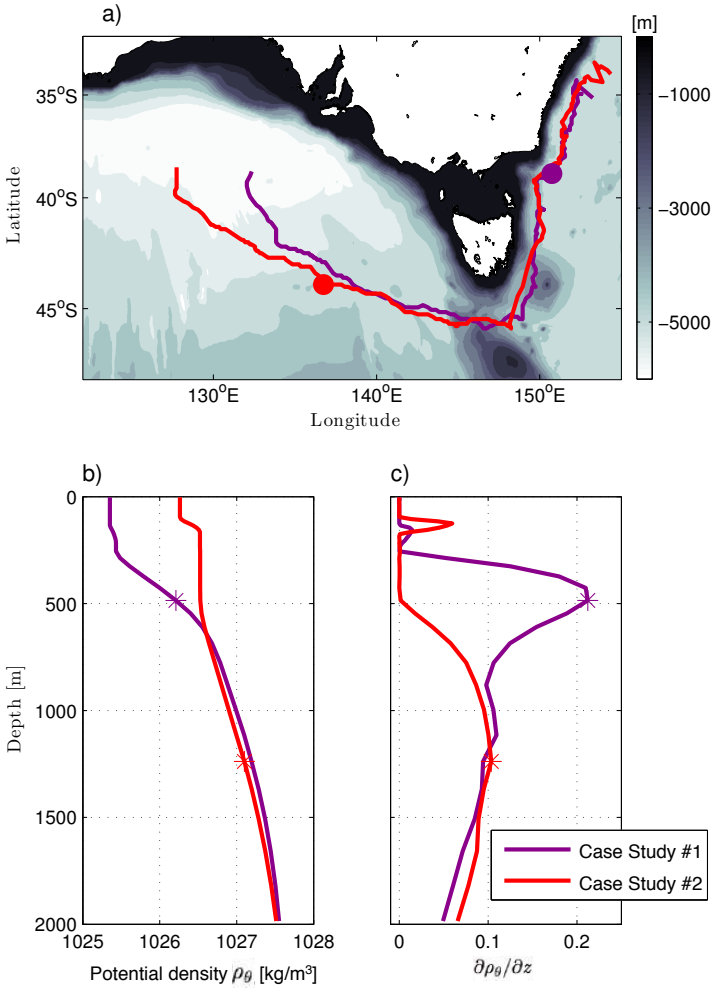


FIGURE 4.14: a) Map indicating the tracks of two anticyclonic eddies chosen as case studies. The red line relates to case study #1, with the selected location for the analysis shown here indicated by the red dot. The purple line and dot relate to case study #2. Grey colours denote bathymetry; b) vertical profile of potential density ($\rho_\theta$) in the eddy centre (i.e., below the maximum SLA) of case studies #1 (red) and #2 (purple); c) as in (b), but for the change of potential density in depth ($\partial\rho_\theta/\partial z$). The stars in (b) and (c) indicate the bottom of the permanent pycnocline.

results from the several warming and cooling seasons the eddy has encountered since its formation (Nilsson and Cresswell, 1981).

$\Delta Q$, $\Delta N^2$, and $\Delta\zeta_R$ are calculated considering subsequent time intervals, in the same way as $\Delta SLA$ is calculated, described in section 4.2. Here, I also choose not to rotate the eddy in the first time interval. In one week, this eddy distorts outwards in longitude and inwards in latitude (Figure 4.15a). $Q$ and $f$ are constant between the weeks analysed ($\Delta Q << Q$ and $\Delta f << f$, Figure 4.15b-c). Therefore, $N^2$ and $\zeta_R$ change together to

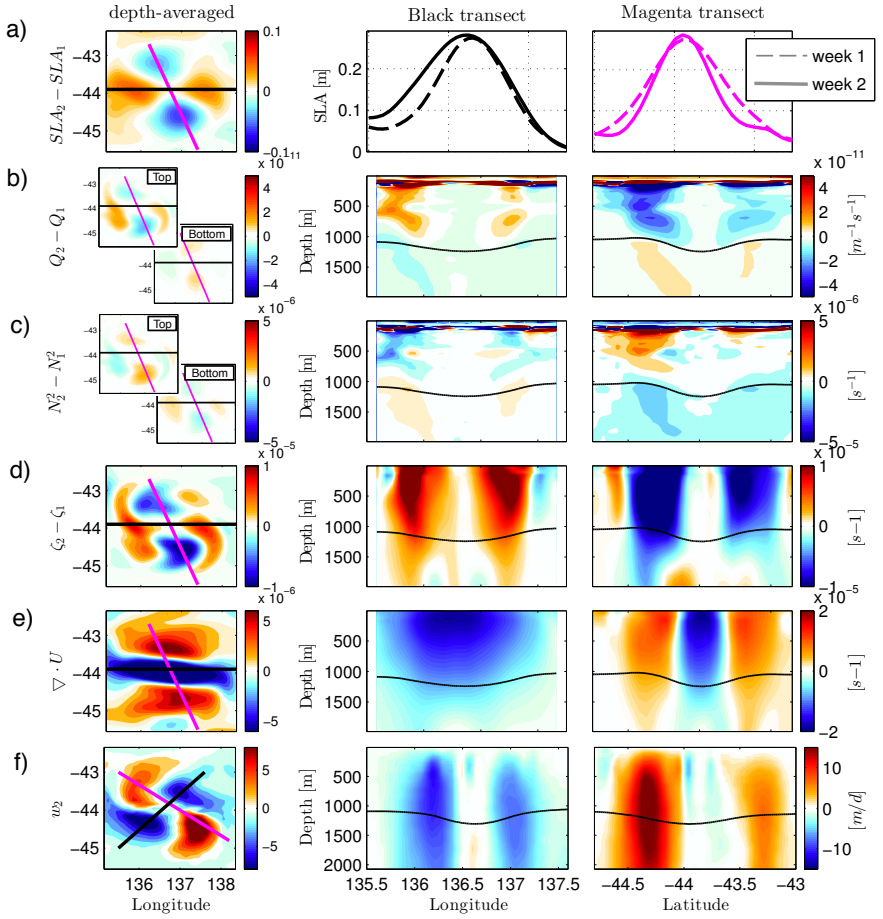


FIGURE 4.15: Change in (a) SLA, (b) depth-averaged potential vorticity ($Q$), (c) depth-averaged stratification ($N^2$), and (d) depth-averaged relative vorticity ($\zeta_R$; colours, left) between subsequent timesteps ($t_1$ and $t_2$) for an anticyclonic eddy in the Eastern Indian Ocean (i.e., case study #1). The black and the magenta lines denote the location of the vertical sections shown in the middle and in the right columns; depth-averaged (e) horizontal divergence ($\bigtriangledown \cdot U_2$) and (f) vertical velocity ($\tilde{w}$) in the final timestep (colours, left). The top and bottom panels in (b) and (c) show the depth-averaged variables above and below the permanent pycnocline. In (d-f) the variables are averaged between 0 and 2000 m. The black and the magenta lines in the left column denote the location of the vertical sections shown in the middle and in the right columns. The black lines in the middle and right columns from (b) to (f) denote the isopycnal at the base of the permanent pycnocline (1027.1 kg/m$^3$).

conserve $Q$, and the relationship between eddy distortion and dynamical changes in the eddy interior can be further assessed.

As the eddy distorts inwards, a region with previously high SLA now has lower SLA (Figure 4.15a, magenta section). This decrease in SLA changes the heave of the isopycnal layers in the ocean below (Figure 4.15c). Above (below) the permanent pycnocline, $N^2$ increases (decreases), as isopycnals previously depressed (compressed) relax back to

their normal state. $\Delta N^2$ above the pycnocline are of order $10^{-6}$ s$^{-1}$, and below, of order $10^{-7}$ s$^{-1}$. This stronger $\Delta N^2$ at the top is expected, as the response of isopycnals to sea level changes decreases in depth. The increase in $N^2$ occurring above the pycnocline is balanced by a gain in negative $\zeta_R$ (i.e. negative $\Delta\zeta_R$), which is consistent in depth (Figure 4.15d). Negative $\zeta_R$ has cyclonic torque in the Southern Hemisphere. A positive vertical velocity (i.e., upward motion) in the final week results from these dynamical changes (Figure 4.15f). The $\tilde{w}$ cells are shifted anti-clockwise in relation to the other variables, as shown before in section 4.3.3. In addition, this inward distortion is associated with divergence of the horizontal flow (Figure 4.15e; magenta section). Therefore, an inward distortion induces upward motion.

As the eddy distorts outwards, a region with previously low SLA now has higher SLA, depressing isopycnals below (Figure 4.15a, black section). Therefore, the layers above the permanent pycnocline become less stratified, seen as a negative $\Delta N^2$ (Figure 4.15c). A negative $\Delta N^2$ above the permanent pycnocline is balanced by a positive $\Delta\zeta_R$ (Figure 4.15d). The positive $\zeta_R$ has anticyclonic torque in the Southern Hemisphere, resulting in a negative vertical velocity (i.e., downward motion) in the final week (Figure 4.15f). In addition, this outward distortion is associated with convergence of the horizontal flow (Figure 4.15e; black section). Therefore, an outward distortion induces downward motion.

A multivariate EOF for eddy #1 is performed, to assess the coherence of the relationship between variables (Figure 4.16). For this analysis, all time intervals of this eddy between southwest Tasmania and its dissipation (i.e. westward propagation; 91 weeks) are considered, and the method described in section 5.2 is followed. The variables combined are $\Delta SLA$, depth-averaged $\Delta\zeta_R$, depth-averaged $\bigtriangledown \cdot U$, and $\tilde{w}$. All the variables have the pattern of alternating cells in modes 2 and 3, resulting in up to 23% of the variance (Figures 4.16d-e). As seen in the daily-averaged fields of this eddy, the $\Delta SLA$ and the $\Delta\zeta_R$ cells are directly related, and both are indirectly related to $\bigtriangledown \cdot U$ and $\tilde{w}$ cells. Therefore, both mechanisms are sustained as eddy #1 propagates westwards in the Eastern Indian Ocean.

#### 4.4.1.2 Eddy #2 off Bass Strait

Off Bass Strait, eddy #2 has a permanent pycnocline located at ~500 m (Figure 4.14c). The dynamical changes associated with the eddy distortion in case study #2 also take place here. An inward distortion increases $N^2$ above the permanent pycnocline, is balanced by a negative $\Delta\zeta_R$, and results in upward motion (Figure 4.17; black section). Conversely, an outward distortion decreases $N^2$ above the permanent pycnocline, is

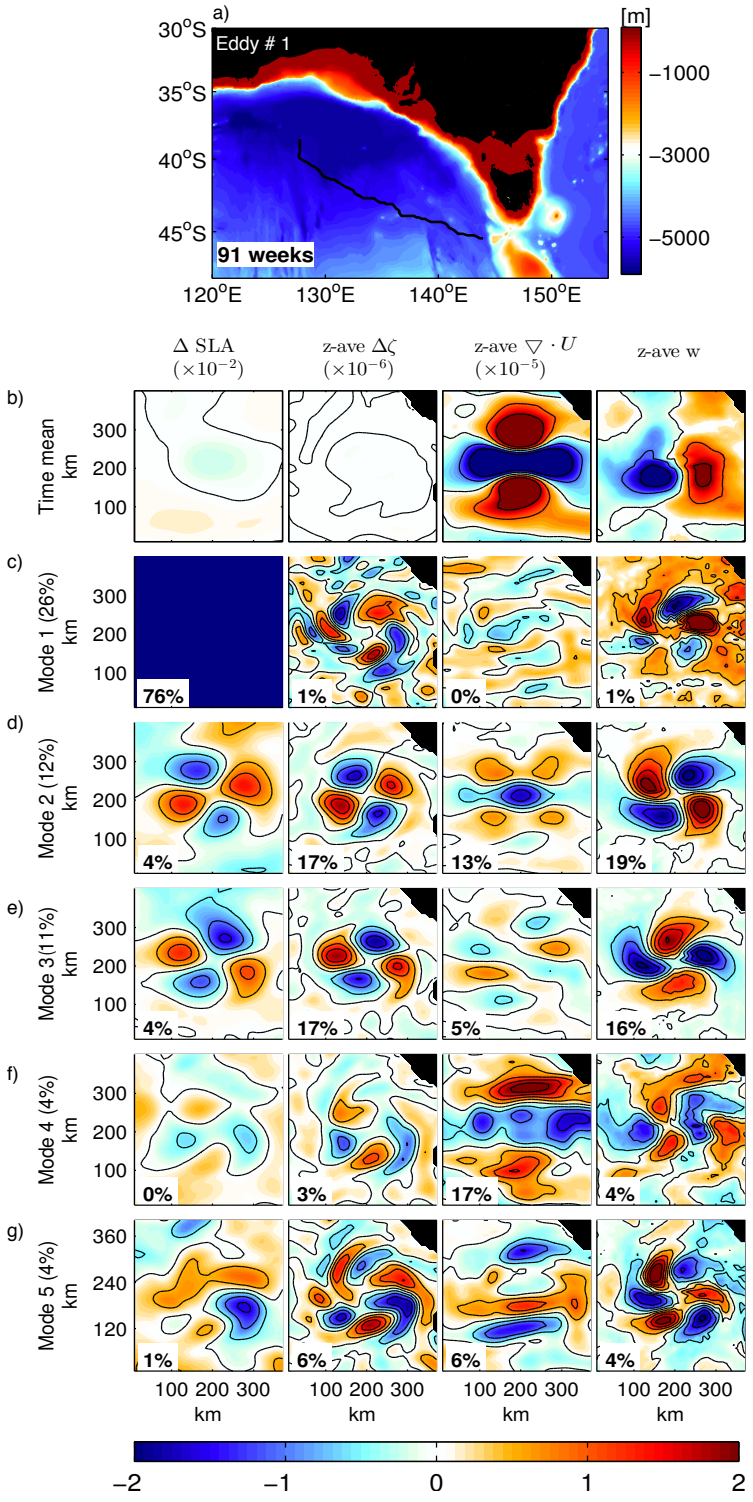


FIGURE 4.16: a) Map indicating the track of an anticyclonic eddy (case study #1) propagating in the Eastern Indian Ocean (black line). Colours denote bathymetry, and the numbers in the bottom left corner indicate the number of weeks taken for this eddy to propagate along the track; b) time mean $\Delta SLA$ and time mean depth-averaged (0-2000 m) relative vorticity ($\zeta_R$), horizontal divergence ($\bigtriangledown \cdot U_2$), and vertical velocity ($\tilde{w}$) for this eddy as it propagates along the track shown in (a); c-g) EOF modes 1-5 of the multi-variate EOF analysis of $\Delta SLA$, $\zeta_R$, $\bigtriangledown \cdot U_2$, and $\tilde{w}$, normalised by the maximum value of each mode and then multiplied by each variable standard deviation, for each eddy (see Section 4.2). Black lines denote null values. Percentages in white boxes are the amount of variance contained in each mode for each variable, and percentages in y-axis label are the amount of variance for the combined variables.

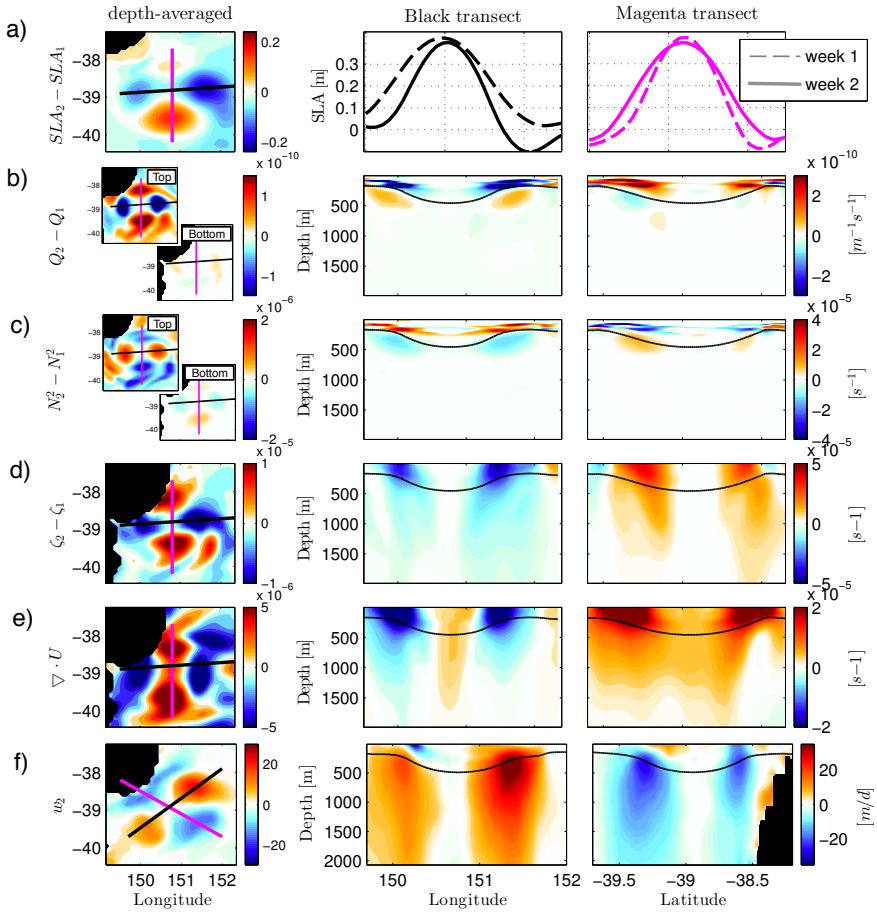


FIGURE 4.17: Same as in Figure 4.15, but for an anticyclonic eddy off Bass Strait (i.e., case study #2). The black lines in the middle and right columns from (b) to (f) denotes the isopycnal in the end of the permanent pycnocline (1026.3 kg/m$^3$)

balanced by a positive $\Delta\zeta_R$, and results in downward motion (Figure 4.17; magenta section).

For the timestep shown in Figure 4.17, the relationship between divergence of the horizontal flow and $\Delta SLA$ is the opposite of the relationship suggested in section 4.4. Despite this opposing relationship, the volume within the eddy is still conserved. Here, the outward distortion (i.e., in latitude) is associated with divergence (Figure 4.17, magenta section) and the inward distortion (i.e., in longitude) is associated with convergence (Figure 4.17e, black section). To determine if this apparent inconsistency is true for other timesteps of this eddy lifetime, I again perform a multivariate EOF analysis of four variables ($\Delta SLA$, $\Delta\zeta_R$, $\bigtriangledown \cdot U$, and $\tilde{w}$). For this analysis, all time intervals of eddy #2 between its formation and south of Tasmania (i.e. southward propagation; 70 weeks) are considered. All the variables have the pattern of alternating cells in modes 1 and

2, summing up to 23% of the variance (Figures 4.18c and d). As suggested in section 4.4, the $\Delta SLA$ and the $\Delta\zeta_R$ cells are directly related, and both are indirectly related to $\bigtriangledown \cdot U$ and $\tilde{w}$ cells. Therefore, in the time interval chosen as a case study (i.e. when the eddy is off Bass Strait; Figures 4.14a, purple dot and 4.17), other forcings acted on the divergence pattern. These forcings might include eddy interaction with bathymetry, with the mean flow, with other mesoscale features, and with the wind.

## 4.5 Discussion and conclusions

The results contained in this Chapter show that alternating cells of vertical velocity are a recurrent feature in anticyclonic eddies formed at the EAC separation region, as seen in a near-global, eddy-resolving model. These cells are most intense between 500 and 1500 metres depths, and are linked to eddy distortion, which is the change in eddy isotropy. This is the first time that these alternating cells have been reported in the literature for a near-global, eddy-resolving ocean model. These alternating upward and downward cells have been previously reported in cyclonic eddies of the Agulhas Return Current (Nardelli, 2013), in an eddy-dipole in the Iceland basin (Pidcock et al., 2013), and in an idealised anticyclonic eddy (Martin and Richards, 2001). In the eddies studied here, the alternating vertical velocity cells have magnitudes of 10-50 m/d, with maximum values at mid-depth (500-1500 m). These velocities are similar to 10-60 m/d vertical velocities, also stronger at mid-depth, reported in the literature (Pollard and Regier, 1992, Martin and Richards, 2001, Nardelli, 2013). The alternating upward and downward cells shown here rotate anti-clockwise as the eddies propagate. A clockwise rotation of alternating upward and downward cells has also been reported in cyclonic eddies of the Agulhas Return Current (Nardelli, 2013).

While daily-averaged fields of vertical velocity within the modelled eddies of the EAC have four or more alternating cells, a time-mean of this variable has two cells only (Figures 4.7b, 4.10b). These cells have 2 m/d magnitude and are downwards at the leading part of the eddy and upwards in the trailing part of the eddy. Therefore, this dual cell pattern is associated with the eddy propagation mechanism described by McGillicuddy et al. (1995). As in previous reports (e.g., Martin and Richards, 2001, Table 4.1), the magnitude of the vertical velocity induced by eddy propagation in eddies is 10 times smaller than the magnitude of the alternating upward and downward cells induced by eddy distortion. The loss of the alternating upward and downward cells in a time-averaged eddy demonstrates the importance of studying eddies as case studies.

Two mechanisms linking the eddy distortion to vertical velocity are suggested here. One mechanism relates to the conservation of $Q$ in the eddy, and the other mechanism, to

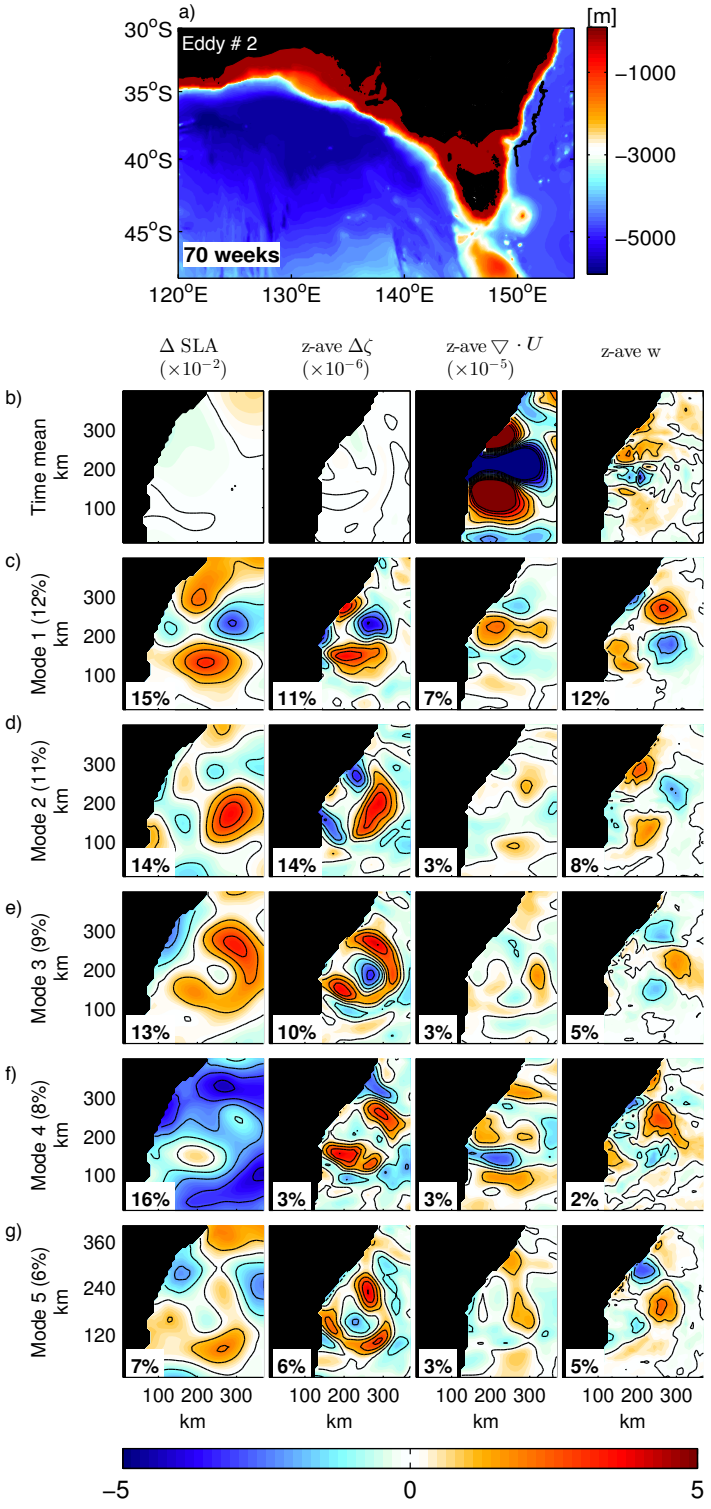


FIGURE 4.18: Same as in Figure 4.16, but for case study #2 propagating southwards, off the eastern Australian shelf break.

the conservation of volume within the eddy. An analysis considering several timesteps of the lives of two eddies suggests these two mechanisms act together. However, in some moments of the eddy lifetime only one mechanism holds, as seen in the eddy off Bass Strait. These analyses show that the mechanisms linking eddy distortion and vertical velocity still require further discussion. Questions that remain unanswered are: When is each mechanism more important than the other? And can the influence of these mechanisms in eddy vertical velocity be isolated?

I highlight three subjects for future investigation of vertical velocity within eddies. The first subject is the eddy distortion mechanism in cyclonic eddies and in Northern Hemisphere eddies. In a study using the output of a global eddy-resolving ocean model, the selected eddies should be coherent (i.e. no filaments), and isolated from other mesoscale features and the bathymetry. Here, the importance of studying eddies as case studies is highlighted. It was only by using this approach that I was able to isolate the pattern of alternating vertical velocity and relate it to eddy distortion. The second subject is the reason for eddy distortion. For this investigation, using idealised eddies with different forcings (e.g. shear strain and eddy-bathymetry interaction) is suggested. The third subject is the impact of the alternating upward and downward cells on primary productivity within the eddy. Other dominant mechanisms that impact primary productivity within eddies must be kept in mind when exploring this subject. These mechanisms include the eddy-Ekman pumping (Martin and Richards, 2001, Siegel et al., 2008), frontal sub-mesoscale processes (Klein and Lapeyre, 2009), and eddy-bathymetry interaction (Oke and Griffin, 2011).

The vertical velocity within ocean eddies is a challenging research topic. Currently, the best tools to investigate this velocity are either outputs from ocean models, as used in this study, or vertical velocities calculated using the Omega equation. It would be useful to study vertical velocity within eddies in a global scale. Satellite altimetry provides this global coverage, and a 25-year temporal coverage. It is shown here that the change in SLA fields is a good proxy for eddy distortion. I expect that future studies will be able to combine the methods shown here and to use the global, long term altimetry data to quantify eddy distortion and vertical velocity within eddies. Using altimetry fields to calculate eddy distortion would provide the scientific community with further information on sub-mesoscale patterns, ageostrophic velocity, and the interior dynamics of ocean eddies. Ultimately, the connection between global satellite altimetry to the vertical velocity below could be used to construct a global estimate of vertical advection of nutrients, carbon, and other properties within oceanic eddies.

# Chapter 5

# Impact of data assimilation on vertical velocities in an eddy resolving ocean model

In the previous Chapter, the circulation within EAC anticyclonic eddies in a free-running, eddy-resolving ocean model is investigated. I show that EAC anticyclonic eddies in OFAM have a dominant vertical velocity pattern in their interior - and that this pattern relates to eddy distortion. In this Chapter, I use a version of this ocean model with data assimilation to determine if the same vertical velocity pattern is still dominant in EAC anticyclonic eddies. In addition, this Chapter also aims to assess the impact of data assimilation on the vertical circulation within eddies from an ocean model.

## 5.1 Introduction

Most eddy-resolving ocean reanalyses and forecast systems assimilate ocean observations using some form of sequential data assimilation (DA). This includes ensemble-based methods (e.g., Oke, 2002, Oke et al., 2005, 2008, Sakov et al., 2012), variational methods (e.g., Powell et al., 2009, Moore et al., 2011, Martin et al., 2015), and other commonly used methods (e.g., Cooper and Haines, 1996, Chassignet et al., 2007). Sequential DA involves an explicit update of the model state at regular intervals (e.g., daily, or every few days). These updates are typically applied to the model either in a single timestep (e.g., Sakov et al., 2012), or over multiple timesteps (e.g., Oke et al., 2008). Moreover, the updates to the model state are generally not "dynamically consistent". That is, they are generally not precise solutions to the model equations.

Updates to a model state are usually applied to all model variables (i.e., temperature, salinity, sea level, and horizontal velocity) and can be regarded as a non-physical forcing term in the model equations. After a model is initialised, it undergoes an adjustment, where its dynamical balance is restored. This typically involves inertial oscillations, unrealistic mixing, and some sort of artificial baroclinic and barotropic adjustment. This process of adjustment of the model to DA is widely regarded as undesirable. In an early study of this issue, Daley (1981) - referring to problems associated with these model adjustments - says that they "are at best a nuisance and at worst can seriously compromise the forecast procedure". Many efforts are made to limit the negative impacts of this adjustment after assimilation.

In a reanalysis system developed under Bluelink - a partnership between CSIRO, the Bureau of Meteorology and the Royal Australian Navy - there have been attempts to reduce the problems associated with the model adjustment to DA. These attempts include the use of nudging (Oke et al., 2005), incremental updating (Oke et al., 2008), and careful generation of the underpinning ensemble (Oke et al., 2013b). Despite these efforts, models with DA are often considered to be inappropriate for detailed dynamical studies, with few exceptions (e.g., Oke and Griffin, 2011, Schiller and Oke, 2015). Although this perception is widespread, very few studies have actually assessed the integrity of the model's dynamical processes in a model run with DA. One way to gain insight into this issue is to look at the behaviour of an unobserved variable in the data-assimilating model.

Free-running models without DA have been widely used to study many different aspects of eddy dynamics (e.g., van Sebille et al., 2010, Cetina-Heredia et al., 2014, Rykova et al., 2017). However, free-running models are generally not able to reliably forecast eddies at the correct time and place. This is because eddy formation and evolution is chaotic and models do not capture all relevant physics of the ocean at all scales. If a study seeks to understand the dynamics of a particular eddy event, a data-assimilating model is probably needed.

The question wished to be answered here is whether a data-assimilating model is suitable for a detailed dynamical analysis of ocean eddies. To gain insight into this question, the vertical velocity within eddies simulated in a data-assimilating model is analysed. The vertical velocity is chosen because it is not observed, and is sensitive to disruptions to a model's dynamical balance (e.g., ageostrophic flow).

As shown in Chapter 4, eddies from a free-running model often have alternating upward and downward cells (Figures 4.6). These cells are coherent over depth, with maximum vertical velocities between ∼500 and 1000 m depth (Figures 4.6). In this Chapter, I aim to first determine if a data-assimilating model can reproduce these cells of alternating

upward and downward motion; and then to investigate how these cells are affected by sequential DA. This study is a step towards better understanding the suitability of data-assimilating ocean models for detailed analysis of ocean circulation and ocean dynamics.

This Chapter is organised with a description of the data-assimilation model and the methods used here in section 5.2, results in section 5.3, a discussion in section 5.4, and conclusions in section 5.5.

This Chapter is based on a manuscript submitted to Ocean Modelling entitled: Pilo, G. S., Oke, P. R., Coleman, R., Rykova, T., and Ridgway, K., **Impact of data assimilation on vertical velocities in an eddy resolving ocean model**.

## 5.2 Data and Methods

### 5.2.1 Bluelink ReANalysis (BRAN)

The free-running model used in version 3p5 of BRAN, hereafter BRAN3p5, is version 3 of OFAM, described in Chapter 2, section 2.2. Here, daily mean fields from BRAN3p5 are used. BRAN3p5 is a multi-year model integration of OFAM, with sequential DA once every 4 days (Oke et al., 2008). Observations that are assimilated include SLA, from along-track satellite altimetry, satellite SST, and *in situ* temperature and salinity from Argo floats, XBTs, and other sources. BRAN3p5 runs from January 1993 to July 2012. Because of the climatological restoring below 2000 m and coarse vertical resolution, as described in section 2.2, only the top 2000 m of BRAN3p5 is considered throughout this study.

The technical process of sequential DA for BRAN3p5 involves the following steps, and is depicted in Figure 5.1. The model "background field", comprised of daily-mean fields of temperature (T), salinity (S), sea level, and the horizontal components of velocity ($u$,$v$) - four days after the previous assimilation step - is compared to observations. Using the Ensemble Optimal Interpolation system, described by Oke et al. (2008, 2013b), the background field is combined with observations, yielding an "analysis field". The analysis field is intended to better match the assimilated observations - and is simply the background field plus an "increment". For BRAN3p5, only T, S, $u$ and $v$ are updated explicitly, using an adaptive nudging scheme (Sandery et al., 2011). Because the calculated analyses are not a precise solution to the model equations, the model fields undergo a "model adjustment", sometimes referred to as the model shock (e.g., Waters et al., 2017). This Chapter seeks to better understand the details of the model

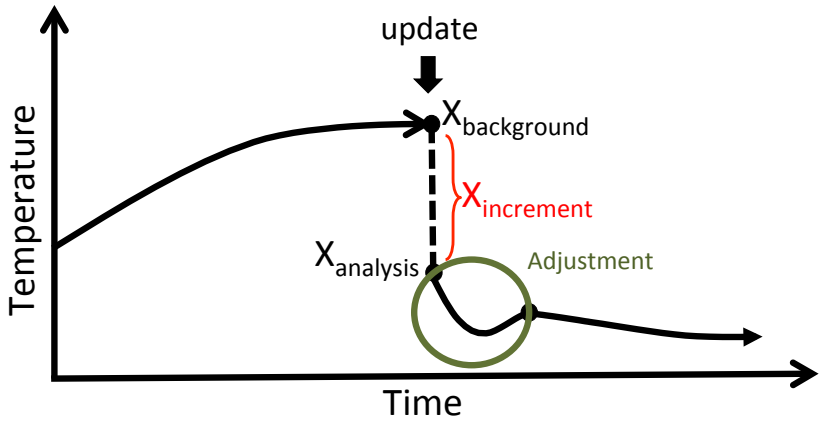


FIGURE 5.1: Schematic depicting the ocean state evolving over time; and then being updated, using DA. The update involves the addition of an increment, $X_{increment}$, to the model background, $X_{background}$, thereby initialising the model with an analysis, $X_{analysis}$. This update is typically followed by a period of adjustment. The state vector X is comprised of T, S, $u$, $v$, and sea level.

adjustment to DA, and specifically how this adjustment affects the modelled velocities, T, and S within eddies.

BRAN3p5 realistically reproduces the vertical structure of the studied region, as shown in a comparison of the anomaly of the 15$^o$C isotherm depth between Sydney, Australia and Wellington, New Zealand (Figures 5.2a and b, blue line in d). The data used for this comparison are the temperature collected by XBTs along this line over 13 years (Figure 5.2a), and the temperature from BRAN3p5 over the same period (Figure 5.2b). The XBT data is assimilated into BRAN3p5 between February 1993 and July 2003, and withheld between September 2003 and December 2006 (Figure 5.2b green and magenta boxes, respectively). For both time periods - when the XBT data are assimilated and withheld - the observations and BRAN3p5 fields agree well.

A comparison between BRAN3p5 fields and fields derived from surface drifting buoys and satellite observations show generally good agreement (Figures 5.2c-f). For this comparison, remotely sensed SST and altimetry are assimilated into BRAN3p5, and data from independent surface drifting buoys are withheld. Both near-surface horizontal velocities, inferred from satellite altimetry (white arrows in panel e-f), and surface drifting buoys (black arrows in panel c-f) match eddy locations in the reanalysis (white arrows in panel c-d) in Figure 5.2. Despite localised differences between BRAN3p5 and observations, the regional circulation and variability in the reanalysis are consistent with observations.

The examples of BRAN3p5 assessment shown in Figure 5.2 represent a small sub-set of comparisons performed by Oke et al. (2013b). Many other aspects of BRAN3p5 have been assessed by comparison with both assimilated and unassimilated observations in

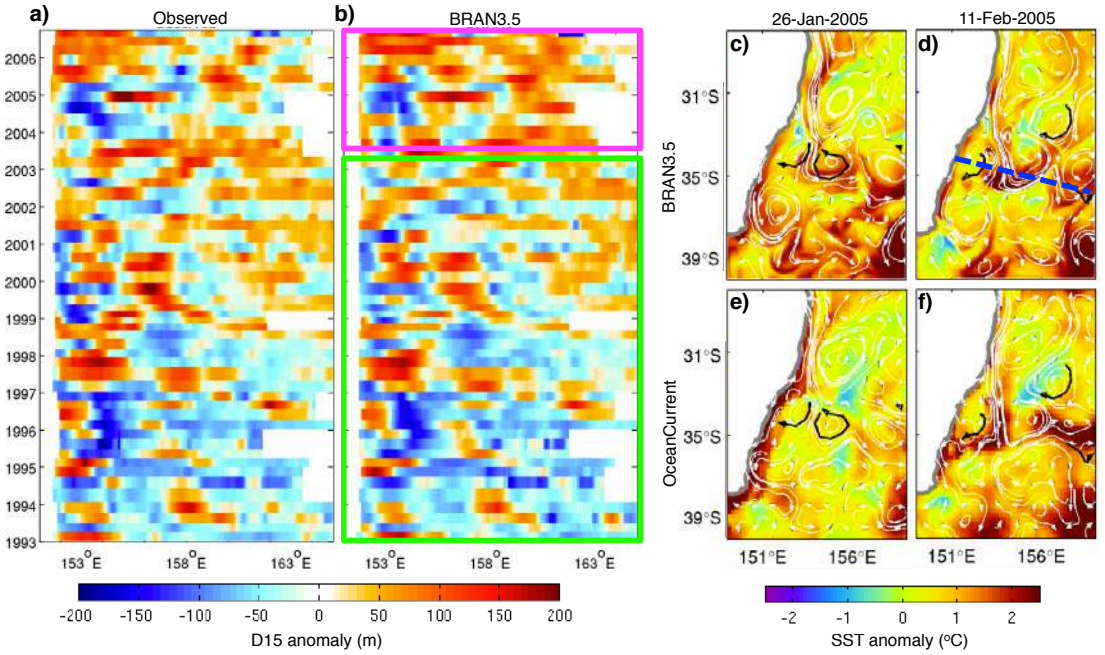


FIGURE 5.2: Comparison between the data-assimilating model (BRAN3p5) and observations. Hovmöller diagram showing the depth anomaly of the 15°C isotherm from XBT observations along (a) the PX34 line, (b) and from BRAN3p5. XBT data along PX34 (dashed blue line in d) are assimilated before July 2003 (green box in b), and withheld thereafter (magenta box in b). The PX34 line is shown in (d); Daily-averaged SST anomalies (colours) and near-surface velocities (white vectors) off south-east Australia from (c-d) BRAN3p5, and (e-f) observations. Surface drifting buoy trajectories are overlaid (black vectors). SST anomalies are with respect to a 15-year seasonal climatology from the model's spin-up. Model velocities represent flow over a 5 day period. Drifter trajectories are for an 8-day period preceding the date of each image (adapted from Oke et al., 2013b).

the published literature (e.g., Oke et al., 2008, Oke and Griffin, 2011, Oke et al., 2013b). Despite the extensive assessment, the vertical velocities of BRAN3p5 - or any other model or reanalysis - remain unvalidated, owing to the paucity of reliable observation-based estimates. Because of this limitation, showing that vertical velocities in BRAN3p5 are correct is not the goal of this study. Instead, I aim to assess the extent to which the vertical velocities in BRAN3p5 are consistent with the vertical velocities of a free-running version of the underpinning model (i.e., OFAM). That is, I seek to determine the extent to which DA improves or degrades the vertical velocities in an eddy-resolving ocean model. As a starting point, I asses whether BRAN3p5 reproduces the patterns of vertical velocities in eddies described in Chapter 4.

### 5.2.2 Eddy tracking

Tracking an eddy in the Tasman Sea in a data-assimilating model is challenging. First, after each update, the position, shape, and SLA associated with each eddy tends to

change. Second, because the Tasman Sea is a highly energetic region, the recurrent eddy-eddy and eddy-bathymetry interactions also change the shape of each eddy. Third, there are observation gaps (e.g., missing data between altimetry tracks) that sometimes lead to the apparent "disappearance" of an eddy for one, or sometimes two, assimilation cycles. All of these factors complicate the process of automatically, or even manually, tracking eddies.

To ensure that the eddy tracking is as accurate as possible, the eddies are manually tracked in SLA fields of BRAN3p5, using the approach described in Chapter 2. The eddies are tracked on consecutive days, until it is no longer evident, with a tolerance of two assimilation cycles (8 days). After tracking, $4^\circ \times 4^\circ \times$ 2000 m "data cubes", centred at the eddy-centre, are extracted from BRAN3p5 - as described in Chapter 2.

### 5.2.3 Empirical Orthogonal Functions

To isolate the coherent components of the vertical velocity fields within the eddies, an Empirical Orthogonal Function (EOF) analysis is performed - equivalent to the analyses in Chapter 4. For this EOF analysis, $4^o \times 4^o$ maps of depth-averaged vertical velocity (0 - 2000 m) are used, for each day of the eddy lifetime. For the EOF analysis, each time-series is de-trended in time, for each grid point. Then, a singular value decomposition of the anomaly field is computed. Five separate EOF analyses of daily time-series of depth-averaged vertical velocities are performed. For the eddies considered here, the time-series span between 180 and 350 days. In a first analysis, all daily fields of vertical velocity for the lifetime of each eddy are considered. In the other analyses, each time series is sub-sampled, and EOF analyses on fields from day 1, 2, 3, and 4 of each assimilation cycle are performed separately. That is, one field every four days is used, representing different days of each assimilation cycle (recall that BRAN3p5 assimilates data every four days). These time-series are hereafter referred to as DA1, DA2, DA3, and DA4; so DA1 includes model fields on the day immediately after each assimilation; DA2 includes model fields two days after each assimilation; and so on.

## 5.3 Results

The extent to which the model velocities - both horizontal and vertical - artificially adjust to the changes introduced during the model update is assessed first. For this assessment, the root mean square (RMS) of depth-averaged eddy kinetic energy is calculated (EKE; computed as $(u^2+v^2)/2$) and the depth-averaged vertical velocity considering DA1, DA2, DA3, and DA4 separately (Figures 5.3a and b, respectively). The volume-averaged EKE

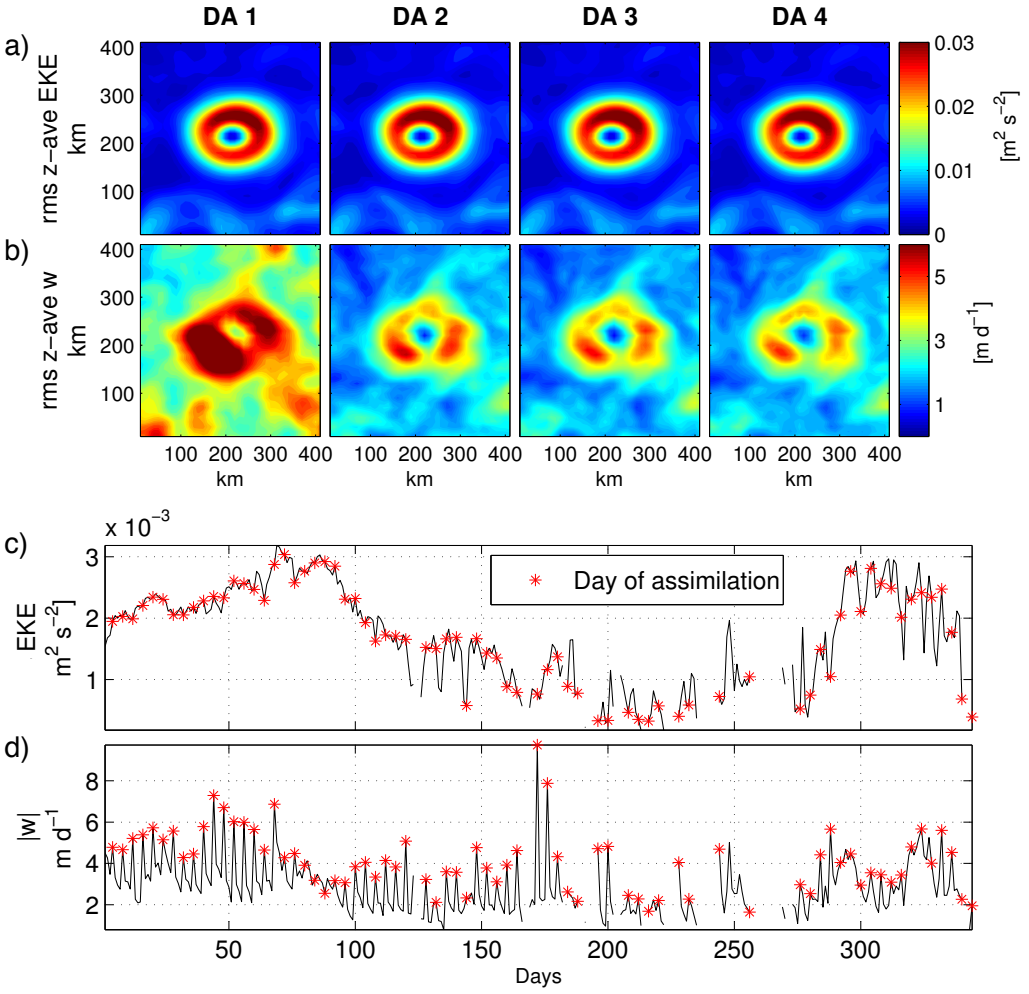


FIGURE 5.3: a) RMS of depth-averaged (0-2000 m) EKE for the first, second, third, and fourth days after DA (DA1, DA2, DA3, and DA4, respectively) for an anticyclonic eddy off eastern Australia; b) same as in (a), but for depth-averaged vertical velocity; c) time series of the volume-averaged EKE, with red stars showing the first day after DA; d) same as in (c), but for volume-averaged absolute vertical velocity. Missing values relate are when a 0.1 m SLA contour could not be defined.

and the volume-averaged absolute vertical velocity contained within the $4^o \times 4^o \times$ 2000 m data cubes are also computed (Figure 5.3c and d, respectively). To demonstrate the features of interest for this study, I first show results for one anticyclonic eddy off eastern Australia (Figure 5.3), one anticyclonic eddy in the Tasman Sea (Figure 5.4), and one cyclonic eddy in the Tasman Sea (Figure 5.5). Results in Figures 5.3, 5.4, and 5.5 are typical of other examples of reanalysed eddies in BRAN3p5 in waters around Tasmania.

There is no obvious systematic adjustment in horizontal velocity immediately following the DA (Figures 5.3a-c, 5.4a-c, and 5.5a-c). The difference between the RMS of EKE in DA1 and DA2-4 is the order of $10^{-4}$ m$^2$/s$^2$, two orders of magnitude smaller than the RMS of total EKE itself. The vertical velocity, however, shows a significant increase in

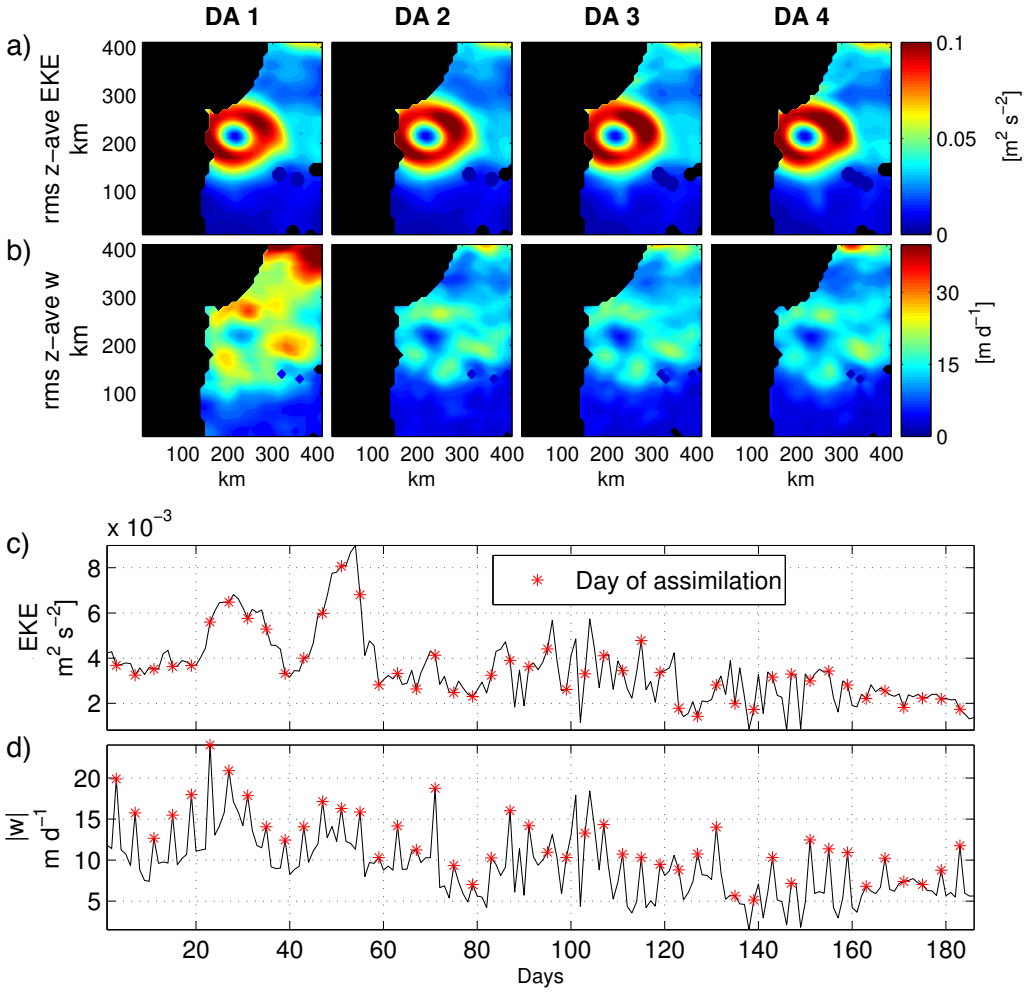


FIGURE 5.4: As in Figure 5.3, but for an anticyclonic eddy in the Tasman Sea.

RMS immediately after assimilation (DA1 in Figures 5.3b, 5.5b, and 5.5b). Additionally, there is a clear spike in absolute vertical velocity on the first day after the update (DA1, denoted by the red stars in Figure 5.3d). The difference between the RMS of vertical velocity in DA1 and DA2-4 is the order of 10 m s$^{-1}$, the same order of magnitude as the RMS of total vertical velocity itself. This indicates that the vertical velocities are sensitive to the introduced changes during the assimilation step. The next step is to better understand this adjustment.

To further examine the impact of the sequential DA on the vertical velocity within eddies, three case studies are selected to be analysed in detail. The first case study is an anticyclonic eddy propagating westwards south of Australia (Figures 5.6a and 5.10). The second case study is an anticyclonic eddy propagating southwards in the Tasman Sea (Figures 5.6b and 5.11). The third case study is a cyclonic eddy propagating eastwards, also in the Tasman Sea (Figures 5.6c and 5.12). These eddies are selected because

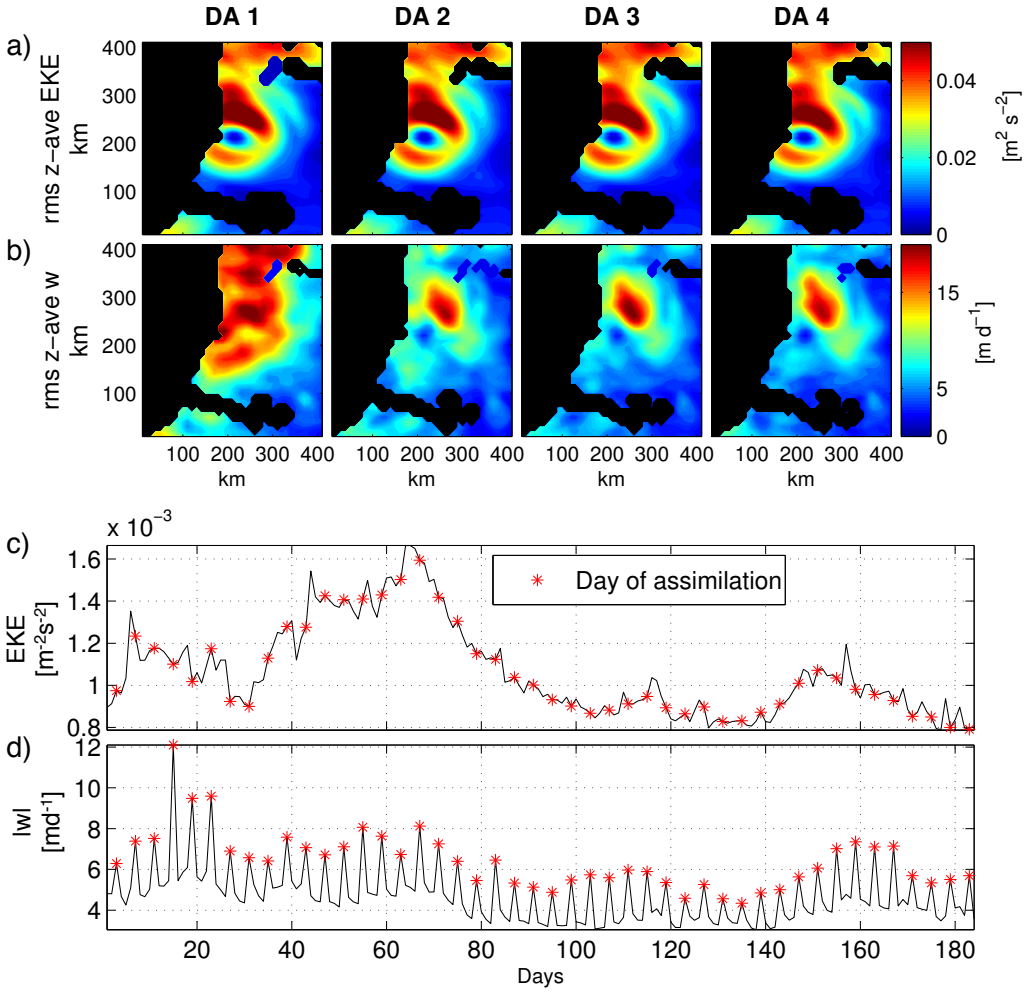


FIGURE 5.5: As in Figure 5.3, but for a cyclonic eddy in the Tasman Sea.

they propagate through different oceanographic regimes. The eddy example south of Australia propagates through deep quiescent waters, and the eddies in the Tasman Sea repeatedly interact with other mesoscale features and are influenced by bathymetry, as shown in Chapter 3. Recall that analysis of vertical velocities in OFAM, with no DA, eddies similar to those considered here show a coherent signal of the alternating cell patterns for vertical velocity (see Figure 4.6 and results from Chapter 4).

Fields of vertical velocity, for the three case studies considered here, show evidence of the upward and downward cells (Figure 5.6), consistent with those described in Chapter 4. This indicates that the process of eddy distortion is present in BRAN3p5. Indeed, analysis of the vertical velocities in these eddies shows that these cells are coherent in depth, with maximum at sub-surface (∼1000 –1500 m). In addition, the vertical velocities within eddies in BRAN3p5 (Figure 5.6) are the same order of magnitude as the vertical velocity within eddies in OFAM with no DA (Figure 4.6). These results confirm

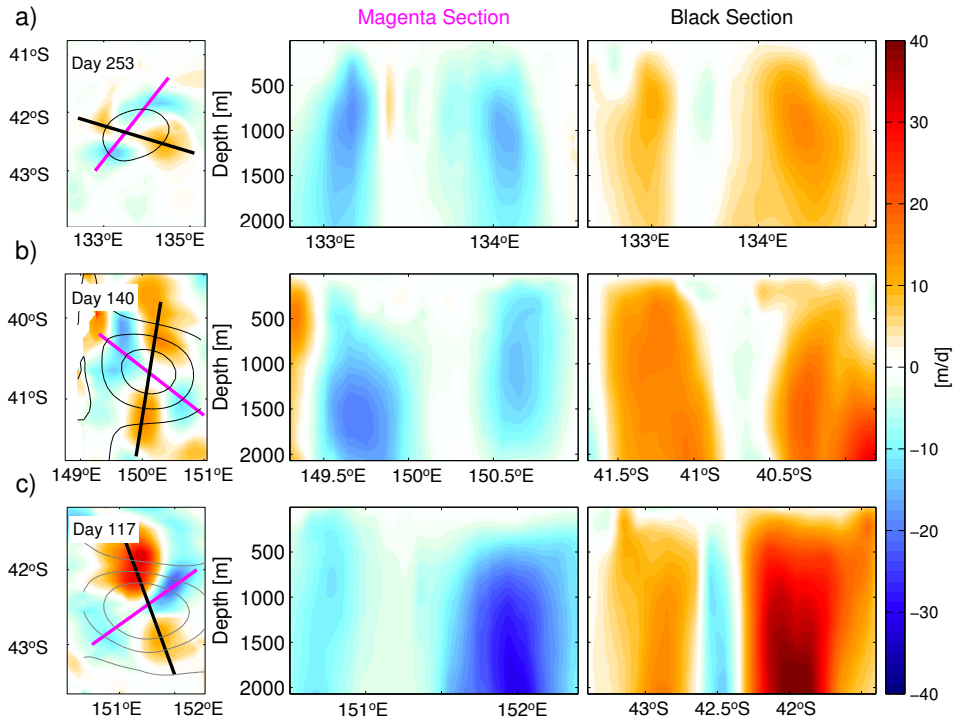


FIGURE 5.6: Alternating cells of depth-averaged (0-2000 m) vertical velocity (colours, left) in a) an anticyclonic eddy off western Tasmania (0.05 m SLA contour), b) an anticyclonic eddy in the Tasman Sea (0.05, 0.15 and 0.25 m SLA contours), and c) a cyclonic eddy in the Tasman Sea (-0.05, -0.15 and -0.25 m SLA contours); The column in the centre (right) are sections of vertical velocity along the magenta (black) lines shown in the left. All daily averages relate to the second day after the data is assimilated into the model (i.e., DA2).

that the data-assimilating model does reproduce the alternating upward and downward cells, both qualitatively and quantitatively, when compared to the free-running model (i.e., OFAM).

As in the free running model (see Chapter 4), patterns of vertical velocity associated with eddy-distortion dominate the leading modes of variability in the data-assimilating model (Figure 5.7). The signal of this pattern is typically partitioned across several EOF modes. The partitioning of the signal occurs due to the rotation of the cells as the eddy propagates, in the same sense of the eddy rotation. In the anticyclonic eddy propagating southwards, the variance attributed to the alternating cells pattern in modes 2, 3, and 4 sums up to 55% of the total variance for vertical velocity (Figure 5.7, Table 5.1). In the other case studies, the combined variance is lower (30% and 34%), but within the range evident in the eddies of the free-running model (Table 5.1).

TABLE 5.1: Combined variances of EOF modes that show alternated upward and downward cells within eddies of the data-assimilating (BRAN) and of the free-running (OFAM) models. For BRAN3p5 eddies, values relate to EOFs calculated considering vertical velocity fields in the first, second, third, and fourth days of the assimilation cycle only (DA1, DA2, DA3, and DA4, respectively), and considering daily fields. For OFAM eddies, values relate to EOFs calculated considering vertical velocity fields in 7-day intervals. The range of values in OFAM eddies relate to 10 eddies propagating westwards in the Eastern Indian Ocean, and to 10 eddies propagating southwards in the Tasman Sea, adapted from Chapter 4.

| Eddy | | Combined variance | | | | |
|---|---|---|---|---|---|---|
| | | DA1 | DA2 | DA3 | DA4 | Daily |
| BRAN3p5 | Westward anticyclonic | 25% | 33% | 34% | 31% | 34% |
| | Southward anticyclonic | 27% | 37% | 45% | 47% | 55% |
| | Eastward cyclonic | 13% | 36% | 38% | 47% | 30% |
| | | 7-day timestep | | | | |
| OFAM | Westward anticyclonic | 25–56% | | | | |
| | Southward anticyclonic | 22–52% | | | | |

The time-series of the EOF amplitudes show fluctuations that are clearly related to the assimilation cycle - showing higher amplitude values on the day after each assimilation (DA1). This is quantified in Figure 5.8, showing the RMS of the time-series of the EOF amplitudes, as a function of the assimilation cycle - gathering amplitudes for DA1, DA2, DA3, and DA4 together (Figure 5.7). The values for the first 10 EOFS, for each of the three eddy case studies are analysed (red, green and blue). The results indicate that the amplitude of the time-series of the EOF amplitudes of the dominant modes - showing the upward and downward cells - are typically 2 times greater in DA1 (Figure 5.8) and sometimes with opposite sign to the amplitudes in DA2, DA3, and DA4 (time-series of the EOF amplitudes in Figure 5.7). Therefore, the amplitude of the vertical velocities associated with eddy distortion is actually larger on the day after each assimilation. This suggests that the model's response to the introduced changes (i.e., the applied increments) is like an "artificial eddy distortion".

To further explore the nature of the increments applied to the model during each assimilation cycle, an EOF analysis on the calculated increments for sea level is performed (Figure 5.9). Because the EOFs are statistical modes, they do not correspond directly to physical processes. However, the dominant EOFs are interpreted here to represent changes in the amplitude, position, or shape of an eddy. Modes with one local extremum close to the eddy centre correspond to changes in eddy amplitude (e.g., Figures 5.9d and 5.9m); modes with two local extrema and approximately zero amplitude close to the eddy centre correspond to changes in eddy position (e.g., Figures 5.9g and 5.9j); and modes with multiple local extrema with approximately zero amplitude close to the eddy centre correspond to changes in eddy shape (e.g., Figures 5.9p and 5.9q). The results in

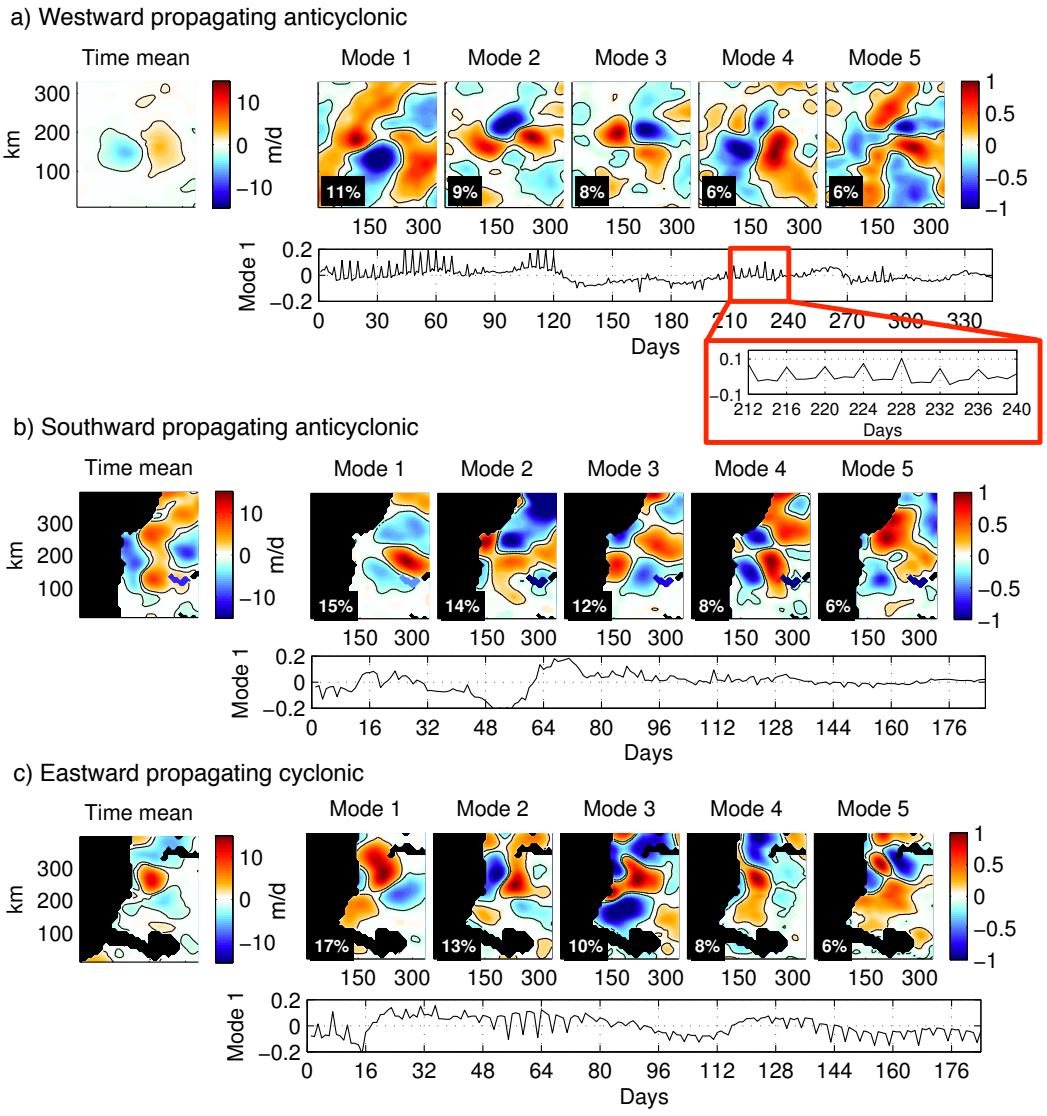


FIGURE 5.7: EOF analysis of depth-averaged vertical velocity (0-2000 m) using daily averaged fields. a), b), and c) are case studies #1 (Figure 5.10), #2 (Figure 5.11), and #3 (Figure 5.12), respectively. Column one is the time mean depth-averaged vertical velocity. Columns two to six are the EOF modes 1-5 normalised by the maximum value of each mode. The time-series of the EOF amplitudes are from EOF mode 1. Percentages in the bottom left corner are the amount of variance contained in each mode. Black contours indicate ± 0.1 m/d vertical velocity. The zoom in (a) shows the time-series of the amplitudes of EOF mode 1 between days 212 and 240 of the eddy lifetime.

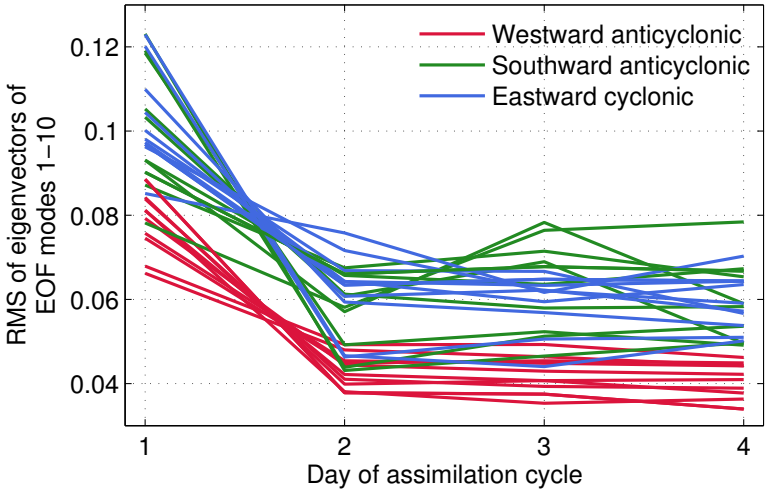


FIGURE 5.8: Root mean square of the first 10 EOF modes of the three eddies in Figure 5.7 considering the first, second, third, and fourth days after DA separately. That is, entries attributed to DA1 are the RMS of each EOF time series, computed from amplitudes sub-sampled on the first day after assimilation.

Figure 5.9 indicate that about half the variance of the sea level increments are related to changes in eddy amplitude or position. However, all of the higher modes - a sub-set of which are included in Figure 5.9 - have multiple local extrema, and are apparently related to changes in eddy shape (i.e., artificial eddy distortion). The structures of these higher modes are not as "clean" as the patterns seen in the EOFs of depth-averaged vertical velocity in Figure 5.7. This is because the artificial distortion associated with the DA is non-conservative (i.e., it doesn't conserve volume), unlike a dynamically-consistent eddy distortion in a dynamically balanced ocean, as the eddies studied in Chapter 4.

To examine the effect of this artificial eddy distortion in the model - and to determine whether these patterns are dominant immediately after assimilation - EOFs of vertical velocity using fields from the first, second, third, and fourth day after the update (i.e., DA1, DA2, DA3, and DA4) separately are computed. That is, for each of the case studies, I subset the time-series using only DA1 fields and re-calculate the EOFs and the time-series of the EOF amplitudes, as previously described in Section 5.2. The results (Figures 5.10, 5.11, and 5.12) indicate that, for all three eddies, the dominant patterns of vertical velocity in DA1 are more complicated than in DA2, DA3, or DA4. The amplified vertical velocities of the upward and downward cells pattern in DA1 is attributed to the fact that the eddy distortion introduced is artificial, and corresponds to changes in the eddy amplitude, position, and shape at the same time - as shown in Figure 5.9. Despite this amplified vertical velocity, the patterns associated with eddy distortion are present - explaining about 13-27% of the total variance in DA1 and 31-47% of the variance in DA4 (Table 5.1).

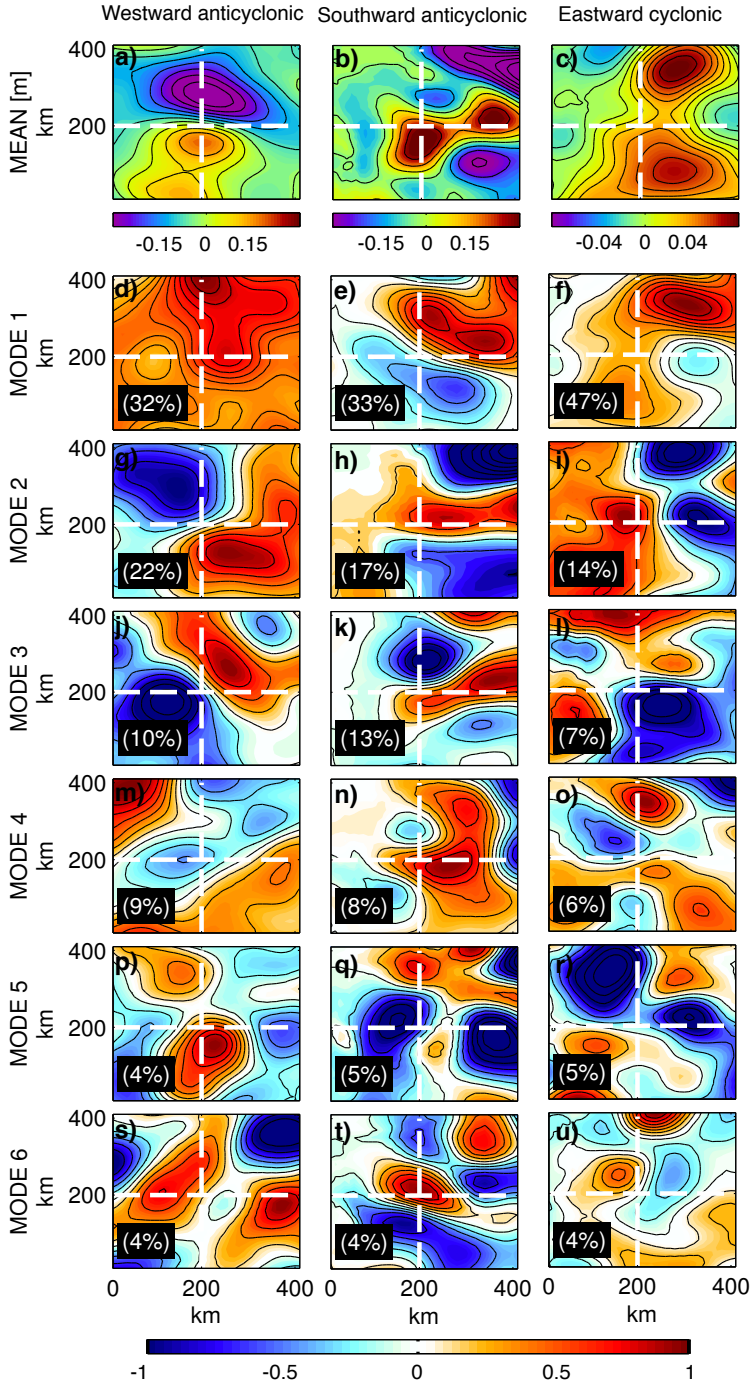


FIGURE 5.9: EOF analysis of the sea level increments (in metres) applied to an anticyclonic eddy propagating westwards (i.e., case study #1; left), an anticyclonic eddy propagating southwards (i.e., case study #2; centre), and a cyclonic eddy propagating eastwards (i.e., case study #3; right). Line one is the time mean sea level increment. Lines two to seven are the EOF modes 1-6 normalised by the maximum value of each mode. The dashed white lines indicate the eddy centre. Percentages in the bottom left corner are the amount of variance contained in each mode, for each eddy.

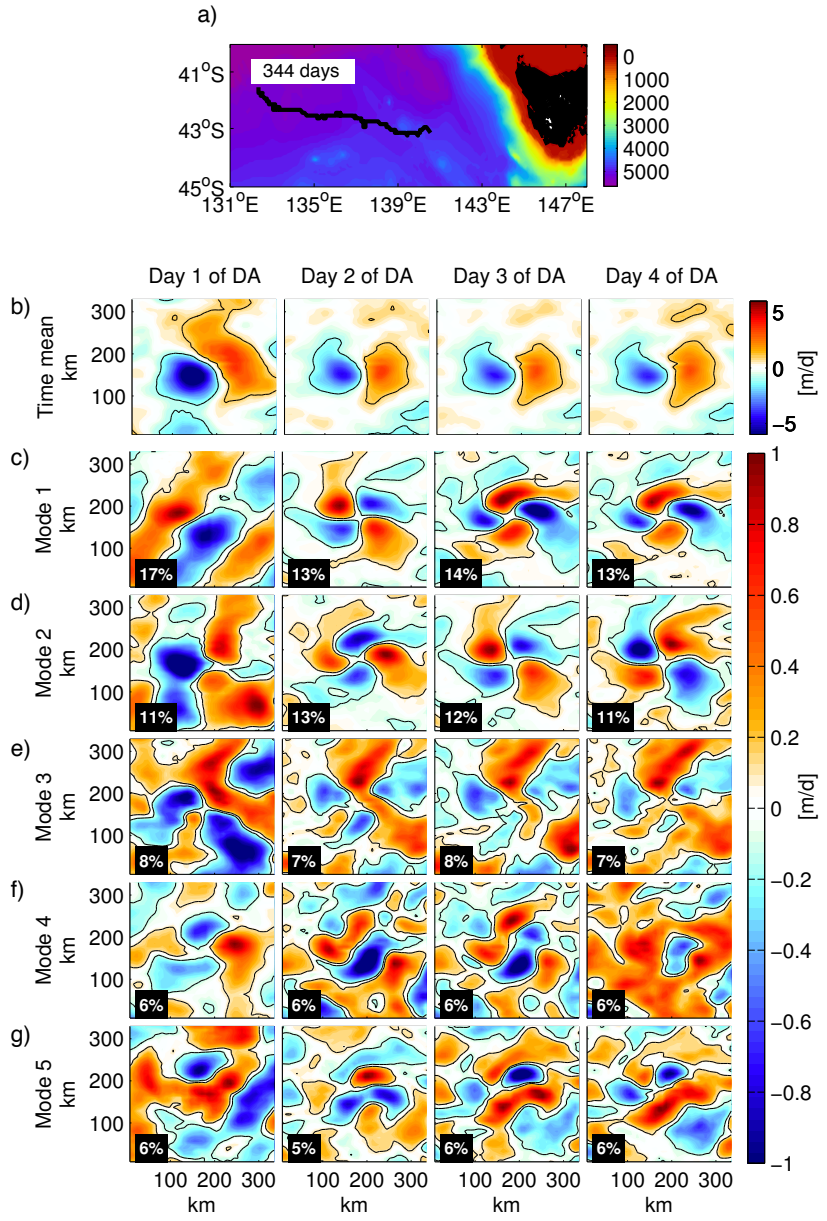


FIGURE 5.10: EOF analysis of depth-averaged (0-2000 m) vertical velocity in an anticyclonic eddy propagating westwards in the Eastern Indian Ocean. a) eddy track (black line) over regional bathymetry (colours); b) time mean depth-averaged vertical velocity considering the first, second, third, and fourth days after DA separately (DA1, DA2, DA3, and DA4, respectively); c-g) EOF modes 1-5 normalised by the maximum value of each mode. Percentages in the bottom left corner are the amount of variance contained in each mode. Contours indicate ± 0.1 m/d vertical velocity.

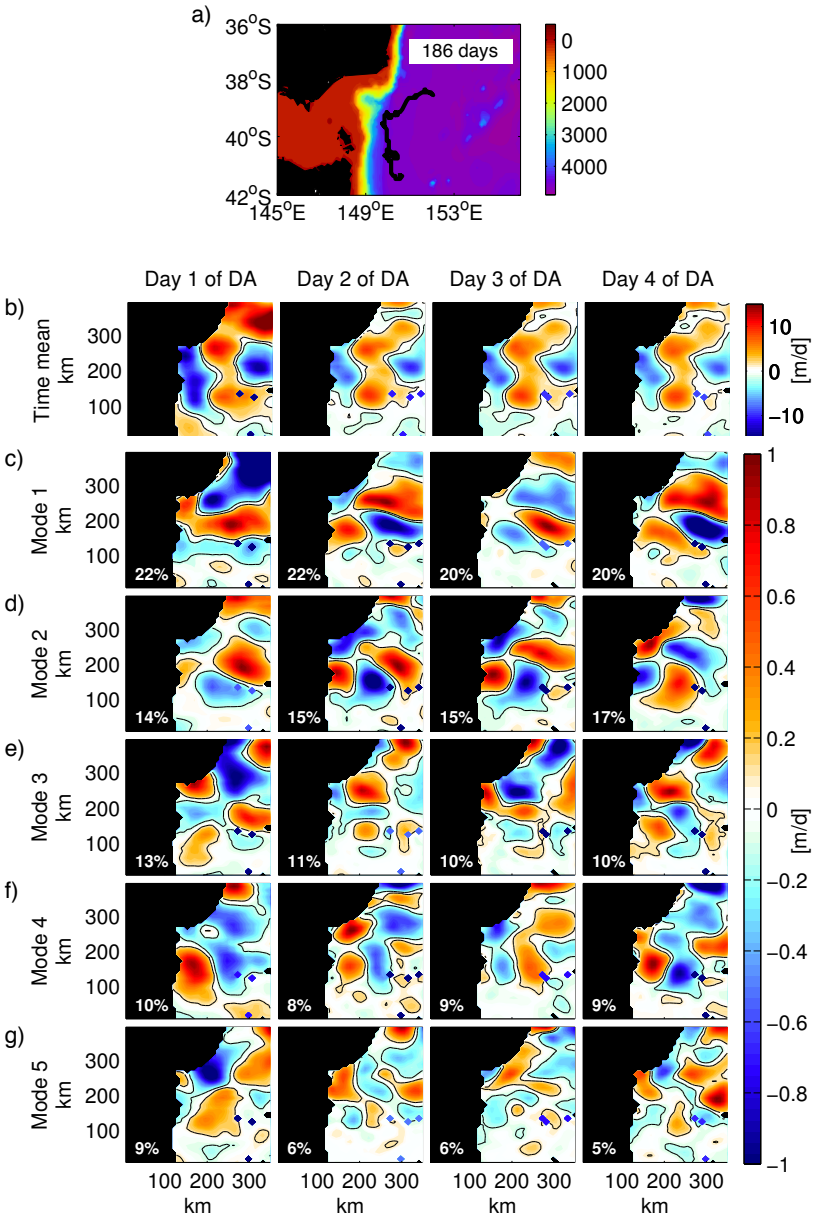


FIGURE 5.11: As in Figure 5.10, but for an anticyclonic eddy propagating southwards in the Tasman Sea.

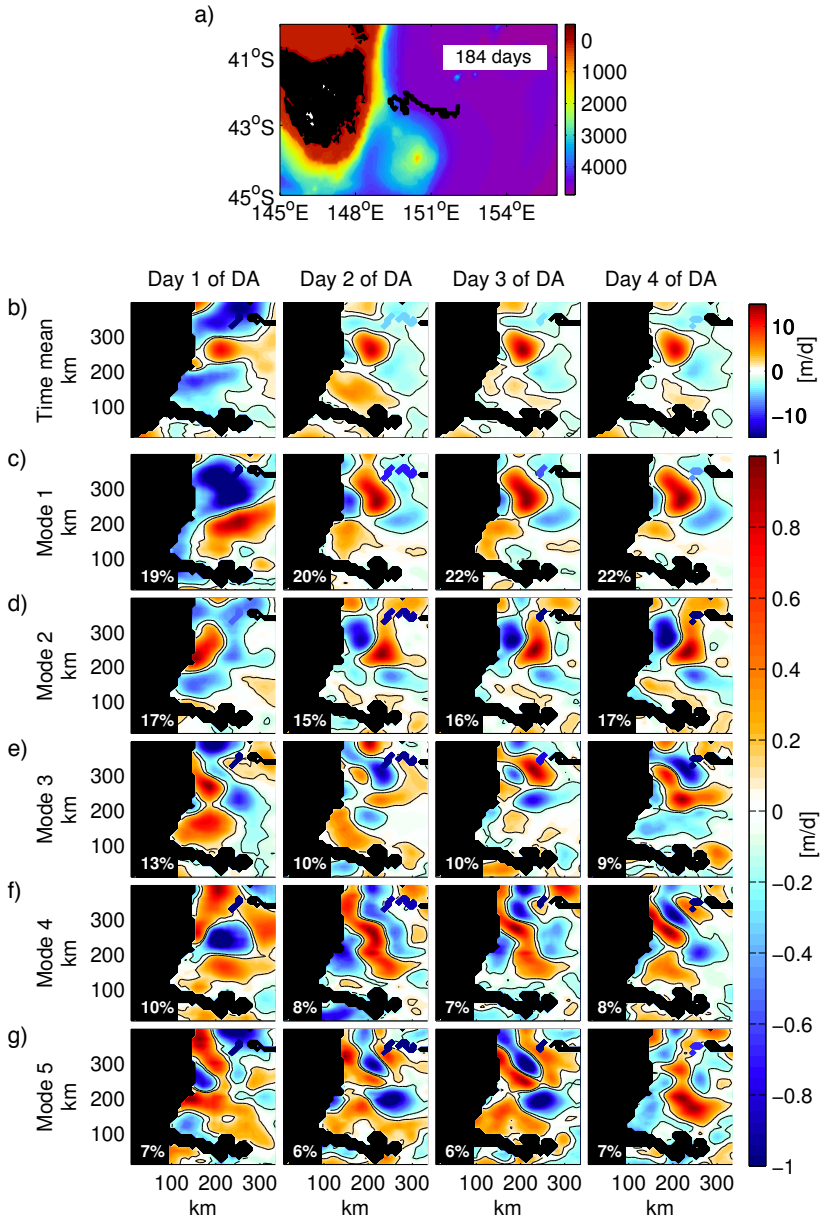


FIGURE 5.12: As in Figure 5.10, but for a cyclonic eddy propagating eastwards in the Tasman Sea.

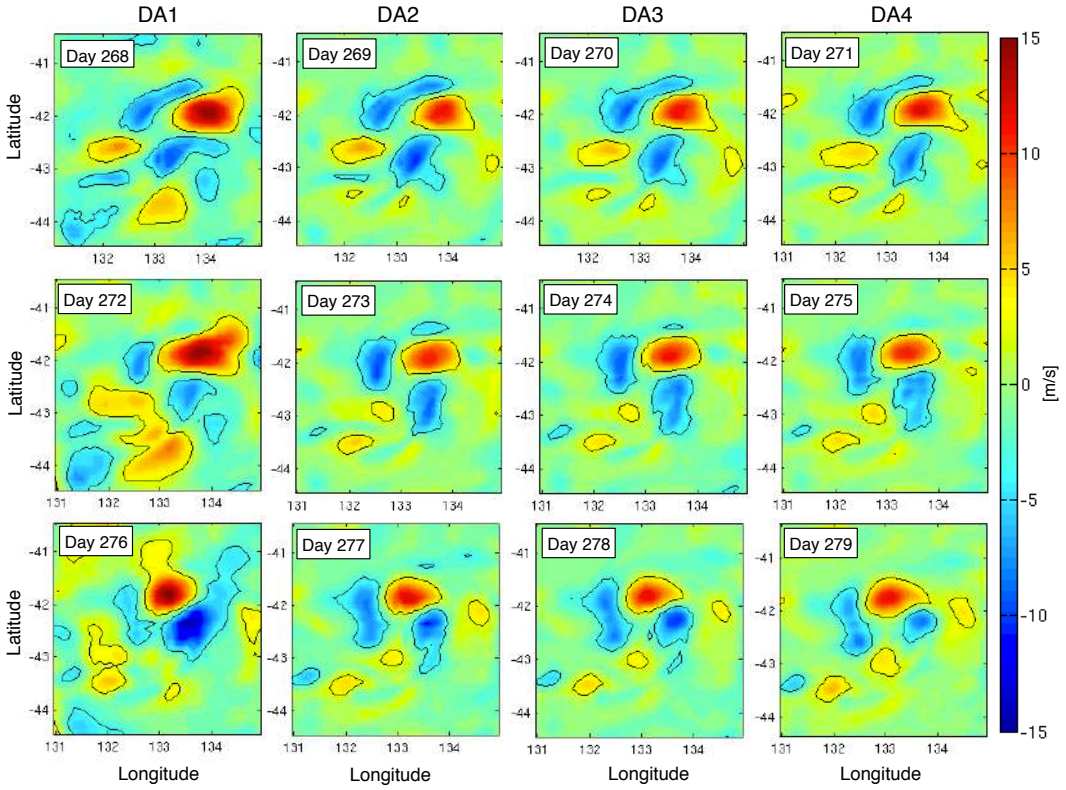


FIGURE 5.13: Daily averages of depth-averaged vertical velocity associated with an anticyclonic eddy of the data-assimilating model (BRAN3p5). Each column relates to the first (DA1), second (DA2), third (DA3), and fourth (DA4) days after data assimilation.

From the analysis of vertical velocity in the data-assimilating model, it is possible to conclude that the model's response to DA is consistent with an artificial eddy distortion. The timescales on which eddies distort in a free-running model, and in the ocean (from altimetry, for example) are about a week (Figure 4.5 and Brassington, 2010). But in the case of a data-assimilating model, the changes are introduced in a single timestep. That is, the changes are imposed artificially over a 5-minute period. This may explain why the amplitude of the dominant modes of vertical velocity are often greater - and the alternating cells pattern is less clear - in DA1, compared to DA2, DA3, and DA4. The impact of data-assimilation is clearly seen in the time-evolution of the vertical velocity field associated with an eddy in the model (Figure 5.13). At the end of each assimilation cycle, the alternating cell pattern is clear, but is then affected by updates to the model (e.g., between days 271 and 272 in Figure 5.13).

Next, I wish to quantify the degree to which the vertical velocities associated with the artificial eddy distortion alter the model's T and S fields. Recall that during the DA process, the model's T, S, $u$, and $v$ are updated with an "analysis". The analysis is constructed by combining the model fields before assimilation, and the observations

at their relevant time and space. Ideally, for a data-assimilating model, the model dynamically evolves the ocean state, seamlessly integrating forward in time from the analysed initial conditions. In practice, owing to dynamical imbalances of the analyses (i.e., the analyses are not a precise solution to the model equations), the model undergoes a period of adjustment. The analyses above show that this adjustment for vertical velocity is rather significant. This must impact T and S through vertical advection. This advection is larger than it should be, because of the model adjustment to DA previously described in Section 5.2 and shown in Figure 5.1. If the vertical velocity on DA1 is conservatively assumed to be entirely associated with the artificial eddy distortion, the impacts of this artificial change on T and S can be estimated. That is, how much the large-amplitude vertical velocity causes the model T and S fields to depart from the imposed analyses can be estimated. With this analysis, I seek to estimate how much the model adjustment takes the model's T and S fields away from the calculated analyses - which are meant to best match observations. That is - how much the model adjustment degrades the model.

Fields of the vertical advection of T (using the term $w\frac{dT}{dz}$) and vertical advection of S (using $w\frac{dS}{dz}$; Figures 5.14, 5.15, and 5.16) are analysed. The pattern of depth-averaged $w\frac{dT}{dz}$ has the same spatial distribution as the pattern of depth-averaged vertical velocity (Figures 5.14a-b, 5.15a-b, and 5.16a-b). This pattern is coherent, and typically of the same sign, throughout the water column (Figures 5.14d, 5.15d, and 5.16d). By contrast, the pattern of depth-averaged $w\frac{dS}{dz}$ is less clear (Figures 5.14c, 5.15c, and 5.16c). This is because the sign of $w\frac{dS}{dz}$ changes at mid-depth (Figures 5.14e, 5.15e, and 5.16e), owing to the presence of intermediate water, which has a sub-surface salinity minima.

Additionally, the vertical advection terms, with units of $^{\circ}C/d$ and $psu/d$, is converted into T and S changes over a day by simply multiplying $w\frac{dT}{dz}$ and $w\frac{dS}{dz}$ by time (resulting in units of $^{\circ}C$ and $psu$). This allows for a direct comparison of the changes associated with vertical advection, given by the model adjustment, with the increments applied to the model during the assimilation step. That is, I can determine whether the artificial changes due to the model adjustment are bigger, or smaller, than the changes due to assimilation. For this comparison, the RMS of volume-averaged T and S changes over a day associated with the model adjustment (Figure 5.17, thin lines) and with the increments applied to the model (Figure 5.17, bold lines) for the three case studies are calculated.

The RMS of $\Delta T$ and $\Delta S$ due to the model adjustment clearly spikes on the first days of each assimilation cycle (thin lines in Figure 5.17). On average, the magnitude of the RMS of these properties in DA1 is 1.5 times larger than in DA2-DA4, for all eddies. This high RMS amplitude in DA1, above the DA2-DA4 time series, is attributable

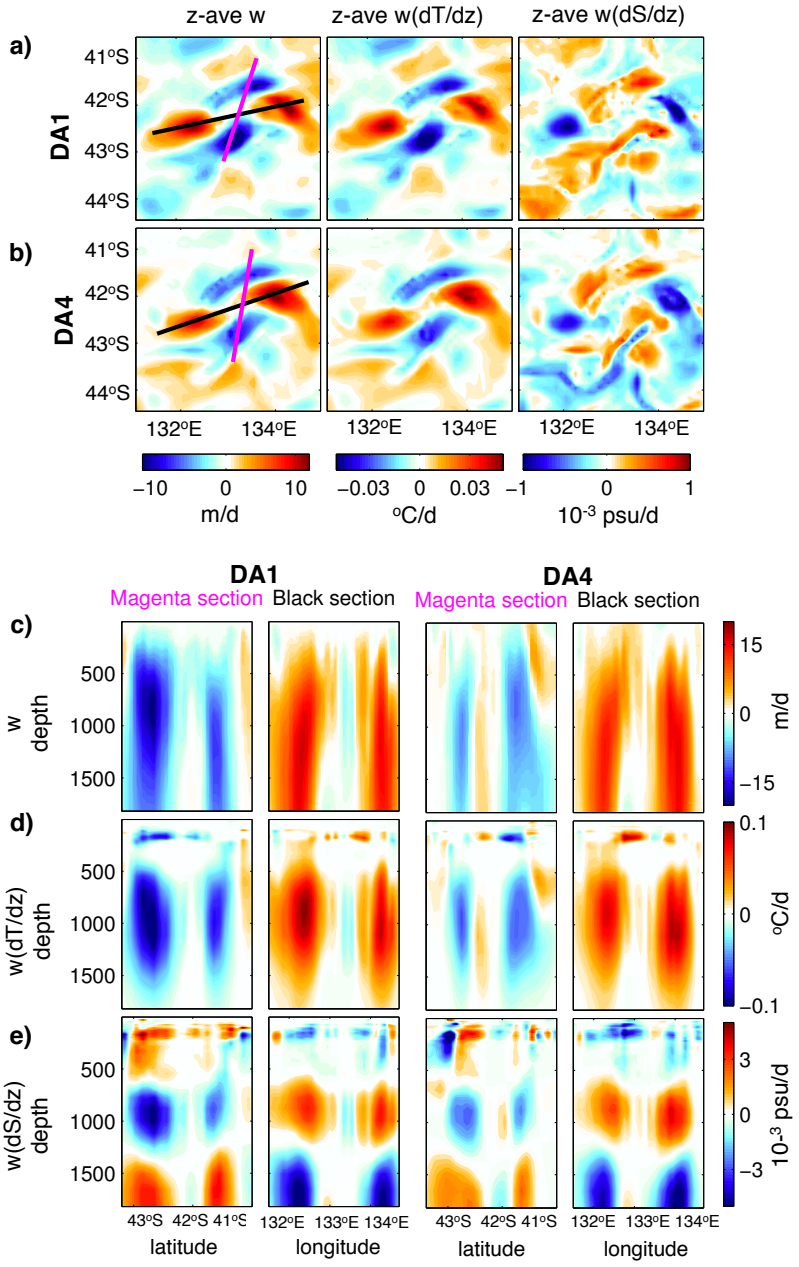


FIGURE 5.14: a) Daily averages of depth-averaged (0-2000 m) vertical velocity (left), $w\frac{dT}{dz}$ (centre), and $w\frac{dS}{dz}$ (right) of an anticyclonic eddy propagating westwards in the Eastern Indian Ocean (Figure 5.10) on the first day after DA (DA1); b) same as in (b), but for the fourth day after DA (DA4); c) vertical sections of vertical velocity in DA1 (first two columns) and in DA4 (last two columns). Magenta and black sections are shown in first column of (a) and (b); d) same as in (c), but for $w\frac{dT}{dz}$; e) same as in (c), but for $w\frac{dS}{dz}$.

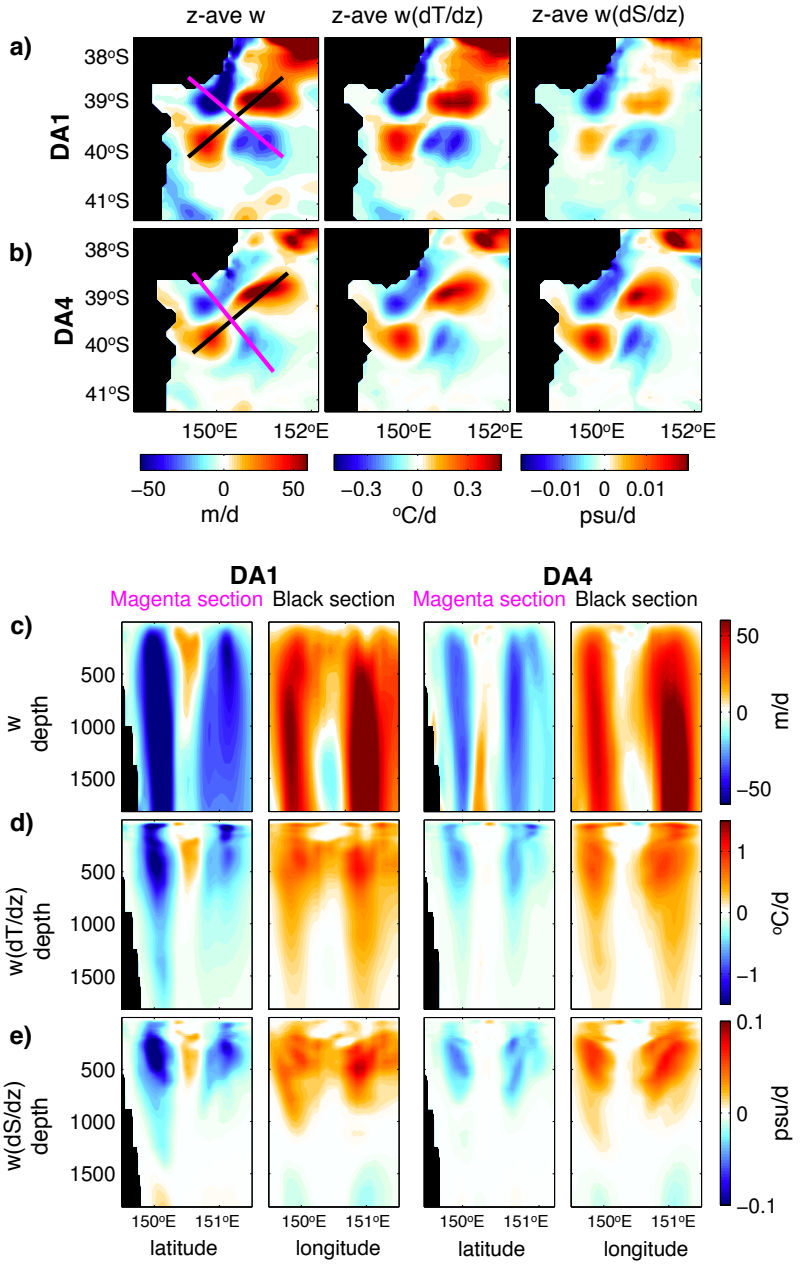


FIGURE 5.15: As in Figure 5.14, but for an anticyclonic eddy propagating southwards in the Tasman Sea.

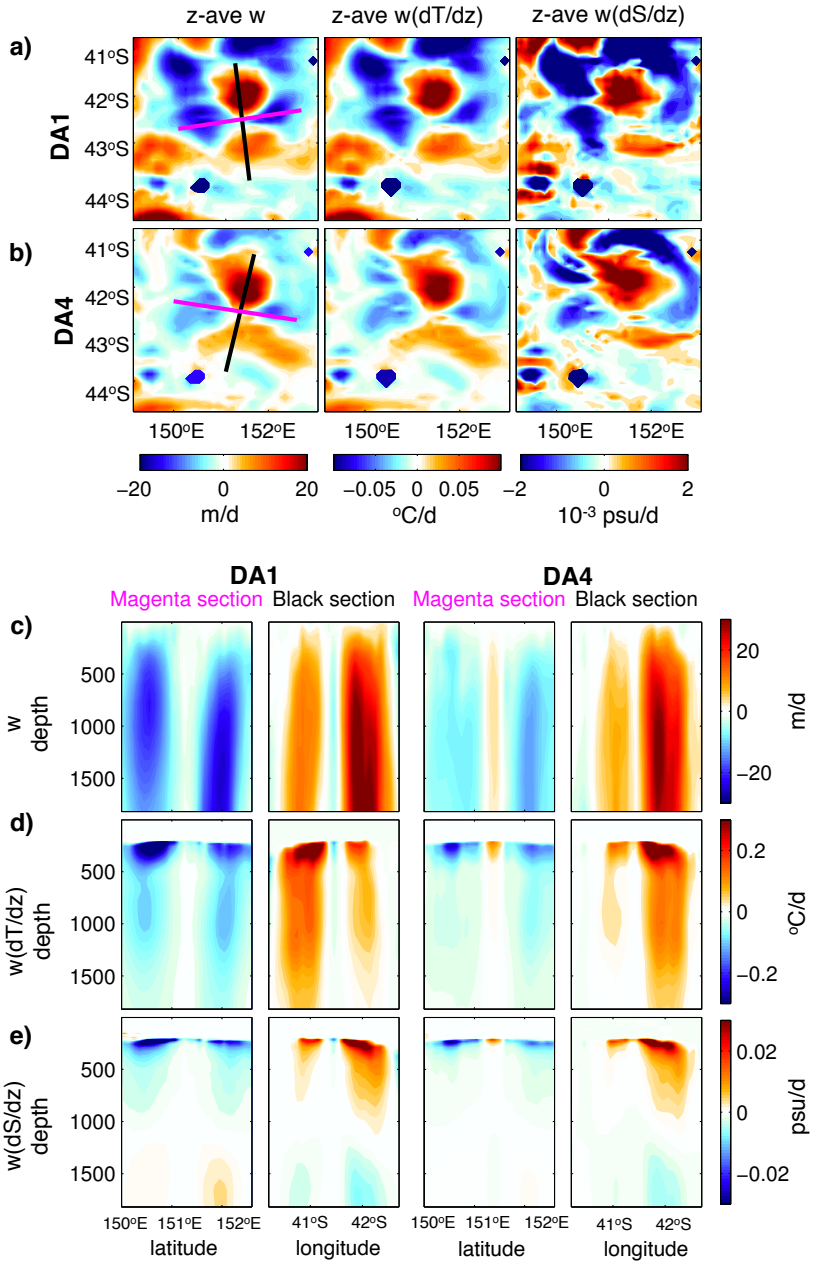


FIGURE 5.16: As in Figure 5.14, but for a cyclonic eddy propagating eastwards in the Tasman Sea.

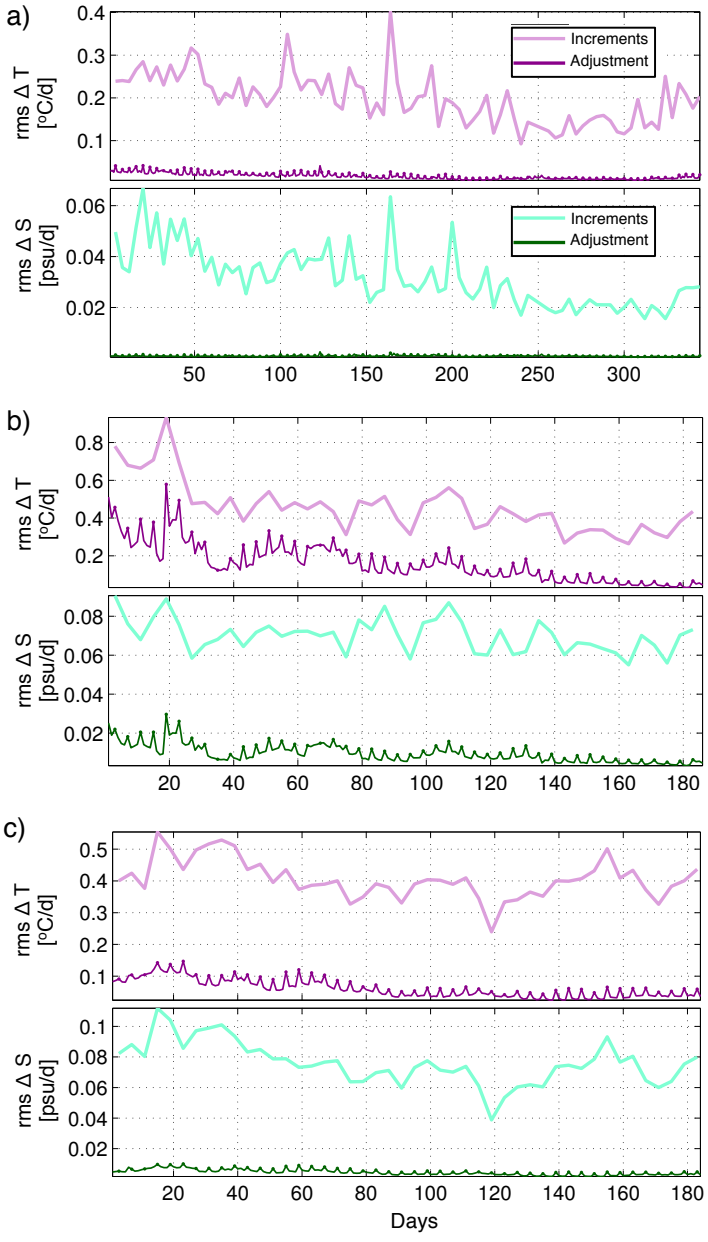


FIGURE 5.17: Time series of the RMS of the volume-averaged vertical advection of temperature (top, purple) and salinity (bottom, green) for a) a westward-propagating anticyclonic eddy, b) a southward-propagating anticyclonic eddy, and c) an eastward-propagating cyclonic eddy. Thin lines are volume-averaged model adjustment. Bold lines are volume-averaged increments applied during DA.

to an amplified vertical advection associated with the model adjustment to DA. This adjustment is largest in example Figure 5.17b - the southward propagating anticyclonic eddy - where the amplified vertical advection after DA is about the same amplitude as the vertical advection in between DA cycles.

Despite the effect of the DA in DA1, the RMS of the model adjustment is still 2 to 10 times smaller than the RMS of the increment (bold lines in Figure 5.17). Sometimes, however, the model adjustment and the increments may have the same RMS magnitude (e.g., around day 20 in Figure 5.17b). Therefore, even with the impact of DA on the vertical velocity within eddies in DA1, the model adjustment of both T and S is still smaller than the increments of T and S applied during update. This analysis indicates that the changes to T and S during the period of model adjustment are small compared to the changes to T and S during the model update (when the increments are applied in each assimilation step).

The key message in Figure 5.17 is that the vertical advection of T and S in the first day after assimilation is higher than in the other days of the cycle. However, even though the vertical advection in DA1 is high, it is not as high as the increments of T and S applied to the model. These results are also shown in Figures 5.18 and 5.19 in the RMS of a vertical section of T and S, and in the RMS of depth-averaged T and S, for all three case studies.

## 5.4 Discussion

The horizontal velocity in a data-assimilating model is expected to adjust on time-scales of one inertial period or longer (the inertial period in this region is close to one day). The time-scales for the adjustment of vertical velocity is less clear. To a large extent, the results show that the vertical velocity appears to adjust within one day. Therefore, this study indicates that vertical velocity in the model adjusts faster than the horizontal velocities.

The upward and downward cells associated with eddy distortion develop on time-scales of about a week (Figure 4.5 and Brassington, 2010), which is much longer that the time-scales of model adjustments after DA. This suggests that analyses of vertical velocity in data-assimilating models may provide meaningful insights into ocean dynamics, provided the adjustment periods are disregarded. That is, care should be taken when using vertical velocities immediately after assimilation.

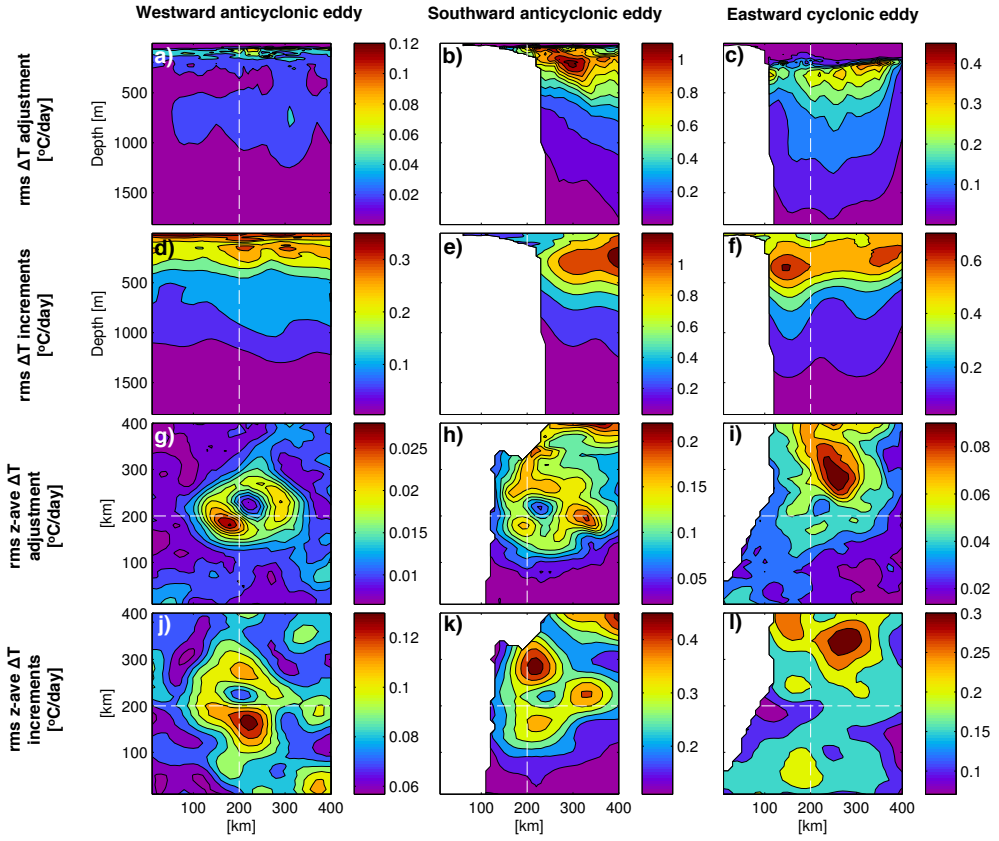


FIGURE 5.18: RMS of the vertical advection of temperature in a vertical section associated with the model's adjustment (a, b, and c) and with increments applied to the model (d, e, and f); RMS of the depth-averaged vertical advection of temperature associated with the model's adjustment (g,h, and i) and with the increments applied to the model (j, k, and l). The dashed white line indicates the eddy centre. Each column refers to a different eddy, identified at the top of the figure.

The upward and downward cells are seen in all dominant modes of the depth-averaged vertical velocity EOFs. Sometimes, however, this pattern is less evident in EOFs considering only the first days after the update (i.e., DA1). This is because in DA1, the eddy distorts artificially, while in DA2, DA3, and DA4, the eddy distorts in a way that is dynamically consistent. In a dynamically consistent ocean, the eddy often distorts inwards in one axis and outwards in the other axis (e.g., inwards in latitude and outwards in longitude; Figures 4.8 and 4.13). Consequently, the loss of volume caused by the inward distortion is mostly compensated by the gain of volume in the outward distortion. An artificial eddy distortion, caused by an artificial update to the model, is more complicated than a natural distortion. During the update, the eddy shape may change completely, with large imbalances introduced, resulting in an adjustment of the model with large changes in amplitude. This artificial eddy distortion may induce a different number of vertical velocity cells at each update, and suddenly change the eddy amplitude and position. Therefore, an artificial eddy distortion seems to add a lot of

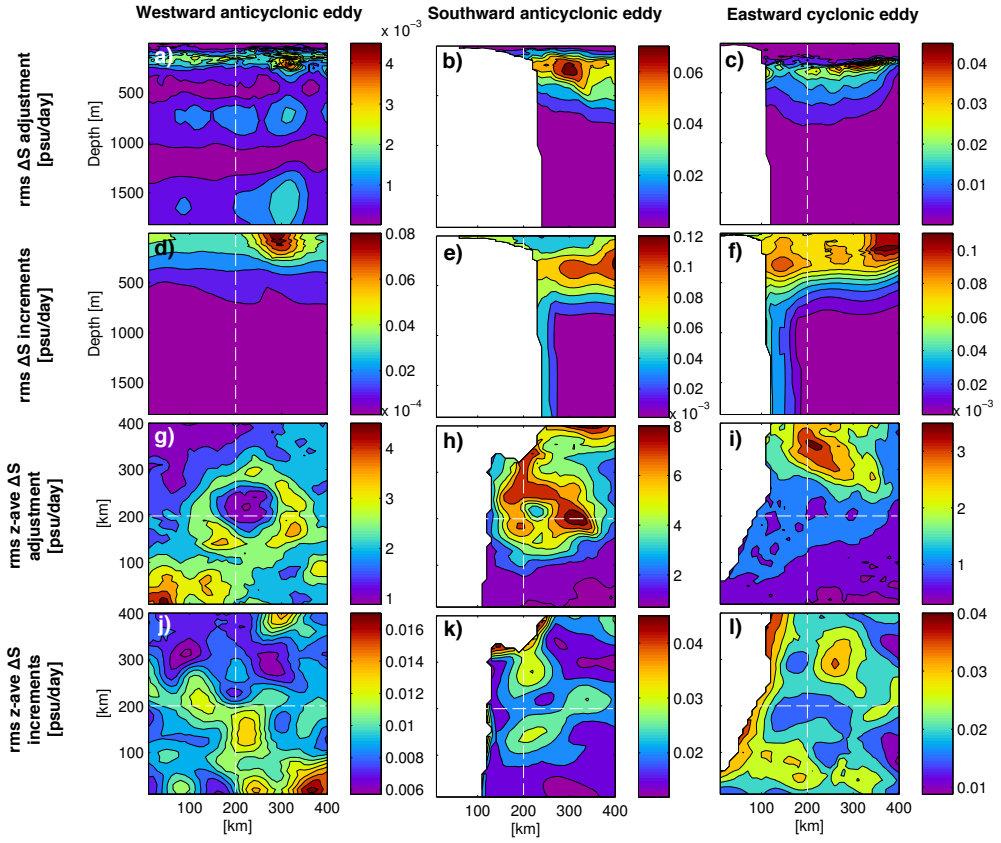


FIGURE 5.19: As in Figure 5.18, but for salinity

noise to the upward and downward cells, disrupting these patterns on the day after the update.

Because of the stronger vertical velocities in DA1, the vertical advection of T and S is 1.5 times greater than in DA2, DA3, and DA4. These higher values in DA1 are here attributed to the impact of artificial eddy distortion only. This is an over-estimate of the impact of artificial eddy distortion. On DA1, the vertical velocity is comprised of two components: one due to the model's artificial adjustment (associated here with artificial eddy distortion), and one due to the model's dynamical variability. It is not straightforward to separate these components. However, it is possible to conclude that the larger-amplitude vertical advection after each assimilation step is attributable to the artificial adjustment of the model. This artificial adjustment causes the model's T and S fields to depart from the imposed analysed T and S fields - thereby degrading the reanalysis. To determine how significant this adjustment is, these changes are compared to the changes explicitly imposed during the assimilation step - the increments. As a result, the increments of T applied to the data-assimilating model during update are up to 5 times larger than the values associated with the model adjustment. In the case of S, the increments are up to 16 times larger than the model adjustment.

However, increments and the model adjustments sometimes have the same magnitude. This indicates that, although the T and S fields degrade after each assimilation step, this degradation is not particularly significant. As systems of DA continue to improve, and as methods for constructing analyses that are more dynamically consistent are developed, this degradation is expected to decrease.

## 5.5 Conclusion

In the version of BRAN analysed here (BRAN3p5; Oke et al., 2008), I find that the response of horizontal velocities to DA are relatively small - with no clear change to time series of EKE, for example. By contrast, the amplitudes of the vertical velocities on the day immediately after assimilation are typically 2 times greater than the vertical velocities at 2, 3, or 4 days after assimilation.

The data-assimilating model reproduces patterns of vertical velocity, associated with eddy distortion, that are comparable to the patterns generated by a free-running model (with no DA). Furthermore, the amplitude of vertical velocity EOF modes showing the eddy-distortion patterns is often greater immediately after assimilation. This leads to the conclusion that the model adjustment to the introduced changes at the time of assimilation is consistent with an artificial eddy distortion.

Analyses of the vertical velocities in the model indicate that the impact of this artificial eddy distortion on the model's T and S fields is typically smaller than the increments applied during the assimilation process itself.

Three case studies of eddies that are representative of the study region are chosen for the analysis. This allows a detailed examination of each case study. The results shown here would benefit from analysis of a larger sample of eddies, and in different oceanic regions.

I was motivated to determine whether a data-assimilating model could reliably be used to examine dynamical processes. Noting the artificial response of the vertical velocity immediately after assimilation, it is possible to conclude that such analyses should be undertaken with caution. Indeed, unlike free-running models, data-assimilating models generally reproduce more realistic variability, with ocean features in approximately the right place and time - but they also are plagued with the problem of dynamical imbalance. These factors should be carefully considered before employing results from a data-assimilating model to understand dynamical processes of the ocean. Furthermore, I hope that the results of this study motivate the ocean DA community to continue developing dynamically-consistent methods for DA.

# Chapter 6

# Summary and Conclusions

The focus of this thesis is on the three-dimensional structure and evolution of EAC eddies. The specific goals are to better understand the pathway of EAC anticyclonic eddies, their spatial and temporal changes of the three-dimensional properties, and the vertical circulation within EAC eddies. In particular, this thesis focuses on large, long-lived anticyclonic eddies that form at the EAC separation region (Figure 1.2, Chapter 1). Most of the results presented here are based on the output from a global, eddy-resolving ocean model (Chapter 2, Section 2.2.1). Although models have many limitations (Chapter 2, Section 2.2.2), they provide a complete picture of the three-dimensional, time-varying ocean circulation - including all relevant variables. Noting these limitations, the key aspects of the ocean model circulation, most relevant to this thesis, are verified against observational products (Chapter 3, Section 3.2.1).

Most recent studies of eddies undertake statistical analyses of a large number of eddies (e.g., Chaigneau et al., 2008, Chelton et al., 2011b, Everett et al., 2012, Petersen et al., 2013, Rykova et al., 2017, Amores et al., 2017). Many of these studies exploit databases generated using automated eddy-tracking algorithms (e.g., Chaigneau et al., 2008, Chelton et al., 2011b, Faghmous et al., 2015). Advantages of such databases include their global coverage and their large sample of eddies. Such studies mostly analyse mean fields or composite fields to quantify "typical" eddy properties. These approaches, however, inevitably eliminate details - that are the focus of this thesis.

To better address the above-stated goals, the analysis performed here is, instead, focussed on a relatively small number of case studies. This means that a careful investigation of the circulation patterns within each eddy, to identify recurrent and robust features, could be undertaken. Results from this investigation are presented in Chapters 3, 4, and 5 of this thesis. Additionally, the choice of analysing a small number of case studies means that I can afford to manually track each eddy (Chapter 2, Section 2.4.2).

This manual eddy-tracking results in a more robust and reliable database (Chapter 2, Section 2.4.2, and Chapter 3, Section 3.2.1).

Another aspect of this thesis, that is somewhat unique, is the method of analysis. For each case study, the eddies are manually tracked - as noted above - and a three-dimensional ocean model "data cube" is extracted, for each timestep of the track of each eddy (Chapter 2, Section 2.4.3). Then, the pathway (Chapter 3), properties (Chapters 3, 4, and 5), and circulation (Chapters 4 and 5) of each case study are investigated in detail, in a reference frame that follows the trajectory of each eddy.

To study the pathway of large, long-lived EAC anticyclonic eddies, both satellite data and ocean model fields are analysed in Chapter 3. This analysis shows that many eddies propagate southwards, from their origin near the EAC separation region, around Tasmania, and leave the Tasman Sea (Chapter 3, Section 3.2.1). They then decay in the Eastern Indian Ocean. This pathway has not been previously documented. Results also show that, as eddies propagate southwards, they often "stall" off south-eastern Australia for several months at near-constant latitudes. The reason for this is not completely clear, but the "stalling" seems to be related to the orientation of the coast and the tendency for eddies to propagate westwards (e.g., Cushman-Roisin et al., 1990, van Leeuwen, 2007, Morrow, 2004, Morrow and Le Traon, 2012, Chapter 3, Section 3.2.1). I also find that, along the pathway, eddies become increasingly barotropic, that their intensity is primarily influenced by merging with other eddies, and that they gradually decay in the absence of eddy-eddy interactions (Chapter 3, Section 3.2.3).

The results from Chapter 3 provide insights into the structural changes of eddies as they propagate along two different regimes: the energetic Tasman Sea, and the quiescent Eastern Indian Ocean.

The evolution of EAC anticyclonic eddies in the Tasman Sea may resemble the evolution of eddies in other WBCs, especially the Brazil Current (BC). The BC separates from the coast similarly to the EAC, forming a meander, and occasionally shedding an anticyclonic eddy (e.g., Olson, 1991, Campos and Olson, 1991, Matano, 1993). The eddies shed by the BC then propagate within the Argentine Basin, a deep region restrained by bathymetry, with high EKE (e.g., Lentini et al., 2006, Saraceno and Provost, 2012, Pilo et al., 2015) - also similar to the Tasman Sea. The BC eddies have received less attention that eddies from other WBCs, with only a few studies describing the three-dimensional structure of averaged BC eddies (e.g., Rykova et al., 2017, Mason et al., 2017). I believe that the study method used in this study (i.e., manually tracking eddies and extracting "data cubes" from an ocean model) would be of great value for investigating the propagation, properties, and evolution of BC eddies. In addition, I suspect that several aspects of the

evolution of EAC eddies - as their recurrent merging, bathymetric steering, and loss of baroclinicity - are also present in BC eddies.

The evolution of EAC anticyclonic eddies in the Eastern Indian Ocean is expected to resemble the evolution of other eddies that freely propagate westwards. Examples of such eddies are the Agulhas Rings (e.g. Schouten et al., 2000), the Leeuwin Current eddies (e.g., Morrow, 2004), the Meddies in the North Atlantic (e.g., Bower et al., 1997), the California Undercurrent eddies (e.g., Pelland et al., 2013), and the Peru-Chile Current eddies (e.g., Chaigneau et al., 2011). Many of these eddies have been reported to have a sub-surface core, similar to the EAC anticyclonic eddies shown in Chapter 3 (Zhang et al., 2014, , and references therein). This suggests that the evolution of EAC eddies in the Eastern Indian Ocean might be similar to the evolution of eddies formed at eastern boundary regions.

An investigation of the vertical velocities within EAC anticyclonic eddies shows alternating upward and downward cells (e.g., Figure 4.6; Chapter 4, Section 4.3.1). These cells have been reported in previous studies (e.g., Martin and Richards, 2001, Nardelli, 2013), but have never been fully explained. One of the main findings of this thesis is to provide a dynamical explanation for these alternating upward and downward cells - and to link the generation of these cells to "eddy distortion". Here, eddy distortion is defined as the change in shape of an eddy (i.e., when an eddy becomes more, or less, isotropic). Eddy distortion can be quantified by considering temporal changes of SLA (e.g., differences between weekly SLA maps of gridded altimetry or model fields). I show that mesoscale changes in SLA are correlated with the vertical motion within eddies, and that the alternating cells pattern explains 30-60% of the variance of vertical velocity within these eddies (Chapter 4, Section 4.3.3). In anticyclonic eddies in the Southern Hemisphere, I show that an inward distortion is associated with upward motion and an outward distortion is associated with downward motion (Figure 4.13; Chapter 4, Section 4.4). Here, two mechanisms that link eddy distortion to vertical velocity are proposed. One mechanism relates to changes in stratification and relative vorticity in the eddy interior. The other mechanism, relates to the divergence of the horizontal flow in different quadrants of the eddy. In each case study, there is evidence for both mechanisms generating the alternating upward and downward cells (Chapter 4, Section 4.4.1). I suspect that both mechanisms explain the upward and downward cells at different times.

In Chapter 5 of this thesis, I investigate the extend to which a data-assimilating ocean model can reproduce the alternating upward and downward cells mentioned. Here, the disruption to the model's dynamical balance is assumed to degrade the vertical velocity fields - rendering the model inappropriate for studies of model dynamics (Chapter 5, Section 5.1, see also discussion in Oke and Griffin, 2011). Indeed, this is a common

presumption amongst the data assimilation community (e.g., Matear and Jones, 2011, Oke and Griffin, 2011). Results show that the alternating cells pattern is present within eddies of the data-assimilating ocean model (Chapter 5, Section 5.3). Additionally, the results confirm that data assimilation can significantly impact eddy dynamics (Chapter 5, Section 5.3). In fact, the vertical velocities in the reanalysed eddies - generated by the data-assimilating model - are particularly sensitive to assimilation. Moreover, results show that the ocean model's response to data assimilation is like an artificial eddy distortion - sometimes even amplifying the vertical velocities in each eddy (Chapter 5, Section 5.3). Data assimilation is often a necessary element of any forecast or reanalysis system (e.g., to initialise chaotic features, such as eddies). At the end of Chapter 5 I conclude that, despite the negative impact of data assimilation on the dynamical balances of a model, results from such model could be used for dynamical analyses. These dynamical analyses should be, however, undertaken carefully, and the role and impact of data assimilation on the relevant fields should be fully quantified.

The findings of this thesis were only possible due to the use of case studies to understand eddy properties. Had mean fields from a large sample of eddies been analysed, the details of the circulation within each eddy - which are the focus here - would have been lost. I recognise that the conclusions drawn from this thesis could be strengthened by analysing a larger sample of eddies. This is intended for a future study. Similarly, analysis of the detailed eddy properties in other regions (e.g., other WBCs) is also a topic worthy of attention.

One of the most exciting prospects that stem from this work is the potential to use maps of SLA to infer vertical velocities within eddies on a global scale. I expect that SLA maps of gridded altimetry could be used to efficiently generate a metric for eddy distortion. If such a metric could be linked to vertical velocities - expected to be regionally and seasonally varying - then developing new metrics for other important ocean properties could be within reach. For example, with a metric of vertical velocity in hand, satellite ocean colour measurements could be used to better quantify primary production (including vertical exchange) on global scales. Similarly, in combination with *in situ* observations (e.g., from Argo floats), the vertical transport of heat and freshwater could be more accurately inferred. These developments require much additional research - but may lead to a transformational change in the field of oceanography, linked to the new generation of satellite altimeter missions, such as the Sentinel-3A, the SWOT, and the Jason-CS missions.

# Bibliography


Allen, J., Smeed, D., Nurser, A., Zhang, J., and Rixen, M. (2001). Diagnosis of vertical velocities with the QG omega equation: an examination of the errors due to sampling strategy. *Deep Sea Research Part I: Oceanographic Research Papers*, 48(2):315–346.

Alpine, J. E. and Hobday, A. J. (2007). Area requirements and pelagic protected areas: is size an impediment to implementation? *Marine and Freshwater Research*, 58(6):558.

Amores, A., Melnichenko, O., and Maximenko, N. (2017). Coherent mesoscale eddies in the North Atlantic subtropical gyre: 3-D structure and transport with application to the salinity maximum. *Journal of Geophysical Research: Oceans*, 122(1):23–41.

Andrade, C. A. and Barton, E. D. (2000). Eddy development and motion in the Caribbean Sea. *Journal of Geophysical Research: Oceans*, 105(C11):26191–26201.

Andrews, J. C., Lawrence, M. W., and Nilsson, C. S. (1980). Observations of the Tasman Front. *Journal of Physical Oceanography*, 10:1854 – 1869.

Andrews, J. C. and Scully-Power, P. (1976). The Structure of an East Australian Current Anticyclonic Eddy. *Journal of Physical Oceanography*, 6:756 – 765.

Arhan, M., Speich, S., Messager, C., Dencausse, G., Fine, R., and Boye, M. (2011). Anticyclonic and cyclonic eddies of subtropical origin in the subantarctic zone south of Africa. *Journal of Geophysical Research*, 116(C11):C11004.

Baird, M. E. and Ridgway, K. R. (2012). The southward transport of sub-mesoscale lenses of Bass Strait Water in the centre of anti-cyclonic mesoscale eddies. *Geophysical Research Letters*, 39(2):1944–8007.

Baird, M. E., Suthers, I. M., Griffin, D. A., Hollings, B., Pattiaratchi, C., Everett, J. D., Roughan, M., Oubelkheir, K., and Doblin, M. (2011). The effect of surface flooding on the physical–biogeochemical dynamics of a warm-core eddy off southeast Australia. *Deep Sea Research Part II: Topical Studies in Oceanography*, 58(5):592–605.

Beal, L. M., Hummon, J. M., Williams, E., Brown, O. B., Baringer, W., and Kearns, E. J. (2008). Five years of Florida Current structure and transport from the Royal

Caribbean Cruise Ship Explorer of the Seas. *Journal of Geophysical Research*, 113(C6):C06001.

Biastoch, A. and Krauss, W. (1999). The Role of Mesoscale Eddies in the Source Regions of the Agulhas Current. *Journal of Physical Oceanography*, 29(9):2303–2317.

Bingham, R. J., Haines, K., and Lea, D. J. (2014). How well can we measure the ocean's mean dynamic topography from space? *Journal of Geophysical Research: Oceans*, 119(6):3336–3356.

Boebel, O., Lutjeharms, J., Schmid, C., Zenk, W., Rossby, T., and Barron, C. (2003). The Cape Cauldron : a regime of turbulent inter-ocean exchange. *Deep-Sea Research Part II*, 50:57–86.

Boland, F. M. and Church, J. A. (1981). The East Australian Current 1978. *Deep Sea Research*, 28A(9):937–957.

Booth, J. and Kamenkovich, I. (2008). Isolating the role of mesoscale eddies in mixing of a passive tracer in an eddy resolving model. *Journal of Geophysical Research: Oceans*, 113(5).

Bouffard, J., Vignudelli, S., Herrmann, M., Lyard, F., Marsaleix, P., Ménard, Y., and Cipollini, P. (2008). Comparison of Ocean Dynamics with a Regional Circulation Model and Improved Altimetry in the North-Western Mediterranean. *Terrestrial, Atmospheric and Oceanic Sciences*, 19(1-2):117.

Bowen, M. M., Wilkin, J. L., and Emery, W. J. (2005). Variability and forcing of the East Australian Current. *Journal of Geophysical Research*, 110(C3):C03019.

Bower, A. S., Armi, L., and Ambar, I. (1997). Lagrangian Observations of Meddy Formation during A Mediterranean Undercurrent Seeding Experiment. *Journal of Physical Oceanography*, 27(12):2545–2575.

Brannigan, L. (2016). Intense submesoscale upwelling in anticyclonic eddies. *Geophysical Research Letters*, 43(7):3360–3369.

Brassington, G. B. (2010). Estimating surface divergence of ocean eddies using observed trajectories from a surface drifting buoy. *Journal of Atmospheric and Oceanic Technology*, 27(4):705–720.

Brassington, G. B., Summons, N., and Lumpkin, R. (2011). Observed and simulated Lagrangian and eddy characteristics of the East Australian Current and the Tasman Sea. *Deep Sea Research Part II: Topical Studies in Oceanography*, 58(5):559–573.

Bryden, H. L., Beal, L. M., and Duncan, L. M. (2005). Structure and transport of the Agulhas current and its temporal variability. *Journal of Oceanography*, 61(3):479–492.

Calado, L., da Silveira, I., Gangopadhyay, A., and de Castro, B. (2010). Eddy-induced upwelling off Cape Sao Tome (22S, Brazil). *Continental Shelf Research*, 30(10-11):1181–1188.

Campos, E. J. D. and Olson, D. B. (1991). Stationary Rossby Waves in Western Boundary Current Extensions. *Journal of Physical Oceanography*, 21:1202 – 1224.

Cetina-Heredia, P., Roughan, M., van Sebille, E., and Coleman, M. A. (2014). Long-term trends in the East Australian Current separation latitude and eddy driven transport. *Journal of Geophysical Research: Oceans*, pages n/a–n/a.

Chaigneau, A., Eldin, G., and Dewitte, B. (2009). Eddy activity in the four major upwelling systems from satellite altimetry (1992–2007). *Progress in Oceanography*, 83(1-4):117–123.

Chaigneau, A., Gizolme, A., and Grados, C. (2008). Mesoscale eddies off Peru in altimeter records: Identification algorithms and eddy spatio-temporal patterns. *Progress in Oceanography*, 79(2-4):106–119.

Chaigneau, A., Le Texier, M., Eldin, G., Grados, C., and Pizarro, O. (2011). Vertical structure of mesoscale eddies in the eastern South Pacific Ocean: A composite analysis from altimetry and Argo profiling floats. *Journal of Geophysical Research*, 116(C11):C11025.

Chapman, R. and Nof, D. (1988). The Sinking of Warm-Core Rings. *Journal of Physical Oceanography*, 18:565 – 583.

Chassignet, E. P., Hurlburt, H. E., Smedstad, O. M., Halliwell, G. R., Hogan, P. J., Wallcraft, A. J., Baraille, R., and Bleck, R. (2007). The HYCOM (HYbrid Coordinate Ocean Model) data assimilative system. *Journal of Marine Systems*, 65(1-4):60–83.

Chelton, D. B. (2013). Mesoscale eddy effects. *Nature Geoscience*, 6(8):594–595.

Chelton, D. B., Gaube, P., Schlax, M. G., Early, J. J., and Samelson, R. M. (2011a). The influence of nonlinear mesoscale eddies on near-surface oceanic chlorophyll. *Science (New York, N.Y.)*, 334(6054):328–32.

Chelton, D. B., Schlax, M. G., Freilich, M. H., and Milliff, R. F. (2004). Satellite Measurements Reveal Persistent Small-Scale Features in Ocean Winds. *Science*, 303(February):978–983.

Chelton, D. B., Schlax, M. G., and Samelson, R. M. (2011b). Global observations of nonlinear mesoscale eddies. *Progress in Oceanography*, 91(2):167–216.

Chelton, D. B., Schlax, M. G., Samelson, R. M., and de Szoeke, R. A. (2007). Global observations of large oceanic eddies. *Geophysical Research Letters*, 34(15):L15606.

Chelton, D. B. and Xie, S.-P. (2010). Coupled Ocean-Atmosphere Interaction at Oceanic Mesoscales. *Oceanography*, 23(4):52–69.

Chen, D., Rothstein, L., and Busalacchi, A. (1994). A hybrid vertical mixing scheme and its application to tropical ocean models. *Journal of Physical Oceanography*, 24:2156–2179.

Cheney, R. E. and Richardson, P. L. (1976). Observed decay of a cyclonic Gulf Stream ring. *Deep Sea Research and Oceanographic Abstracts*, 23(2):143–155.

Condie, S. and Condie, R. (2016). Retention of plankton within ocean eddies. *Global Ecology and Biogeography*, pages 1264–1277.

Cooper, M. and Haines, K. (1996). Altimetric assimilation with water property conservation. *Journal of Geophysical Research: Oceans*, 101(C1):1059–1077.

Cotroneo, Y., Budillon, G., Fusco, G., and Spezie, G. (2013). Cold core eddies and fronts of the Antarctic Circumpolar Current south of New Zealand from in situ and satellite data. *Journal of Geophysical Research: Oceans*, 118(5):2653–2666.

Cresswell, G. R. (1982). The coalescence of two East Australian current warm-core eddies. *Science (New York, N.Y.)*, 215(4529):161–4.

Cresswell, G. R. (2000). Currents of the continental shelf and upper slope of tasmania. *Papers and Proceedings of the Royal Society of Tasmania*, 133(3):21–31.

Cresswell, G. R. and Legeckis, R. (1986). Eddies off southeastern Australia. *Deep Sea Research*, 33(11/12):1527–1562.

Cresswell, G. R. and Peterson, J. (1993). The Leeuwin Current south of Western Australia. *Marine and Freshwater Research*, 44(2):285.

Cushman-Roisin, B., Chassignet, E. P., and Tang, B. (1990). Westward Motion of Mesoscale Eddies. *Journal of Physical Oceanography*.

Cushman-Roisin, B., Heil, W. H., and Nof, D. (1985). Oscillations and rotations of elliptical warm-core rings. *Journal of Geophysical Research*, 90(C6):11756.

Daley, R. (1981). Normal mode initialization. *Reviews of Geophysics*, 19(3):450.

Davidson, P. a., Staplehurst, P. J., and Dalziel, S. B. (2006). On the evolution of eddies in a rapidly rotating system. *Journal of Fluid Mechanics*, 557:135.

de Boyer Montégut, C. (2004). Mixed layer depth over the global ocean: An examination of profile data and a profile-based climatology. *Journal of Geophysical Research*, 109(C12):C12003.

De Ruijter, W. P. M., Biastoch, A., Drijfhout, S. S., Lutjeharms, J. R. E., Matano, R. P., Pichevin, T., Van Leeuwen, P. J., and Weijer, W. (1999). Indian-Atlantic interocean exchange: Dynamics, estimation and impact. *Journal of Geophysical Research*, 104(C9):20885–20910.

de Steur, L. and van Leeuwen, P. (2009). The influence of bottom topography on the decay of modeled Agulhas rings. *Deep Sea Research Part I: Oceanographic Research Papers*, 56(4):471–494.

Dee, D. and Uppala, S. (2009). Variational bias correction of satellite radiance data in the ERA-interim reanalysis. *Q. J. T. Meteorolo. Soc.*, 135(644):1830–1841.

Deng, X., Griffin, D. A., Ridgway, K. R., Featherstone, J. A. C. W. E., White, N. J., and Cahill, M. (2011). Satellite altimetry for geodetic, oceanographic and climate studies in the Australian region.

Dewar, W. K. and Flierl, G. R. (1987). Some effects of the wind on rings. *Journal of Physical Oceanography*, 17:1653–1667.

Dibarboure, G., Lauret, O., Mertz, F., Rosmorduc, V., and Maheu, C. (2009). *AVISO SSALTO / DUACS User Handbook : ( M ) SLA and ( M ) ADT Near-Real Time and Delayed Time Products*. Number March.

Doglioli, A. M., Blanke, B., Speich, S., and Lapeyre, G. (2007). Tracking coherent structures in a regional ocean model with wavelet analysis: Application to Cape Basin eddies. *Journal of Geophysical Research*, 112(C5):C05043.

Dong, C., Lin, X., Liu, Y., Nencioli, F., Chao, Y., Guan, Y., Chen, D., Dickey, T., and McWilliams, J. C. (2012). Three-dimensional oceanic eddy analysis in the Southern California Bight from a numerical product. *Journal of Geophysical Research*, 117:C00H14.

Dong, C., McWilliams, J. C., Liu, Y., and Chen, D. (2014). Global heat and salt transports by eddy movement. *Nature Communications*, 5.

Douglass, E. M. and Richman, J. G. (2015). Analysis of ageostrophy in strong surface eddies in the Atlantic Ocean. *Journal of Geophysical Research: Oceans*, pages n/a–n/a.

Drijfhout, S. S., Katsman, C. a., De Steur, L., Van der Vaart, P. C. F., Van Leeuwen, P. J., and Veth, C. (2003). Modeling the initial, fast Sea-Surface Height decay of Agulhas ring "Astrid". *Deep-Sea Research Part II: Topical Studies in Oceanography*, 50(1):299–319.

Ducet, N., Le Traon, P. Y., and Reverdin, G. (2000). Global high-resolution mapping of ocean circulation from TOPEX/Poseidon and ERS-1 and -2. *Journal of Geophysical Research*, 105(C8):19477.

Dufois, F., Hardman-Mountford, N. J., Greenwood, J., Richardson, A. J., Feng, M., Herbette, S., and Matear, R. (2014). Impact of eddies on surface chlorophyll in the South Indian Ocean. *Journal of Geophysical Research: Oceans*, 119(11):8061–8077.

Dufois, F., Hardman-Mountford, N. J., Greenwood, J., Richardson, A. J., Feng, M., and Matear, R. J. (2016). Anticyclonic eddies are more productive than cyclonic eddies in subtropical gyres because of winter mixing. *Science Advances*, 2(5):e1600282–e1600282.

Early, J. J., Samelson, R. M., and Chelton, D. B. (2011). The Evolution and Propagation of Quasigeostrophic Ocean Eddies *. *Journal of Physical Oceanography*, 41(8):1535–1555.

Ertel, H. (1940). Ein neuer hydrodynamischer Wirbelsatz. *Meteorol. Z.*, 59:277–281.

Everett, J. D., Baird, M. E., Oke, P. R., and Suthers, I. M. (2012). An avenue of eddies: Quantifying the biophysical properties of mesoscale eddies in the Tasman Sea. *Geophysical Research Letters*, 39(16):L16608.

Everett, J. D., Baird, M. E., Roughan, M., Suthers, I. M., and Doblin, M. A. (2014). Relative impact of seasonal and oceanographic drivers on surface chlorophyll a along a Western Boundary Current. *Progress in Oceanography*, 120:340–351.

Faghmous, J. H., Frenger, I., Yao, Y., Warmka, R., Lindell, A., and Kumar, V. (2015). A daily global mesoscale ocean eddy dataset from satellite altimetry. *Scientific Data*, 2:150028.

Falkowski, P. G., Ziemann, D., Kolber, Z., and Bienfang, P. K. (1991). Role of eddy pumping in enhancing primary production in the ocean. *Nature*, 352(6330):55–58.

Fang, F. and Morrow, R. (2003). Evolution, movement and decay of warm-core Leeuwin Current eddies. *Deep Sea Research Part II: Topical Studies in Oceanography*, 50(12-13):2245–2261.

Feng, M., Colberg, F., Slawinski, D., Berry, O., and Babcock, R. (2016). Ocean circulation drives heterogeneous recruitments and connectivity among coral populations on the North West Shelf of Australia. *Journal of Marine Systems*, 164:1–12.

Ferrari, R. and Wunsch, C. (2009). Ocean Circulation Kinetic Energy: Reservoirs, Sources, and Sinks. *Annual Review of Fluid Mechanics*, 41(1):253–282.

Flierl, G. R. (1979). A Simple Model for the Structure of Warm and Cold Core Rings. *Journal of Geophysical Research*, 84(C2):781 – 785.

Flierl, G. R. (1984). Rossby Wave Radiation from a Strongly Nonlinear Warm Eddy. *Journal of Physical Oceanography*, 14:47–58.

Flierl, G. R. and McGillicuddy, D. J. (2002). Mesoscale and submesoscale physical-biological interactions. *The sea*, 12:113–185.

Flierl, G. R. and Mied, R. P. (1985). Frictionally induced circulations and spin down of a warm-core ring. *Journal of Geophysical Research*, 90(C5):8917–8927.

Franks, P. J. S., Wroblewski, J. S., and Flierl, G. R. (1986). Prediction of phytoplankton growth in response to the frictional decay of a warm-core ring. *Journal of Geophysical Research*, 91(C6):7603.

Frenger, I., Münnich, M., Gruber, N., and Knutti, R. (2015). Southern Ocean eddy phenomenology. *Journal of Geophysical Research: Oceans*, pages n/a–n/a.

Fu, L. and Cazenave, A. (2000). *Satellite altimetry and earth sciences: a handbook of techniques and applications*. Academic Press, vol. 69 edition.

Fu, L., Chelton, D., Le Traon, P., and Morrow, R. (2010). Eddy dynamics from satellite altimetry. *Oceanography*, 23(4):14–25.

Ganachaud, A., Cravatte, S., Melet, A., Schiller, A., Holbrook, N. J., Sloyan, B. M., Widlansky, M., Bowen, M., Verron, J., and Willes, P. (2014). The Southwest Paci c Ocean circulation and climate experiment (SPICE). *Journal of Geophysical Research : Oceans*, 119(11):7660–7686.

Gaube, P., Chelton, D. B., Samelson, R. M., Schlax, M. G., and O'Neill, L. W. (2015). Satellite Observations of Mesoscale Eddy-Induced Ekman Pumping. *Journal of Physical Oceanography*, 45(1):104–132.

Gaube, P., Chelton, D. B., Strutton, P. G., and Behrenfeld, M. J. (2013). Satellite observations of chlorophyll, phytoplankton biomass, and Ekman pumping in nonlinear mesoscale eddies. *Journal of Geophysical Research: Oceans*, 118(12):6349–6370.

Gill, A. E. (1982). *Atmosphere-Ocean Dynamics*. Academic Press, New York.

Gill, A. E., Green, J. S. A., and Simmons, A. J. (1974). Energy partition in the large-scale ocean circulation and the production of mid-ocean eddies. *Deep Sea Research*, 21(June 1973).

Godfrey, J. S., Cresswell, G. R., Golding, T. J., Pearce, A. F., and Boyd, R. (1980). The Separation of the East Australian Current. *Journal of Physical Oceanography*, 10(3):430–440.

Griffies, S. M. (2009). Elements of MOM4p1. *GFDL Ocean Group Tech- nical Report 6, Tech. rep., NOAA/Geophysical Fluid Dynamics Laboratory.*

Griffies, S. M. and Hallberg, R. W. (2000). Biharmonic friction with a Smagorinsky-like viscosity for use in large-scale eddy- permitting ocean models. *Monthly Weather Review*, 128:2935–2946.

Griffies, S. M., Harrison, M. L., Pacanowski, R. C., and Rosati, A. (2004). A Technical guide to MOM4. *GFDL Ocean Group Tech. Rep. 5*, NOAA/Geoph.

Grimshaw, R., Tang, Y., and Broutman, D. (1994). The effect of vortex stretching on the evolution of barotropic eddies over a topographic slope. *Geophysical & Astrophysical Fluid Dynamics*, 76(1-4):43–71.

Hall, C. and Lutjeharms, J. (2011). Cyclonic eddies identified in the Cape Basin of the South Atlantic Ocean. *Journal of Marine Systems*, 85(1-2):1–10.

Henson, S. A. and Thomas, A. C. (2008). A census of oceanic anticyclonic eddies in the Gulf of Alaska. *Deep Sea Research Part I: Oceanographic Research Papers*, 55(2):163–176.

Hill, K. L., Rintoul, S. R., Oke, P. R., and Ridgway, K. (2010). Rapid response of the East Australian Current to remote wind forcing: The role of barotropic-baroclinic interactions. *Journal of Marine Research*, 68(3):413–431.

Hill, K. L., Rintoul, S. R., Ridgway, K. R., and Oke, P. R. (2011). Decadal changes in the South Pacific western boundary current system revealed in observations and ocean state estimates. *Journal of Geophysical Research*, 116(C1):C01009.

Hogg, N. G. (1992). On the transport of the gulf stream between cape hatteras and the grand banks. *Deep Sea Research Part A. Oceanographic Research Papers*, 39(7-8):1231–1246.

Holte, J., Straneo, F., Moffat, C., Weller, R., and Farrar, J. T. (2013). Structure and surface properties of eddies in the southeast Pacific Ocean. *Journal of Geophysical Research: Oceans*, 118(5):2295–2309.

Hope, P., Keay, K., Pook, M., Catto, J., Simmonds, I., Mills, G., McIntosh, P., Risbey, J., and Berry, G. (2014). A Comparison of Automated Methods of Front Recognition for Climate Studies: A Case Study in Southwest Western Australia. *Monthly Weather Review*, 142(1):343–363.

Hu, J., Gan, J., Sun, Z., Zhu, J., and Dai, M. (2011). Observed three-dimensional structure of a cold eddy in the southwestern South China Sea. *Journal of Geophysical Research: Oceans*, 116(5):1–11.

Imawaki, S., Uchida, H., Ichikawa, H., Fukasawa, M., and Umatani, S.-i. (2001). Satellite altimeter monitoring the Kuroshio Transport south of Japan. *Geophysical Research Letters*, 28(1):17–20.

Isern-Fontanet, J., Garcia-Ladona, E., and Font, J. (2003). Identification of Marine Eddies from Altimetric Maps. *Journal of Atmospheric and Oceanic Technology*, 20:772–778.

Jayne, S. R., Hogg, N. G., Waterman, S. N., Rainville, L., Donohue, K. a., Randolph Watts, D., Tracey, K. L., McClean, J. L., Maltrud, M. E., Qiu, B., Chen, S., and Hacker, P. (2009). The Kuroshio Extension and its recirculation gyres. *Deep Sea Research Part I: Oceanographic Research Papers*, 56(12):2088–2099.

Jayne, S. R. and Marotzke, J. (2002). The Oceanic Eddy Heat Transport*. *Journal of Physical Oceanography*, 32(12):3328–3345.

Kamenkovich, V. M., Leonov, Y. P., and Nechaev, D. A. (1996). On the Influence of bottom topography on the Agulhas Eddy. *Journal of Physical Oceanography*.

Kang, D. and Curchitser, E. N. (2013). Gulf Stream eddy characteristics in a high-resolution ocean model. *Journal of Geophysical Research: Oceans*, 118(9):4474–4487.

Kep, S. L. (1984). A climatology of cyclogenesis, cyclone tracks and cyclolysis in the Southern Hemisphere for the period 1972-1981.

Kiss, A. E. (2002). Potential vorticity "crises", adverse pressure gradients, and western boundary current separation. *Journal of Marine Research*, 60(6):779–803.

Klein, P. and Lapeyre, G. (2009). The Oceanic Vertical Pump Induced by Mesoscale and Submesoscale Turbulence. *Annual Review of Marine Science*, 1(1):351–375.

Koszalka, I., Bracco, A., McWilliams, J. C., and Provenzale, A. (2009). Dynamics of wind-forced coherent anticyclones in the open ocean. *Journal of Geophysical Research: Oceans*, 114(8):1–14.

Kurczyn, J. A., Beier, E., Lavín, M. F., Chaigneau, A., and Godínez, V. M. (2013). Anatomy and evolution of a cyclonic mesoscale eddy observed in the northeastern Pacific tropical-subtropical transition zone. *Journal of Geophysical Research: Oceans*, 118:n/a–n/a.

Langlais, C. E., Rintoul, S. R., and Zika, J. D. (2015). Sensitivity of Antarctic Circumpolar Current Transport and Eddy Activity to Wind Patterns in the Southern Ocean. *Journal of Physical Oceanography*, 45(4):1051–1067.

Lankhorst, M. (2006). A Self-Contained Identification Scheme for Eddies in Drifter and Float Trajectories. *Journal of Atmospheric and Oceanic Technology*, 23(11):1583–1592.

Le Traon, P. and Dibarboure, G. (2002). Velocity Mapping Capabilities of Present and Future Altimeter Missions : The Role of High-Frequency Signals. *Journal of Atmospheric and Oceanic Technology*, 19(12):2077–2087.

Le Traon, P. and Dibarboure, G. (2004). An Illustration of the Contribution of the TOPEX/Poseidon—Jason-1 Tandem Mission to Mesoscale Variability Studies. *Marine Geodesy*, 27(1-2):3–13.

Le Traon, P., Nadal, F., and Ducet, N. (1998). An improved mapping method of multisatellite altimeter data. *J. Atmos. Oceanic Technol.*, 15(2):522–534.

Lee, C. M. and Brink, K. H. (2010). Observations of storm-induced mixing and Gulf Stream Ring incursion over the southern flank of Georges Bank: Winter and summer 1997. *Journal of Geophysical Research*, 115(C8):C08008.

Lee, H., Rosati, A., and Spelman, M. (2006). Barotropic tidal mixing effects in a coupled climate model: ocean conditions in the northern Atlantic,. *Ocean Model*, 11:464–470.

Legal, C., Klein, P., Treguier, A.-M., and Paillet, J. (2007). Diagnosis of the Vertical Motions in a Mesoscale Stirring Region. *Journal of Physical Oceanography*, 37(5):1413–1424.

Lentini, C. A. D., Goni, G. J., and Olson, D. B. (2006). Investigation of Brazil Current rings in the confluence region. *Journal of Geophysical Research*, 111(C6):C06013.

Lévy, M., Klein, P., and Treguier, A.-M. (2001). Impact of sub-mesoscale physics on production and subduction of phytoplankton in an oligotrophic regime. *Journal of Marine Research*, 59(4):535–565.

Lindstrom, E., Lukas, R., Fine, R., Firing, E., Godfrey, J. S., Meyers, G., and Tsuchiya, M. (1987). The western equatorial Pacific Ocean circulation study. *Nature*, (330):533–537.

Ling, S. D., Johnson, C. R., Ridgway, K. R., Hobday, A. J., and Haddon, M. (2009). Climate-driven range extension of a sea urchin: inferring future trends by analysis of recent population dynamics. *Global Change Biology*, 15(3):719–731.

Lutjeharms, J. and Ansorge, I. (2001). The Agulhas Return Current. *Journal of Marine Systems*, 30(1-2):115–138.

Macdonald, H. S., Roughan, M., Baird, M. E., and Wilkin, J. (2013). A numerical modeling study of the East Australian Current encircling and overwashing a warm-core eddy. *Journal of Geophysical Research: Oceans*, 118(1):301–315.

Macdonald, H. S., Roughan, M., Baird, M. E., and Wilkin, J. L. (2016). The formation of a cold-core eddy in the East Australian Current. *Continental Shelf Research*, 114:72–84.

Mahadevan, A., Thomas, L. N., and Tandon, A. (2008). Comment on "Eddy/Wind Interactions Stimulate Extraordinary Mid-Ocean Plankton Blooms". *Science*, 320(5875):448b–448b.

Marchesiello, P. and Middleton, J. H. (2000). Modeling the East Australian Current in the Western Tasman Sea. *Journal of Physical Oceanography*, 30:2956–2971.

Martin, A. P. and Richards, K. J. (2001). Mechanisms for vertical nutrient transport within a North Atlantic mesoscale eddy. *Deep Sea Research Part II*, 48:757–773.

Martin, M., Balmaseda, M., Bertino, L., Brasseur, P., Brassington, G., Cummings, J., Fujii, Y., Lea, D., Lellouche, J.-M., Mogensen, K., Oke, P., Smith, G., Testut, C.-E., Waagbø, G., Waters, J., and Weaver, A. (2015). Status and future of data assimilation in operational oceanography. *Journal of Operational Oceanography*, 8(sup1):s28–s48.

Mason, E., Pascual, A., Gaube, P., Ruiz, S., Pelegrí, J. L., and Delepoulle, A. (2017). Subregional characterization of mesoscale eddies across the Brazil-Malvinas Confluence. *Journal of Geophysical Research: Oceans*, 122(4):3329–3357.

Mason, E., Pascual, A., and McWilliams, J. C. (2014). A New Sea Surface Height–Based Code for Oceanic Mesoscale Eddy Tracking. *Journal of Atmospheric and Oceanic Technology*, 31(5):1181–1188.

Mata, M. M., Wijffels, S. E., Church, J. A., and Tomczak, M. (2006). Eddy shedding and energy conversions in the East Australian Current. *Journal of Geophysical Research*, 111(C9):C09034.

Matano, R. P. (1993). On the Separation of the Brazil Current from the Coast. *Journal of Physical Oceanography*, 23(1):79–90.

Matano, R. P. and Beier, E. J. (2003). A kinematic analysis of the Indian / Atlantic interocean exchange. *Deep Sea Research II*, 50:229–249.

Matear, R. J., Chamberlain, M. A., Sun, C., and Feng, M. (2013). Climate change projection of the Tasman Sea from an Eddy-resolving Ocean Model. *Journal of Geophysical Research: Oceans*, 118(6):2961–2976.

Matear, R. J. and Jones, E. (2011). Marine Biogeochemical Modelling and Data Assimilation. In *Operational Oceanography in the 21st Century*, pages 295–317. Springer Netherlands, Dordrecht.

Mazloff, M. R., Gille, S. T., and Cornuelle, B. (2014). Improving the geoid: Combining altimetry and mean dynamic topography in the California coastal ocean. *Geophysical Research Letters*, 41(24):8944–8952.

McDonald, N. R. (1998). The decay of cyclonic eddies by Rossby wave radiation. *Journal of Fluid Mechanics*, 361(September 2000):237–252.

McGillicuddy, D. and Robinson, A. (1997). Eddy-induced nutrient supply and new production in the Sargasso Sea. *Deep Sea Research Part I: Oceanographic Research Papers*, 44(8):1427–1450.

McGillicuddy, D. J. (2015). Formation of Intrathermocline Lenses by Eddy-Wind Interaction. *Journal of Physical Oceanography*, 45(2):606–612.

McGillicuddy, D. J. (2016). Mechanisms of Physical-Biological-Biogeochemical Interaction at the Oceanic Mesoscale. *Annual Review of Marine Science*, 8:13.1–13.36.

McGillicuddy, D. J., Anderson, L. A., Bates, N. R., Bibby, T., Buesseler, K. O., Carlson, C. A., Davis, C. S., Ewart, C., Falkowski, P. G., Goldthwait, S. A., Hansell, D. A., Jenkins, W. J., Johnson, R., Kosnyrev, V. K., Ledwell, J. R., Li, Q. P., Siegel, D. A., and Steinberg, D. K. (2007). Eddy/wind interactions stimulate extraordinary mid-ocean plankton blooms. *Science (New York, N.Y.)*, 316(5827):1021–6.

McGillicuddy, D. J., Anderson, L. A., Doney, S. C., and Maltrud, M. E. (2003). Eddy-driven sources and sinks of nutrients in the upper ocean: Results from a 0.1 resolution model of the North Atlantic. *Global Biogeochemical Cycles*, 17(2):n/a–n/a.

McGillicuddy, D. J., Robinson, a. R., and McCarthy, J. J. (1995). Coupled physical and biological modelling of the spring bloom in the North Atlantic (II): Three dimensional bloom and post-bloom processes. *Deep-Sea Research Part I: Oceanographic Research Papers*, 42(8):1359–1398.

McGillicuddy, D. J., Robinson, A. R., Siegel, D. A., Jannasch, H. W., Johnson, R., Dickey, T. D., McNeil, J., Michaels#, A. F., and Knap, A. H. (1998). Influence of mesoscale eddies on new production in the Sargasso Sea. *Nature*, 394(6690):263–266.

McWilliams, J. C., Graves, L. P., and Montgomery, M. T. (2003). A Formal Theory for Vortex Rossby Waves and Vortex Evolution. *Geophysical & Astrophysical Fluid Dynamics*, 97(4):275–309.

Moore, A. M., Arango, H. G., Broquet, G., Edwards, C., Veneziani, M., Powell, B., Foley, D., Doyle, J. D., Costa, D., and Robinson, P. (2011). The Regional Ocean Modeling System (ROMS) 4-dimensional variational data assimilation systems. *Progress in Oceanography*, 91(1):50–73.

Morrow, R. (2004). Divergent pathways of cyclonic and anti-cyclonic ocean eddies. *Geophysical Research Letters*, 31(24):L24311.

Morrow, R., Church, J. A., Coleman, R., Chelton, D. B., and White, N. (1992). Eddy momentum flux and its contribution to the Southern Ocean momentum balance. *Nature*, 357(482-484).

Morrow, R., Coleman, R., Church, J., and Chelton, D. (1994). Surface Eddy Momentum Flux and Velocity Variances in the Southern Ocean from Geosat Altimetry.

Morrow, R. and Le Traon, P. Y. (2012). Recent advances in observing mesoscale ocean dynamics with satellite altimetry. *Advances in Space Research*, 50(8):1062–1076.

Nakano, H., Tsujino, H., and Sakamoto, K. (2013). Tracer transport in cold-core rings pinched off from the Kuroshio Extension in an eddy-resolving ocean general circulation model. *Journal of Geophysical Research: Oceans*, 118(10):5461–5488.

Nan, F., He, Z., Zhou, H., and Wang, D. (2011). Three long-lived anticyclonic eddies in the northern South China Sea. *Journal of Geophysical Research*, 116(C5):C05002.

Nardelli, B. B. (2013). Vortex waves and vertical motion in a mesoscale cyclonic eddy. *Journal of Geophysical Research: Oceans*, 118(10):5609–5624.

Nelson, D. M., McCarthy, J. J., Joyce, T. M., and Ducklow, H. W. (1989). Enhanced near-surface nutrient availability and new production resulting from the frictional decay of a Gulf Stream warm-core ring. *Deep Sea Research Part A. Oceanographic Research Papers*, 36(5):705–714.

Nemcek, N., Ianson, D., and Tortell, P. D. (2008). A high-resolution survey of DMS, CO 2 , and O 2 /Ar distributions in productive coastal waters. *Global Biogeochemical Cycles*, 22(2):n/a–n/a.

Nencioli, F., Kuwahara, V. S., Dickey, T. D., Rii, Y. M., and Bidigare, R. R. (2008). Physical dynamics and biological implications of a mesoscale eddy in the lee of Hawai'i: Cyclone Opal observations during E-Flux III. *Deep Sea Research Part II: Topical Studies in Oceanography*, 55(10-13):1252–1274.

Nilsson, C. and Cresswell, G. (1981). The formation and evolution of East Australian current warm-core eddies. *Progress in Oceanography*, 9(3):133–183.

Nilsson, C. S., Andrews, S. C., and Scully-Power, P. (1977). Observations of Eddy Formation off East Australia. *Journal of Physical Oceanography*, 7(5):659–669.

Nof, D. (1983). The translation of isolated cold eddies on a sloping bottom. *Deep Sea Research Part A. Oceanographic Research Papers*, 30(2):171–182.

Nurser, A. J. G. and Zhang, J. W. (2000). Eddy-induced mixed layer shallowing and mixed layer/thermocline exchange. *Journal of Geophysical Research: Oceans*, 105(C9):21851–21868.

Oke, P. R. (2002). Assimilation of surface velocity data into a primitive equation coastal ocean model. *Journal of Geophysical Research*, 107(C9):3122.

Oke, P. R., Brassington, G. B., Griffin, D. A., and Schiller, A. (2008). The Bluelink ocean data assimilation system (BODAS). *Ocean Modelling*, 21(1-2):46–70.

Oke, P. R., Brassington, G. B., Griffin, D. A., and Schiller, A. (2010). Ocean data assimilation : a case for ensemble optimal interpolation. *Australian Meteorological and Oceanographic Journal*, 59:67–76.

Oke, P. R. and England, M. H. (2004). Oceanic Response to Changes in the Latitude of the Southern Hemisphere Subpolar Westerly Winds. *Journal of Climate*, 17:1040–1054.

Oke, P. R. and Griffin, D. A. (2011). The cold-core eddy and strong upwelling off the coast of New South Wales in early 2007. *Deep-Sea Research Part II*, 58(5):574–591.

Oke, P. R., Griffin, D. A., Schiller, A., Matear, R. J., Fiedler, R., Mansbridge, J., Lenton, A., Cahill, M., Chamberlain, M. A., and Ridgway, K. (2013a). Evaluation of a near-global eddy-resolving ocean model. *Geosci. Model Dev*, 6(591-615):2013.

Oke, P. R., Sakov, P., Cahill, M. L., Dunn, J. R., Fiedler, R., Griffin, D. A., Mansbridge, J. V., Ridgway, K. R., and Schiller, A. (2013b). Towards a dynamically balanced eddy-resolving ocean reanalysis: BRAN3. *Ocean Modelling*, 67:52–70.

Oke, P. R., Schiller, A., Griffin, D. A., and Brassington, G. B. (2005). Ensemble data assimilation for an eddy-resolving ocean model of the Australian region. *Quarterly Journal of the Royal Meteorological Society*, 131(613):3301–3311.

Oliveira, L. R., Piola, A. R., Mata, M. M., and Soares, I. D. (2009). Brazil Current surface circulation and energetics observed from drifting buoys. *Journal of Geophysical Research*, 114(C10):C10006.

Oliver, E. C. J. and Holbrook, N. J. (2014). Extending our understanding of South Pacific gyre 'spin-up': Modelling the East Australian Current in a future climate. *Journal of Geophysical Research: Oceans*, pages n/a–n/a.

Oliver, E. C. J., O'Kane, T. J., and Holbrook, N. J. (2015). Projected changes to Tasman Sea eddies in a future climate. *Journal of Geophysical Research: Oceans*, 120(11):7150–7165.

Olson, D. B. (1991). Rings in the ocean. *Annual Rev. Earth Planet. Sci.*, 19:283–311.

Pallas-Sanz, E. and Viudez, A. (2007). Three-dimensional ageostrophic motion in mesoscale vortex dipoles. *Journal of Physical Oceanography*, 37(1):84–105.

Paterson, H. L., Knott, B., and Waite, A. M. (2007). Microzooplankton community structure and grazing on phytoplankton, in an eddy pair in the Indian Ocean off Western Australia. *Deep Sea Research Part II: Topical Studies in Oceanography*, 54(8-10):1076–1093.

Pegliasco, C., Chaigneau, A., and Morrow, R. (2015). Main eddy vertical structures observed in the fourmajor Eastern Boundary Upwelling Systems. *Journal of Geophysical Research : Oceans*, pages 1–26.

Pelland, N. A., Eriksen, C. C., and Lee, C. M. (2013). Subthermocline Eddies over the Washington Continental Slope as Observed by Seagliders , 2003 – 09. *Journal of Physical Oceanography*, 43:2025–2053.

Petersen, M. R., Williams, S. J., Maltrud, M. E., Hecht, M. W., and Hamann, B. (2013). A three-dimensional eddy census of a high-resolution global ocean simulation. *Journal of Geophysical Research: Oceans*, 118(4):1759–1774.

Peterson, R. G., Stramma, L., Ray, G. P., and Amma, L. S. (1991). Upper-level circulation in the South Atlantic Ocean. *Progress in Oceanography*, 26(1):1–73.

Pidcock, R., Martin, A., Allen, J., Painter, S. C., and Smeed, D. (2013). The spatial variability of vertical velocity in an Iceland basin eddy dipole. *Deep-Sea Research Part I: Oceanographic Research Papers*, 72:121–140.

Pilo, G. S., Mata, M. M., and Azevedo, J. L. L. (2015). Eddy surface properties and propagation at Southern Hemisphere western boundary current systems. *Ocean Science*, 11(4):629–641.

Pollard, R. T. and Regier, L. a. (1992). Vorticity and Vertical Circulation at an Ocean Front.

Polzin, K. L. (2010). Mesoscale Eddy–Internal Wave Coupling. Part II: Energetics and Results from PolyMode. *Journal of Physical Oceanography*, 40(4):789–801.

Pook, M. J., Risbey, J. S., and McIntosh, P. C. (2012). The Synoptic Climatology of Cool-Season Rainfall in the Central Wheatbelt of Western Australia. *Monthly Weather Review*, 140(1):28–43.

Powell, B., Moore, A., Arango, H., Di Lorenzo, E., Milliff, R., and Leben, R. (2009). Near real-time ocean circulation assimilation and prediction in the Intra-Americas Sea with ROMS. *Dynamics of Atmospheres and Oceans*, 48(1-3):46–68.

Qiu, B. and Chen, S. (2004). Seasonal Modulations in the Eddy Field of the South Pacific Ocean. *Journal of Physical Oceanography*, 34:1515–1527.

Qiu, B., Kelly, K. A., and Joyce, T. M. (1991). Mean flow and variability in the Kuroshio Extension from Geosat altimetry data. *Journal of Geophysical Research*, 96(C10):18491.

Reynolds, R. W., Smith, T. M., Liu, C., Chelton, D. B., Casey, K. S., and Schlax, M. G. (2007). Daily High-Resolution-Blended Analyses for Sea Surface Temperature. *Journal of Climate*, 20(22):5473–5496.

Ridgway, K. R. (2007). Long-term trend and decadal variability of the southward penetration of the East Australian Current. *Geophysical Research Letters*, 34(13):n/a–n/a.

Ridgway, K. R., Coleman, R. C., Bailey, R. J., and Sutton, P. (2008). Decadal variability of East Australian Current transport inferred from repeated high-density XBT transects, a CTD survey and satellite altimetry. *Journal of Geophysical Research*, 113(C8):C08039.

Ridgway, K. R. and Dunn, J. R. (2003). Mesoscale structure of the mean East Australian Current System and its relationship with topography. *Progress in Oceanography*, 56(2):189–222.

Ridgway, K. R. and Dunn, J. R. (2007). Observational evidence for a Southern Hemisphere oceanic supergyre. *Geophysical Research Letters*, 34(13):L13612.

Ridgway, K. R. and Godfrey, J. S. (1997). Seasonal cycle of the East Australian Current. *Journal of Geophysical Research*, 102(C10):22,921 – 22,936.

Ridgway, K. R. and Godfrey, J. S. (2015). The source of the Leeuwin Current seasonality. *Journal of Geophysical Research: Oceans*, 120(10):6843–6864.

Ridgway, K. R. and Hill, K. (2009). The East Australian Current. In Poloczanska, E., Hobday, A., and Richardson, A., editors, *A Marine Climate Change Impacts and Adaptation Report Card for Australia 2009*, pages 1–16. NCCARF Publication 05/09,.

Rio, M. H., Schaeffer, P., Moreaux, G., Lemoine, J. M., and Bronner, E. (2009). A new mean dynamic topography computed over the global ocean from GRACE data, altimetry and in-situ measurements. *Poster communications at OceanObs09 symposium*, 25.

Roberts, M. J., Ternon, J.-F., and Morris, T. (2014). Interaction of dipole eddies with the western continental slope of the Mozambique Channel. *Deep Sea Research Part II: Topical Studies in Oceanography*, 100:54–67.

Rocha, C. B., da Silveira, I. C. A., Castro, B. M., and Lima, J. A. M. (2014). Vertical structure, energetics, and dynamics of the Brazil Current System at 22S-28S. *Journal of Geophysical Research: Oceans*, 119(1):52–69.

Rochford, D. J. (1957). The identification and nomenclature of the surface water masses in the Tasman Sea (data to the end of 1954). *Marine and Freshwater Research*, 8(4):369–413.

Roemmich, D. and Gilson, J. (2001). Eddy Transport of Heat and Thermocline Waters in the North Pacific : A Key to Interannual / Decadal Climate Variability ? *Journal of Physical Oceanography*, 31:675–687.

Rosell-Fieschi, M., Rintoul, S. R., Gourrion, J., and Pelegrí, J. L. (2013). Tasman Leakage of intermediate waters as inferred from Argo floats. *Geophysical Research Letters*, 40(20):5456–5460.

Rossby, T., Flagg, C., Ortner, P., and Hu, C. (2011). A tale of two eddies: Diagnosing coherent eddies through acoustic remote sensing. *Journal of Geophysical Research: Oceans*, 116(12):1–17.

Roughan, M., Keating, S. R., Schaeffer, A., Cetina Heredia, P., Rocha, C., Griffin, D., Robertson, R., and Suthers, I. M. (2017). A tale of two eddies: The biophysical characteristics of two contrasting cyclonic eddies in the East Australian Current System. *Journal of Geophysical Research: Oceans*.

Rousselet, L., Doglioli, A. M., Maes, C., Blanke, B., and Petrenko, A. A. (2016). Impacts of mesoscale activity on the water masses and circulation in the Coral Sea. *Journal of Geophysical Research: Oceans*, 121(10):7277–7289.

Rykova, T. and Oke, P. R. (2015). Recent freshening of the East Australian Current and its eddies. *Geophysical Research Letters*, 42:9369–9378.

Rykova, T., Oke, P. R., and Griffin, D. A. (2017). A comparison of the structure, properties, and water mass composition of quasi-isotropic eddies in western boundary currents in an eddy-resolving ocean model. *Ocean Modelling*, 114:1–13.

Sadarjoen, I. A. and Post, F. H. (2000). Detection , quantification , and tracking of vortices using streamline geometry. *Computer & Graphics*, 24:333–341.

Sakov, P., Counillon, F., Bertino, L., Lisæter, K. A., Oke, P. R., and Korablev, A. (2012). TOPAZ4: an ocean-sea ice data assimilation system for the North Atlantic and Arctic. *Ocean Science*, 8(4):633–656.

Samelson, R. M., Schlax, M. G., and Chelton, D. B. (2014). Randomness, Symmetry, and Scaling of Mesoscale Eddy Life Cycles. *Journal of Physical Oceanography*, 44(3):1012–1029.

Sandery, P. A., Brassington, G. B., and Freeman, J. (2011). Adaptive nonlinear dynamical initialization. *Journal of Geophysical Research*, 116(C1):C01021.

Saraceno, M. and Provost, C. (2012). On eddy polarity distribution in the southwestern Atlantic. *Deep Sea Research Part I: Oceanographic Research Papers*, 69:62–69.

Sasaki, Y. N., Minobe, S., Schneider, N., Kagimoto, T., Nonaka, M., and Sasaki, H. (2008). Decadal Sea Level Variability in the South Pacific in a Global Eddy-Resolving Ocean Model Hindcast. *Journal of Physical Oceanography*, 38(8):1731–1747.

Schiller, A., Oke, P., Brassington, G., Entel, M., Fiedler, R., Griffin, D., and Mansbridge, J. (2008). Eddy-resolving ocean circulation in the Asian–Australian region inferred from an ocean reanalysis effort. *Progress in Oceanography*, 76(3):334–365.

Schiller, A. and Oke, P. R. (2015). Dynamics of ocean surface mixed layer variability in the Indian Ocean. *Journal of Geophysical Research: Oceans*, 120(6):4162–4186.

Schiller, A. and Ridgway, K. R. (2013). Seasonal mixed-layer dynamics in an eddy-resolving ocean circulation model. *Journal of Geophysical Research: Oceans*, 118(7):3387–3405.

Schmid, C., Boebel, O., Zenk, W., Lutjeharms, J. R. E., Garzoli, S. L., Richardson, P. L., and Barron, C. (2003). Early evolution of an Agulhas Ring. *Deep Sea Research Part II*, 50:141–166.

Schouten, M. W., Ruijter, W. P. M. D., Leeuwen, P. J. V., and Lutjeharms, J. R. E. (2000). Translation , decay and splitting of Agulhas rings in southeastern Atlantic Ocean. *Journal of Geophysical Research*, 105(C9):21,913 – 21,925.

Shapiro, G. I., Meschanov, S. L., and Emelianov, M. V. (1995). Mediterranean lens "Irving" after its collision with seamounts. *Oceanologica Acta*, 18:309–318.

Shi, C. and Nof, D. (1994). The Destruction of Lenses and Generation of Wodons. *Journal of Physical Oceanography*, 24(6):1120–1136.

Siegel, A. and Weiss, J. B. (1997). A wavelet-packet census algorithm for calculating vortex statistics. *Physics of Fluids*, 9(7):1988–1999.

Siegel, D. A., Court, D., Menzies, D., Peterson, P., Maritorena, S., and Nelson, N. (2008). Satellite and in situ observations of the bio-optical signatures of two mesoscale eddies in the Sargasso Sea. *Deep Sea Research Part II: Topical Studies in Oceanography*, 55(10-13):1218–1230.

Siegel, D. A., Mcgillicuddy, D. J., and Fields, E. A. (1999). Mesoscale eddies , satellite altimetry , and new production in the Sargasso Sea. *Journal of Geophysical Research*, 104(C6):13,359 – 13,379.

Siegel, D. A., Peterson, P., McGillicuddy, D. J., Maritorena, S., and Nelson, N. B. (2011). Bio-optical footprints created by mesoscale eddies in the Sargasso Sea. *Geophysical Research Letters*, 38(13):n/a–n/a.

Simmons, L. and Nof, D. (2000). Islands as eddy splitters. *Journal of Marine Research*, 58:919–956.

Sloyan, B., Ridgway, K. R., and Cowley, R. (2016). The East Australian Current and property transport at 27oS from 2012 to 2013. *Journal of Physical Oceanography*, 46(3):993–1008.

Souza, J. M. A. C., de Boyer Montégut, C., and Le Traon, P. Y. (2011). Comparison between three implementations of automatic identification algorithms for the quantification and characterization of mesoscale eddies in the South Atlantic Ocean. *Ocean Science*, 7(3):317–334.

Speich, S., Blanke, B., and Cai, W. (2007). Atlantic meridional overturning circulation and the Southern Hemisphere supergyre. *Geophysical Research Letters*, 34(23):n/a–n/a.

Speich, S., Blanke, B., de Vries, P., Drijfhout, S., Döös, K., Ganachaud, A., and Marsh, R. (2002). Tasman leakage: A new route in the global ocean conveyor belt. *Geophysical Research Letters*, 29(10):55–1–55–4.

Stammer, D. (1998). On Eddy Characteristics, Eddy Transports, and Mean Flow Properties. *Journal of Physical Oceanography*, 28(4):727–739.

Stammer, D. and Cazenave, A. (2017). *Satellite Altimetry Over Oceans and Land Surfaces*. CRC Press.

Stern, M. E. (1965). Interaction of a uniform wind stress with a geostrophic vortex. *Deep-Sea Research*, 12(November 1964):355–367.

Strass, V. H. (1994). Mesoscale Instability and Upwelling. Part 2: Testing the Diagnostics of Vertical Motion with a Three-Dimensional Ocean Front Model. *Journal of Physical Oceanography*, 24(8):1759–1767.

Streten, N. A. and Troup, A. J. (1973). A synoptic climatology of satellite observed cloud vortices over the Southern Hemisphere. *Quarterly Journal of the Royal Meteorological Society*, 99(419):56–72.

Suthers, I. M., Young, J. W., Baird, M. E., Roughan, M., Everett, J. D., Brassington, G. B., Byrne, M., Condie, S. A., Hartog, J. R., Hassler, C. S., Hobday, A. J., Holbrook, N. J., Malcolm, H. A., Oke, P. R., Thompson, P. A., and Ridgway, K. (2011). The strengthening East Australian Current, its eddies and biological effects — an introduction and overview. *Deep Sea Research Part II: Topical Studies in Oceanography*, 58(5):538–546.

Sutyrin, G. G. (2016). On sharp vorticity gradients in elongating baroclinic eddies and their stabilization with a solid-body rotation. *Geophysical Research Letters*, 43(11):5802–5811.

Sweeney, E. N., McGillicuddy, D. J., and Buesseler, K. O. (2003). Biogeochemical impacts due to mesoscale eddy activity in the Sargasso Sea as measured at the Bermuda Atlantic Time-series Study (BATS). *Deep Sea Research Part II: Topical Studies in Oceanography*, 50(22-26):3017–3039.

Tilburg, C. E., Hurlburt, H. E., O'Brien, J. J., and Shriver, J. F. (2001). The Dynamics of the East Australian Current System: The Tasman Front, the East Auckland Current, and the East Cape Current. *Journal of Physical Oceanography*, 31:2917–2943.

Tilburg, C. E., Subrahmanyam, B., and O'Brien, J. J. (2002). Ocean color variability in the Tasman Sea. *Geophysical Research Letters*, 29(10):125–1–125–4.

Tintoré, J., Gomis, D., Alonso, S., and Parrilla, G. (1991). Mesoscale dynamics and vertical motion in the Alboran Sea.

Tomczak, M. and Godfrey, J. S. (2013). *Regional Oceanography: an introduction.*, volume 0. Elsevior.

Tranter, D. J., Carpenter, D. J., and Leech, G. S. (1986). The coastal enrichment effect of the East Australian Current eddy field. *Deep Sea Research Part A. Oceanographic Research Papers*, 33(11-12):1705–1728.

Tranter, D. J., Leech, G. S., and Vaudrey, D. J. (1982). Biological significance of surface flooding in warm-core ocean eddies. *Nature*, 297(5867):572–574.

Tranter, D. J., Parker, R. R., and Cresswell, G. R. (1980). Are warm-core eddies unproductive?

Uysal, Z. (2006). Vertical distribution of marine cyanobacteria Synechococcus spp. in the Black, Marmara, Aegean, and eastern Mediterranean seas. *Deep Sea Research Part II: Topical Studies in Oceanography*, 53(17-19):1976–1987.

Valcke, S. and Verron, J. (1997). Interactions of Baroclinic Isolated Vortices : The Dominant Effect of Shielding. *Journal of Physical Oceanography*, 27:524–541.

van Leeuwen, P. J. (2007). The Propagation Mechanism of a Vortex on the $\beta$ Plane. *Journal of Physical Oceanography*, 37(9):2316–2330.

van Sebille, E., England, M. H., Zika, J. D., and Sloyan, B. M. (2012). Tasman leakage in a fine-resolution ocean model. *Geophysical Research Letters*, 39(6):n/a–n/a.

van Sebille, E., van Leeuwen, P. J., Biastoch, A., and de Ruijter, W. P. M. (2010). On the fast decay of Agulhas rings. *Journal of Geophysical Research*, 115(C3):C03010.

Venaille, A., Vallis, G. K., and Smith, K. S. (2011). Baroclinic Turbulence in the Ocean: Analysis with Primitive Equation and Quasigeostrophic Simulations. *Journal of Physical Oceanography*, 41(9):1605–1623.

Villas Bôas, A. B., Sato, O. T., Chaigneau, A., and Castelão, G. P. (2015). The signature of mesoscale eddies on the air-sea turbulent heat fluxes in the South Atlantic Ocean. *Geophysical Research Letters*, 42(6):1856–1862.

Viudez, A. and Dritschel, D. G. (2003). Vertical velocity in mesoscale geophysical flows. *J. Fluid Mech*, 483:199–223.

Waite, A. M., Stemmann, L., Guidi, L., Calil, P. H. R., Hogg, A. M., Feng, M., Thompson, P. A., Picheral, M., and Gorsky, G. (2016). The wineglass effect shapes particle export to the deep ocean in mesoscale eddies. *Geophysical Research Letters*, 43:9791–9800.

Waterman, S. and Jayne, S. R. (2011). Eddy-Mean Flow Interactions in the Along-Stream Development of a Western Boundary Current Jet: An Idealized Model Study. *Journal of Physical Oceanography*, 41(4):682–707.

Waters, J., Bell, M. J., Martin, M. J., and Lea, D. J. (2017). Reducing ocean model imbalances in the equatorial region caused by data assimilation. *Quarterly Journal of the Royal Meteorological Society*, 143(702):195–208.

Waugh, D. W., Abraham, E. R., and Bowen, M. M. (2006). Spatial variations of stirring in the surface ocean: A case study of the Tasman Sea. *Journal of Physical Oceanography*, 36(3):526–542.

Wilkin, J. L. and Zhang, W. F. G. (2007). Modes of mesoscale sea surface height and temperature variability in the East Australian Current. *Journal of Geophysical Research : Oceans*, 112.

Woodham, R., Brassington, G. B., Robertson, R., and Alves, O. (2013). Propagation characteristics of coastally trapped waves on the Australian Continental Shelf. *Journal of Geophysical Research: Oceans*, 118(9):4461–4473.

Wunsch, C. (1997). The Vertical Partition of Oceanic Horizontal Kinetic Energy. *Journal of Physical Oceanography*, 27(8):1770–1794.

Wunsch, C. (1999). Where do ocean eddy heat fluxes matter? *Journal of Geophysical Research*, 104(C6):13,235 – 13,249.

Wunsch, C. and Stammer, D. (1998). Satellite Altimetry, the Marine Geoid, and the Oceanic General Circulation. *Annual Review of Earth and Planetary Sciences*, 26(1):219–253.

Wyrtki, K. (1960). The Surface Circulation in the Coral and Tasman Seas. *Division of Fisheries and Oceanography Technical Paper No. 8*.

Wyrtki, K. (1962). The subsurface water masses in the western South Pacific Ocean. *Australian Journal of Marine and Freshwater Research*, 13:18–47.

Wyrtki, K., Magaard, L., and Hager, J. (1976). Eddy energy in the oceans. *Journal of Geophysical Research*, 81(15):2641–2646.

Xu, C., Zhai, X., and Shang, X.-d. (2016). Work done by atmospheric winds on mesoscale. *Journal of Geophysical Research : Oceans*, pages 1–7.

Yang, G., Wang, F., Li, Y., and Lin, P. (2013). Mesoscale eddies in the northwestern subtropical Pacific Ocean: Statistical characteristics and three-dimensional structures. *Journal of Geophysical Research: Oceans*, 118(4):1906–1925.

Yang, G., Yu, W., Yuan, Y., Zhao, X., Wang, F., Chen, G., Liu, L., and Duan, Y. (2015). Characteristics, vertical structures, and heat/salt transports of mesoscale eddies in the southeastern tropical Indian Ocean. *Journal of Geophysical Research: Oceans*, 120(3):n/a–n/a.

Yasuda, I., Okuda, K., and Hirai, M. (1992). Evolution of a Kuroshio warm-core ring—variability of the hydrographic structure. *Deep Sea Research Part A. Oceanographic Research Papers*, 39:S131–S161.

Ypma, S. L., van Sebille, E., Kiss, A. E., and Spence, P. (2016). The separation of the East Australian Current: A Lagrangian approach to potential vorticity and upstream control. *Journal of Geophysical Research: Oceans*, 121(1):758–774.

Zhang, Z., Li, C., Zhao, W., Tian, J., and Qu, T. (2014). Subthermocline eddies observed by Argo floats in the subtropical northwestern Pacific Ocean in Spring 2014. *Geophysical Research Letters*, pages 6438–6445.

Zhang, Z., Tian, J., Qiu, B., Zhao, W., Chang, P., Wu, D., and Wan, X. (2016). Observed 3D Structure, Generation, and Dissipation of Oceanic Mesoscale Eddies in the South China Sea. *Scientific Reports*, 6(1):24349.

Zhang, Z., Zhang, Y., Wang, W., and Huang, R. X. (2013). Universal structure of mesoscale eddies in the ocean. *Geophysical Research Letters*, 40(14):3677–3681.

# List of Figures

# List of Tables

# Appendix A: "Do East Australian Current anticyclonic eddies leave the Tasman Sea?"

AGU PUBLICATIONS

JGR

Journal of Geophysical Research: Oceans

RESEARCH ARTICLE

10.1002/2015JC011026

# Do East Australian Current anticyclonic eddies leave the Tasman Sea?

**Gabriela S. Pilo[1,2], Peter R. Oke[2], Tatiana Rykova[2], Richard Coleman[1,3], and Ken Ridgway[2]**

[1]Institute for Marine and Antarctic Studies, University of Tasmania, Hobart, Tasmania, Australia, [2]CSIRO Oceans and Atmosphere Flagship, Hobart, Tasmania, Australia, [3]Antarctic Climate and Ecosystems CRC, Hobart, Tasmania, Australia

**Key Points:**
- EAC anticyclones propagate from the Tasman Sea toward the Indian Ocean
- EAC anticyclones decay along path and amplify due to merging with other eddies
- EAC anticyclones become more barotropic along their path

**Supporting Information:**
- Supporting Information S1

**Correspondence to:**
G. S. Pilo,
Gabriela.SemoliniPilo@utas.edu.au

**Citation:**
Pilo, G. S., P. R. Oke, T. Rykova, R. Coleman, and K. Ridgway (2015), Do East Australian Current anticyclonic eddies leave the Tasman Sea?, *J. Geophys. Res. Oceans*, *120*, 8099–8114, doi:10.1002/2015JC011026.

Received 8 JUN 2015
Accepted 16 NOV 2015
Accepted article online 19 NOV 2015
Published online 18 DEC 2015



**Abstract** Using satellite altimetry and high-resolution model output we analyze the pathway of large, long-lived anticyclonic eddies that originate near the East Australian Current (EAC) separation point. We show that 25–30% of these eddies propagate southward, around Tasmania, leave the Tasman Sea, and decay in the Great Australian Bight. This pathway has not been previously documented owing to poor satellite sampling off eastern Tasmania. As eddies propagate southward, they often "stall" for several months at near-constant latitude. Along the pathway eddies become increasingly barotropic. Eddy intensity is primarily influenced by merging with other eddies and a gradual decay otherwise. Surface temperature anomaly associated with anticyclonic eddies changes as they propagate, while surface salinity anomaly tends to remain relatively unchanged as they propagate.

## 1. Introduction

Ocean eddies play a critical role in the distribution of heat and other properties in the world's oceans [e.g., *Wunsch*, 1999; *Jayne and Marotzke*, 2002]. The most energetic eddies are found in western boundary current (WBC) regions [*Chelton et al.*, 2011]. The East Australian Current (EAC) is the WBC of the South Pacific Subtropical Gyre. It is characterized by a warm, poleward current that flows as a jet between about 20–31°S off eastern Australia before separating from the coast at 31–32°S [*Godfrey et al.*, 1980]. At this latitude band, the EAC retroflects and degenerates into a complex field of mesoscale eddies [e.g., *Nilsson and Cresswell*, 1980; *Ridgway and Godfrey*, 1997]. The EAC anticyclonic eddies form in the retroflection region (denoted in Figure 1) approximately every 90–100 days [e.g., *Bowen et al.*, 2005; *Mata et al.*, 2006]. These eddies have been shown to be important for the circulation, influencing the water mass distribution and transformation in the Tasman Sea, coastal upwelling [e.g., *Tranter et al.*, 1982] and biological productivity [e.g., *Griffiths and Brandt*, 1983; *Baird et al.*, 2011; *Everett et al.*, 2012].

Previous analyses of EAC eddies indicate that they typically stay close to the continental slope between their formation region and about 40°S [*Everett et al.*, 2012; *Pilo et al.*, 2015]. However, some large anticyclonic eddies have also been identified off south-eastern Tasmania. For example, *Baird and Ridgway* [2012] and *Pilo et al.* [2015] show anticyclonic eddies, tracked in gridded altimetry, propagating from the Southern Tasman Sea region, crossing south of Tasmania, and advecting toward to the Great Australian Bight (GAB, Figure 1). We also note that the westward flow south of Tasmania is a component of the so-called Southern Ocean super-gyre, described by *Ridgway and Dunn* [2007]. This super-gyre is reported to include a continuous flow, on average, southward off south-eastern Australia, around the southern tip of Tasmania, and extending toward the Indian Ocean. These papers lead us to hypothesize that long-lived EAC eddies may follow this pathway. While it is agreed that EAC anticyclonic eddies propagate southward to about 40°S, the link between eddies shed by the EAC and eddies that propagate toward the GAB is unclear.

In this paper, we make a direct link between EAC anticyclonic eddies, that form in the EAC retroflection (~31°S) and leave the region, and anticyclonic eddies propagating toward the GAB (Figure 1, white line). Using data from an eddy-resolving, near-global ocean model and gridded sea level anomaly (SLA) maps, we manually track anticyclonic eddies that originate in the EAC retroflection and leave this formation region—and follow their evolution as they flow southward, adjacent to the continental slope, to the southern tip of Tasmania. This link between EAC eddies and eddies near the GAB has not been previously documented.

AGU Journal of Geophysical Research: Oceans 10.1002/2015JC011026

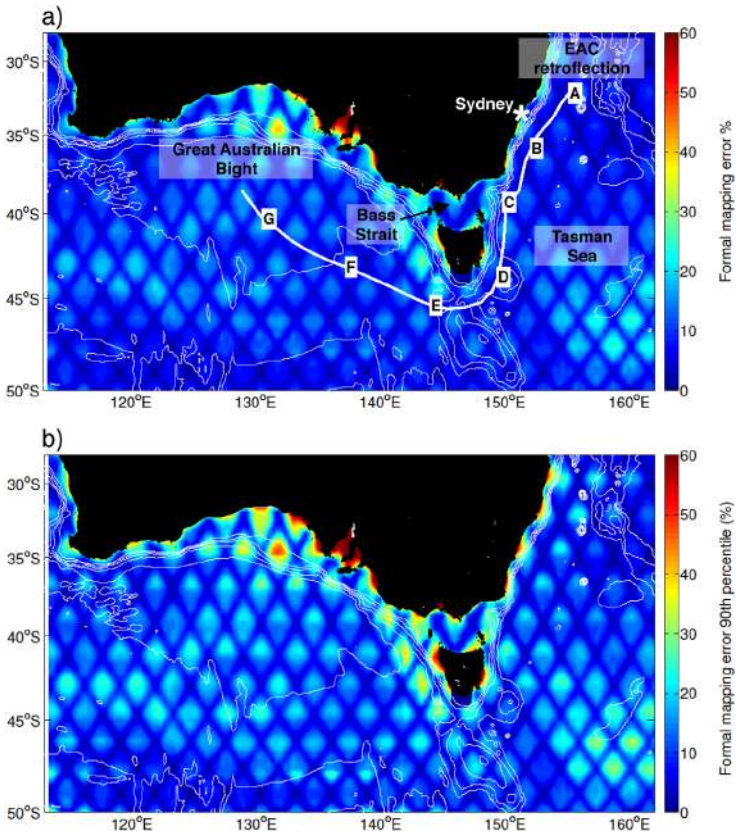


**Figure 1.** (a) Map of the time-averaged (1993–2012) and (b) 90th percentile formal mapping error, presented as a percentage of the signal variance, for the Aviso Reference Series SLA maps. White contours show topography from 1000 to 6000 m spaced every 1000 m. The thick white line denotes the eddy pathway that is discussed throughout this paper.

Details of the ocean model and observations used in this study are described in section 2, along with a description of our eddy-tracking method used here. Results are presented in section 3, where we look closely at the evolution of two ocean model eddies. Discussion and conclusions on our main findings are presented in section 4.

## 2. Data and Methods

### 2.1. Model

In this study, we use the output from the last 19 years of a 36 year run of the Ocean Forecasting Australian Model, version 3 (OFAM3) [*Oke et al.*, 2013]—a near-global eddy-resolving configuration of the GFDL Modular Ocean Model, version 4p1 [*Griffies et al.*, 2004]. The model has 1/10° horizontal grid spacing between 75°S and 75°N. The vertical grid is $z^*$, with 51 vertical levels, with 5 m spacing near the surface, 10 m spacing at 200 m depth, and coarser below that. OFAM3 is forced with 3 hourly surface heat, freshwater, and momentum fluxes from ERA-interim [*Dee and Uppala*, 2009], with restoring to monthly SST [*Reynolds et al.*, 2007, 10 day restoring time scale]; weak restoring to surface climatological salinity (180 day restoring) [*Ridgway and Dunn*, 2003]; and weak restoring to climatological temperature and salinity below 2000 m depth (restoring time scale of 180 days). *Oke et al.* [2013] provide a comprehensive description of all aspects of OFAM3, and show that the mean and variability of the model fields generally agree well with observations.

### 2.2. Observations

We supplement the analysis of the model fields with gridded SLA maps from two different products. We use SLA maps from the Aviso Reference Series (1/3° grid, 7 day maps using data from two altimeters [*Ducet et al.*, 2000]); and OceanCurrent (1/4° grid, 4 day maps using data from all available altimeters [*Deng et al.*,

AGU Journal of Geophysical Research: Oceans 10.1002/2015JC011026

2010]). We use OceanCurrent (an Australian data set produced by the Integrated Marine Observing System—IMOS) in addition to Aviso, because it has been extensively validated in the region of interest. Both Aviso and OceanCurrent use different versions of the same ~7 km resolution along-track altimetry (i.e., processed independently). The length scales used for the objective mapping range from 100 km in the zonal and meridional directions at 60°S–60°N, to 250 (350) km in the meridional (zonal) direction at the equator.

### 2.3. Limitations

Both the model and altimeter-based products used in this study have limitations. The model only represents a subset of the ocean variability. Horizontally, the model resolves features larger than ~50 km (five model grid points). Furthermore, the model has poor vertical resolution at depth, particularly below 2000 m, where temperature and salinity fields are restored to climatology [*Oke et al*., 2013]. For this reason, we restrict our analysis of the model fields to the top 2000 m. The model also has limitations associated with resolution and accuracy of surface forcing fields and topography. These limitations result in some systematic errors in the model, as described by *Oke et al*. [2013].

Although the altimetry gridded SLA fields are based on observations, they also have limitations. The altimeter products depend strongly on the assumed decorrelation length-scales and on the sampling of the altimeter tracks. For the Aviso Reference Series used here (i.e., maps produced by merging data from two satellites) the mapping error is below 10% of the signal variance for most of the study region (Figure 1a) [*Le Traon et al*., 1998], but can reach more than 25% of the signal variance (see the formal mapping error 90th percentile in Figure 1b). However, there are local maxima in the mapping error (Figure 1) that, as we will argue, have important implications for this study. The repeat cycle of different altimeters is between 10 and 35 days, and the average spacing between altimeter tracks in the merged product is about 40 km at midlatitudes. Consequently, it is reasonable to expect that the altimeter SLA maps do not reproduce all of the true mesoscale variability of the ocean. This means that analyses of the mesoscale ocean circulation based solely on SLA maps may sometimes be misleading. Indeed, the eddy pathway we identify in this study is not clear in gridded SLA fields or in SLA-derived products [e.g., *Chelton et al*., 2011]. We show that this lack of clarity in the observations is explained by relatively high mapping error at a key region along the identified EAC eddy pathway (e.g., off north-eastern and central-eastern Tasmania; see Figure 1). It is likely that this is why the eddy pathway we identify has not been previously documented.

### 2.4. Eddy Tracking

In this study, we track eddies manually. We chose this approach for two reasons. First, because we are analyzing only a small number of eddies we can afford to track each eddy carefully. This is crucial during complex "events," such as merging, observation gaps, and periods when the eddy becomes anisotropic. Second, the EAC is a challenging region for automated eddy-detection algorithms. Authors of different automated eddy-tracking methods [e.g., *Chaigneau et al*., 2008; *Chelton et al*., 2011] note that the algorithms are not perfect. Specifically, they note that such algorithms may perform poorly when eddies merge or when the flow field is particularly complex. We also note that manual tracking of features has a long history in atmospheric and meteorological research [e.g., *Hope et al*., 2014] and it has also been used to validate automatic eddy tracking in oceanographic research [e.g., *Chaigneau et al*., 2008; *Faghmous et al*., 2015]. However, even the manual tracking of eddies in this region was challenging—especially when using the observational products.

We recognize that manual tracking is somewhat subjective. To demonstrate the validity of the eddy tracks, we provide animations showing the evolution of modeled SLA fields for the study region and the tracked eddies using both modeled and observed fields (available online at http://www.youtube.com/GabrielaPilo).

In this study, we select anticyclonic eddies that form in the EAC retroflection region (~31°S). We track the selected eddy by locating closed positive SLA contours every 7 (OFAM3 and Aviso) or 4 (OceanCurrent) days. The center of the eddy is considered to be the location of the maximum positive SLA within the closed SLA contour. Consistent with the approach described by *Chelton et al*. [2011], we consider an eddy to be continuous in time if it is evident at consecutive time steps, with a tolerance of three time steps. That is, if the eddy is not clearly seen for three time steps, its trajectory is assumed to end.

AGU Journal of Geophysical Research: Oceans 10.1002/2015JC011026

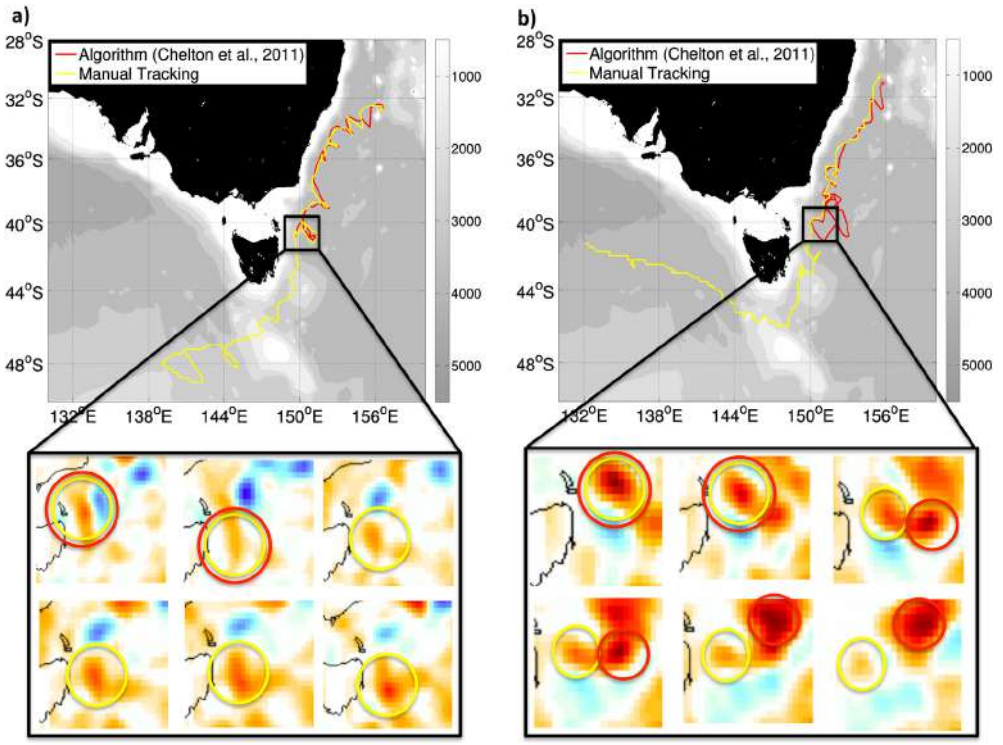


**Figure 2.** (a and b) Examples of eddy tracks using automated eddy detection (red) [*Chelton et al.*, 2011] and manual tracking (yellow). Eddies were tracked in Aviso Reference Series sea level anomaly (SLA) gridded data sets. The bottom plots show a sequence of weekly SLA maps spanning the time when the tracks diverge; yellow (red) circles show the eddy perimeters from the manual (automatic) approach.

Eddies merge with other eddies as they propagate. In this study, we assume that if one eddy merges with another eddy its trajectory continues. This assumption is consistent with the observations described by *Cresswell* [1982], where two EAC anticyclonic eddies merged and the resulting eddy had the properties of the original eddies—with two layers of different water masses stacked at different depths.

In general, as the eddies propagate they lose energy and SLA decreases along their path. We track each eddy until its SLA becomes smaller than 0.05 m in OFAM3 and 0.1 m in Aviso and OceanCurrent. We use a larger threshold for the observational products because they have a smaller signal-to-noise ratio, mainly due to sampling error. By contrast, the model does not include noise due to sampling error. The eddy trajectory is also terminated if the eddy can no longer be identified as a closed SLA contour feature.

We have undertaken a comparison of eddy tracks using *Chelton et al.* [2011]'s Global Eddy Dataset version 3, and our manual tracking of eddies. Our comparisons with Chelton's database show cases when tracks end prematurely (e.g., Figure 2a; eddy #145708), or jump to an adjacent (different) eddy (e.g., Figure 2b; eddy #188703). The colored maps in Figure 2 show SLA around the time when the different tracking methods yield different results. In the first case (Figure 2a), the eddy changes its shape for 4 weeks and is no longer considered the same eddy by the automated eddy-detection algorithm. In the second case (Figure 2b), the tracked eddy approaches a different (larger) eddy, but the two eddies do not merge. The automated eddy-detection algorithm subsequently tracks the other eddy instead (red circles in SLA maps in Figure 2b). The manual approach continues tracking the original eddy as it continues southward (yellow circles in SLA maps in Figure 2b).

After manually tracking the eddies, we then extract all model fields at each time step (i.e., sea level and three-dimensional fields of temperature, salinity, and three components of velocity) for an $8^\circ \times 8^\circ$ "box," centered on the eddy center. The eddy center is given by the local SLA maximum nearest the identified eddy location.

AGU Journal of Geophysical Research: Oceans 10.1002/2015JC011026

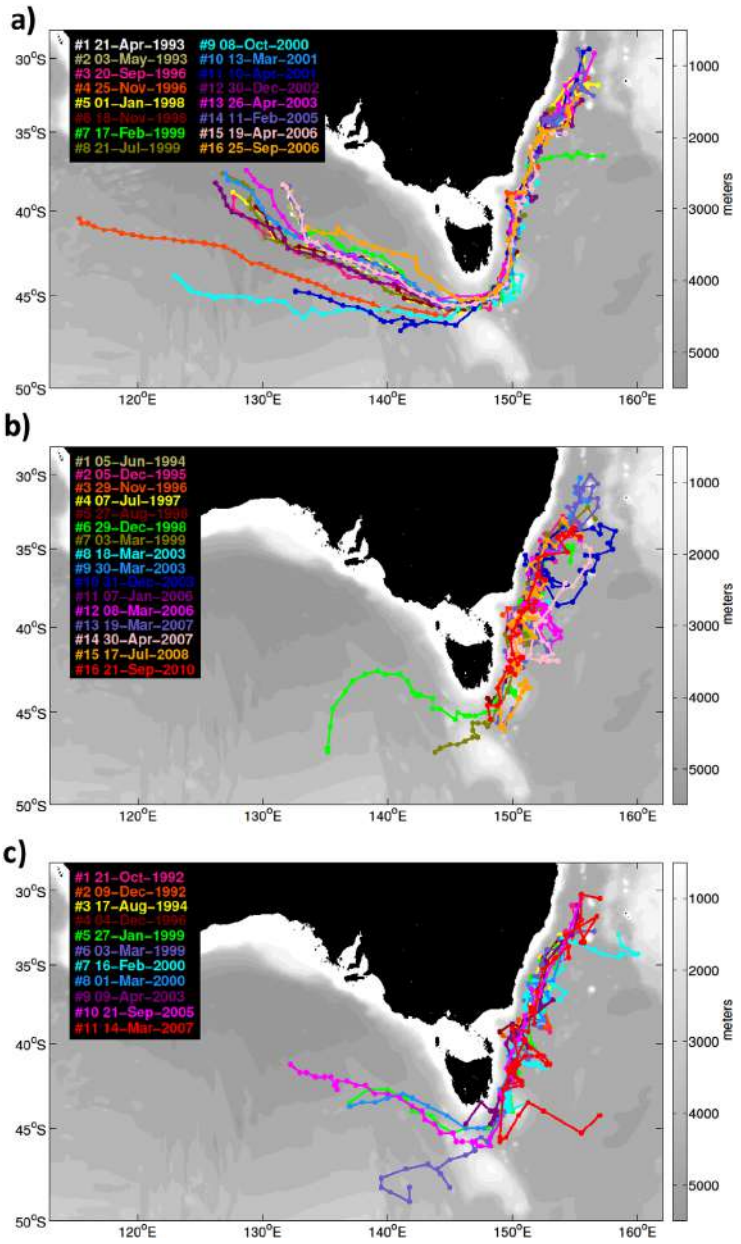


**Figure 3.** Tracks of anticyclonic eddies (colors) from (a) the model, (b) OceanCurrent, and (c) Aviso. Each eddy is identified in the legend by their start date. Gray shading denotes bathymetry and the dots along each path denote monthly time steps.

## 3. Results

### 3.1. Eddy Pathway

The tracks of the EAC anticyclonic eddies identified in the model and observations are displayed in Figure 3. In total, we track 16 eddies in the model, 16 eddies in OceanCurrent, and 11 eddies in Aviso. We find that many of the tracked eddies that leave the Tasman Sea follow a consistent pathway. This pathway begins in the EAC retroflection region, then extends southward, adjacent to the continental slope of south-eastern Australia, to the southern tip of Tasmania; and then continues toward the GAB. All 16 of the eddies tracked in the model roughly follow this pathway, 2 out of 16 eddies tracked in OceanCurrent, and 3 out of 11 eddies tracked in Aviso "survive" beyond Tasmania (i.e., only a 15–25% survival rate). We note that eddies

AGU Journal of Geophysical Research: Oceans 10.1002/2015JC011026

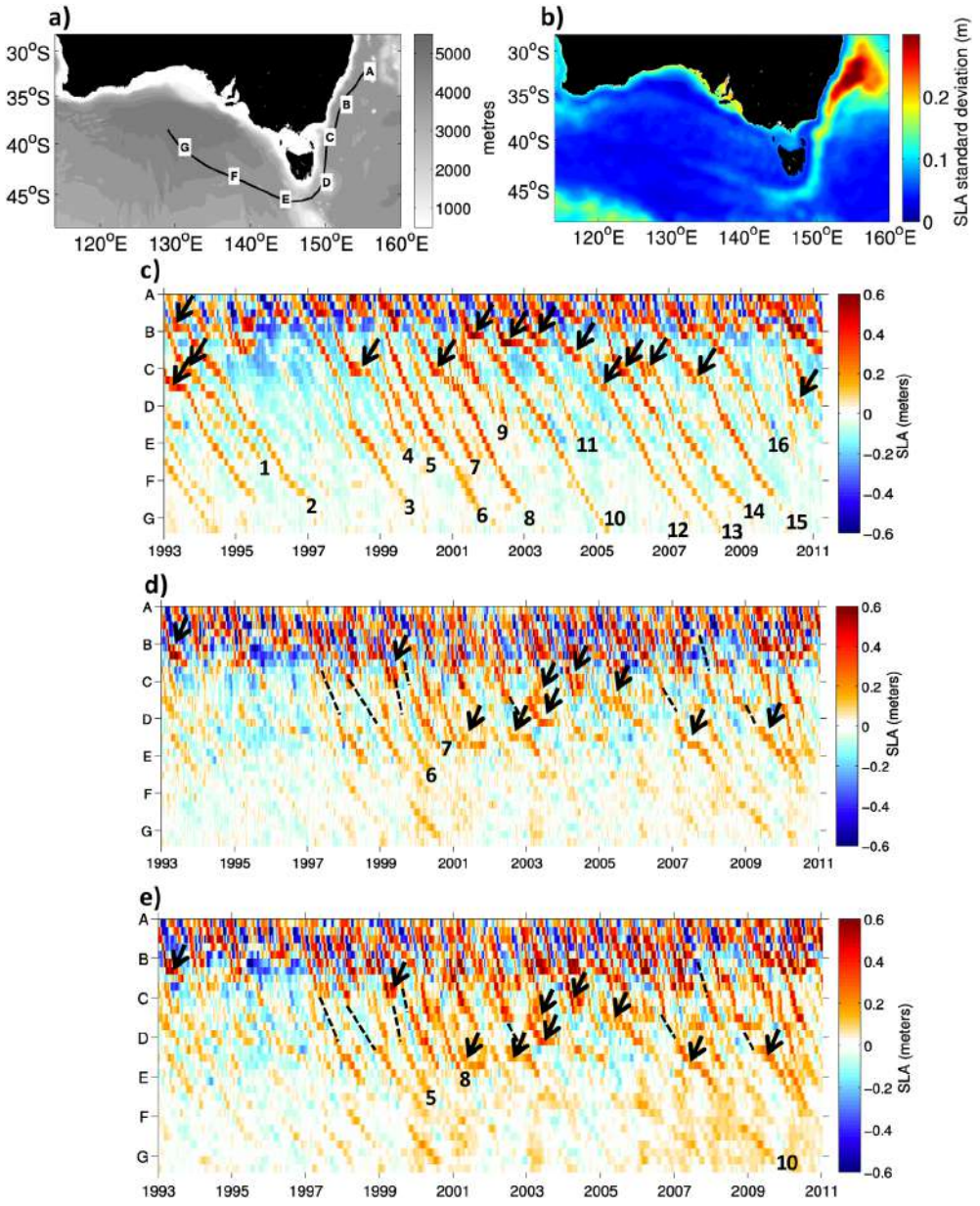


**Figure 4.** (a) Idealized pathway of anticyclonic eddies shed by the EAC retroflection in the model, overlaid on (a) bathymetry and (b) sea level anomaly (SLA) standard deviation from the model between 1993 and 2012 (colors). The letters (A to G) indicate key locations along the pathway. Hovmöller diagrams of SLA from (c) the model, (d) OceanCurrent, and (e) Aviso along A–G pathway with numbers relating to eddies from Figure 3; dashed lines indicate unresolved connections between observed eddies; black arrows denote moments when eddy propagation "stalls" along their path.

tracked in OceanCurrent and Aviso products are not always the same. This indicates that there are differences also between the observation-based products (due in part to different processing and number of altimeters used), and not only between the observations and the model.

To examine the temporal variability along the mean pathway—which is clearest in the model results (Figure 3a)—we produce Hovmöller diagrams of SLA from each data set along an idealized pathway (Figure 4). The idealized pathway (denoted A–G in Figure 4a) is not perfect, because the eddies do not always stay on this pathway (Figure 3). Despite this limitation, the evolution of positive SLAs along this idealized pathway is very clear in the model

AGU Journal of Geophysical Research: Oceans 10.1002/2015JC011026

**Table 1.** OFAM3 and Aviso Tracked Eddies' Mean Propagation Speed Between the EAC Retroflection Region and Off Sydney (A–B), Off Sydney and South of Tasmania (B–E), and at the Deep Basin South of Australia (E–G)[a]

| | A–B | B–E | E–G |
|---|---|---|---|
| OFAM3 | 5.5 ± 1.4 | 2.8 ± 0.4 | 3.2 ± 0.4 |
| Aviso | 8.0 ± 1.6 | 6.9 ± 1.4 | 3.6 ± 2.8 |

[a]Aviso's E–G section speed was calculated after four eddies only.

fields (Figure 4c), with all anomalies transiting beyond Tasmania, and 11 out of 16 making it to "G," along the pathway. These eddies take up to 5 years to complete their path.

Approximately 65–75 eddies are generated at the EAC retroflection region over a 19 year period [e.g., *Mata et al.*, 2006]. However, not all these eddies leave the region, remaining there and interacting with other eddies [*Mata et al.*, 2006]. In the model, 19 eddies formed in the EAC retroflection leave the Tasman Sea. Therefore, 25–30% of large anticyclonic eddies formed in the EAC retroflection leave the region and propagate southward, along the eddy pathway.

High SLA standard deviation values at the retroflection region are represented in the Hovmöller diagrams (Figure 4b; between "A" and "B"). Between these locations there is an alternance in cyclonic and anticyclonic eddies (negative and positive anomalies in Figures 4c–4e), indicating the high mesoscale activity.

The propagation of EAC anticyclonic eddies between "C" and "D" and beyond "E" is less clear in the observations (Figures 4d and 4e). However, we here suggest that eddies in the ocean do propagate along these paths—but, as they lose amplitude, their signal in the gridded products becomes less clear. Note that the section between C and D, in Figure 4a, spans a region where the mapping error is relatively high (between 20% and 25% of the signal variance and more than 25% in the 90th percentile; Figure 1). We denote (with black dashed lines in Figures 4c and 4d) several times when our analysis shows that eddies continue along the idealized pathway, despite a lack of signal in the gridded SLA in the observations. This is discussed further below.

Note that we do not expect an observed eddy to be evident in the model at the same time and location. This is because we are using fields from a "free" model run, with no data assimilation, and because eddy formation is somewhat chaotic. However, we do expect the model to generate eddies with realistic characteristics (size, shape, and amplitude), and we expect them to evolve in a manner consistent with observations (with a similar path, propagation speed, and time-evolution [*Oke et al.*, 2008; *Schiller et al.*, 2008; *Oke et al.*, 2013]).

As part of their southward propagation many of the eddies "stall" at some point. These events are denoted by black arrows in Figures 4c–4e. In the model fields, the eddies often stall near "B" and "C" locations, off Sydney and off Bass Strait, respectively. In the gridded SLA fields, 3–4 eddies stall around Bass Strait, and 4–5 eddies stall off south-eastern Tasmania (with just one stalling near Sydney). These "stalling" events often last for several months when EAC anticyclonic eddies are quasi-stationary.

We can see differences in eddies propagation speeds when looking at OFAM3 and the altimetry Hovmöler diagrams (Figure 4). These different speeds are summarized in Table 1, indicating that the propagation speed of the observed and modeled eddies are comparable when they first form and as they propagate toward the GAB; but the observed eddies propagate about twice as fast as the model eddies as they move southward toward Tasmania. In part, the discrepancy between B and E is because the modeled eddies tend to "stall" for longer than the observed eddies. However, we note that the propagation speeds of the model eddies are consistent with other reports of eddy propagation speeds in this region from other observational studies [e.g., *Zhang et al.*, 2014, see their Figure S2].

We noted above that several observed eddies moving along the idealized pathway appear discontinuous (see the dashed lines in Figures 4d and 4e). The location where the eddies "disappears" is often between "C" and "D," off eastern Tasmania (where the mapping error has a local maximum; Figure 1). We also note that the amplitude of the eddies when they "disappear" is small ($<$0.1 m), and hence close to the merged altimetry product resolution.

To test the altimetric sampling of the region off eastern Tasmania during periods of eddy transiting, we choose four eddies tracked in OceanCurrent gridded SLA maps (Figure 5). Two examples (Figures 5a and 5b) show cases when there is poor altimetric sampling and the eddies "disappear" in the region of relatively high mapping error (Figure 1). Two examples (Figures 5c and 5d) show cases when there is good altimetric

AGU Journal of Geophysical Research: Oceans 10.1002/2015JC011026

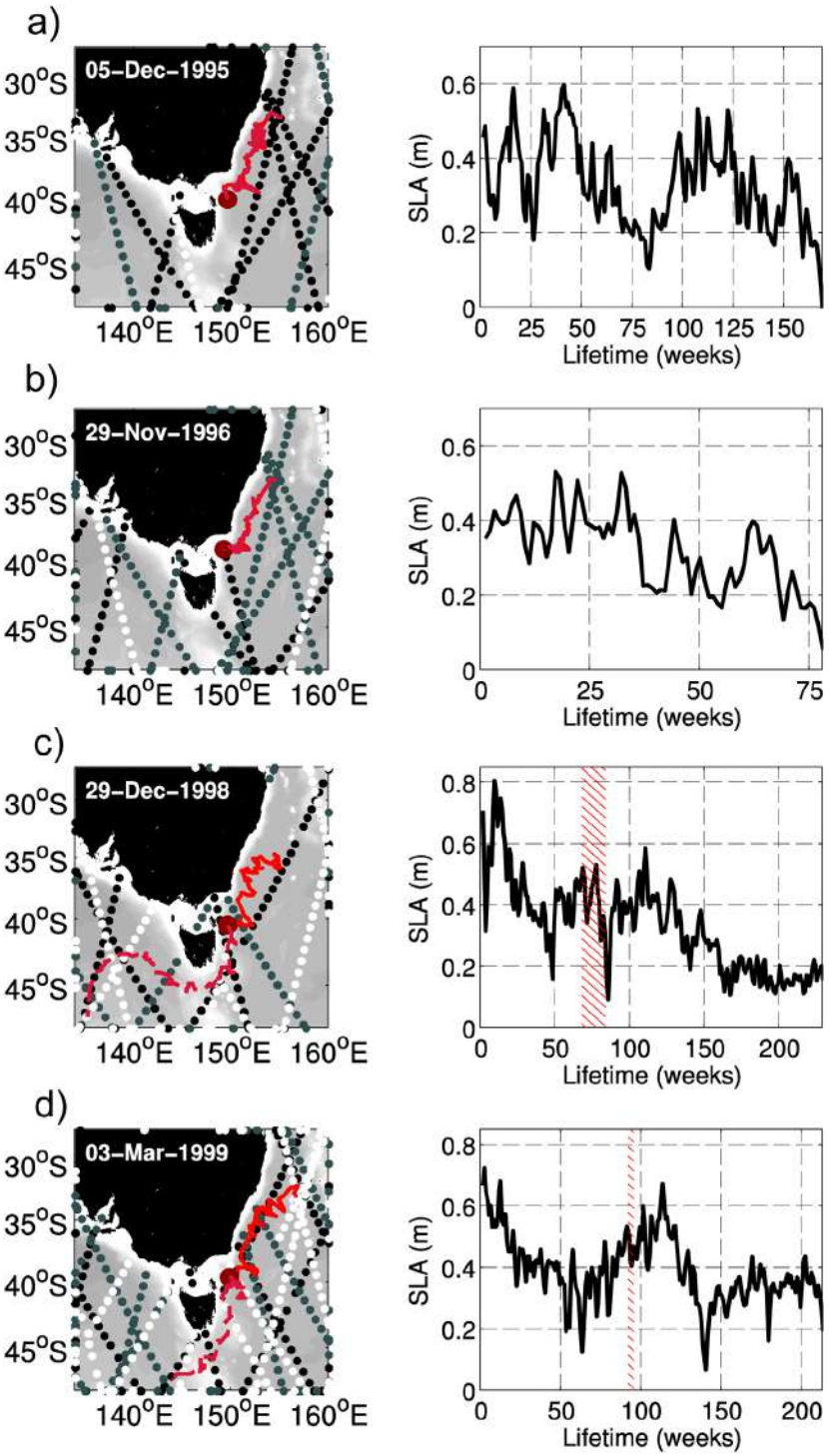


**Figure 5.** Maps of tracked eddies from OceanCurrent (left plots, red lines). The left plots in row show tracks that (a and b) end off Bass Strait and (c and d) extend beyond Tasmania. The dots show data points along altimeter tracks when eddies are off Bass Strait (time *t*). Black, gray and white dots denote times $t-2$, $t-1$, and *t*, respectively. The right plots show times series of sea level anomalies for each eddy. The hatched region indicates proximity to Bass Strait slope.

AGU Journal of Geophysical Research: Oceans 10.1002/2015JC011026

sampling and the eddy pathway continues beyond Tasmania. We show that eddies that dissipate (i.e., "disappear") off Bass Strait were under-sampled. Also, due to their reduced SLA (plots in Figure 5, showing SLA ~5 cm) they are not well resolved in the SLA gridding process, which has comparable errors (~5 cm). Therefore, we attribute this "disappearance" to relatively high mapping error and poor altimetric sampling of the region off eastern Tasmania during periods of eddy transit (see Figures 1 and 5).

The fact that the Hovmöller diagrams (Figures 4d and 4e) show these eddies "reappearing" at about the right time (assuming approximately steady southward propagation; see dashed lines) suggests that indeed the true eddies do regularly transit along the pathway. However, the gridded SLA altimetry fields do a relatively poor job of capturing this variability.

### 3.2. Eddy Evolution

To examine the temporal variability of sea surface properties along the mean pathway we produce Hovmöller diagrams of Sea Surface Temperature (SST; Figure 6), Sea Surface Salinity (SSS; Figure 7), and their anomalies (SSTA and SSSA) from the model along the idealized pathway.

A SST front between warm tropical waters from the Coral Sea (>22°C) and cold temperate waters from the Tasman Sea (<10°C) occurs in the region of interest (Figure 6a). The mean location of this front is at 40°S, extending further south off the eastern Australia coast, due to advection of warmer waters by the EAC and its eddies. Therefore, eddies propagating along the pathway are formed in warmer regions and propagate toward colder regions. The SSTA standard deviation displays higher values close to the EAC retroflection and southeast of Tasmania (Figure 6b). Here the seasonal signal was removed, therefore this variability is mainly attributed to local mesoscale variability.

The evolution of SST along the pathway has a strong seasonal signal (Figure 6c). This signal hinders the observation of eddies propagation on the SST Hovmöller diagram. Despite this hindering, it is possible to see the SST signature of the eddies previously seen in the model SLA Hovmöller diagram (Figure 4b) propagating along the pathway. With the seasonal signal removed, the SSTA associated with the eddies is clearer (Figure 6d). Due to their warm-core nature, EAC anticyclonic eddies are seen as a positive SSTA. Although less persistent than the eddies' positive SLA (Figure 4c), positive SSTA can be tracked as far as "F," off western Tasmania, in most cases (e.g., eddies 2, 3, 6, 8, 10, 12, 13).

A SSS front between saltier tropical waters from the Coral Sea (>35.6 psu) and fresh temperate waters from the Tasman Sea (<35 psu) occurs in this region (Figure 7a). The mean location of this front is at 40°S, extending further south off eastern Australia coast toward Tasmania. The eddy pathway transits through different SSS values, encountering saltier waters of the EAC and fresher waters south of Australia. The standard deviation of SSSA displays higher values close to the EAC retroflection, south of Tasmania and south of Western Australia (Figure 7b). This variability is not attributed to a seasonal signal. At the EAC retroflection, this variability can be explained by the variable location of the EAC itself. South of Tasmania, this variability can be explained by movements of the subtropical convergence [*Wyrtki*, 1960; *Ridgway and Dunn*, 2003].

The evolution of SSS along the pathway has no strong seasonal signal (Figure 7c). In this case, the salinity differences between the Coral and the Tasman Seas (between "C" and "D" in the SSS Hovmöller diagram) are the very clear. Even with this strong signal, the signature of the eddies' propagation along the pathway is evident. The saltier EAC water entrained by the eddies during their formation is retained along the entire pathway. Consideration of seasonal anomalies of SSS yields a clearer picture of the eddy propagation along the pathway (Figure 7d). However, after the "D" location we see a misleading increase in SSSA. This increase does not represent an increase in eddies' SSS, but a higher SSSA due to the eddy propagating along a highly variable region (Figure 7b).

#### 3.2.1. Case Studies

The Hovmöller diagrams (Figures 4c–4e) show that eddies' surface signals fluctuates with time. The eddies' SLA signal often slowly decreases as the eddies propagate, and sometimes increases over just a few weeks, both in the model and the observations. To better understand this, we present two detailed descriptions of model eddies, hereafter Eddy #3 and Eddy #9. These eddies are representative of the sample of model eddies included in this study (the same details for all model eddies are included in supporting information Figures S1–S14).

AGU Journal of Geophysical Research: Oceans 10.1002/2015JC011026

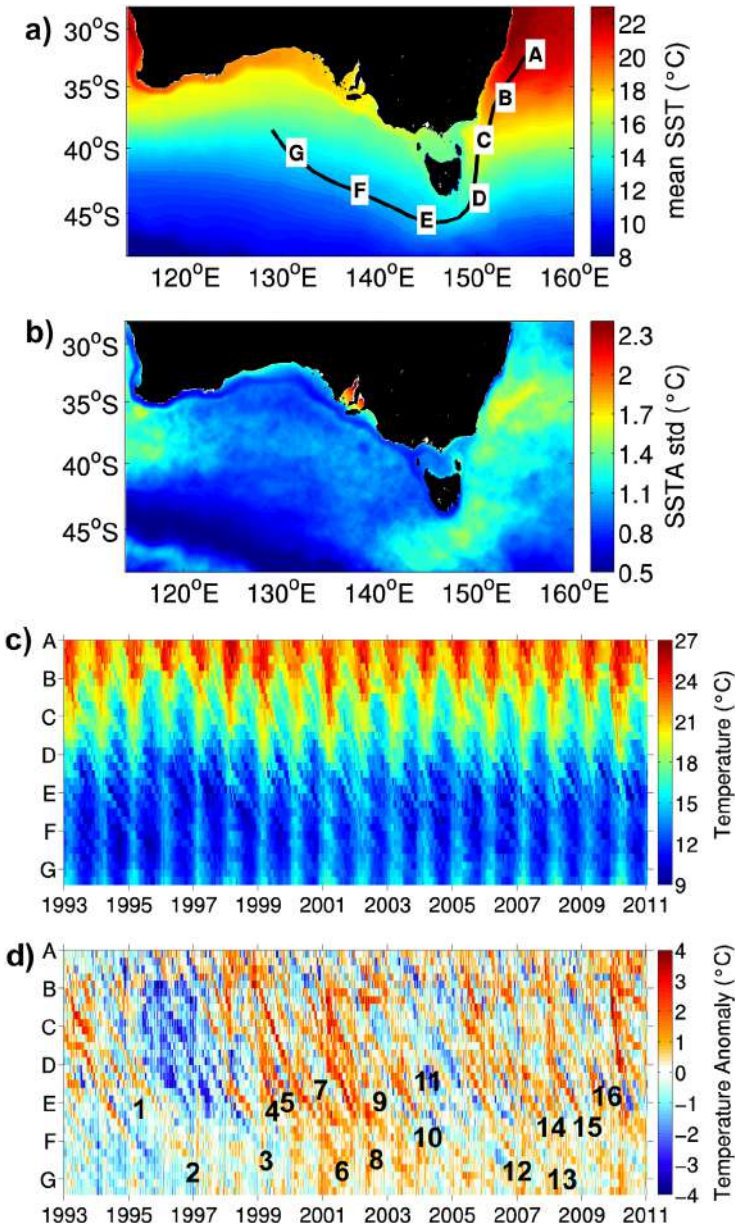


**Figure 6.** Eddies' surface temperature evolution; (a) idealized pathway of anticyclonic eddies shed by the EAC retroflection in the model, overlaid on mean sea surface temperature (SST) from the model between 1993 and 2012. The letters (A–G) indicate key locations along the pathway; (b) map of SST Anomaly (SSTA) standard deviation from the model between 1993 and 2012; (c) Hovmöller diagram of SST from the model along A–G pathway; (d) as for Figure 6c, but for SSTA with numbers relating to eddies from Figure 3a.

Here we show various eddy characteristics, including their amplitude, horizontal velocity vertical profile, and barotropic-baroclinic partitioning, as the eddies propagate along the pathway. To quantify the barotropic-baroclinic partitioning of the eddies as they evolve, we compute the normal vertical modes along their path (Figure 8c). This is achieved by solving the Sturm-Liouville eigenvalue problem [e.g., *Wunsch*, 1997; *Venaille et al.*, 2011], using the Coriolis parameter and profiles of velocity and the buoyancy frequency. At each time step, we use an average profile that is midway between the eddy center and the edge of the eddy to the east—usually about 100 km east of the eddy center. We then compute the ratio of the first and second eigenvalue to the sum of all eigenvalues, quantifying the percentage of the velocity profile that projects onto the zeroth mode (the barotropic mode) and the first baroclinic mode. Sensitivity

AGU Journal of Geophysical Research: Oceans 10.1002/2015JC011026

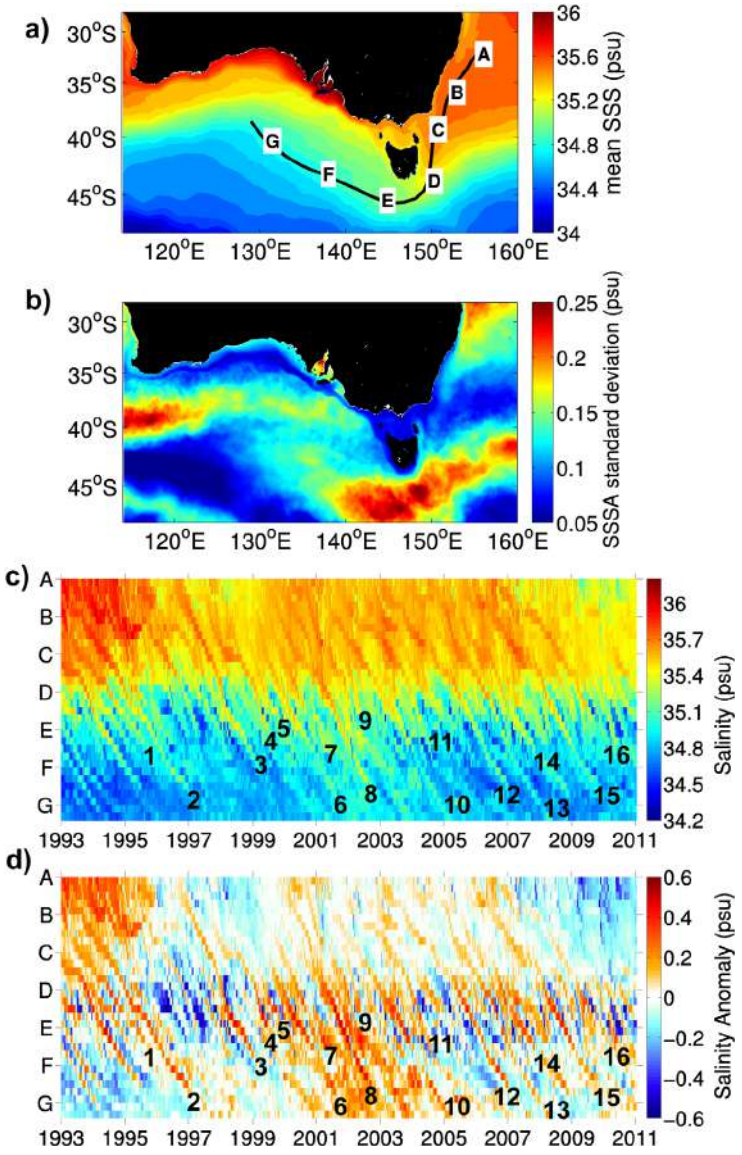


**Figure 7.** Eddies' surface salinity evolution; (a) as for Figure 6a, but for Sea Surface Salinity (SSS); (b) as for Figure 6b, but for SSS Anomaly (SSSA); (c) as for Figure 6c, but for SSS; (d) as for Figure 6d, but for SSSA.

tests indicate no significant difference when using average profiles on the eastern or western side of each eddy.

### 3.2.2. First Case Study: Eddy #3

Eddy #3's SLA changes as the eddy propagates (Figure 8a). When the eddy is between the EAC retroflection region ("A") and southeast of Tasmania ("D") the SLA varies between 0.17 and 0.45 m. SLA increases sharply after eddy merging events (red lines between "A" and "D"), but slowly decrease otherwise. After the eddy propagates beyond Tasmania the SLA decays, reaching ∼0.1 m before dissipating completely.

The eddy's horizontal velocity vertical profile also changes as it propagates along the pathway. To demonstrate that, we show snapshots of Eddy #3 immediately after it forms (Figure 8b, left), when it is located off Bass Strait (Figure 8b, middle), and when it propagates toward the GAB (Figure 8b, right). Immediately after formation the velocity field is surface-intensified with values of over 1 m/s, with moderate velocities penetrating to depths of about 1800 m, and with strong vertical shear—characteristic of a strongly baroclinic

AGU Journal of Geophysical Research: Oceans 10.1002/2015JC011026

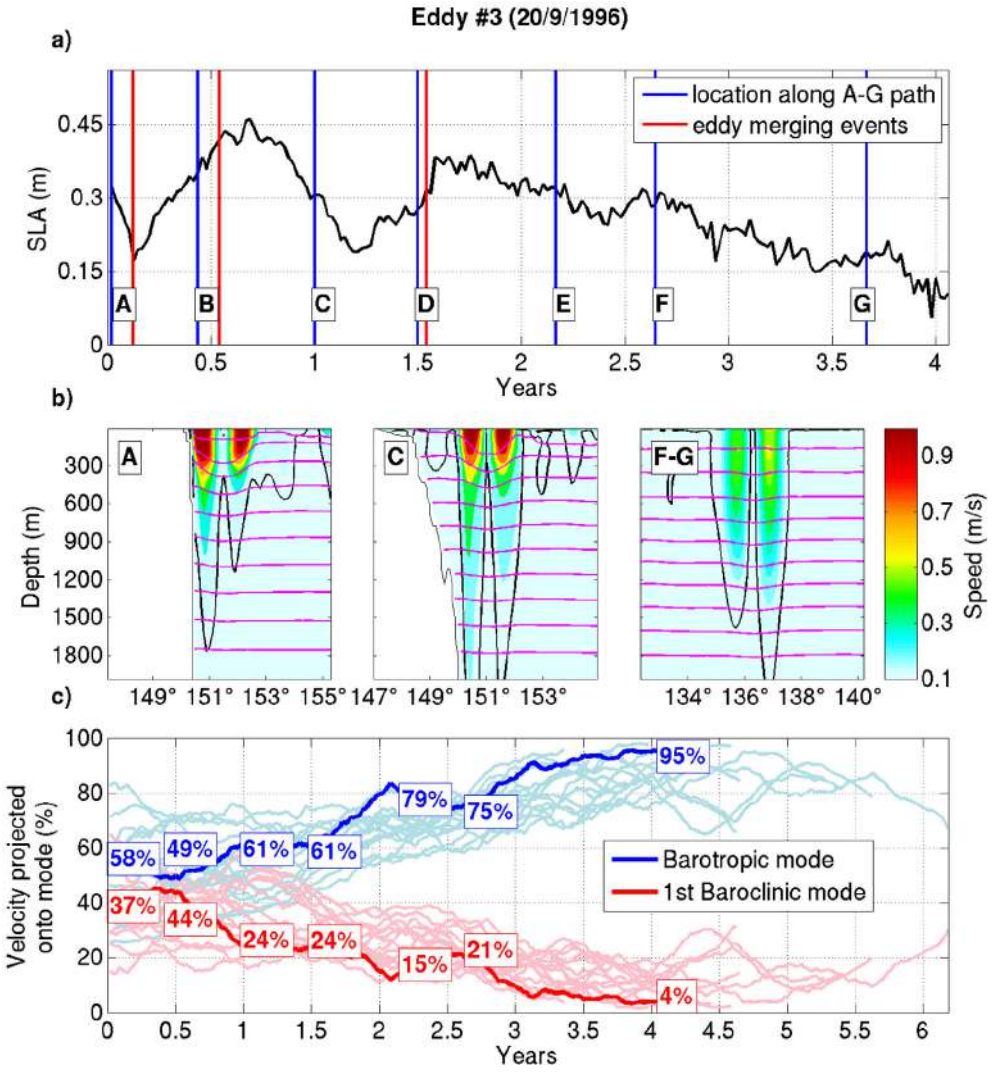


**Figure 8.** (a) Times series of SLA at the center of Eddy #3; (b) snapshots of velocity (color; black contour denoting 0.1 cm/s) and potential density (magenta contours; contour intervals are 0.1 kg/m$^3$) near "A," "C," and "F–G" locations; and (c) time series of the percentage of velocity that projects onto the barotropic (blue) and first baroclinic (red) modes for Eddy #3 (bold lines) and for all other model eddies (thin lines). The percentages at each point, "A–G," are denoted in boxes. Note that axes in subplots a and c are different.

flow. By the time Eddy #3 propagates to Bass Strait, it has weaker surface velocity, when compared to its formation period. The eddy still shows deep penetration of the velocities (over 2000 m), and weakening vertical shear. The eddy velocity is much weaker by the time it reaches the GAB, and is characterized by a velocity field that shows weak vertical shear—characteristic of a quasi-barotropic flow. Note that the maximum velocities are subsurface at "F-G"—centered around 200 m depth.

The velocity profiles suggest that the eddy is more baroclinic when it first forms, and becomes more barotropic as it propagates along the pathway. Low-pass filtered time series of the ratio of eigenvalues, quantifying the barotropic-baroclinic partitioning, are shown in Figure 8c, with results for Eddy #3 (bold lines) and for all other eddies (thin lines). The results in Figure 8c quantify what is evident in Figure 8b—namely that Eddy #3 becomes more barotropic along its path, with 58% of the velocity explained by the barotropic mode when the eddy forms, increasing to 95% as it approaches the GAB. Conversely, the percentage of the velocity field projecting onto the first baroclinic mode decreases from 37%, when Eddy #3 first forms, to 4% as it reaches the GAB.

AGU Journal of Geophysical Research: Oceans 10.1002/2015JC011026

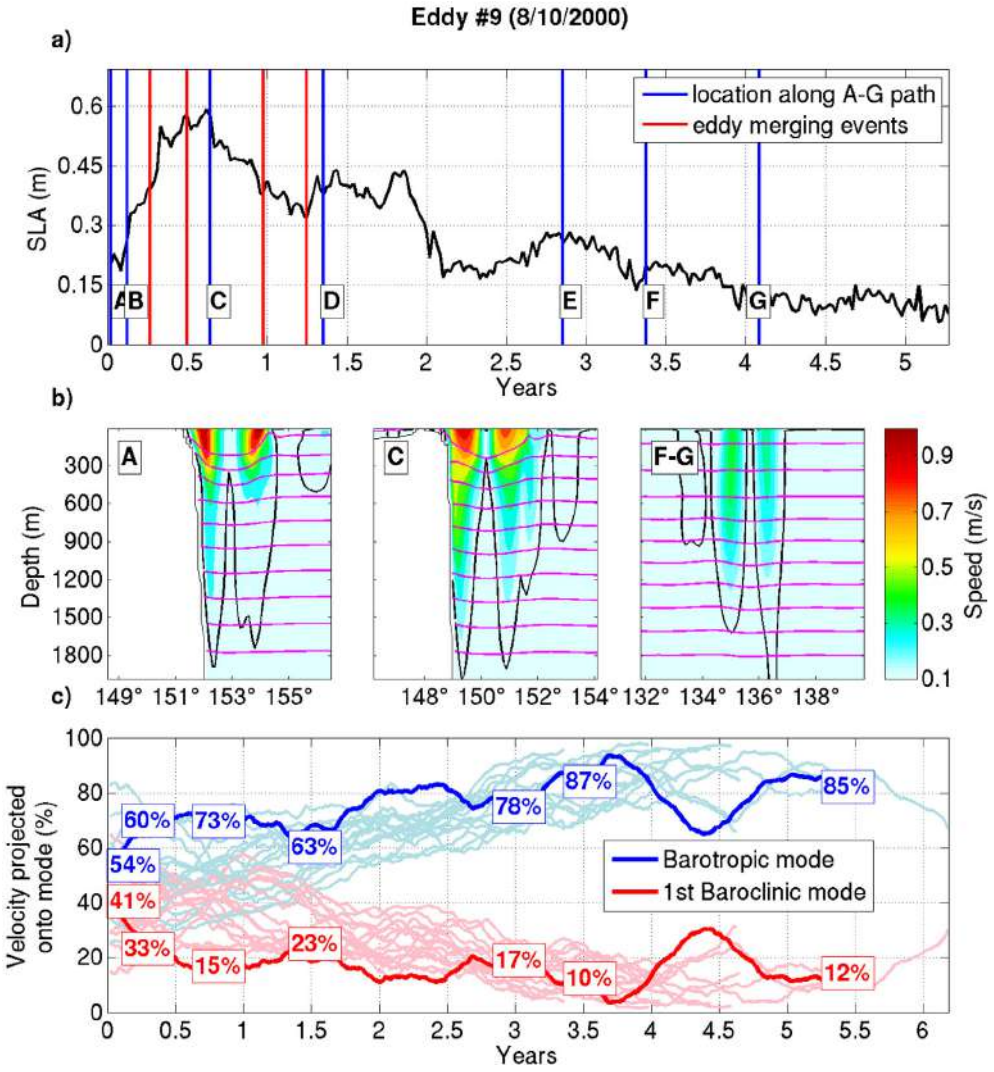


**Figure 9.** As in Figure 8, but for Eddy #9.

### 3.2.3. Second Case Study: Eddy #9

Eddy #9's SLA changes as the eddy propagates (Figure 9). Here on one merging event, there was no increase in eddy SLA. Similar to Eddy #3, the SLA varies between the EAC retroflection ("A") and southeast of Tasmania ("D"), decreasing almost monotonically when the eddy is propagating toward the GAB (i.e., after "E").

This eddy's vertical velocity profile also changes as it propagates along the pathway. Immediately after formation (Figure 9b, left) the velocity field is surface-intensified with values of ~0.8 m/s, with lower velocities penetrating deeper than 1800 m. The velocity profile for Eddy #9 is more asymmetric than for Eddy #3, with larger velocities penetrating deeper on its western flank. We believe this asymmetry to be caused by the eddy interaction with the continental slope, and further studies on this matter are underway. By the time Eddy #9 propagates to Bass Strait, it has weaker surface velocity when compared to its formation period. The eddy still shows deep penetration of the velocities (over 2000 m), and a much weaker vertical shear. The eddy velocity, as its vertical shear, is much weaker by the time it reaches the GAB. Here the maximum velocities are also subsurface—centered around 300 m depth.

Eddy #9 becomes more barotropic along its path, with 54% of the velocity explained by the barotropic mode when the eddy forms, increasing to ~80% before the eddy dissipates. Conversely, the percentage of

AGU Journal of Geophysical Research: Oceans 10.1002/2015JC011026

the velocity field projecting onto the first baroclinic mode decreases from 41%, when Eddy #9 first forms, to ~15% before the eddy dissipates.

From these two case studies (and also the eddies shown in the supporting information), we conclude that it is common for an eddy to merge at least 3 times along its path, with most merging events occurring in the Tasman Sea (before "D" in Figure 4). During merging events the SLA typically increases by 0.05–0.25 m. In between merging events, and after the eddy propagates beyond Tasmania, it is typical for an eddy to slowly decrease in amplitude, primarily owing to the loss of energy [e.g., *Flierl*, 1984; *Qiu et al.*, 1997; *McDonald*, 1998].

## 4. Discussion and Conclusions

In this study, we show that EAC long-lived anticyclonic eddies mostly follow a consistent pathway and leave the Tasman Sea. Specifically, we find that ~25–30% of anticyclonic eddies that form in the EAC retroflection region propagate southward, adjacent to the continental slope, and transit south of Tasmania. Besides advection by the EAC extension, *Shi and Nof* [1994] suggest that the "image effect" can be the driver for the propagation of EAC anticyclonic eddies southward. After crossing south of Tasmania, the eddies propagate west-north-westward, toward the GAB. This part of the pathway is consistent with the existing literature [*Ridgway and Dunn*, 2007; *Baird et al.*, 2011]. The west-north-westward propagation is also consistent with previous reports of anticyclonic eddy paths in other regions [e.g., *Morrow*, 2004; *Chelton et al.*, 2011]. Based on our analysis, we suggest that most EAC anticyclonic eddies that follow the identified pathway finally decay in the deep basin south of the GAB. However, *Cresswell and Peterson* [1993] sampled an anticyclonic eddy off the southern tip of Western Australia (~177°E) carrying Bass Strait waters. Their observations imply that some eddies have propagated further northwest, well beyond the pathway identified in our study.

The interaction between eddies and the mean flow has been extensively studied in Northern Hemisphere WBCs [e.g., *Waterman and Jayne*, 2011, and references therein], and in the Agulhas Current [e.g., *Biastoch and Krauss*, 1999; *de Ruijter et al.*, 1999], and to a smaller extent in the Brazil Current [*Oliveira et al.*, 2009; *Rocha et al.*, 2014] and in the East Australian Current [*Bowen et al.*, 2005; *Mata et al.*, 2006]. Within the EAC region, eddies might regulate the local recirculation where the current separates from the coast [*Mata et al.*, 2006].

In the EAC retroflection, newly formed eddies can either coalesce with the EAC [*Nilsson and Cresswell*, 1980] or grow and leave the region [*Mata et al.*, 2006; *Everett et al.*, 2012; *Pilo et al.*, 2015]. EAC anticyclonic eddies that coalesce with the EAC lose barotropic energy to the mean flow [*Mata et al.*, 2006]. EAC anticyclonic eddies that grow and leave the region receive both baroclinic and barotropic energy from the mean flow [*Bowen et al.*, 2005; *Mata et al.*, 2006]. As the eddies move southward their baroclinic energy is lost back to the mean flow [*Mata et al.*, 2006]. Our results are consistent with this energy loss in Figures 8 and 9, where eddies slowly decay after leaving the EAC retroflection and become less baroclinic as they propagate along the pathway. Exceptions to this slow eddy decay occur during eddy merging events, as shown here, and during eddy interactions with other local instabilities [*Mata et al.*, 2006]. The interaction between eddies and the mean flow is clearly important to EAC eddies, their evolution, and propagation. We plan to study the energetics of these interactions in the future.

We find that the SLA amplitude of these eddies fluctuates along the pathway. The primary cause of these fluctuations is merging with other eddies. Typically, a merging event results in an increase in the maximum SLA. In the absence of any merging events, the amplitude of the eddies gradually decrease, as expected [*Flierl*, 1984; *Qiu et al.*, 1997; *McDonald*, 1998]. We note that some of the eddies decay faster if they "stall" off Bass Strait. During those periods, the eddies often "push up" against the continental slope, remaining at a near-constant latitude for several months. We hypothesize that these eddies encounter stronger than usual bottom stress on the continental slope, explaining their enhanced decrease in amplitude. This "stalling" behavior has been previously reported by *Nilsson et al.* [1977]. The authors sampled one anticyclonic eddy off New South Wales (~35°S) that remains in the same region for 7 weeks. The volume of that eddy decreased by 10–30% during the stalling period. We are investigating changes in eddy amplitude and volume during "stalling" in more detail in another study.

While the SSTA signature of the eddies change as they propagate, decreasing in eddies' later life stages, the SSSA signature of the eddies persists along the pathway. The eddies' SSTA signature, although present, is weak. This weakness can be attributed to vertical mixing with cooler Tasman Sea waters, surface heat loss,

AGU Journal of Geophysical Research: Oceans 10.1002/2015JC011026

capping [*Tranter et al.*, 1980; *Cresswell and Legeckis*, 1986] and flooding effects [*Tranter et al.*, 1982; *Baird et al.*, 2011]. In the later stages of eddies' "lives" the SSTA is almost absent, when compared to the SLA signature. This may be due to the eddies' tendency to have a subsurface core during these final stages (Figures 8 and 9). The eddies' SSSA signal persists as eddies propagate along the pathway. Our SSSA Hovmöler diagram (Figure 7d) shows a freshening of waters close to the EAC retroflection ("A" location), as also seen in Argo floats data [*Rykova and Oke*, 2015].

Consideration of Hovmöller diagrams of different variables (Figures 4c, 6d, and 7d) reveals a different pattern between 1995 and 1997. During this period no eddies propagate along the pathway. Also, there are smaller values of SLA, SSTA, and SSSA when compared to post-1997 years. The 1995–1997 period is associated with a reduced southward EAC transport and increased eastward Tasman Front transport [*Ridgway et al.*, 2008; *Hill et al.*, 2011]. We expect that a weaker EAC transport may lead to fewer eddies being shed and a smaller magnitude of SSTA and SSSA in that region.

We find that altimetry sampling is problematic off eastern Tasmania (Figure 1). There are relatively long periods when no altimeter tracks cross the described eddy pathway, resulting in a local maximum in the mapping error of the gridded SLA (see Figure 1). As a result, this identified eddy pathway has not been documented previously. This study, instead, made use of an eddy-resolving ocean model output (which of course is imperfect, but has sufficient spatiotemporal coverage for studies of mesoscale variability) to complement the analysis of observation-based gridded SLA fields. This allowed us to see the eddy pathway more clearly.

The EAC anticyclonic eddy pathway shown here provides a direct connection, albeit over several years, between the EAC retroflection region and the GAB. Thus, it allows for advection of EAC waters well beyond the Tasman Sea. As the eddies propagate southward, they interact with different regions along the Australian continental shelf break. This interaction can lead to local changes in ocean temperature and biogeochemistry, that ultimately affect habitat conditions for the marine biota.

**Acknowledgments**

Gabriela S. Pilo acknowledges support by the CAPES Foundation, Brazilian Ministry of Education (grant 0520-13-6). The authors gratefully acknowledge input from Maxim Nikurashin, that led to improvements in this work, and the comments from both anonymous reviewers. The Reference Series' Aviso altimeter products were produced by Ssalto/Duacs and distributed by Aviso, with support from Cnes (http://www.aviso.altimetry.fr/duacs, downloaded in September/2013). The Ocean Current altimeter products were produced by CSIRO and distributed by the Integrated Marine Observing System (http://oceancurrent.imos.org.au, downloaded in February/2014). OFAM3 was developed under Bluelink: a partnership between CSIRO, the Bureau of Meteorology, and the Royal Australian Navy (http://wp.csiro.au/bluelink/, downloaded in January/2014). The global eddy data set was developed and made freely available by D. Chelton and M. Schlax (cioss.coas.oregonstate.edu/eddies/, downloaded in December/2011).

## References

Baird, M. E., and K. R. Ridgway (2012), The southward transport of sub-mesoscale lenses of Bass Strait Water in the centre of anti-cyclonic mesoscale eddies, *Geophys. Res. Lett.*, *39*, L02603, doi:10.1029/2011GL050643.

Baird, M. E., I. M. Suthers, D. A. Griffin, B. Hollings, C. Pattiaratchi, J. D. Everett, M. Roughan, K. Oubelkheir, and M. Doblin (2011), The effect of surface flooding on the physicalbiogeochemical dynamics of a warm-core eddy off southeast Australia, *Deep Sea Res., Part II*, *58*(5), 592–605, doi:10.1016/j.dsr2.2010.10.002.

Biastoch, A., and W. Krauss (1999), The role of mesoscale eddies in the source regions of the Agulhas Current, *J. Phys. Oceanogr.*, *29*(9), 2303–2317, doi:10.1175/1520-0485(1999)029<2303:TROMEI>2.0.CO;2.

Bowen, M. M., J. L. Wilkin, and W. J. Emery (2005), Variability and forcing of the East Australian Current, *J. Geophys. Res.*, *110*, C03019, doi:10.1029/2004JC002533.

Chaigneau, A., A. Gizolme, and C. Grados (2008), Mesoscale eddies off Peru in altimeter records: Identification algorithms and eddy spatio-temporal patterns, *Prog. Oceanogr.*, *79*(2–4), 106–119, doi:10.1016/j.pocean.2008.10.013.

Chelton, D. B., M. G. Schlax, and R. M. Samelson (2011), Global observations of nonlinear mesoscale eddies, *Prog. Oceanogr.*, *91*(2), 167–216, doi:10.1016/j.pocean.2011.01.002.

Cresswell, G. R. (1982), The coalescence of two East Australian current warm-core eddies, *Science*, *215*(4529), 161–164, doi:10.1126/science.215.4529.161.

Cresswell, G. R., and R. Legeckis (1986), Eddies off southeastern Australia, *Deep Sea Res., Part A*, *33*(11/12), 1527–1562, doi:10.1016/0198-0149(86)90066-X.

Cresswell, G. R., and J. Peterson (1993), The Leeuwin Current south of Western Australia, *Aust. J. Mar. Freshwater Res.*, *44*(2), 285–303, doi:10.1071/MF9930285.

Dee, D. P., and S. Uppala (2009), Variational bias correction of satellite radiance data in the ERA-interim reanalysis, *Q. J. R. Meteorol. Soc.*, *135*(644), 1830–1841, doi:10.1002/qj.493.

Deng, X., D. A. Griffin, K. Ridgway, J. A. C. W. E. Featherstone, N. J. White, and M. Cahill (2010), Satellite altimetry for geodetic, oceanographic and climate studies in the Australian region, in *Coastal Altimetry*, edited by P. C. S. Vignudelli, A. G. Kostianoy, and J. Benveniste, pp. 473–508, Springer, Berlin.

de Ruijter, W. P. M., P. J. van Leeuwen, and J. R. E. Lutjeharms (1999), Generation and evolution of natal pulses: Solitary meanders in the Agulhas current, *J. Phys. Oceanogr.*, *29*(12), 3043–3055, doi:10.1175/1520-0485(1999)029<3043:GAEONP>2.0.CO;2.

Ducet, N., P. Y. Le Traon, and G. Reverdin (2000), Global high-resolution mapping of ocean circulation from TOPEX/Poseidon and ERS-1 and −2, *J. Geophys. Res.*, *105*(C8), 19,477–19,498, doi:10.1029/2000JC900063.

Everett, J. D., M. E. Baird, P. R. Oke, and I. M. Suthers (2012), An avenue of eddies: Quantifying the biophysical properties of mesoscale eddies in the Tasman Sea, *Geophys. Res. Lett.*, *39*, L16608, doi:10.1029/2012GL053091.

Faghmous, J. H., I. Frenger, Y. Yao, R. Warmka, A. Lindell, and V. Kumar (2015), A daily global mesoscale ocean eddy dataset from satellite altimetry, *Sci. Data*, *2*, 150028, doi:10.1038/sdata.2015.28.

Flierl, G. R. (1984), Rossby wave radiation from a strongly nonlinear warm eddy, *J. Phys. Oceanogr.*, *14*, 47–58.

Godfrey, J. S., G. R. Cresswell, T. J. Golding, A. F. Pearce, and R. Boyd (1980), The separation of the East Australian Current, *J. Phys. Oceanogr.*, *10*(3), 430–440, doi:10.1175/1520-0485(1980)010<0430:TSOTEA>2.0.CO;2.

AGU Journal of Geophysical Research: Oceans 10.1002/2015JC011026

Griffies, S. M., M. L. Harrison, R. C. Pacanowski, and A. Rosati (2004), A technical guide to MOM4, *GFDL Ocean Group Tech. Rep. 5*, NOAA/Geophys. Fluid Dyn. Lab. [Available at www.gfdl.noaa.gov.]

Griffiths, F., and S. Brandt (1983), Mesopelagic crustacea in and around a warm-core eddy in the Tasman Sea off eastern Australia, *Aust J. Mar. Freshwater Res.*, *34*(4), 609–623, doi:10.1071/MF9830609.

Hill, K. L., S. R. Rintoul, K. R. Ridgway, and P. R. Oke (2011), Decadal changes in the South Pacific western boundary current system revealed in observations and ocean state estimates, *J. Geophys. Res.*, *116*, C01009, doi:10.1029/2009JC005926.

Hope, P., K. Keay, M. Pook, J. Catto, I. Simmonds, G. Mills, P. McIntosh, J. Risbey, and G. Berry (2014), A comparison of automated methods of front recognition for climate studies: A case study in Southwest Western Australia, *Mon. Weather Rev.*, *142*(1), 343–363, doi:10.1175/MWR-D-12-00252.1.

Jayne, S. R., and J. Marotzke (2002), The oceanic eddy heat transport, *J. Phys. Oceanogr.*, *32*(12), 3328–3345, doi:10.1175/1520-0485(2002)032<3328:TOEHT>2.0.CO;2.

Le Traon, P.-Y., F. Nadal, and N. Ducet (1998), An improved mapping method of multisatellite altimeter data, *J. Atmos. Oceanic Technol.*, *15*(2), 522–534, doi:10.1175/1520-0426(1998)015<0522:AIMMOM>2.0.CO;2.

Mata, M. M., S. E. Wijffels, J. A. Church, and M. Tomczak (2006), Eddy shedding and energy conversions in the East Australian Current, *J. Geophys. Res.*, *111*, C09034, doi:10.1029/2006JC003592.

McDonald, N. R. (1998), The decay of cyclonic eddies by Rossby wave radiation, *J. Fluid Mech.*, *361*, 237–252, doi:10.1017/S0022112098008696.

Morrow, R. (2004), Divergent pathways of cyclonic and anti-cyclonic ocean eddies, *Geophys. Res. Lett.*, *31*, L24311, doi:10.1029/2004GL020974.

Nilsson, C., and G. Cresswell (1980), The formation and evolution of East Australian current warm-core eddies, *Prog. Oceanogr.*, *9*(3), 133–183, doi:10.1016/0079-6611(80)90008-7.

Nilsson, C. S., S. C. Andrews, and P. Scully-Power (1977), Observations of eddy formation off East Australia, *J. Phys. Oceanogr.*, *7*(5), 659–669, doi:10.1175/1520-0485(1977)007<0659:OOEFOE>2.0.CO;2.

Oke, P. R., G. B. Brassington, D. A. Griffin, and A. Schiller (2008), The Bluelink ocean data assimilation system (BODAS), *Ocean Modell.*, *21*(1–2), 46–70, doi:10.1016/j.ocemod.2007.11.002.

Oke, P. R., et al. (2013), Evaluation of a near-global eddy-resolving ocean model, *Geosci. Model Dev.*, *6*, 591–615, doi:10.5194/gmd-6-591-2013.

Oliveira, L. R., A. R. Piola, M. M. Mata, and I. D. Soares (2009), Brazil Current surface circulation and energetics observed from drifting buoys, *J. Geophys. Res.*, *114*, C10006, doi:10.1029/2008JC004900.

Pilo, G. S., M. M. Mata, and J. L. L. Azevedo (2015), Eddy surface properties and propagation at Southern Hemisphere western boundary current systems, *Ocean Sci.*, *11*(4), 629–641, doi:10.5194/os-11-629-2015.

Qiu, B., W. Miao, and P. Muller (1997), Propagation and decay of forced and free baroclinic Rossby waves in off-equatorial oceans, *J. Phys. Oceanogr.*, *27*(11), 2405–2417, doi:10.1175/1520-0485(1997)027<2405:PADOFA>2.0.CO;2.

Reynolds, R. W., T. M. Smith, C. Liu, D. B. Chelton, K. S. Casey, and M. G. Schlax (2007), Daily high-resolution-blended analyses for sea surface temperature, *J. Clim.*, *20*(22), 5473–5496, doi:10.1175/2007JCLI1824.1.

Ridgway, K. R., and J. R. Dunn (2003), Mesoscale structure of the mean East Australian Current system and its relationship with topography, *Prog. Oceanogr.*, *56*(2), 189–222, doi:10.1016/S0079-6611(03)00004-1.

Ridgway, K. R., and J. R. Dunn (2007), Observational evidence for a Southern Hemisphere oceanic supergyre, *Geophys. Res. Lett.*, *34*, L13612, doi:10.1029/2007GL030392.

Ridgway, K. R., and J. S. Godfrey (1997), Seasonal cycle of the East Australian Current, *J. Geophys. Res.*, *102*(C10), 22,921–22,936.

Ridgway, K. R., R. C. Coleman, R. J. Bailey, and P. Sutton (2008), Decadal variability of East Australian Current transport inferred from repeated high-density XBT transects, a CTD survey and satellite altimetry, *J. Geophys. Res.*, *113*, C08039, doi:10.1029/2007JC004664.

Rocha, C. B., I. C. A. Da Silveira, B. M. Castro, and J. A. M. Lima (2014), Vertical structure, energetics, and dynamics of the Brazil Current System at 22S-28S, *J. Geophys. Res. Oceans*, *119*, 52–69, doi:10.1002/2013JC009143.

Rykova, T., and P. R. Oke (2015), Recent freshening of the East Australian Current and its eddies, *Geophys. Res. Lett.*, *42*, doi:10.1002/2015GL066050, in press.

Schiller, A., P. Oke, G. Brassington, M. Entel, R. Fiedler, D. Griffin, and J. Mansbridge (2008), Eddy-resolving ocean circulation in the Asian-Australian region inferred from an ocean reanalysis effort, *Prog. Oceanogr.*, *76*(3), 334–365, doi:10.1016/j.pocean.2008.01.003.

Shi, C., and D. Nof (1994), The destruction of lenses and generation of wodons, *J. Phys. Oceanogr.*, *24*(6), 1120–1136, doi:10.1175/1520-0485(1994)024<1120:TDOLAG>2.0.CO;2.

Tranter, D. J., R. R. Parker, and G. R. Cresswell (1980), Are warm-core eddies unproductive?, *Nature*, *284*, 540–542, doi:10.1038/284540a0.

Tranter, D. J., G. S. Leech, and D. J. Vaudrey (1982), Biological significance of surface flooding in warm-core ocean eddies, *Nature*, *297*(5867), 572–574, doi:10.1038/297572a0.

Venaille, A., G. Vallis, and K. S. Smith (2011), Baroclinic turbulence in the ocean: Analysis with primitive equation and quasigeostrophic simulations, *J. Phys. Oceanogr.*, *41*, 1605–1623, doi:10.1175/JPO-D-10-05021.1.

Waterman, S., and S. R. Jayne (2011), Eddy-mean flow interactions in the along-stream development of a western boundary current jet: An idealized model study, *J. Phys. Oceanogr.*, *41*(4), 682–707, doi:10.1175/2010JPO4477.1.

Wunsch, C. (1997), The vertical partition of oceanic horizontal kinetic energy, *J. Phys. Oceanogr.*, *27*(8), 1770–1794.

Wunsch, C. (1999), Where do ocean eddy heat fluxes matter?, *J. Geophys. Res.*, *104*(C6), 13,235–13,249.

Wyrtki, B. (1960), The surface circulation in the coral and Tasman Seas, *Tech. Pap. 8, Div. Fish. Oceanogr.*, Cronulla, Australia.

Zhang, Z., W. Wang, and B. Qiu (2014), Oceanic mass transport by mesoscale eddies, *Science*, *345*(6194), 322–324, doi:10.1175/2459.1.

# Appendix B: Supporting Information for "Do East Australian Current anticyclonic eddies leave the Tasman Sea?"

JOURNAL OF GEOPHYSICAL RESEARCH

# Supporting Information for "Do East Australian Current eddies leave the Tasman Sea?"

DOI: XX.XXXX

Gabriela S. Pilo[1,2], Peter R. Oke[2], Tatiana Rykova[2], Richard Coleman[1,3],

Ken Ridgway[2]

**Contents of this file**

1. Text S1 – S14

2. Figures S1 – S14

**Introduction**

---

Corresponding author: Gabriela Pilo, UTAS, Hobart TAS 7001, Australia. (Gabriela.SemoliniPilo@utas.edu.au)

[1]Institute for Marine and Antarctic

Studies, University of Tasmania, Hobart

TAS 7001, Australia

[2]CSIRO Oceans and Atmosphere

Flagship, Hobart, Australia.

[3]Antarctic Climate and Ecosystems CRC,

Hobart TAS 7001, Australia.

The Supporting Information contains 14 figures. These figures are the same as Figures 8 and 9 in the manuscript, but for all eddies tracked in the model - summarising some key aspects of each eddy's evolution.

**Text S1– 14.**

In the manuscript we select Eddies #3 and #9 as case studies. Here we show the same analysis for the remaining 14 eddies tracked in the model. All eddies display similar characteristics as they evolve, with changes in amplitude (SLA) due to merging events (Figures 8a and 9a and Figures S1a–S14a) and general decay otherwise. Also, the velocity fields associated with each eddy generally becomes more barotropic and less baroclinic along their path .

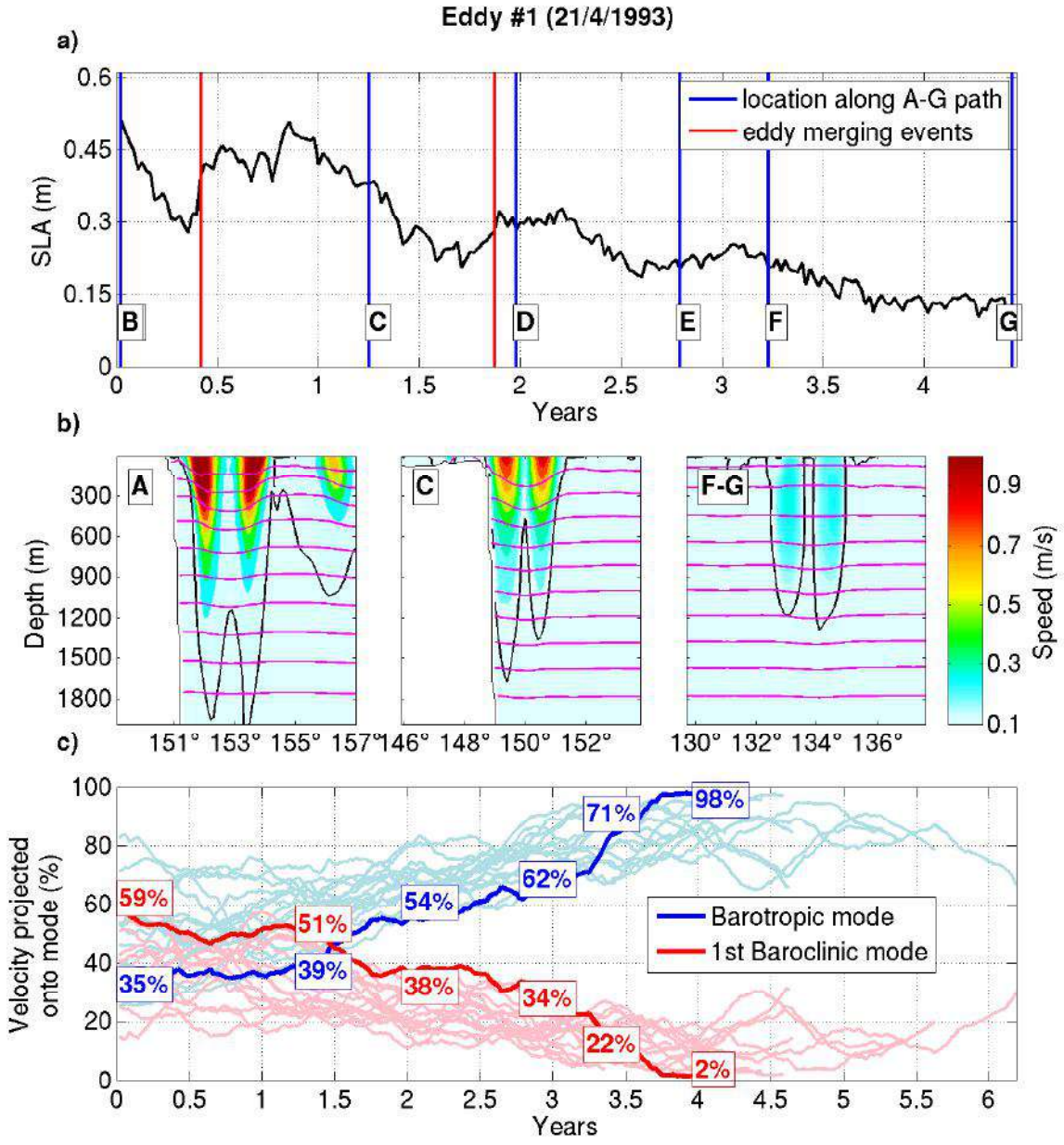


**Figure S1.** Times series of SLA at the centre of Eddy#1; (b) Snapshots of velocity (colour; black contour denoting 0.1 cm/s) and potential density (magenta contours; contour intervals are 0.1 kg/m$^3$) near points "A", "C" and "F-G" locations; and (c) time-series of the percentage of velocity that projects onto the barotropic (blue) and 1st baroclinic (red) modes for Eddy#1 (bold lines) and for all other model eddies (thin lines). The percentages at each point, A–G, are denoted in boxes. Note that axes in subplots a and c are different.

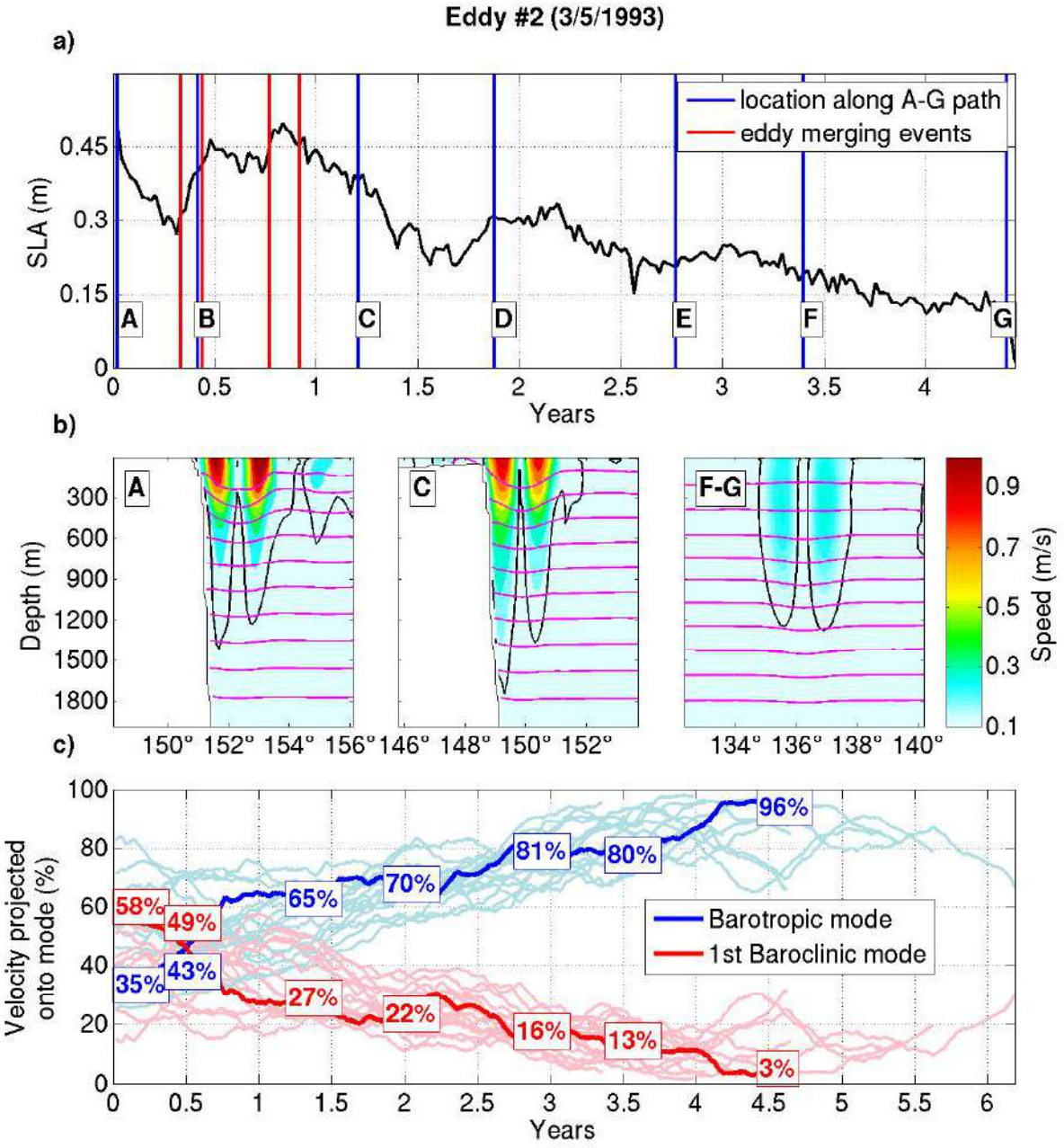


**Figure S2.** As for Figure S1, except for Eddy#2.

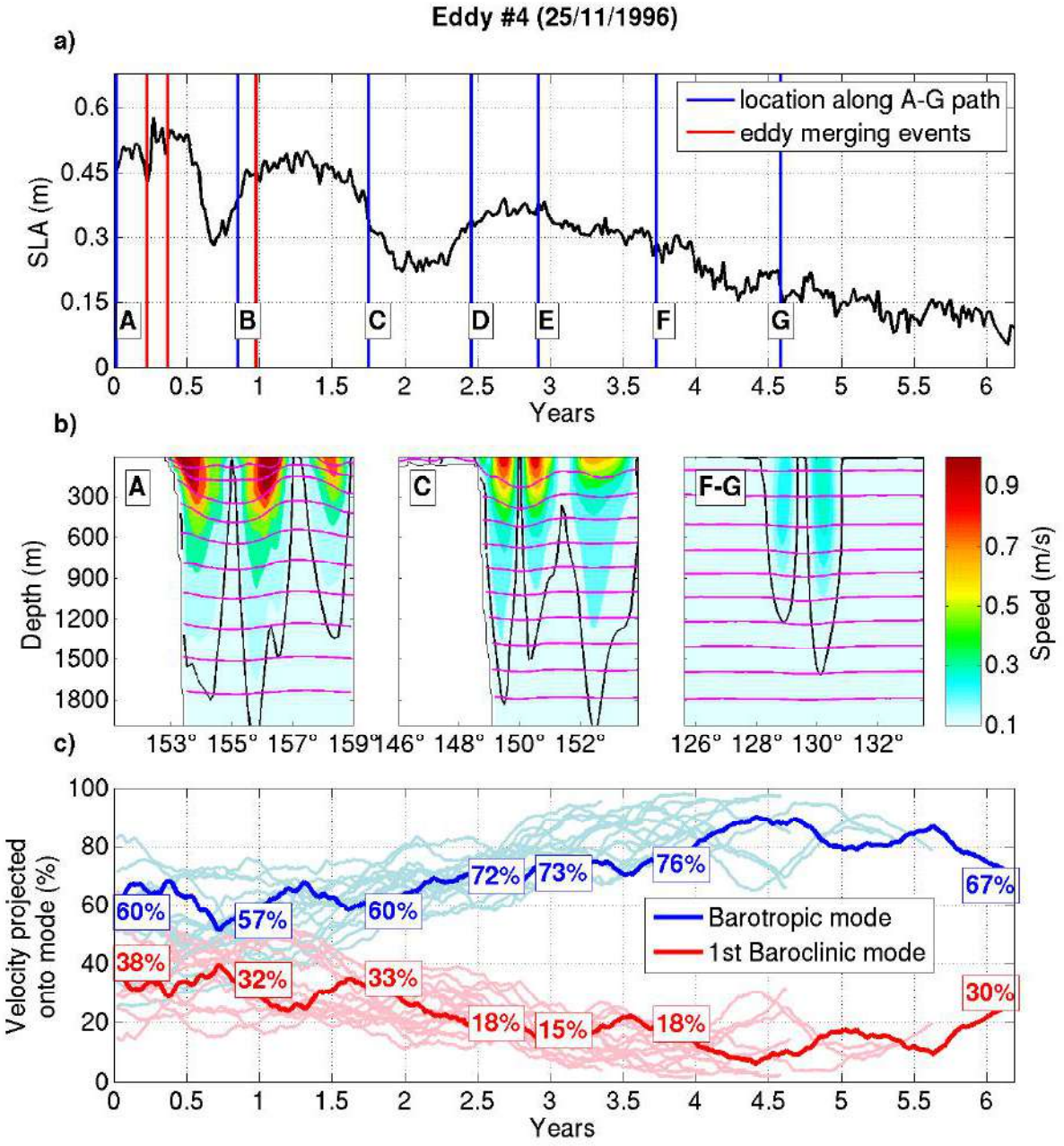


**Figure S3.** As for Figure S1, except for Eddy#4.

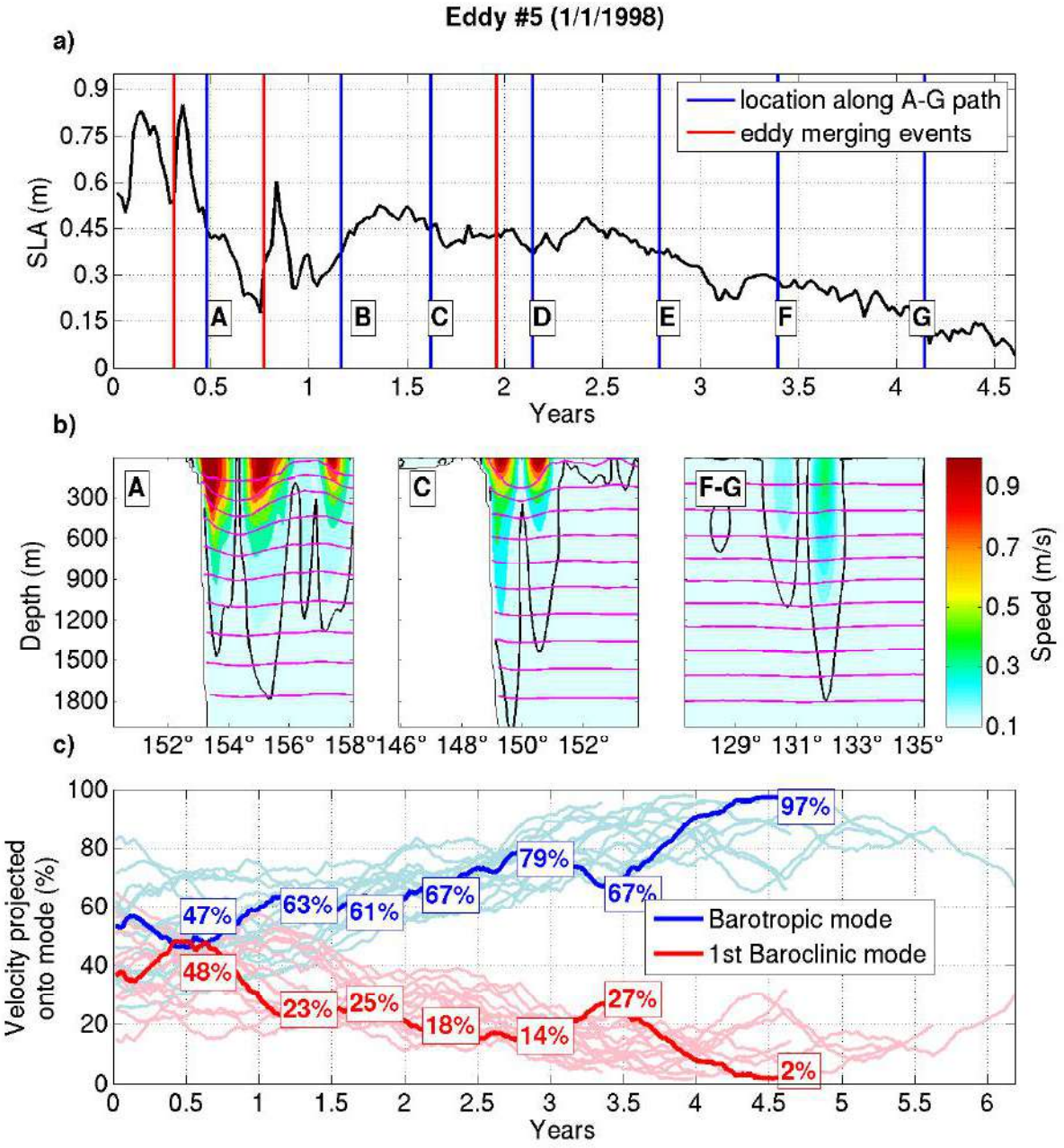


**Figure S4.** As for Figure S1, except for Eddy#5.

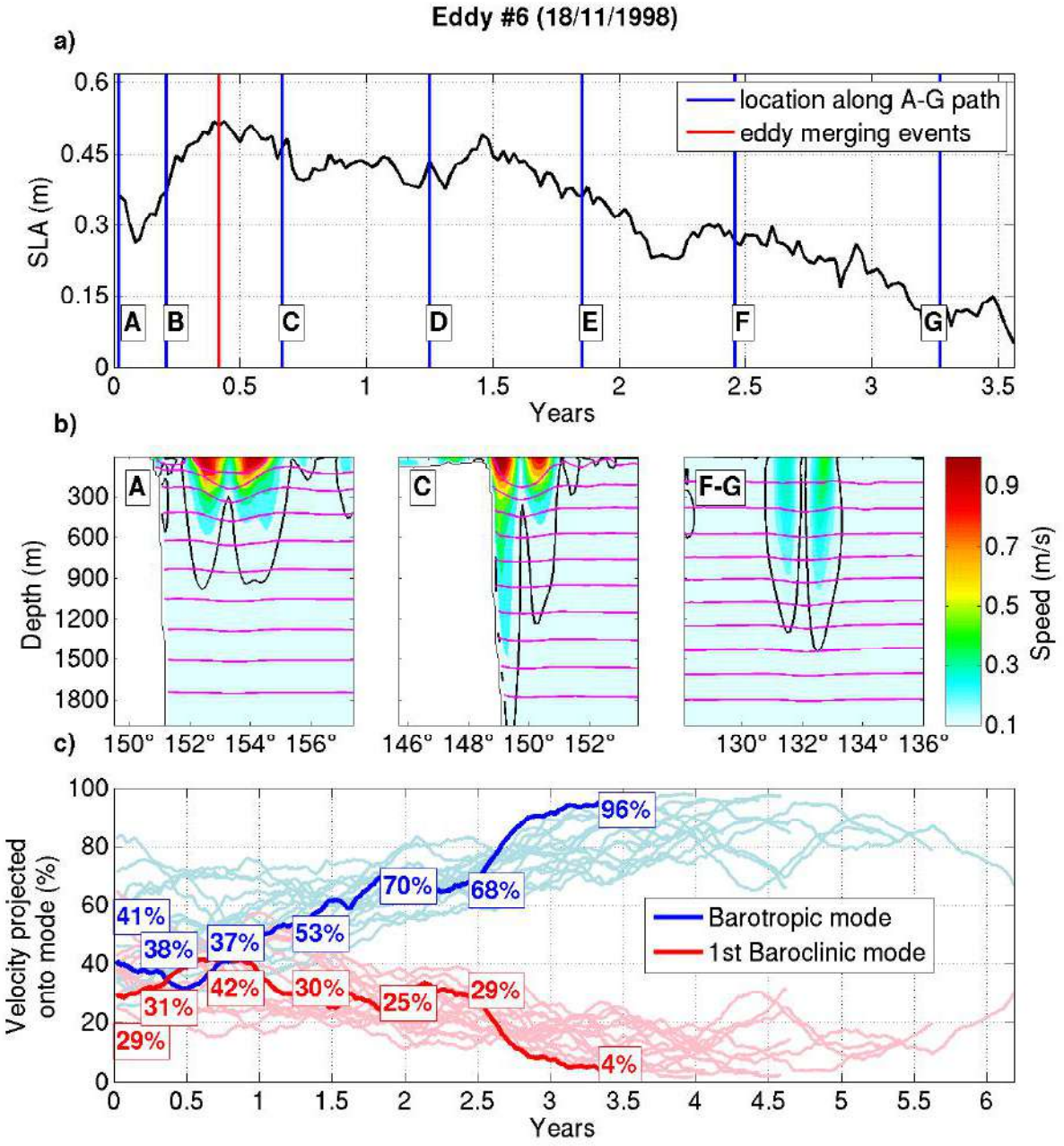


**Figure S5.** As for Figure S1, except for Eddy#6.

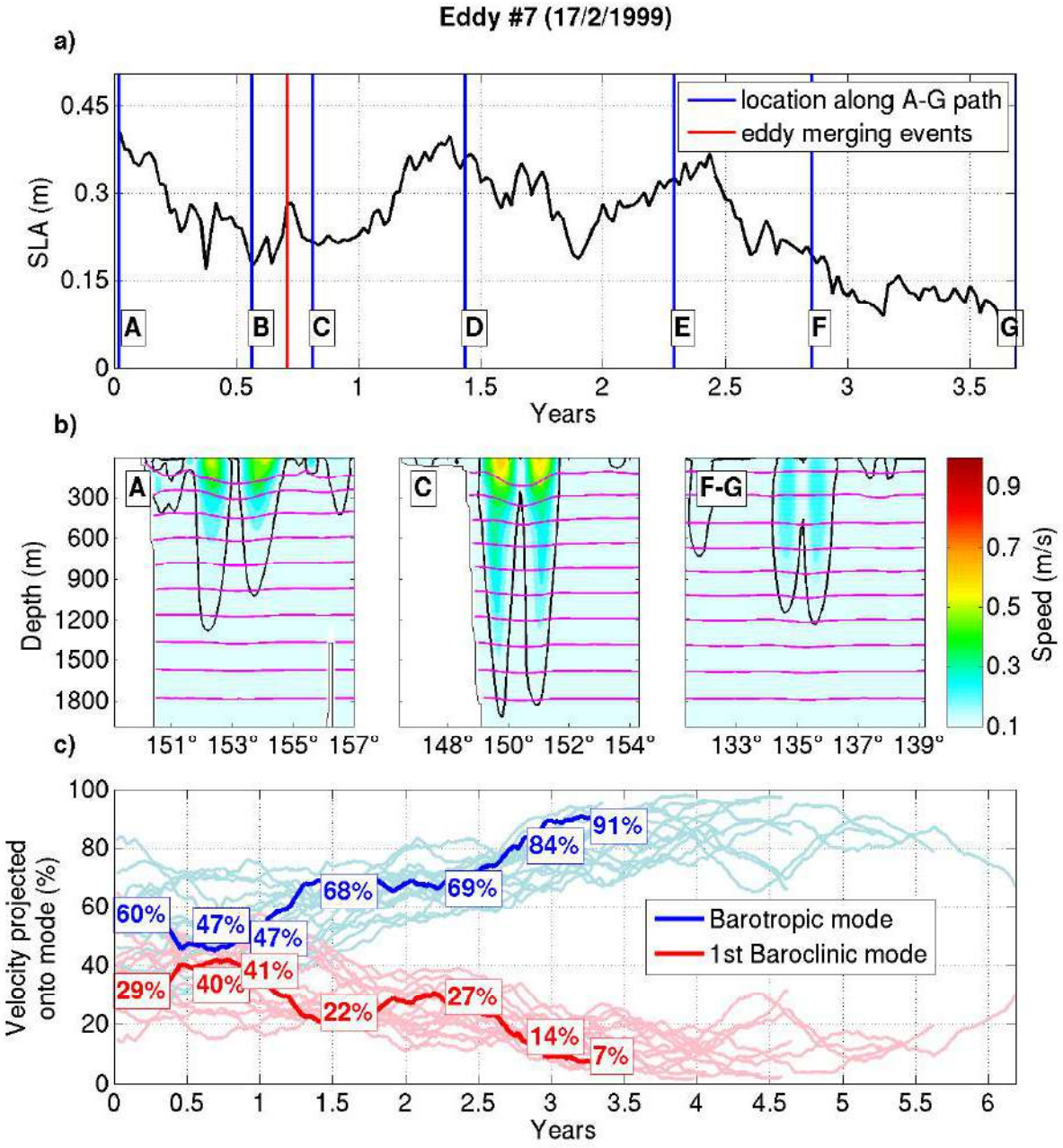


**Figure S6.** As for Figure S1, except for Eddy#7.

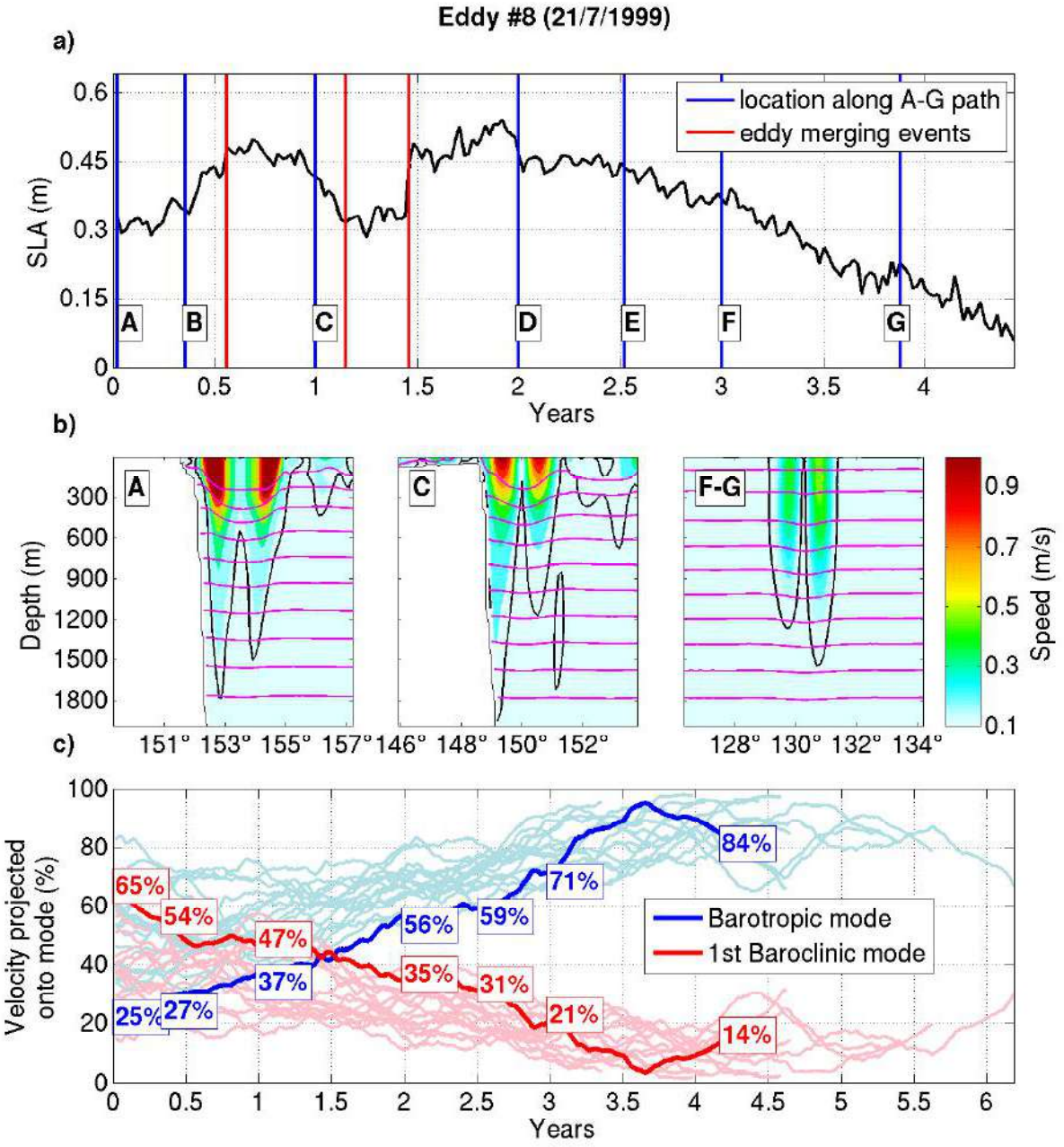


**Figure S7.** As for Figure S1, except for Eddy#8.

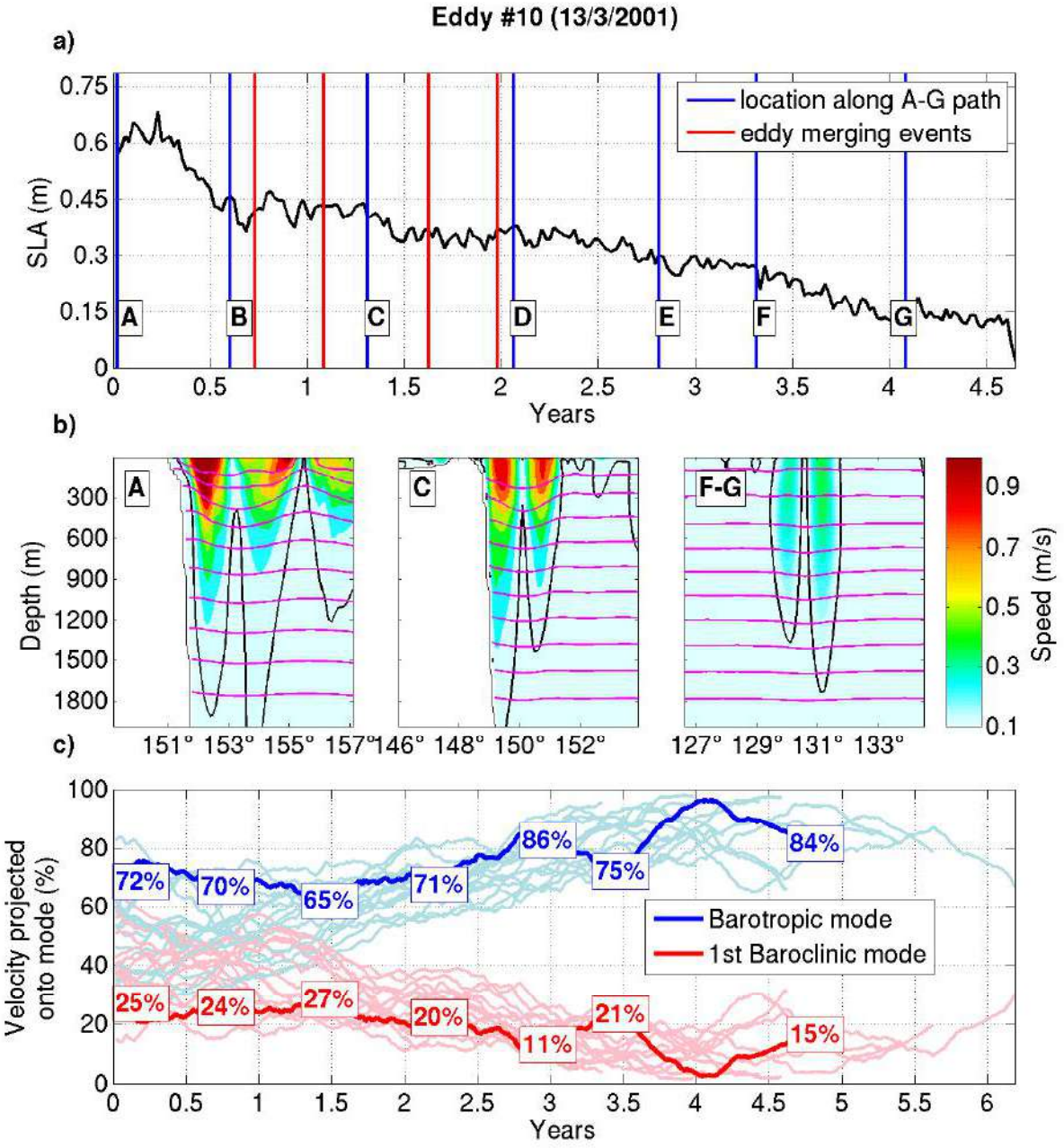


**Figure S8.** As for Figure S1, except for Eddy#10.

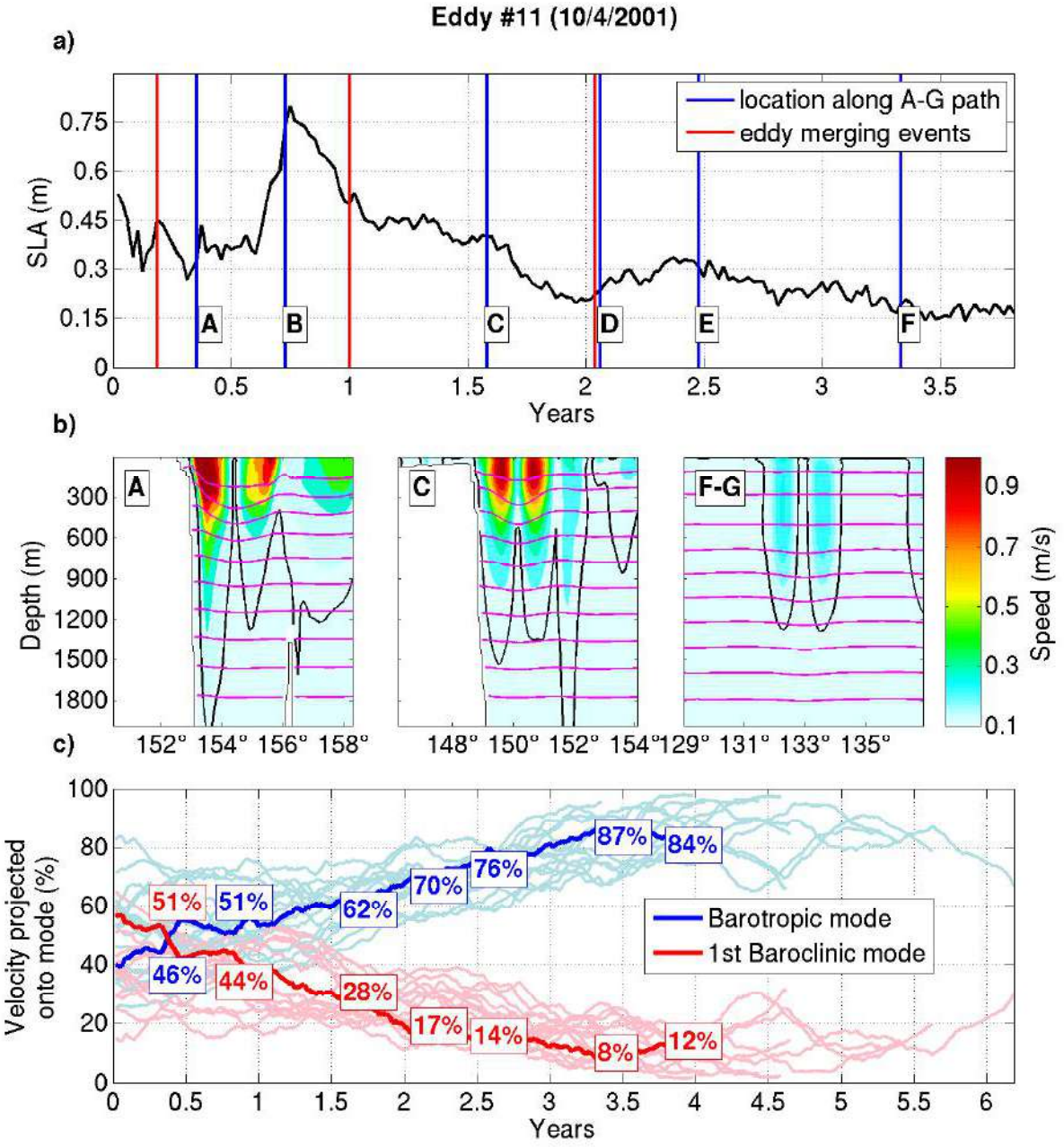


**Figure S9.** As for Figure S1, except for Eddy#11.

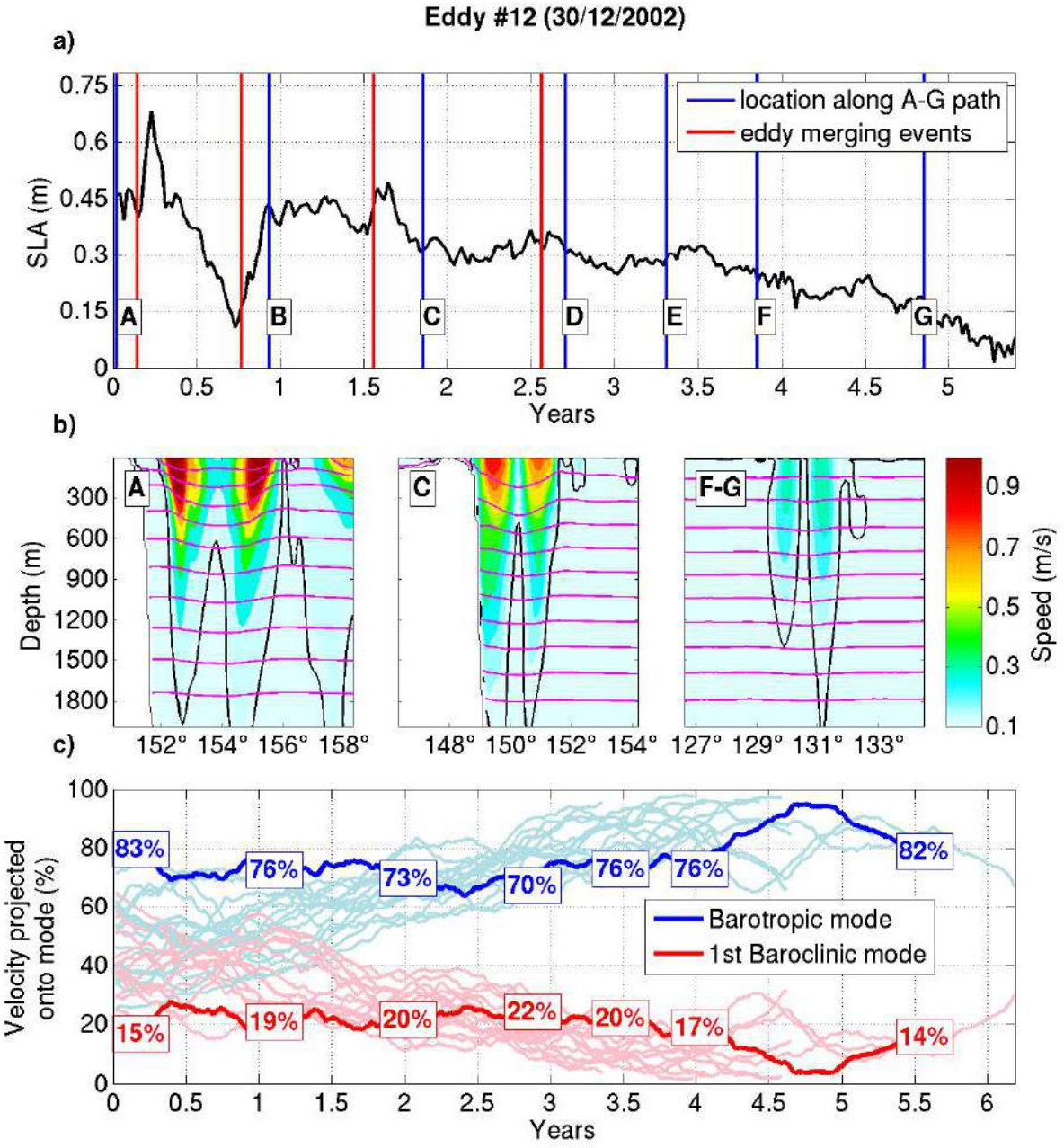


**Figure S10.** As for Figure S1, except for Eddy#12.

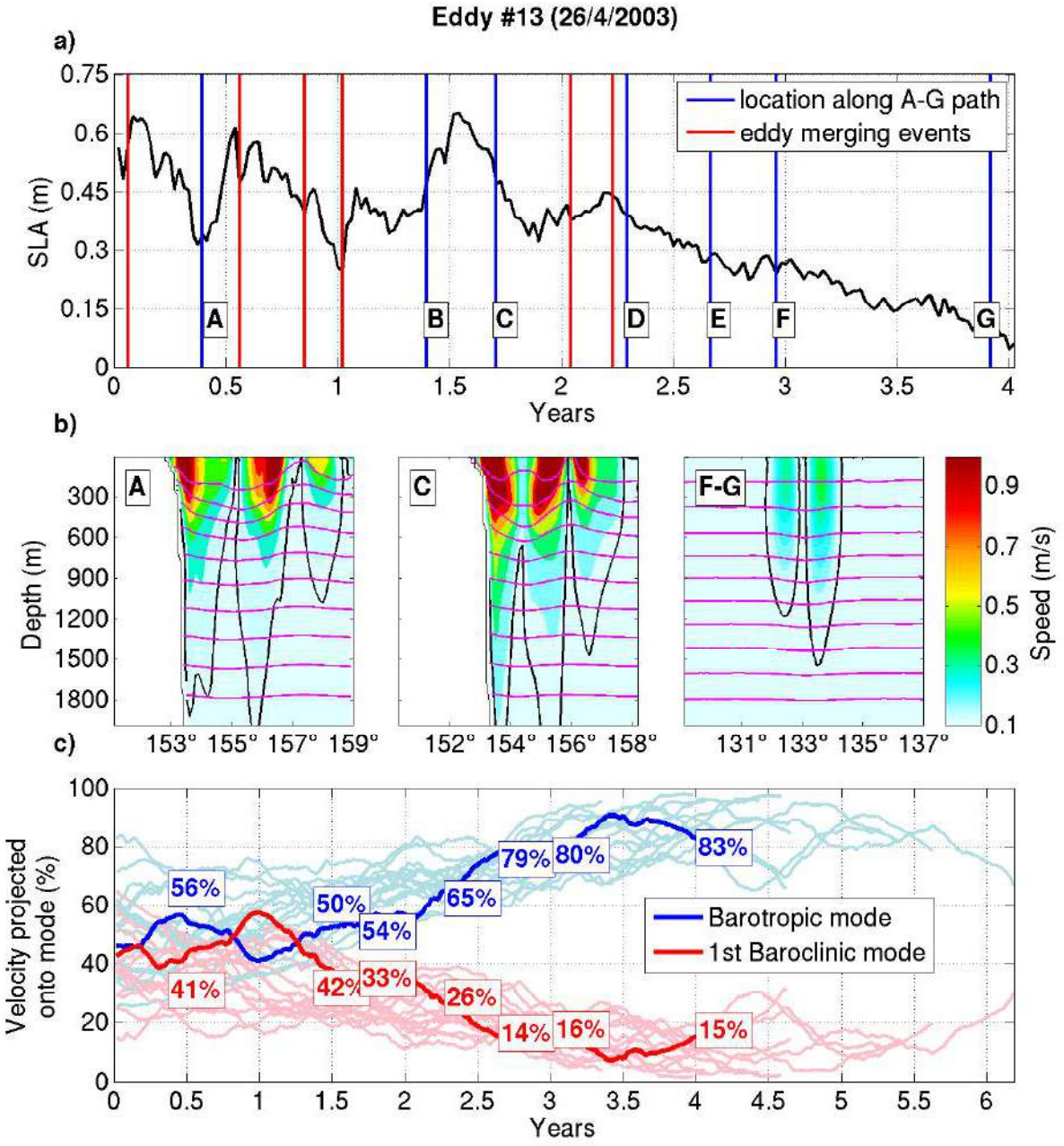


**Figure S11.** As for Figure S1, except for Eddy#13.

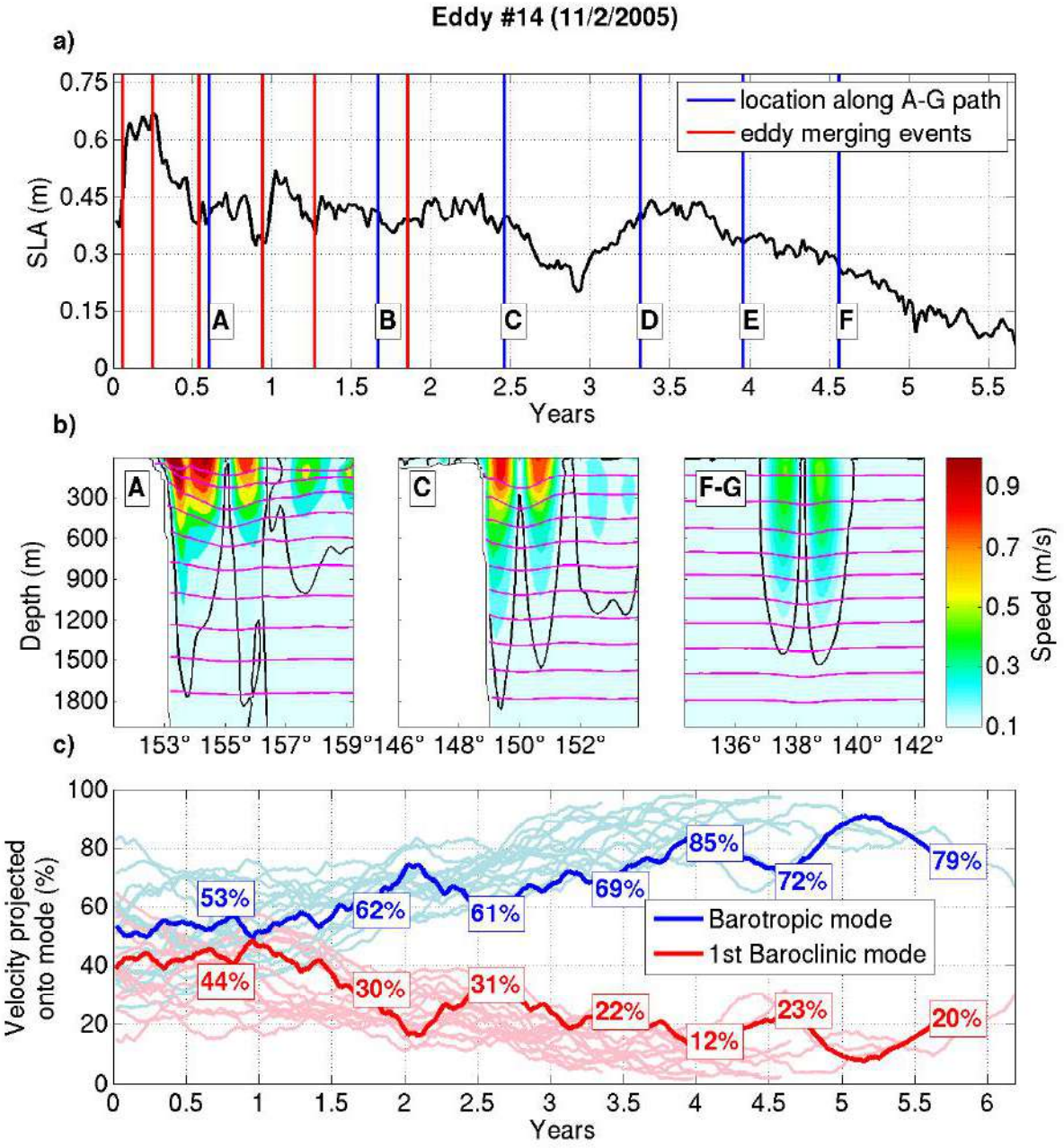


**Figure S12.** As for Figure S1, except for Eddy#14.

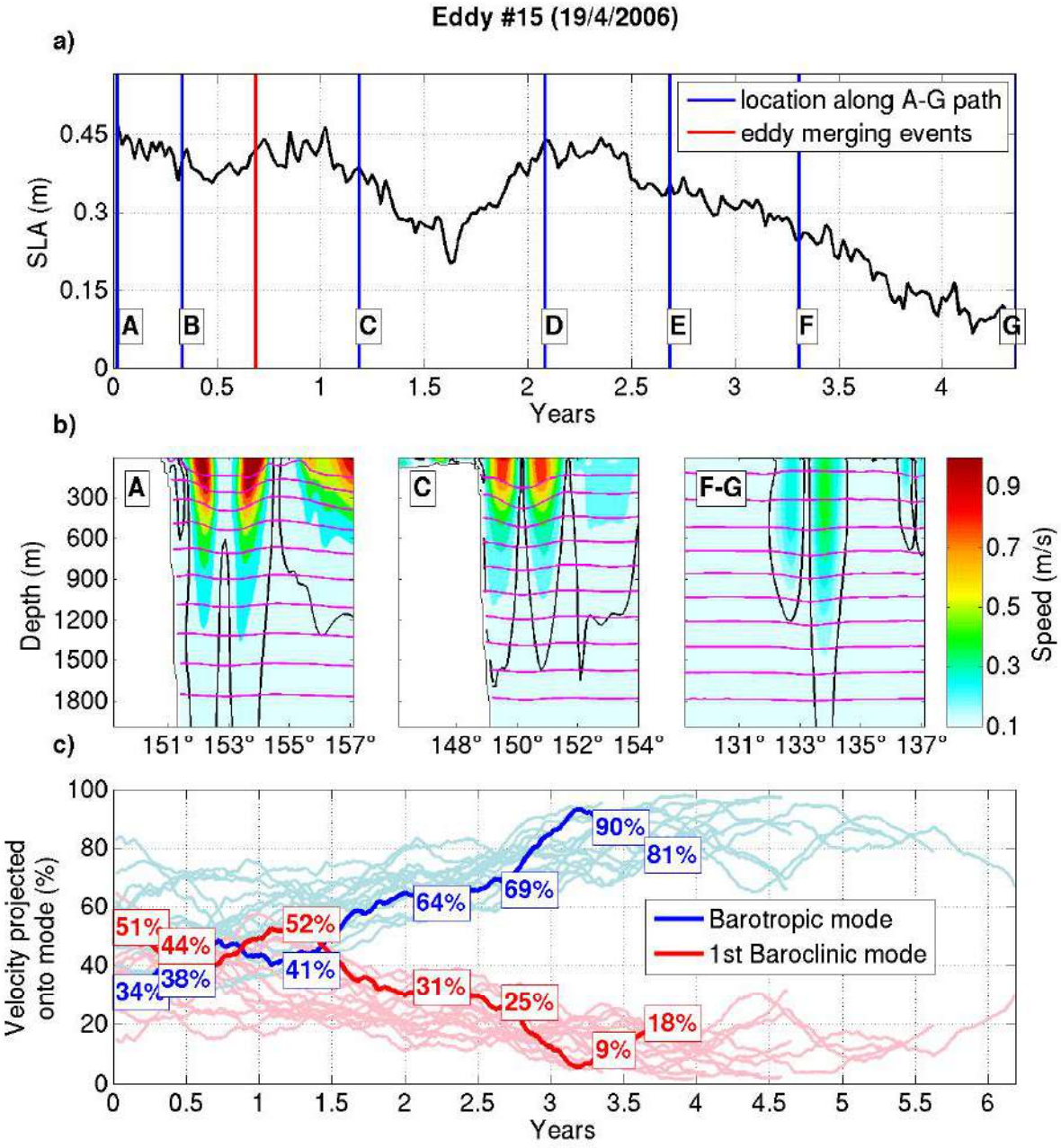


**Figure S13.** As for Figure S1, except for Eddy#15.

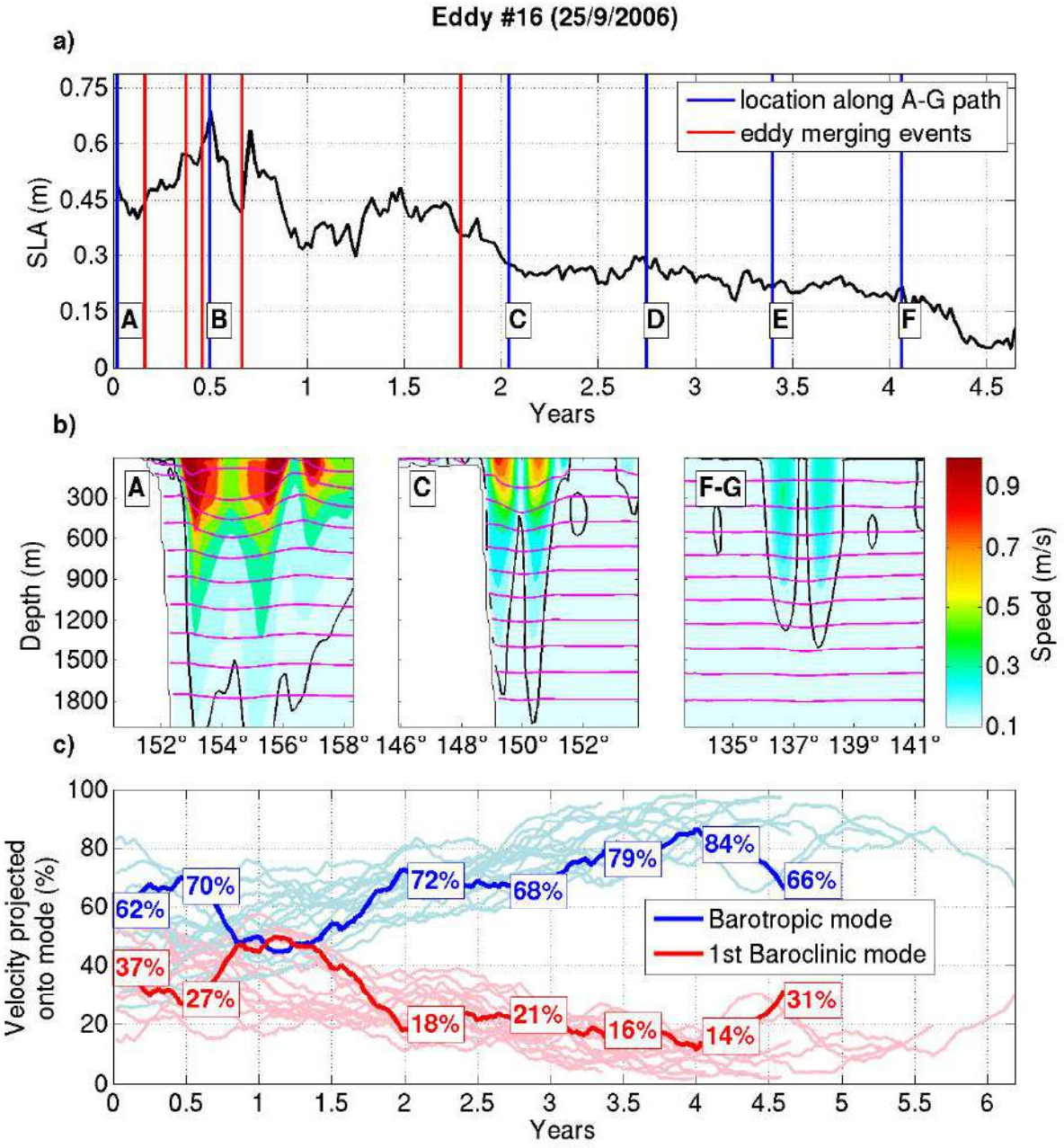


**Figure S14.** As for Figure S1, except for Eddy#16.

# Appendix C: "Patterns of Vertical Velocity Induced by Eddy Distortion in an Ocean Model"

AGU PUBLICATIONS

JGR

Journal of Geophysical Research: Oceans

RESEARCH ARTICLE

10.1002/2017JC013298

# Patterns of Vertical Velocity Induced by Eddy Distortion in an Ocean Model

**Gabriela S. Pilo[1,2], Peter R. Oke[2], Richard Coleman[1,3], Tatiana Rykova[2], and Ken Ridgway[2]**

[1]Institute for Marine and Antarctic Studies, University of Tasmania, Hobart, Tas, Australia, [2]CSIRO Oceans and Atmosphere Flagship, Hobart, Tas, Australia, [3]Antarctic Climate and Ecosystems CRC, Hobart, Tas, Australia

**Key Points:**
- Eddies from the East Australian Current have alternating upward and downward cells in their interior
- Upward and downward cells are induced by change in eddy isotropy
- Change in sea level anomaly is a good proxy for change in eddy isotropy

**Supporting Information:**
- Supporting Information S1

**Correspondence to:**
G. S. Pilo,
Gabriela.SemoliniPilo@utas.edu.au

**Citation:**
Pilo, G. S., Oke, P. R., Coleman, R., Rykova, T., & Ridgway, K. (2018). Patterns of vertical velocity induced by eddy distortion in an ocean model. *Journal of Geophysical Research: Oceans*, *123*. https://doi.org/10.1002/2017JC013298

Received 21 JUL 2017
Accepted 26 FEB 2018
Accepted article online 7 MAR 2018



**Abstract** Vertical motions within eddies play an important role in the exchange of properties and energy between the upper ocean and the ocean interior. Here we analyze alternating upward and downward cells in anticyclonic eddies in the East Australian Current region using a global eddy-resolving model. The cells explain over 50% of the variance of vertical velocity within these eddies. We show that the upward and downward cells relate to eddy distortion, defined as the change in eddy shape over time. In anticyclonic eddies in the Southern Hemisphere, an inward distortion is associated with upward motion and an outward distortion is associated with downward motion. We discuss two mechanisms that link eddy distortion to vertical velocity. One mechanism relates to changes in stratification and relative vorticity in the eddy interior. The other mechanism relates to divergence of the horizontal flow in different quadrants of the eddy. We show that mesoscale changes in sea level anomaly can be used to infer the vertical motion within eddies.

## 1. Introduction

Vertical velocities within ocean eddies play an important role in the exchange of properties between the ocean surface and the ocean interior (e.g., Nurser & Zhang, 2000; Roemmich & Gilson, 2001), and in ecological and biogeochemical processes (e.g., Gaube et al., 2013; Klein & Lapeyre, 2009; McGillicuddy et al., 1998; Siegel et al., 2011). The upward motion within eddies promotes primary productivity, by uplifting high-nutrient waters from the ocean interior to the euphotic zone (e.g., Chelton, 2013; McGillicuddy et al., 1998). The downward motion within eddies exports tracers out of the euphotic zone and into the deep ocean (e.g., Klein & Lapeyre, 2009; McGillicuddy et al., 2003).

Despite its relevance, the vertical circulation within eddies has received less attention than other aspects of eddy dynamics. This is mostly because the vertical velocity in the ocean cannot easily be directly measured. Therefore, studies of vertical velocity within eddies rely on indirect diagnostics through the Omega equation (e.g., Martin & Richards, 2001; Nardelli, 2013; Pollard & Regier, 1992; Tintoré et al., 1991) and other methods (Strass, 1994). These diagnostics, however, require observations with high spatial and temporal resolution—both hard to achieve when observing mesoscale eddies (Allen et al., 2001; Martin & Richards, 2001). Another way to study the vertical circulation in the ocean is by analyzing the output of numerical models (e.g., Flierl & Mied, 1985; Pallas-Sanz & Viudez, 2007; Viudez & Dritschel, 2003). Modeled vertical velocity, however, cannot be easily validated against observations, and results from idealized simulations are not always applicable to real ocean eddies.

Due to the difficulties in studying vertical circulation in the ocean, McGillicuddy and Robinson (1997) and McGillicuddy et al. (1998) propose an indirect method to estimate vertical advection by mesoscale eddies—the eddy pumping mechanism. This mechanism is most relevant during the formation and strengthening of eddies, and it relates the vertical movement of isopycnals to the vertical velocity in the eddy center. The eddy pumping mechanism, however, has led to the misconception that cyclonic eddies are always upwelling and anticyclonic eddies are always downwelling. In fact, the terms "upwelling eddy" and "downwelling eddy" have been widely cited in the specialized literature (e.g., Alpine & Hobday, 2007; Nemcek et al., 2008; Oliver & Holbrook, 2014; Paterson et al., 2007; Tilburg et al., 2002; Uysal, 2006). The dominant upward or downward motion within eddies promoted by eddy pumping is a simplified view—patterns of vertical velocity within eddies are more complicated than that.

AGU Journal of Geophysical Research: Oceans 10.1002/2017JC013298

Besides the eddy pumping mechanism, the vertical circulation within eddies is also affected by eddy propagation (McGillicuddy et al., 1995), submesoscale processes (e.g., Brannigan, 2016; Lévy et al., 2001; Mahadevan et al., 2008), eddy interactions with the surrounding environment, as the wind (e.g., Dewar & Flierl, 1987; Gaube et al., 2015; Martin & Richards, 2001; Siegel et al., 2011; Stern, 1965), the ocean floor (e.g., Oke & Griffin, 2011), and other eddies (e.g., Pidcock et al., 2013), and eddy perturbation (Martin & Richards, 2001; Nardelli, 2013; Viudez & Dritschel, 2003). Here we focus on the effect of eddy perturbation in the vertical circulation.

The perturbation of the geostrophic balance of eddies induces alternating upward and downward cells that rotate around the eddy (Martin & Richards, 2001; Nardelli, 2013; Viudez & Dritschel, 2003). The nature, duration, and intensity of the perturbation dictate the number and strength of the vertical velocity cells (Martin & Richards, 2001). These cells extend radially from the eddy center to its perimeter. The changes in the eddy dynamics that link the perturbation of the eddy geostrophic balance to the alternating upward and downward cells still require further investigation. Nardelli (2013) provides indications that the basic dynamics of the alternating upward and downward cells relate to the propagation of vortex Rossby waves around the eddy (McWilliams et al., 2003). The author notes, however, that a complete characterisation of the eddy dynamics is complex.

Eddies are most intense and abundant close to western boundary currents (WBCs; Fu et al., 2010; Olson, 1991; Wyrtki et al., 1976). There, eddies often interact with other eddies and with the mean flow (Biastoch & Krauss, 1999; Bowen et al., 2005; Mata et al., 2006; Rocha et al., 2014; Waterman & Jayne, 2011). Because of these interactions, the geostrophic balance of these eddies is perturbed. Hence, the ageostrophic vertical circulation is expected to be stronger within eddies close to WBCs than within eddies in other oceanic regions.

In the East Australian Current (EAC), the WBC of the South Pacific, there has been several studies on the properties and dynamics of eddies (e.g., Roughan et al., 2017; Rykova et al., 2017; Rykova & Oke, 2015), the interaction of eddies with other eddies (Cresswell & Legeckis, 1986), the mean flow (e.g., Mata et al., 2006; Nilsson & Cresswell, 1981), and the ocean bottom (e.g., Oke & Griffin, 2011), and the impact of eddies on productivity (e.g., Everett et al., 2012) and marine biota (e.g., Suthers et al., 2011 and references therein). However, only one study describes the vertical circulation within an eddy in the EAC region. Oke and Griffin (2011) investigate the properties of a cyclonic eddy interacting with the eastern Australian continental shelf break. They show upwelling where the eddy appears to interact with the shelf break, downwelling in the opposite part of the eddy, and a nutrient enrichment in the euphotic zone in the vicinity of the eddy. Whether this vertical velocity pattern is common for EAC cyclonic eddies, or even existent within EAC anticyclonic eddies, is still unknown. Understanding the vertical circulation within long-lived EAC anticyclonic eddies is particularly relevant. EAC anticyclonic eddies have been shown to impact several oceanic regions as they propagate southward, leave the Tasman Sea, and reach the Eastern Indian Ocean (Pilo et al., 2015). These eddies have been shown to entrap coastal water organisms (Baird et al., 2011; Tranter et al., 1982), and affect the distribution of marine species (Ling et al., 2009). In addition, the number and strength of EAC anticyclonic eddies is predicted to increase in future climate scenarios (Oliver et al., 2015).

The purpose of this paper is to investigate patterns in the vertical circulation within EAC anticyclonic eddies. Specifically, we focus on the cells of upward and downward motion caused by the perturbation of the geostrophic flow of these eddies. We refer to this perturbation as "eddy distortion"—the change of eddy shape over time. Here we aim to further understand the mechanisms through which vertical velocity and eddy distortion are connected, and to gain additional understanding of this complex eddy dynamics. To this end, we use the output of a global, eddy-resolving model.

In the next section, we describe the ocean model used in this study, the eddies investigated, and our analysis methods. In section 3, we show patterns of vertical velocity and eddy distortion in EAC anticyclonic eddies. In section 4, we discuss mechanisms that link the change in eddy shape and vertical velocity, followed by a discussion and conclusions in section 5.

## 2. Data and Methods

We investigate eddies using the Ocean Forecasting Australia Model, version 3 (OFAM; Oke et al., 2013). OFAM is a near-global eddy-resolving model with a horizontal resolution of 1/10° and 51 vertical levels. The

AGU Journal of Geophysical Research: Oceans 10.1002/2017JC013298

vertical grid z* has 5 m spacing near the surface, 10 m spacing at 200 m depth, 120 m spacing at 1,000 m depth, and coarser grid spacing below that (Figure 1e, dashed lines). In this study, we show many results in depths between 500 and 1,500 m, where the vertical spacing ranges from 60 to 150 m. The model is run for

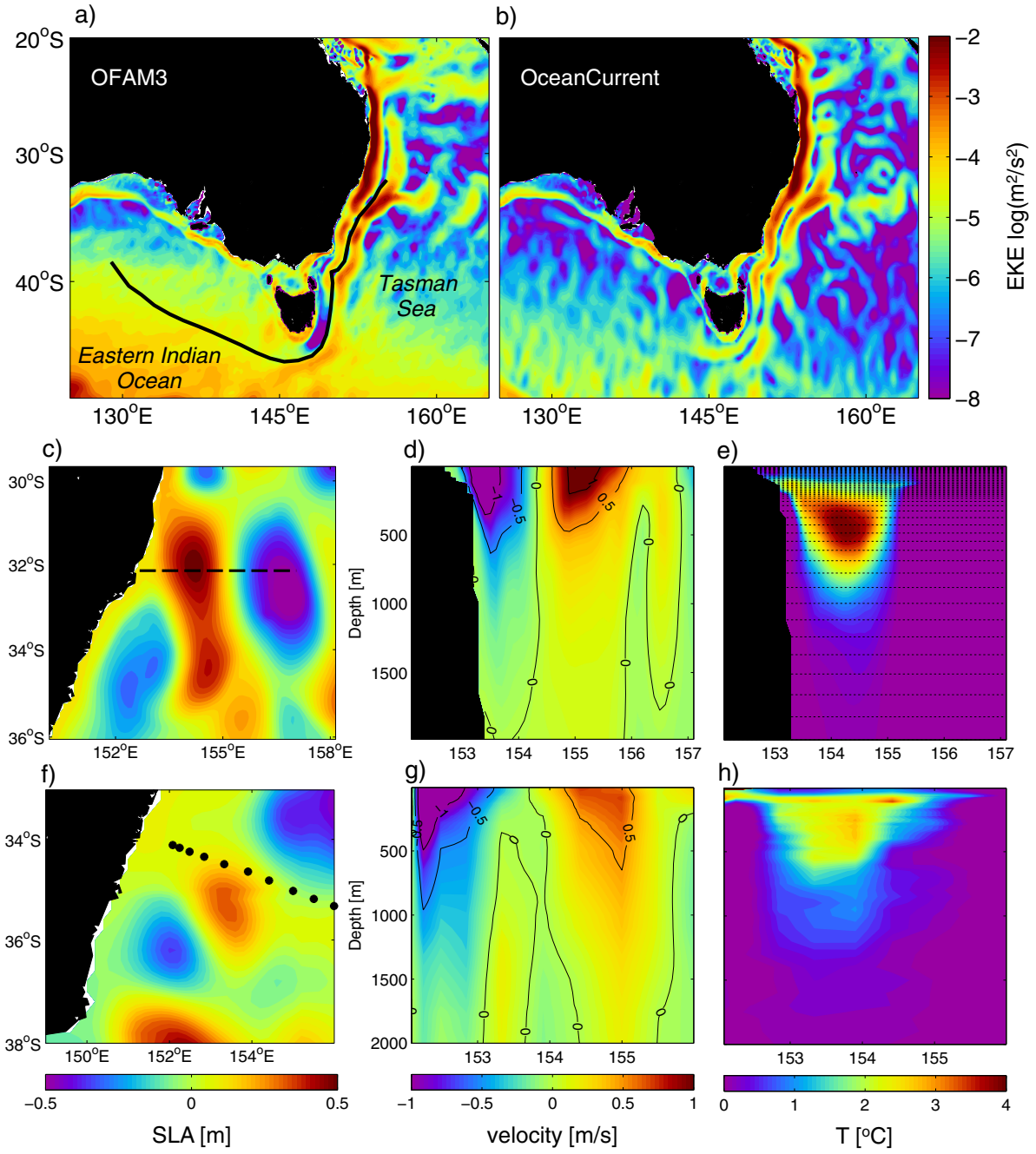


**Figure 1.** Comparison of the mean EKE between 2000 and 2005 from (a) OFAM and (b) OceanCurrent altimetry products (Deng et al., 2011); (c) SLA associated with an EAC anticyclonic eddy from the model; the dashed line indicates the location of the vertical section shown in (d) and (e); (d) modeled meridional velocity (colors and contours, spaced every 0.5 m/s) and (e) modeled temperature anomaly associated with the eddy shown in Figure 1c. The dotted vertical lines represent vertical levels of OFAM; (f) SLA from OceanCurrent altimetry products associated with a sampled EAC anticyclonic eddy (adapted from Ridgway et al., 2008); the black dots indicate CTD sampling stations; (g) geostrophic current relative to 2,000 dB computed from temperature and salinity fields (colors and contours, spaced every 0.5 m/s); (h) observed temperature, with CARS climatology (Ridgway & Dunn, 2003) removed.

AGU Journal of Geophysical Research: Oceans 10.1002/2017JC013298

36 years, with an 18 year spin-up, and forced with 3-hourly surface heat, freshwater, and momentum fluxes from ERA-Interim (Dee & Uppala, 2009), with restoring to monthly sea surface temperature (Reynolds et al., 2007, 10 day *e*-folding time scale); weak restoring to surface climatological salinity (Ridgway & Dunn, 2003, 180 day *e*-folding); and weak restoring to climatological temperature and salinity below 2,000 m depth (restoring time scale of 180 days). Because of the climatological restoring at depth and coarse vertical resolution, we only consider the top 2,000 m of the model fields throughout the manuscript.

We validate both horizontal and vertical representations of the eddy field in the model. First, we compare the mean eddy kinetic energy (EKE) between the model and a 1/4° resolution gridded altimetry product from OceanCurrent (Deng et al., 2011). Then, we compare vertical sections of geostrophic velocity and temperature anomaly between a modeled and an observed eddy.

The model realistically reproduces both the location and strength of the high EKE region off the east Australian continental shelf (Figures 1a and 1b). This high EKE region is associated with the meandering EAC and its eddies—both cyclonic and anticyclonic—, extending from where the EAC separates from the continental shelf break (∼32°S) to the east of Tasmania (∼42°S). Despite localised differences between the model and observations, the modeled regional circulation and variability are well represented.

The observed eddy used for comparison was sampled in May 2001 in full depth CTD casts (Ridgway et al., 2008, Figures 1f–1h). It is not mandatory for the dates of the observed eddy and the modeled eddy to be the same, as OFAM is a free-running model. Eddies from the EAC, however, display seasonal changes (Rykova & Oke, 2015). Therefore, it is important to compare eddies occurring in the region in the same season. The modeled eddy in Figures 1c–1e dates from May 1996. Despite being stronger than the sampled eddy (i.e., higher SLA, geostrophic velocity, and temperature anomaly), the dynamics and vertical structure of the modeled eddy are realistic. In both eddies, the geostrophic velocity (Figures 1d and 1g) and temperature (Figures 1e and 1h) signals penetrate below 1,000 m, with maximum temperature anomaly between ∼200 and 600 m. We regard the model output to be suitable for investigating the dynamics of eddies from the EAC, consistent with previous studies (Oke & Griffin, 2011; Pilo et al., 2015; Rykova & Oke, 2015).

We analyze the vertical velocity in ten anticyclonic eddies that originate where the EAC separates from the continental shelf break (∼31°S). We track the selected eddy by locating closed 0.1 m sea level anomaly (SLA) contours in weekly SLA fields, between 1993 and 2012. An eddy is continuous in time if it is evident at consecutive weeks, with a tolerance of 3 weeks. We track each eddy until the SLA associated with it becomes smaller than 0.1 m, or until it can no longer be identified as a closed contour feature. The tracking method, pathway, and evolution of these eddies are described in Pilo et al. (2015). After formation at the EAC separation region, the eddies propagate southward adjacent to the shelf break, cross south of Tasmania, and then advect westward toward the Eastern Indian Ocean (Figure 1a, black line). As they move along this pathway, eddies generally become deeper and more barotropic (Pilo et al., 2015).

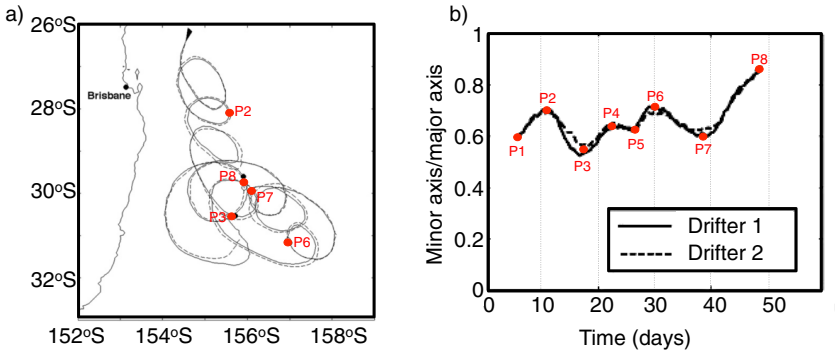


**Figure 2.** (a) Position of two surface drifters trapped in an anticyclonic eddy in the Tasman Sea between 21 February and 22 April 2007. Red points indicate the averaged location of the drifters 10, 20, 30, 40, and 50 days after their launch. (b) Time series of the ratio between the minor and the major axes of ellipses fitted to the trajectories shown in Figure 2a. Inflections on ratio curves are indicated by red points (P1–P8; adapted from Brassington, 2010).

AGU Journal of Geophysical Research: Oceans 10.1002/2017JC013298

For some of the analyses in this paper, we separate the eddy pathway according to the main direction of eddy propagation: southward and westward. As eddies propagate southward (i.e., between the EAC separation and off east Tasmania), they interact with bathymetry, with other eddies, and with a strong mean flow. In this part of the pathway, the vertical velocity can be induced by several mechanisms. As eddies propagate westward (i.e., off west Tasmania and the Eastern Indian Ocean), they are isolated, and the surrounding flow is quasi-quiescent. In this part of the pathway, eddies are more likely to behave as isolated case studies, and the vertical velocity induced by eddy distortion and eddy propagation to have clearer signals. In addition, as eddies propagate south

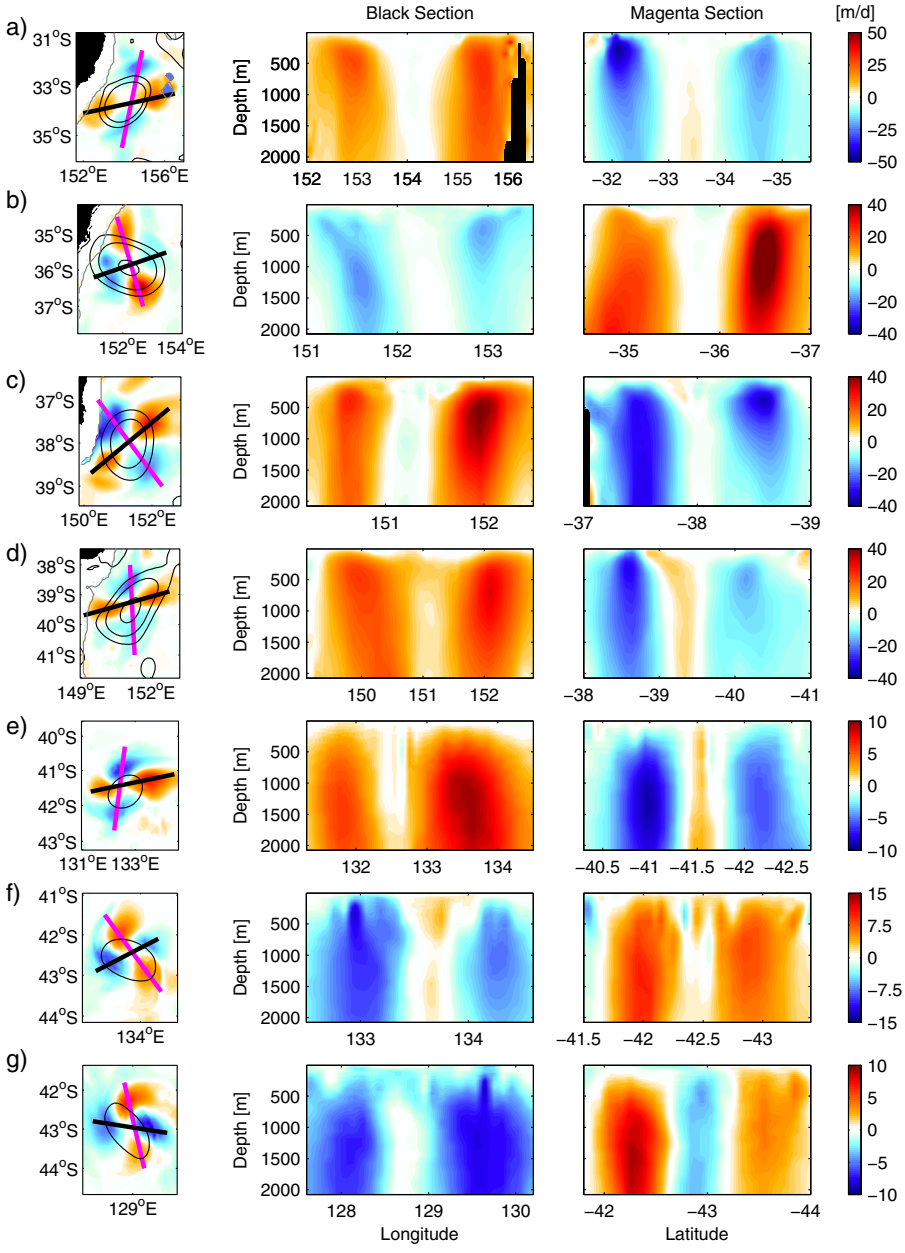


**Figure 3.** (left) Depth-averaged (0–2,000 m) vertical velocity (colors) in (a–g) seven EAC anticyclonic eddies from a near-global, eddy-resolving ocean model. Black lines indicate 0.1, 0.25, and 0.5 m sea level anomaly contours. Grey lines indicate the 3,000 m isobath. (right) The bold black (magenta) line indicates the location of the vertical section shown in the center. Note the different scales of vertical velocity for each eddy.

AGU Journal of Geophysical Research: Oceans 10.1002/2017JC013298

of Tasmania, between 146°E and 150°E, they become highly incoherent, shed a lot of filaments, and interact with seamounts and oceanic rises. Hence, the region south of Tasmania is not included in our analyses.

The vertical velocity is the least reliable variable in any ocean model, including the model used in this study. We perform an Empirical Orthogonal Function (EOF) analysis to eliminate the noise and to isolate the

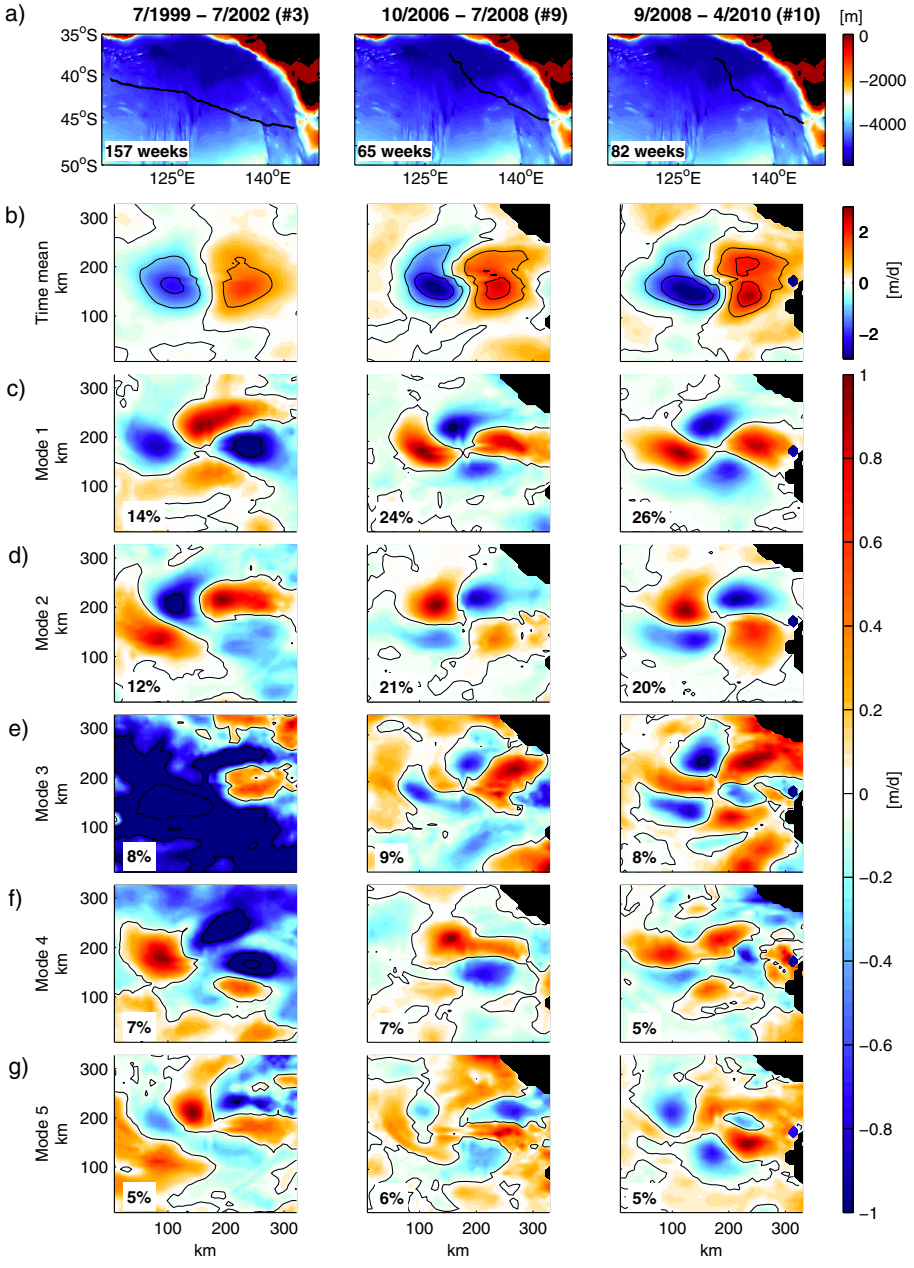


**Figure 4.** (a) Maps indicating the tracks (black lines) of three anticyclonic eddies propagating in the Eastern Indian Ocean. Colors denote bathymetry, and the numbers in the bottom left corners indicate the number of weeks taken for each eddy to propagate along the tracks. The numbers of the eddies (i.e., #3, #9, and #10) relate to Table 1. (b) Time mean depth-averaged (0–2,000 m) vertical velocity ($\tilde{w}$) for each eddy as they propagate along the tracks shown in Figure 4a. (c–g) EOF modes 1–5 of an EOF analysis of $\tilde{w}$, normalized by the maximum value of each mode, for each eddy. Black lines denote null $\tilde{w}$. The percentages in the bottom left corner are the amount of variance contained in each mode, for each eddy.

AGU Journal of Geophysical Research: Oceans 10.1002/2017JC013298

**Table 1**
*Results From a Single-Variable EOF Analysis of Depth-Averaged Vertical Velocity ($\tilde{w}$) and From a Multivariate EOF Analysis of $\tilde{w}$ and Change in Sea Level Anomaly ($\Delta SLA$) for 10 Anticyclonic Eddies*

| | Southward $\tilde{w}$ | | Westward $\tilde{w}$ | | Southward combined $\tilde{w}$ and $\Delta SLA$ | | Westward combined $\tilde{w}$ and $\Delta SLA$ | |
|---|---|---|---|---|---|---|---|---|
| | EOF modes | Combined variance (%) | EOF modes | Combined variance (%) | EOF modes | Combined variance (%) | EOF modes | Combined variance (%) |
| #1 | 1, 2, 5 | 45 | 1–3 | 49 | 1–4 | 51 | 1–3 | 37 |
| #2 | 1, 2, 4, 6, 7 | 52 | 1–4, 6 | 56 | 1, 3, 6 | 32 | 2, 3, 6,7 | 19 |
| #3 | | | 1, 2, 6 | 31 | | | 2, 3 | 10 |
| #4 | | | 1–6 | 50 | | | 1–5 | 57 |
| #5 | 1, 2, 6, 7 | 47 | 1, 2 | 25 | 1, 2 | 38 | 2–4 | 15 |
| #6 | 1, 2 | 38 | 1, 2, 4 | 46 | 1, 2 | 33 | 2, 3 | 19 |
| #7 | 1, 9 | 22 | 1–3 | 38 | 1 | 19 | 2–4 | 26 |
| #8 | 1, 2 | 37 | 1, 2, 4 | 48 | 1, 2, 6 | 34 | 2, 3 | 18 |
| #9 | | | 1, 2 | 45 | | | 1–3 | 53 |
| #10 | | | 1–3 | 54 | | | 1–3, 5 | 58 |

*Note*. The modes and the combined variances shown relate to the alternating cells of positive and negative values seen in Figures 4 and 6. The propagation of the 10 eddies is divided into two sections: southward, between the EAC separation region and east of Tasmania, and westward, in the Eastern Indian Ocean. Absent values in the southward section are due to the presence of shallow regions along the eddy path that hinder the results from the EOF analysis.

coherent components of the vertical velocity fields. The patterns of vertical velocity shown here are coherent, as we show in section 3.1. For the EOF analysis we use 4° × 4° maps of depth-averaged vertical velocity ($\tilde{w}$) for each time step of the eddy lifetime. First, we detrend the variable in time. Then, we compute a singular value decomposition of the anomaly field. The depths considered for the EOF analysis range from 0 to 600 m when eddies propagate southward and from 0 to 2,000 m when eddies propagate westward. This difference is because southward-propagating eddies move through shallower regions and extend to shallower depths than the westward-propagating eddies (Pilo et al., 2015).

We also perform a multivariate EOF analysis combining $\tilde{w}$ and changes in SLA ($\Delta SLA$). $\Delta SLA$ is calculated by subtracting the SLA field in the first time step from the SLA field in the second time step, with weekly time

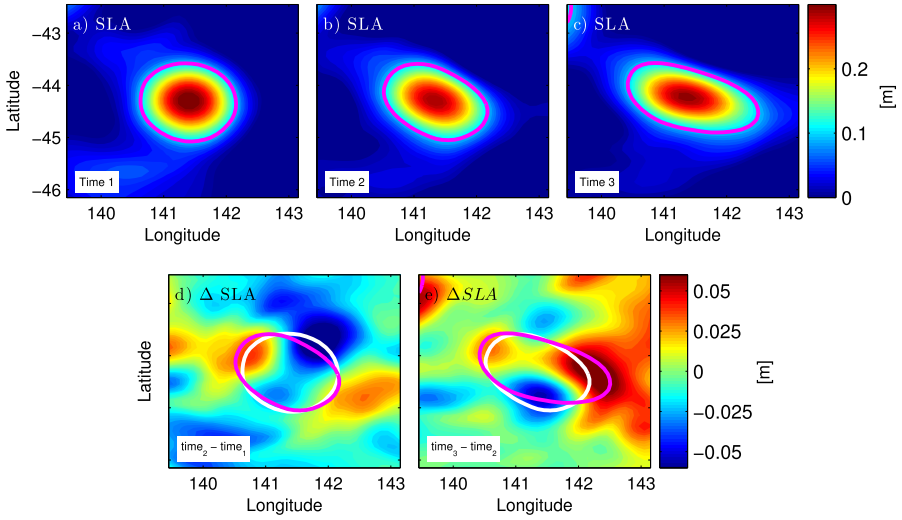


**Figure 5.** (a–c) Sea level anomaly (SLA) associated with one anticyclonic eddy at three subsequent weeks (times 1–3). The magenta line denotes the 0.1 m SLA contour; (d) change in SLA ($\Delta SLA$) between times 2 (shown in Figure 5b) and 1 (shown in Figure 5a). The magenta line denotes the 0.1 m SLA contour in time 2, and the white line denotes the 0.1 m SLA contour in time 1; (e) as in Figure 5d, but for times 3 (shown in Figure 5c) and 2 (shown in Figure 5b).

AGU Journal of Geophysical Research: Oceans 10.1002/2017JC013298

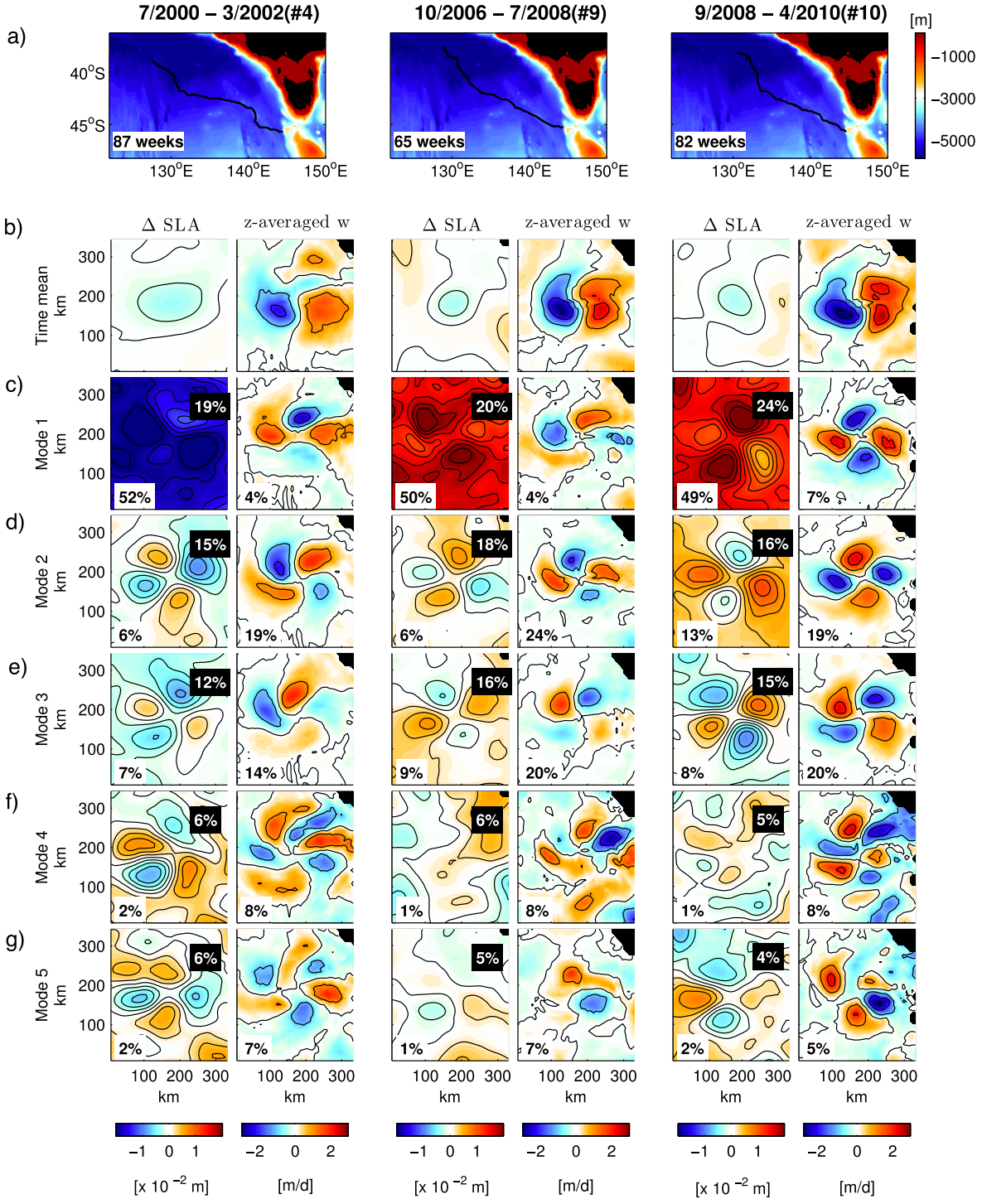


**Figure 6.** (a) Maps indicating the tracks of three anticyclonic eddies propagating in the Eastern Indian Ocean (black lines). Colors denote bathymetry, and the numbers in the bottom left corners indicate the number of weeks taken for each eddy to propagate along the tracks. The numbers of the eddies (i.e., #4, #9, and #10) relate to Table 1. (b) Time mean change in SLA ($\Delta SLA$) and time mean depth-averaged (0–2,000 m) vertical velocity ($\tilde{w}$) for each eddy as they propagate along the tracks shown in Figure 6a. (c–g) EOF modes 1–5 of the multivariate EOF analysis of $\Delta SLA$ and $\tilde{w}$, normalized by the maximum value of each mode and then multiplied by each variable standard deviation, for each eddy (see section 3.3). Black lines denote null values. Percentages in white (black) boxes are the amount of variance contained in each mode for each variable (combined variable).

AGU Journal of Geophysical Research: Oceans 10.1002/2017JC013298

steps. These fields are aligned relative to the eddy center (maximum SLA). We then compare this weekly $\Delta SLA$ with the $\tilde{w}$ field in the second time step. For the multivariate EOFs, we normalize the variables by dividing each by their standard deviation, and build a combined matrix. We then detrend this combined matrix in time and perform the EOF analysis of the anomaly field. We calculate the variance of individual variables for each mode by dividing the EOF mode variance of a single variable by the variance of this variable's original signal.

Besides the 7 day interval used in the EOF analyses described above, we also test a shorter (e.g., 3 days) and a longer (e.g., 30 days) time interval. For a shorter interval the $\tilde{w}$ cells are absent, and for a longer interval the $\tilde{w}$ cells are present—but are less clear than in a 7 day interval. The results from this sensitivity test suggest that the eddy distorts—and hence impacts $\tilde{w}$—on a time interval between 3 and 30 days, and close to a time interval of 7 days. These results are supported by the findings of Brassington (2010), who shows the ratio between the minor and the major axes of ellipses fitted to the trajectory of two surface drifters trapped in an anticyclonic eddy in the Tasman Sea (Figure 2). This ratio—another proxy for eddy distortion—changes every ∼5–10 days, to a large extent (i.e., between the red points in Figure 2b). This means that, on time intervals shorter than ∼5–10 days, the eddy does not distort, and in time intervals longer than ∼5–10 days the eddy distorts more than once. For example, between P2 and P7 (30 days apart), the ratio between the minor and the major axes of the ellipses is reduced by 14% (i.e., the eddy becomes more isotropic). However, the ratio changes five times over these 30 days, and the eddy becomes more or less isotropic each time. The change between P2 and P7, therefore, is an unrealistic assessment of eddy distortion. In the same way, an EOF analysis considering $\Delta SLA$ with a 30 day interval would also be unrealistic. Considering the results from the sensitivity tests and the findings by Brassington (2010), we determine the weekly time interval to be appropriate for the analyses performed here. This time interval seems to correspond to the time scale on which EAC eddies typically distort, or change shape. However, this time scale might be dependent on the interactions of the eddy with the mean flow, the wind, the ocean floor, and with other eddies.

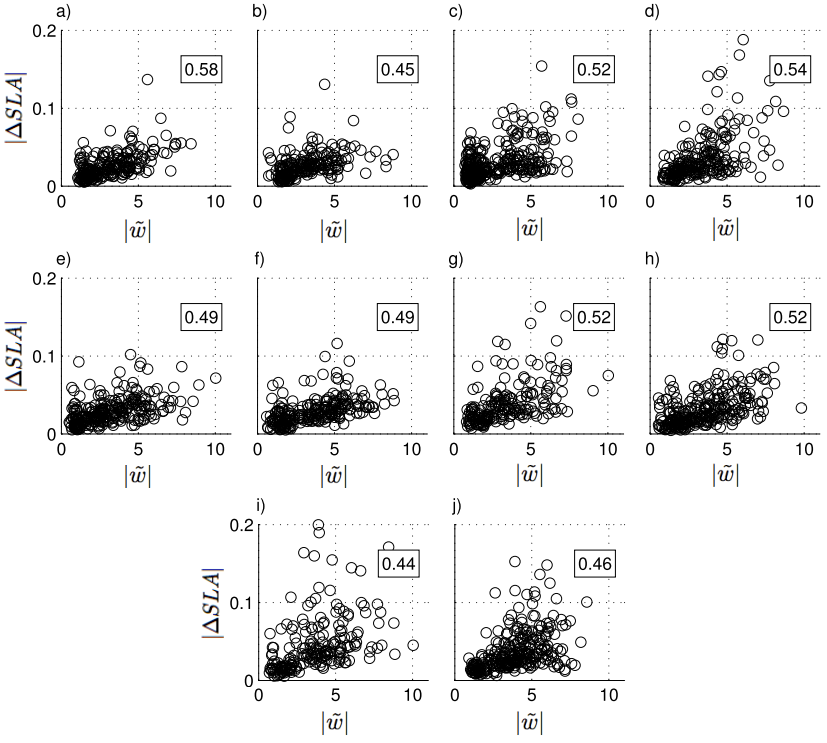


**Figure 7.** Values of absolute depth-averaged vertical velocity ($|\tilde{w}|$) and absolute change in sea level anomaly ($|\Delta SLA|$) (a–j) for 10 anticyclonic eddies for all time steps of their propagation between the EAC separation region to the Eastern Indian Ocean. The numbers in the boxes denote the correlation coefficient between these values.

AGU Journal of Geophysical Research: Oceans 10.1002/2017JC013298

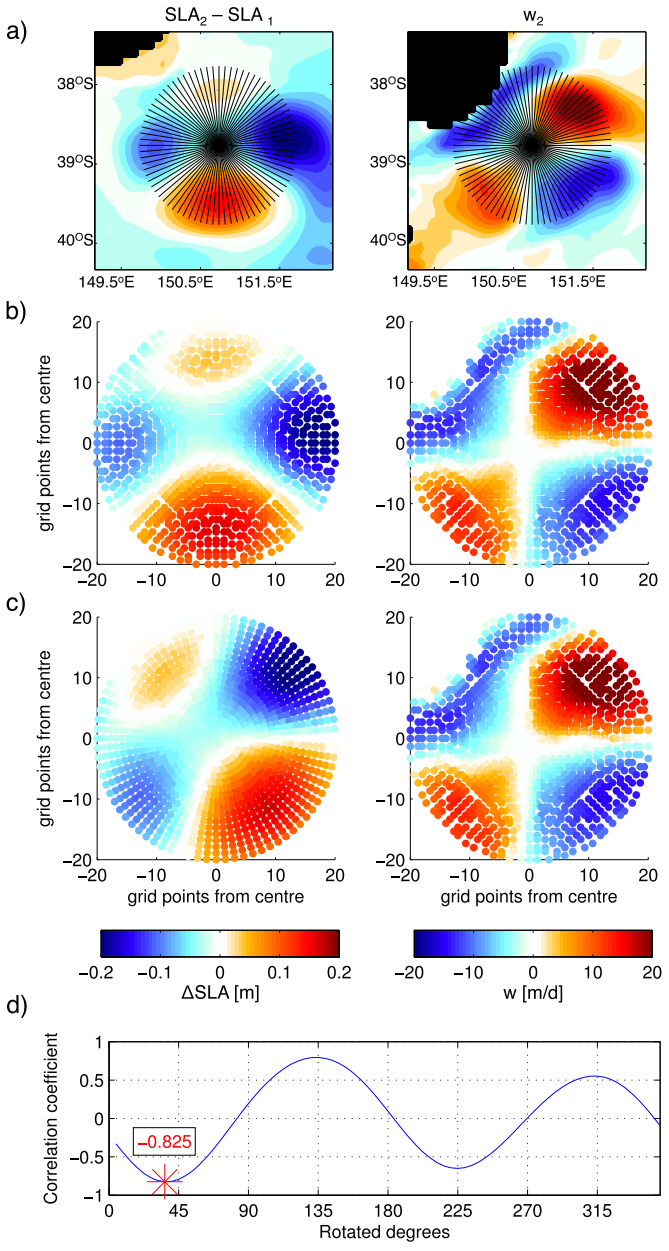


**Figure 8.** (a) (left) $\Delta SLA$ and (right) $\tilde{w}$ (colors) fields associated with an anticyclonic eddy located off Bass Strait. The black lines indicate the grid onto which these fields will be regridded; (b) as in Figure 8a, but with values in a radial grid; (c) as in Figure 8b, but with (left) $\Delta SLA$ rotated 31.5° anticlockwise, to match (right) $\tilde{w}$; (d) two-dimensional correlation coefficient between $\Delta SLA$ and $\tilde{w}$ from Figure 8b, considering different rotation angles for (left) $\Delta SLA$ (Figure 8b). The star indicates the correlation coefficient between the rotated $\Delta SLA$ and the nonrotated $\tilde{w}$ shown in Figure 8c.

## 3. Results

### 3.1. Eddy Vertical Velocity

The $\tilde{w}$ (surface to 2,000 m) in anticyclonic eddies formed at the EAC has alternating upward and downward cells (Figure 3, first column). These cells are stronger at depth (500–1,500 m), in most cases do not reach the surface, and are, sometimes, asymmetric (Figure 3; second and third columns). As eddies propagate, $\tilde{w}$ cells rotate in the same direction as the eddy rotation (i.e., anticlockwise). The existence of these $\tilde{w}$ cells indicates that the eddies are not in geostrophic balance and are, therefore, ageostrophic.

This pattern of alternating cells is seen along the whole eddy pathway (black line in Figure 1a). As eddies propagate southward, they are relatively strong (maximum SLA $>$ 0.5 cm) and have strong vertical velocity (up to 50 m/d in magnitude; Figures 3a–3d). Conversely, as eddies propagate westward, they are relatively weak (maximum SLA $<$ 0.2 cm) and have weaker vertical velocity (up to 15 m/d in magnitude; Figures 3e–3g).

We expect the pattern of alternating cells to be clearer and easier to observe in westward-propagating eddies than in southward-propagating eddies, owing to the quiescent aspect of the Eastern Indian Ocean. However, in both sections of the pathway, the pattern is clear and explains 22–56% of the combined variance of $\tilde{w}$ (Figure 4 and Table 1). This high variance is present regardless of the interactions between the eddy, the mean flow, the ocean bottom, and other eddies. Here we consider the combined variance of different EOF modes because the pattern of alternating cells rotates in time, appearing in up to six modes in the simple EOF analysis. In eddy #10, for example, the alternating $\tilde{w}$ cells are seen in modes 1–3 (Figure 4, third column). Despite this pattern distribution in different EOF modes, the results show that the alternating upward and downward cells are coherent in eddies that are either isolated or interacting with the surrounding environment.

### 3.2. Eddy Distortion

The isotropy of an eddy changes as it propagates in the ocean (e.g., Brassington, 2010; Cushman-Roisin et al., 1985). We refer to these changes in eddy isotropy as eddy distortion. Several factors are likely to contribute to eddy distortion, including interactions with bathymetry, with the mean flow, and with other mesoscale features. An example of eddy distortion is shown in Figure 5, with a semiisotropic eddy (Figure 5a) distorting in the northwest-southeast direction (Figures 5b and 5c) for 2 weeks. The $\Delta SLA$ field, obtained by subtracting SLA fields between subsequent weeks, shows alternating cells of positive and negative $\Delta SLA$ (Figures 5d and 5e). A positive cell indicates that the eddy distorted *toward* this area, and a negative cell indicates that the eddy distorted *away* from this area, relative to the previous week.

We considered rotating the SLA field in the first time interval before calculating $\Delta SLA$. This approach would isolate changes associated with eddy distortion from changes associated with eddy rotation. We would have to assume, however, that eddies rotate as a solid body. This is not true, and we could not determine a rotation value appropriate for the analysis. We tested different rotation values for the SLA field in the first time interval and all the $\Delta SLA$ calculated exhibited alternating cells (see supporting information). For all rotation values, the cells had similar intensity, but different spatial distribution. With these results in

AGU Journal of Geophysical Research: Oceans 10.1002/2017JC013298

mind, we chose not to rotate the eddy in the first time interval and to know that the associated error is qualitative, and not quantitative.

### 3.3. Eddy Vertical Velocity and Distortion

Patterns of both $\tilde{w}$ and $\Delta SLA$ have alternating cells of positive and negative values. A multivariate EOF analysis, combining these variables, shows that $\tilde{w}$ and $\Delta SLA$ vary together (Figure 6) and explain 18–51% of the combined variance (Table 1). Again, we consider the combined variance of different EOF modes because the patterns of both variables rotate in time, appearing in several EOF modes (Figure 6).

Figure 6 shows three case studies of eddies propagating westward in the Eastern Indian Ocean. In these eddies, the pattern of alternating cells for both $\tilde{w}$ and $\Delta SLA$ is seen in the first three modes of variance (Figures 6c–6e). The $\tilde{w}$ cells are shifted anticlockwise in relation to the $\Delta SLA$ cells (e.g., Figure 6d, first and second plots). This shift is due to the nonrotation of the SLA field in the first time interval (see section 3.2 and supporting information), and because we compare a change in time ($\Delta SLA$) to an instant field ($\tilde{w}$). If these were Southern Hemisphere cyclonic eddies, the $\tilde{w}$ cells would be shifted clockwise in relation to the $\Delta SLA$ cells. Despite the anticlockwise shift, all $\Delta SLA$ and $\tilde{w}$ pairs agree, and are inversely related (i.e., the cells of one variable are positive at the same time the cells of the other variable are negative). This means that an outward distortion (positive $\Delta SLA$) is associated with downward motion (negative $\tilde{w}$), and an inward distortion (negative $\Delta SLA$) is associated with upward motion (positive $\tilde{w}$).

To further show the relationship between $\Delta SLA$ and $\tilde{w}$ within eddies, we calculate the correlation between these variables (Figure 7). First, we isolate the values of absolute $\Delta SLA$ and absolute $\tilde{w}$ within a circle of 140 km radius centered in the eddy center (i.e., maximum SLA). Second, we calculate the spatial mean of these values. This process is repeated at each time interval as the eddy propagates. Therefore, the variables that are correlated at each time interval are the mean absolute $|\Delta SLA|$ and the mean absolute $|\tilde{w}|$ within the eddy. The rationale for relating these variables is that the stronger the eddy distortion (i.e., the higher the values of $|\Delta SLA|$), the stronger the vertical circulation within the eddy.

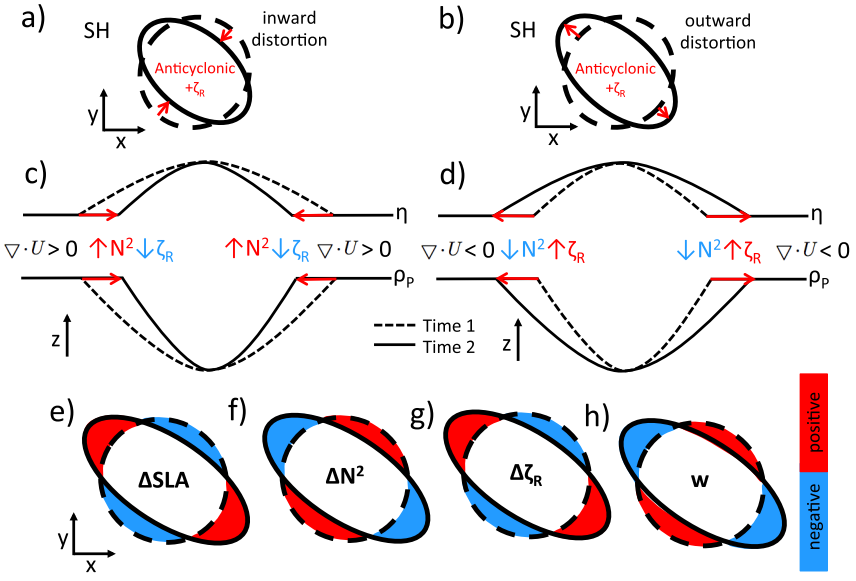


**Figure 9.** Schematics of a Southern Hemisphere (SH) anticyclonic eddy distorting (a) inward and (b) outward; changes in stratification ($N^2$) and in relative vorticity ($\zeta_R$) in the eddy interior associated with an (c) inward and (d) outward distortion shown in. $\eta$ is the ocean's free surface and $\rho_P$ is the isopycnal at the bottom of the permanent pycnocline. (e) Changes in SLA ($\Delta SLA$), (f) stratification ($\Delta N^2$), and (g) relative vorticity ($\Delta\zeta_R$) between subsequent time steps associated with eddy distortion. The vertical velocity pattern in the final time step associated with these distortions is shown in (h). From Figures 9a–9h, the dashed black lines indicate the eddy shape before distortion, and the solid black line indicates the eddy shape after distortion.

AGU Journal of Geophysical Research: Oceans 10.1002/2017JC013298

For the ten anticyclonic eddies analyzed in this study, the correlation between $|\Delta SLA|$ and $|\tilde{w}|$ ranges from 0.44 to 0.58 (Figure 7). Note that this correlation is always positive because we compare absolute values of $\Delta SLA$ and $\tilde{w}$. Also note that the values within the 140 km-radius circle established here mostly include waters from the eddy interior, but there is some contribution from waters from the surrounding ocean. Despite the relatively low correlation values in Figure 7, the results indicate that there is some correlation between $|\Delta SLA|$ and $|\tilde{w}|$.

Another way to correlate the $\Delta SLA$ and the $\tilde{w}$ cells is by performing a two-dimensional correlation analysis. In this analysis, the $\Delta SLA$ at each point within the eddy is compared to the $\tilde{w}$ considering all depth layers below these points (remember that $\tilde{w}$ is the depth-averaged vertical velocity). However, because of the anticlockwise shift of $\tilde{w}$ cells in relation to the $\Delta SLA$ cells described above, the correlation coefficient resulting from this two-dimensional analysis is low. To eliminate this shift between the patterns, we rotate the $\Delta SLA$ fields anticlockwise, until they match the nonrotated $\tilde{w}$ fields.

Figure 8 shows an example of a two-dimensional correlation analysis for a particularly clear example. This analysis is done as follows. First, we regrid the $\Delta SLA$ and the $\tilde{w}$ fields onto a radial grid (Figure 8a). This grid has a ~160 km radius centered in the eddy center, and has a resolution of ~8.3 km × 4.5° (80 radial lines with 20 grid points per line; Figure 8d). We then rotate the regridded $\Delta SLA$ values one radial line (i.e., 4.5°) at a time, from zero to 360°. For each rotation we calculate the two-dimensional correlation coefficient (Figure 8d). As the $\Delta SLA$ rotates, the correlation coefficient oscillates between positive and negative values. Because we show in Figure 6 that $\Delta SLA$ and $\tilde{w}$ have an inverse relationship, we look for the first minimum correlation coefficient as we rotate $\Delta SLA$ anticlockwise (red star in Figure 8d). For the example shown in Figure 8, the correlation coefficient between the nonrotated $\Delta SLA$ pattern and the $\tilde{w}$ pattern is −0.33. After the $\Delta SLA$ pattern is rotated, this value increases to −0.82.

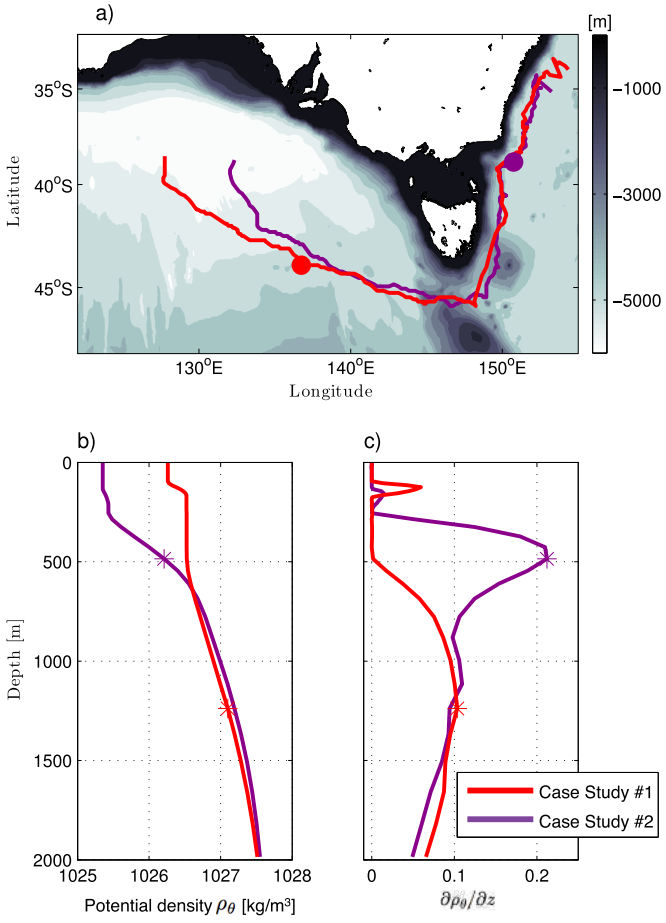


**Figure 10.** (a) Map indicating the tracks of two anticyclonic eddies chosen as case studies. The red lines relates to case study #1, with the selected location for the analysis shown here indicated by the red dot. The purple line and dot relate to case study #2. Grey colors denote bathymetry. (b) Vertical profile of potential density ($\rho_\theta$) in the eddy center (i.e., below the maximum SLA) of case studies #1 (red) and #2 (purple). (c) As in Figure 10b, but for the change of potential density in depth ($\partial\rho_\theta/\partial z$). The stars in Figures 10b and 10c indicate the bottom of the permanent pycnocline.

## 4. Linking Eddy Distortion to Vertical Velocity

We now discuss two mechanisms that link eddy distortion to vertical velocity. One mechanism is based on the conservation of potential vorticity ($Q$) and the other, on the conservation of volume—relating to the convergence and divergence of the horizontal flow as the eddy distorts.

The first mechanism, based on conservation of potential vorticity ($Q$), focuses on the relationship between stratification and relative vorticity within the eddy. The isopycnic Ertel's potential vorticity $Q$ (Ertel, 1940; Gill, 1982), considering the horizontal velocity components to be depth independent, is

$$Q=(f+\zeta_R)\frac{N^2}{g}, \tag{1}$$

where $f$ is the Coriolis parameter, $\zeta_R$ is the vertical component of the relative vorticity ($\partial v/\partial x-\partial u/\partial y$), $g$ is the acceleration of gravity, and $N^2$ is the Brunt-Väisälä frequency:

$$N^2=\frac{g}{\rho}\frac{\partial\rho}{\partial z}, \tag{2}$$

where $\rho_{theta}$ is the potential density and $z$ are depth levels.

$Q$ relates stratification and $\zeta_R$ of a rotating fluid and is conserved in an adiabatic, frictionless motion. We assume $Q$ to be conservative and $f$ to be constant between time intervals. To conserve $Q$, a change in $N^2$

AGU Journal of Geophysical Research: Oceans 10.1002/2017JC013298

has a compensating change in $\zeta_R$. In this manner, the conservation of $Q$ connects the eddy distortion to the alternating cells of vertical velocity, and we explain the concept schematically in Figure 9. As an eddy distorts, it changes the SLA and the underlying stratification ($N^2$), as isopycnals move vertically (Figures 9a–9d). The change in SLA impacts the $N^2$ because, to a large extent, the sea surface height represents the integral properties of the water column below. As $Q$ is conservative, when stratification changes, $\zeta_R$ also changes. A decrease in $N^2$ is compensated by a gain in positive $\zeta_R$, which has anticyclonic rotation in the Southern Hemisphere. Conversely, an increase in $N^2$ is compensated by a gain in negative $\zeta_R$, which has cyclonic rotation in the Southern Hemisphere. The changes in the sea level and in the eddy interior are seen as alternating cells of $\Delta SLA$, $\Delta N^2$ and $\Delta\zeta_R$ (Figures 9e–9g). Due to conservation of momentum and the rotation associated with the $\Delta\zeta_R$, upward and downward cells develop (Figure 9h). These interior changes in the eddy may explain the pattern of alternating cells seen in $\tilde{w}$.

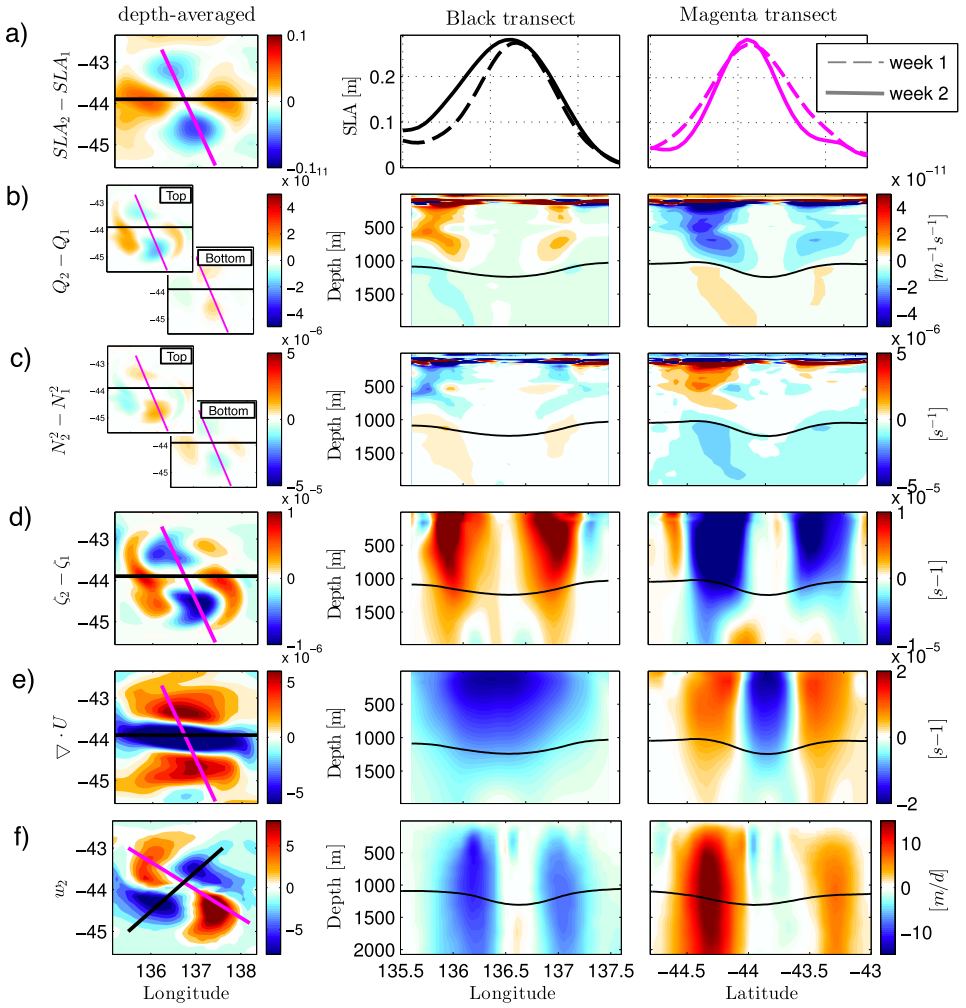


**Figure 11.** Change in (a) sea level anomaly (SLA), (b) depth-averaged potential vorticity ($Q$), (c) depth-averaged stratification ($N^2$), and (d) depth-averaged relative vorticity ($\zeta_R$; colors, left) between subsequent time steps ($t_1$ and $t_2$) for an anticyclonic eddy in the Eastern Indian Ocean (i.e., case study #1). The black and the magenta lines denote the location of the vertical sections shown in the middle and in the right columns; depth-averaged (e) horizontal divergence ($\nabla \cdot U_2$) and (f) vertical velocity ($\tilde{w}$) in the final time step (colors, left). The top and bottom plots in Figures 11b and 11c show the depth-averaged variables above and below the permanent pycnocline. In Figures 11d–11f, the variables are averaged between 0 and 2,000 m. The black and the magenta lines in the left column denote the location of the vertical sections shown in the middle and in the right columns. The black lines in the middle and right columns from Figure 11b to 11f denote the isopycnal at the base of the permanent pycnocline (1,027.1 kg/m$^3$).

AGU Journal of Geophysical Research: Oceans 10.1002/2017JC013298

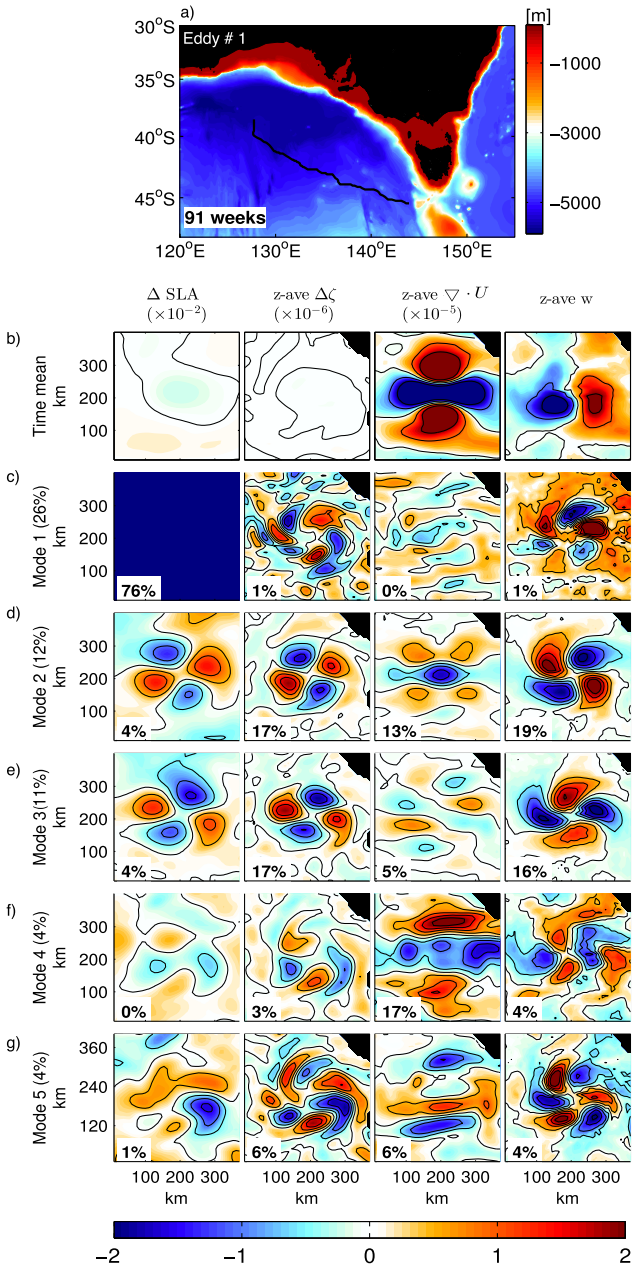


**Figure 12.** (a) Map indicating the track of an anticyclonic eddy (case study #1) propagating in the Eastern Indian Ocean (black line). Colors denote bathymetry, and the number in the bottom left corner indicate the number of weeks taken for this eddy to propagate along the track. (b) Time mean change in SLA ($\Delta SLA$) and time mean depth-averaged (0–2,000 m) relative vorticity ($\zeta_R$), horizontal divergence ($\nabla \cdot U_2$), and vertical velocity ($\tilde{w}$) for this eddy as it propagates along the track shown in Figure 12a. (c–g) EOF modes 1–5 of the multivariate EOF analysis of $\Delta SLA$, ($\zeta_R$), $\nabla \cdot U_2$, and $\tilde{w}$, normalized by the maximum value of each mode and then multiplied by each variable standard deviation, for each eddy (see section 3.3). Black lines denote null values. Percentages in white boxes are the amount of variance contained in each mode for each variable, and percentages in *y* axis label are the amount of variance for the combined variables.

The second mechanism, based on the conservation of volume, relies on the continuity within the eddy as it distorts. The eddies studied here are ageostrophic and, therefore, the divergence of their horizontal flow is nonzero. An inward distortion relates to divergence of the flow, inducing upward motion. Conversely, an outward distortion relates to convergence of the flow, inducing downward motion. This mechanism results in the same $\tilde{w}$ pattern as the mechanism proposed before.

### 4.1. Case Studies

We test these mechanisms considering two case studies of anticyclonic eddies, both originating in the EAC separation region. First, we show model fields at two locations along the trajectory of these eddies. Second, for a robust analysis, we calculate combined EOFs considering more time steps of the lifetime of these eddies.

For eddy #1, we investigate its structure when it is located in the Eastern Indian Ocean (Figure 10a, red dot). For eddy #2, we investigate its structure when it is located off Bass Strait (Figure 10a, purple dot). The structure of these eddies, in these different locations, differs in several ways. When eddy #1 is located in the Eastern Indian Ocean, it has a subsurface core, is relatively weak (0.3 m SLA and 0.4 m/s rotation speed), and is isolated from the bottom and from strong mean flow interactions. When eddy #2 is located off Bass Strait, it is surface intensified, relatively strong (0.5 m SLA and 1.2 m/s rotation speed), and interacts with the continental shelf break. Surface intensified eddies depress both the seasonal and the permanent pycnoclines. Conversely, eddies with a subsurface core have a thick layer of water that deepens the permanent pycnocline but shoals the seasonal pycnocline (e.g., mode water eddies; McGillicuddy, 2015). We define the permanent pycnocline as the maximum vertical density gradient that is not associated with the surface mixed layer. This pycnocline can be relatively shallow in surface intensified eddies (Figures 10b and 10c; purple lines) and relatively deep in eddies with a subsurface core (Figures 10b and 10c; red lines).

#### 4.1.1. Eddy #1 in the Eastern Indian Ocean

When eddy #1 is located in the Eastern Indian Ocean, it has a mixed layer extending down to 500 m and a permanent pycnocline located at ~1,300 m (Figures 10b and 10c). The thick mixed layer results from the several warming and cooling seasons the eddy has encountered since its formation (Nilsson & Cresswell, 1981). At this location, 76% of the horizontal velocity of the eddy is projected onto the barotropic mode, and 18% is projected onto the first baroclinic mode (Pilo et al., 2015).

We calculate $\Delta Q$, $\Delta N^2$, and $\Delta \zeta_R$ considering subsequent time intervals, in the same manner as we calculate $\Delta SLA$, described in section 2. Here we also choose not to rotate the eddy in the first time interval. In 1 week, this eddy distorts outward in longitude and inward in latitude (Figure 11a). $Q$ and $f$ are constant between the weeks analyzed ($\Delta Q \ll Q$ and $\Delta f \ll f$). Therefore, $N^2$ and $\zeta_R$ change together to conserve $Q$, and we can further assess how the eddy distortion relates to dynamical changes in the eddy interior.

As the eddy distorts inward, a region with previously high SLA now has lower SLA (Figure 11a, magenta section). This decrease in SLA

AGU Journal of Geophysical Research: Oceans 10.1002/2017JC013298

changes $N^2$ below (Figure 11c). Above (below) the permanent pycnocline, $N^2$ increases (decreases), as isopycnals previously depressed (compressed) relax back to their normal state. The $\Delta N^2$ above the pycnocline is of order $10^{-6}$ $s^{-1}$, and below, of order $10^{-7}$ $s^{-1}$. This stronger $\Delta N^2$ at the top is expected, as the response of isopycnals to sea level changes decreases in depth. The increase in $N^2$ occurring above the pycnocline is balanced by a gain in negative $\zeta_R$, which is consistent in depth (Figure 11d). Negative $\zeta_R$ has cyclonic rotation in the Southern Hemisphere. A positive vertical velocity (i.e., upward motion) in the final week results from these dynamical changes (Figure 11f). The $\tilde{w}$ cells are shifted anticlockwise in relation to the other variables, as shown before in section 3.3. In addition, this inward distortion is associated with divergence of the horizontal flow (Figure 11e; magenta section). Therefore, we conclude that an inward distortion induces upward motion.

As the eddy distorts outward, a region with previously low SLA now have higher SLA, depressing isopycnals below (Figure 11a, black section). Therefore, the layers above the permanent pycnocline become less stratified, seen as a negative $\Delta N^2$ (Figure 11c). A negative $\Delta N^2$ above the permanent pycnocline is balanced by a positive $\Delta\zeta_R$ (Figure 11d). The positive $\zeta_R$ has anticyclonic rotation in the Southern Hemisphere, resulting in a negative vertical velocity (i.e., downward motion) in the final week (Figure 11f). In addition, this outward distortion is associated with convergence of the horizontal flow (Figure 11e; black section). Therefore, we conclude that an outward distortion induces downward motion.

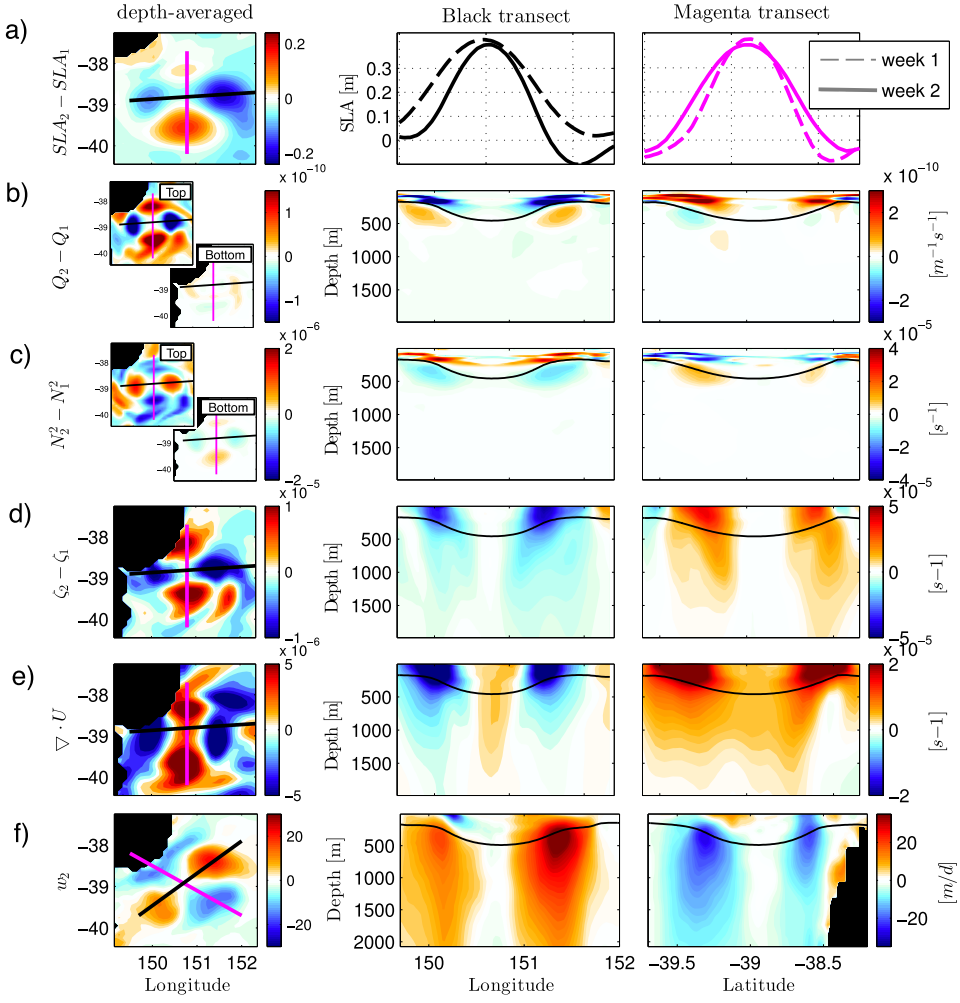


**Figure 13.** Same as in Figure 11, but for an anticyclonic eddy off Bass Strait (i.e., case study #2). The black lines in the middle and right columns from (b) to (f) denotes the isopycnal in the end of the permanent pycnocline (1,026.3 kg/m$^3$).

AGU Journal of Geophysical Research: Oceans 10.1002/2017JC013298

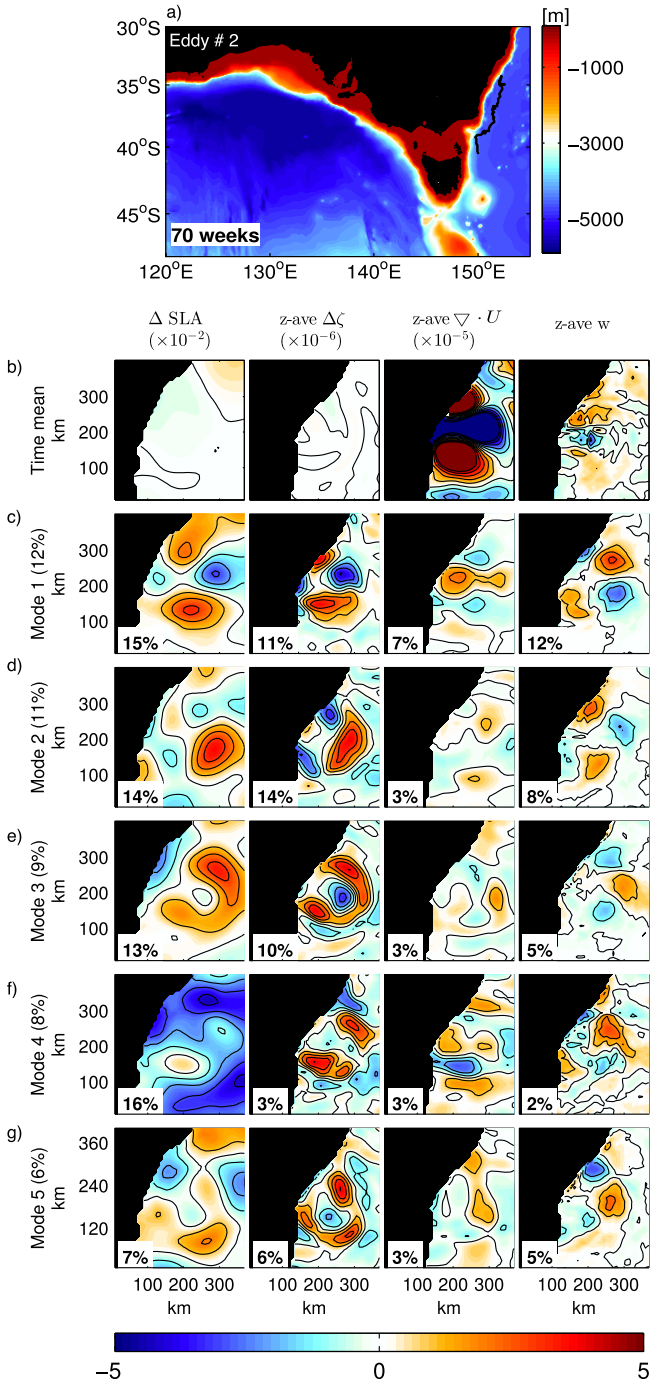


**Figure 14.** Same as in Figure 12, but for case study #2 propagating southward, off the eastern Australian shelf break.

We perform a multivariate EOF for eddy #1, to assess the coherence of the relationship between variables (Figure 12). For this analysis, we consider all time intervals of this eddy between southwest Tasmania and its dissipation (i.e., westward propagation; 91 weeks), and we follow the method described in section 2. The variables combined are $\Delta SLA$, depth-averaged $\Delta\zeta_R$, depth-averaged $\nabla \cdot U$, and $\tilde{w}$. All the variables show the pattern of alternating cells in modes 2 and 3, resulting in up to 23% of the variance (Figures 12d and 12e). As seen in this eddy daily-averaged fieds, the $\Delta SLA$ and the $\Delta\zeta_R$ cells are directly related, and both are indirectly related to $\nabla \cdot U$ and $\tilde{w}$ cells. Therefore, both mechanisms are sustained as eddy #1 propagates westward in the Eastern Indian Ocean.

#### 4.1.2. Eddy #2 Off Bass Strait

When eddy #2 is located off Bass Strait, it has a permanent pycnocline located at ~500 m (Figure 10c). At this location, 65% of the horizontal velocity of the eddy is projected onto the barotropic mode, and 27% is projected onto the first baroclinic mode (Pilo et al., 2015). The dynamical changes associated with the eddy distortion in case study #1 also take place here. An inward distortion increases $N^2$ above the permanent pycnocline, is balanced by a negative $\Delta\zeta_R$, and results in upward motion (Figure 13; black section). Conversely, an outward distortion decreases $N^2$ above the permanent pycnocline, is balanced by a positive $\Delta\zeta_R$, and results in downward motion (Figure 13; magenta section).

For the time step shown in Figure 13, the relationship between divergence of the horizontal flow and $\Delta SLA$ is the opposite of the relationship suggested in section 4. Despite this opposing relationship, the volume within the eddy is still conserved. Here the outward distortion (i.e., in latitude) is associated with divergence (Figure 13e, magenta section), and the inward distortion (i.e., in longitude) is associated with convergence (Figure 13e, black section). To determine if this apparent inconsistency is true for other time steps of this eddy lifetime we again perform a multivariate EOF analysis of four variables ($\Delta SLA$, $\Delta\zeta_R$, $\nabla \cdot U$, and $\tilde{w}$). For this analysis, we consider all time intervals of eddy #2 between its formation and south of Tasmania (i.e., southward propagation; 70 weeks). All the variables show the pattern of alternating cells in modes 1 and 2, summing up to 23% of the variance (Figures 14c and 14d). As suggested in section 4, the $\Delta SLA$ and the $\Delta\zeta_R$ cells are directly related, and both are indirectly related to $\nabla \cdot U$ and $\tilde{w}$ cells. Therefore, we conclude that, in the time interval chosen as a case study (i.e., when the eddy is off Bass Strait; Figures 10a, purple dot and 13), other forcings acted on the divergence pattern. These forcings might include eddy interaction with the bottom, with the mean flow, with other mesoscale features, and with the wind.

## 5. Discussion and Conclusion

We show that alternating cells of vertical velocity are a recurrent feature in anticyclonic eddies formed at the EAC separation region, as seen in a near-global, eddy-resolving model. These cells are most intense between 500 and 1,500 m depths, and are linked to eddy distortion, which is the change in eddy isotropy. These alternating upward and downward cells have been previously reported in cyclonic eddies of the Agulhas Return Current (Nardelli, 2013), in an eddy-dipole in the Iceland basin (Pidcock et al., 2013), and in an idealized anticyclonic eddy (Martin & Richards, 2001). In the eddies studied here, the alternating vertical velocity cells have magnitudes